Dissertation

zur Erlangung des akademischen Grades

"Doktor der Naturwissenschaften"

im Promotionsfach Chemie

The concept of quantum sensing from a chemical point of view

Investigations on sensor optimization and application-relevant implementations

---

vorgelegt

dem Fachbereich Chemie, Pharmazie und Geowissenschaften
der Johannes Gutenberg-Universität Mainz

von

René Wieczorek
geboren in Görlitz

Mainz, November 2019

This dissertation was carried out at the Institut of Physical Chemistry at the Johannes Gutenberg-Universität Mainz from November 2014 to December 2015 and at the Department of Physics at the Universität Osnabrück from January 2015 to November 2019.

D77 (Dissertation Johannes Gutenberg-Universität Mainz)

Dean of Faculty

1st Report

2nd Report

Submitted	November 11th, 2019
Oral examination	December 13th, 2019

Abstract

Quantum sensing is a research field evolving recently in which accumulates both a deeper theoretical understanding of the underlying principles of using quantum systems for the detection of physical quantities and their application in concrete scientific issues.

The present thesis examines the topic of quantum sensing under various aspects that are predominantly chemically motivated.

First, the term quantum sensing is defined and its underlying physical principles are described with special reference to the magnetic resonance methods which were predominantly used to obtain the results presented.
Next, the sensors investigated and applied in this thesis are presented: **1.** the endohedral $^{14}N@C_{60}$ fullerene as a molecular implementation and **2.** the diamond-hosted negatively charged nitrogen-vacancy (NV^-) center. Depending on the nature of the diamond matrix, the latter type can be further subdivided according to its effective size which results in either **2.1** nanodiamond-based or **2.2** bulk diamond embedded NV^- center sensors. The size differentiation is accompanied by different sensing applications which are discussed accordingly.

Future applications have been discussed for $N@C_{60}$, each of which is based on the preserved $S = 3/2$ electron spin of the intercalated nitrogen atom shielded by the fullerene molecule. These include primarily the use as quantum bit in a carbon nanotube-based quantum computer and as sensor of spin-dependent currents in fullerene-based semiconductor and organic solar cell devices. Optically detected magnetic resonance (ODMR) measurements of collaborators on material provided by us have shown that the detection of a single $^{14}N@C_{60}$ molecule spin is possible. Yet, the electron spin resonance spectrum obtained by ODMR is corrupted by additional signals. A plausible assignment can be given with positively or negatively charged fullerene species. Their spectroscopic characterization is incomplete especially for fullerene cations due to their chemical instability. In this thesis a revision of a literature-known protocol - the oxidation of fullerenes using zeolite-supported iron(III) - is conducted. Its characterization by different methods (X-ray diffraction and nitrogen sorption measurements as well as EPR spectroscopy) and the use of $^{14}N@C_{60}$ as a high-accurate standard make it possible to precisely determine the g factor of C_{60}^+, C_{70}^+ and $C_{120}O_2^{2\bullet}$.

The advancement of the protocol using Ce(IV) leads to a significant reduction of the thermal demand of the oxidation reaction and it is applied to the extent that a first attempt is made to measure a bulk C_{60}^{+}-N@C_{60} coupling spectrum.

Nanodiamond is a material which sizes on the scale of few nanometers. In current research endeavors it aroused interest due to its specific properties. Examples of its application are provided by the detection of magnetic fields within biological cells, the utilization as non-bleaching fluorescence label, and the implementation as a cell compartment penetrating drug delivery agent. The nanodiamond surface is of decisive importance in each of this contexts. Either it serves as a functionalization platform, which must be adapted to the molecules to be tethered by chemical processes, in order to name the latter application example, or it acts as a source of interference since it comprises carbon-inherent radicals. This affects the first two applications and in particular NV^{-} center-based quantum sensing. Therefore, in this thesis the objective is pursued to functionalize the surface using novel chemical methods and thereby reduce the surface spin density. This is achieved with a fluorination and a hydrazonation approach. Also, the treatment with strong bases can provide a slight improvement. The analytical methods used to characterize the results of the chemical functionalization processes include X-ray photoelectron, infrared absorption and bulk EPR spectroscopy. Furthermore, the effect of decreased surface radical density due to base treatment is confirmed by ODMR measurements on clusters containing about 30 single-digit nanodiamonds.

The detection of physical and chemical processes at the level of individual molecules is of decisive importance. On this scale classical methods can only provide average values of physical quantities. But both the understanding of how original nanomaterials function and the knowledge about the emergence of ensemble properties on the basis of their individual subsystems are of academic and application-related interest.
We present results which demonstrate the detection of an electron transfer reaction between the diamond surface and few nickel bis(diphenyldithiolene) complex molecules. The corresponding sensor is provided by the NV^{-} center. Supported by quantum chemical calculations we can assume statements about the concrete mechanism of the reaction and first statements about the adsorption geometry of the transition metal complex are possible.

Thus, this work can be regarded as a contribution to have improved a relatively

recent physical measuring technique on the material level and to have led to a concrete and novel implementation.

Abstract in German

Die Quantensensorik (engl. *quantum sensing*) ist ein sich neuerdings entwickelndes Forschungsgebiet, in dem sich theoretische und anwendungsbezogene Ansätze vereinen. Dabei werden die zugrundeliegenden physikalischen Prinzipien untersucht, die notwendig sind, um die Wechselwirkung zwischen Quantensystemen und ihrer Umgebung unter dem Gesichtspunkt eines Messprozesses zu verstehen. Prägnant ist hier etwa, dass die im Zusammenhang mit der Verwendung von Quantensystemen als Quantenbits für störend erachtete Dekohärenz nun als Signaltransduktionsmechanismus aufgefasst werden kann.
Außerdem wird die Entwicklung neuer meist im Größenregime weniger Atomabmessungen angesiedelter Sensoren forciert und zuletzt die Anwendung in konkreten Fragestellungen betrieben.
Die vorliegende Arbeit betrachtet *quantum sensing* unter verschiedenen Fragestellungen, die vorwiegend chemisch motiviert sind.

Zunächst wird der Begriff *quantum sensing* definiert und es werden dessen physikalische Grundlagen mit besonderer Berücksichtigung der hier verwendeten Magnetresonanz-Methoden erläutert.

Weiterhin werden die verwendeten Sensoren vorgestellt: **1.** Als molekulare Realisierung das endohedrale $^{14}N@C_{60}$-Fulleren ($^{14}N@C_{60}$) und **2.** das Diamant-inhärente, negativ geladene Stickstofffehlstellen-Zentrum (NV^--Zentrum). Dieser Typ kann in Abhängigkeit von der Beschaffenheit der Diamantmatrix hinsichtlich seiner effektiven Größe weiter unterteilt werden gemäß **2.1** Nanodiamant-basierte und **2.2** in *bulk*-Diamant, d.h. Diamanten einer makroskopischen Ausdehnung, eingebettete NV^--Zentrum-Sensoren. Mit der vorgenommen Größendifferenzierung gehen verschiedene Einsatzmöglichkeiten einher, die entsprechend beleuchtet werden.

Für $^{14}N@C_{60}$ sind zukünftige Anwendungen diskutiert worden, die jeweils auf den durch das Fulleren-Molekül konservierten $S = \frac{3}{2}$-Elektronspin des inkalierten atomaren Stickstoffs abstellen. Vorrangig gehören dazu die Verwendung als Quantenbit in einem Kohlenstoffnanoröhren-basierten Quantencomputer und als Sensor spinabhängiger Ströme in Fulleren-basierten Halbleiter- und organischen Solarzellensystemen. Optisch detektierte Magnetresonanz (ODMR)-Messungen von Kollaborationspartnern an von uns zur Verfügung gestelltem Material haben zum ersten Mal gezeigt, dass die Detektion des Spins eines einzelnen $^{14}N@C_{60}$-Moleküls

möglich ist. Das mittels ODMR erhaltene Elektronenspinresonanz (EPR)-Spektrum ist allerdings durch zusätzliche Signale korrumpiert. Eine naheliegende Zuschreibung findet sich in positiv oder negativ geladenen Fullerenspezies. Deren spektroskopische Charakterisierung ist insbesondere für Fulleren-Kationen unvollständig, was auf ihre chemische Instabilität zurückzuführen ist. Hier wird eine Revision eines Literatur-bekannten Verfahrens - der Eisen(III)-vermittelten Oxidation an Zeolithen - vorgenommen. Dessen Charakterisierung mittels verschiedener Methoden (Röntgendiffraktometrie, Stickstoff-Physiosorptionsmessungen und EPR-Spektroskopie) und die Verwendung von $^{14}N@C_{60}$ als hochgenauem Standard ermöglichen es, den g-Faktor von $C_{60}{}^{+}$, $C_{70}{}^{+}$ und $C_{120}O_2{}^{2\bullet}$ präzise zu bestimmen. Die Weiterentwicklung des Protokolls unter Verwendung von Ce(IV) führt zu einer deutlichen Absenkung des thermischen Bedarfs der Oxidationsreaktion und sie wird dahingehend angewendet, dass ein erster Versuch zur Messung eines C_{60}-Kation-$N@C_{60}$-Kopplungsspektrums unternommen wurde.

Nanodiamant ist ein Material im Größenbereich bis zu wenigen Nanometern, das durch seine spezifischen Eigenschaften in der aktuellen Forschung vielseitige Anwendung findet - etwa zur Detektion von magnetischen Feldern innerhalb von biologischen Zellen, als photostabiler Fluoreszenz-Marker oder als Zellkompartimente penetrierender Wirkstoff-Transporter. Hierbei kommt der Nanodiamantberfläche eine entscheidende Bedeutung zu, insofern sie entweder als Funktionalisierungsplattform dient, die den jeweilig anzubindenen Molekülen gemäß durch chemische Verfahren angepasst werden muss, um das letztgenannte Anwendungsbeispiel zu benennen, oder als Träger von Radikalen als Störquelle auftritt. Dies betrifft die beiden erstgenannten Verwendungsmöglichkeiten und insbesondere die NV^{-}-Zentrums-unterstützten Quantensensorik. In dieser Arbeit wird deshalb das Ziel verfolgt, durch neuartige chemische Methoden, die Oberfläche so zu funktionalisieren, dass zugleich deren Radikaldichte vermindert wird. Dies gelingt mit einem Fluorierungs- und einem Hydrazonierungsansatz, wobei auch die Behandlung mit starken Basen eine wenn auch nur leichte Verbesserung erbringt. Die zugehörigen analytischen Methoden, um das Ergebnis der verschiedenen chemischen Verfahren zu charakterisieren, umfasst die Röntgenphotoelektronen-, die Infrarotabsorptions- und die klassische EPR-Spektroskopie. Weiterhin wird der Radikaldichte-senkende Einfluss der Basenbehandlung auf die Oberfläche mit Hilfe von ODMR-Messungen an Agglomeraten von etwa 30 Nanodiamanten bestätigt.

Die Detetektion von physikalischen und chemischen Vorgängen auf der Ebene

einzelner Moleküle ist von entscheidender Bedeutung. Klassische Methoden können auf dieser Skala lediglich Mittelwerte von physikalischen Größen liefern. Aber sowohl das Verständnis der Funktionsweise von originären Nanomaterialien als auch die Gewinnung von Erkenntnissen über das Zustandekommen von Ensembleeigenschaften auf Grundlage ihre einzelnen Teilsysteme sind von akademischen und anwendungsbezogenem Interesse.
Wir stellen Ergebnisse vor, in denen der Nachweis einer Elektronentransfer-Reaktion zwischen der Diamantoberfläche und einiger weniger Nickel-bis(diphenyldithiolen)-Komplexmoleküle erbracht wird. Der entsprechende Sensor wird durch das NV^--Zentrum gestellt. Unterstützt durch quantenchemische Rechnungen können Aussagen über den konkreten Mechanismus der Reaktion vermutet werden.

Insofern kann diese Arbeit als Beitrag angesehen werden, ein relativ neues physikalisches Messverfahren auf materieller Ebene verbessert und einer konkreten Anwendung zugeführt zu haben.

Acknowledgements

In lieu of an opening quotation, I wish to state with greatest emphasis at this stage:

"No man is an island entire of itself; every man
is a piece of the continent, a part of the main;
...
And therefore never send to know for whom
the bells tolls; It tolls for thee."

which words are true so much, that two poets, John Donne, from whose poem I borrowed these lines, and Ernest Hemingway, who took the last ones of it and wrote a novel, could not refrain from proliferating them.

Thus, there should be so many deserving my thanks and indeed, here we go:

1. I would like to thank Prof. Dr. ??? for giving me the opportunity to undertake my doctoral thesis under his supervision. Finally, that he had an open ear whenever it was required.

2. I am grateful to Prof. Dr. ???, who acts as chairman of the examination committee.

3. My thanks go to Prof. Dr. ??? and Prof. Dr. ??? both of whom have agreed to be part of my examination board.

4. My sincere gratitude go to ???, without whom there would be no word here as it is now. There would also be no café relaxation, no puzzle foxes and nobody would have put on glasses.

5. I would like to thank ???, who has always helped me with every one of my small and large laboratory problems, and her connections within the institute have been extremely helpful. I would also like to thank ???, who actively supported me in my early days in Osnabrück and who always showed interest in all technical and experimental questions.

6. Dr. ??? I owe my thanks for the time we spent together in Mainz during our undergraduate studies - it was so many long nights! - and the first year of my doctoral thesis time, the help during the relocation, and also the last given encouragement.

7. My special thanks go to Dr. ???, Dr. ???, and ??? for the constructive collaboration which results in an interesting publication.

8. I am indebted to Dr. ??? for providing us with a sample that not only helped to cut the Gordian knot of month-lasting troubleshooting, but also enabled some nice results.

9. ??? I would like to thank for a good cooperation in many areas, which was always characterized by the fact that one could rely on each other.

10. I would like to thank the team of the precision mechanics workshop headed by ??? and the electrical workshop team headed by ??? as well as ??? as manager of the chemicals store for being extremely helpful at all times.

11. I thank all our Bachelor students, also known as 158 Street Gang, for their dedicated, creative, and helpful service during their time with us, namely ???, ???, ???, ???, ???, and ???. The same applies to ???, our current Master student.

I thank my family, my family-in-law, and my friends for their support and understanding. A special thanks goes to my dear sister-in-law ??? for every good meal that we had together, especially during our holidays in Turkey.

And with words that are even older than the poem quoted above: "So the last shall be first", ???, for simply everything and even more. Tu kalbema dori. Ma tera bisjor dost dorom.

Contents

0 Introduction

According to *Karl Popper's* epistemology it is but one experimental result contradicting the implications of a certain scientific statement that allows for its rejection.[1] Alternatively, a new model must be developed then, that is consistent with empirically data obtained previously. Basically, this interplay between theoretical predictions and experimental testing constitutes the method of empirical science. So, it is plausible to state that the process of measuring physical quantities in the course of experiments is one of the decisive aspects in the development of our scientific understanding of nature.

While these explanations seem to be almost trivial, they become concise when assumptions at the scale of individual molecules are to be tested. How can models of such objects be falsified if measuring apparata are available that only allow us to fathom large ensembles of them? And even more, how are we supposed to generate models at all when system's parameters are not fully in our hand? A simple example may introduce the underlying problem.

Let us assume that on an ideally flat surface alkenes may be present whose substitution pattern is given by −RHC=CHR− where R is sterically more demanding than H (see Fig. 1). In the gas phase it is generally expected that the energy of the *trans* alkene is lower than that of the *cis* conformation because of steric conditions (denoted as E_{steric} in Fig. 1**AI**) and the existence of an activation barrier for the transition between both conformers. On the surface, however, agostic interactions E_{agostic} between surface atoms and protons, which we suppose to be stronger for *cis* alkenes due to specific surface reconstruction, may now ensure that the energy difference between the systems *cis* isomer-substrate and *trans* isomer-substrate is annihilated, i.e., the destabilizing contribution E_{steric} is compensated by E_{agostic} for the *cis* isomer, and for the *trans* isomer, conversely, the energy of the substrate is risen due to unfavorable E_{agostic}. Further substrate-molecule interactions may also weaken the π bond so that the barrier to rotation is strongly reduced. The corresponding energy levels (lower scheme) and the total potential including all interactions (upper trace) are demonstrated in Fig. 1**AIIa**, where the potential consists of two minima of equal energy and transitions between them are barely hindered.

Now, if we were to investigate this system in terms of its temporal evolution, what would be the result of a "Which conformer?" measurement, that we consider as being designed to be sensitive to the *cis* isomer, while the *trans* isomer should be silent? For the time-resolved ensemble measurement on many molecules, which

takes place so to speak from a distance and is therefore indicated by a naked eye in Fig. 1, it can be expected that fast transitions between the two conformers which, in addition, are uncorrelated regarding different molecules will give us a constant signal since on average an equal number of alkenes is in the *cis* and the *trans* conformation (see Fig. 1**AIIb**). However, inspecting a specific molecule over time and provided that we have sufficient time resolution compared to the conformers' lifetimes, we may obtain energy "blinking" of the molecules while they inter-pass between the two energy levels (see Fig. 1**AIIb**, where the single molecule (SM) measurement is indicated by a magnifier). The autocorrelation of first measurement's signal trace is $\varphi(\tau) = \overline{S(t)\,S(t+\tau)} = \lim_{T_0\to\infty}\frac{1}{T_0}\int_0^{T_0} S(t)\,S(t+\tau)\,\mathrm{d}t =$ const.; thus the process seems to be totally deterministic as we already inferred from the signal trace (see Fig. 1**AIIc**). However, the results obtained on a SM lead to $\varphi(\tau) = \lim_{T_0\to\infty}\frac{1}{T_0}\int_0^{T_0} S(t)\,S(t+\tau)\,\mathrm{d}t = e^{-\frac{\tau}{\tau_\delta}}$, with conformer transition time constant τ_δ and sufficient normalization (see Fig. 1**AIIc**).[2] From this it can be deduced that the presence of a conformer at time τ can only be attributed to the fact that it already existed at time t for $\tau \ll \tau_\delta$. This finding, although not particularly surprising, can only be obtained by measurement on a SM, the ensemble method completely masks this behavior. If we dare to draw a conclusion from this simple example in regard to a practical application, such as the catalysis of *cis*/*trans* isomerization, we can deduce that the reaction on this particular surface takes place under full kinetic control since otherwise we would have seen an equilibrium-related contribution in

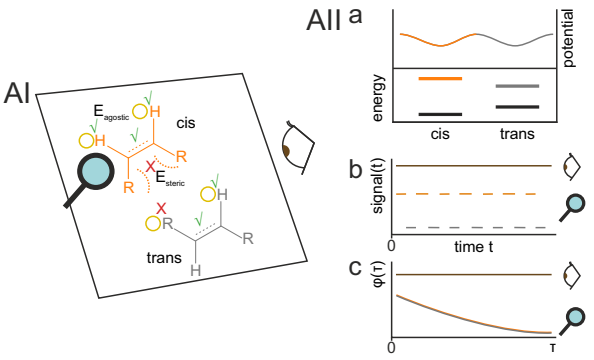

Figure 1: Single molecules (SM) on surfaces and their investigation. **(AI)** Two alkenes which tend to isomerize equally likely in *cis*/ *trans* conformation due to concerted, molecule-inherent (E_{steric}) and specific surface atom (yellow bordered circle)-molecule interactions symbolized by E_{agostic} and weakened π bond, which are stabilizing (green tick) or destabilizing (red cross). **(AII) a** The energy of the *cis* conformer (orange bar), the *trans* conformer (gray bar) and the subtrate (black bar), respectively. The aforementioned interactions cause a symmetric potential (upper trace). **b** and **c** depict temporal signal outcome and autocorrelation $\varphi(\tau)$ for ensemble (eye) and SM observation (magnifier).

$\varphi(\tau)$. The ensemble measurement, however, does not allow us to make any statement about possible process dynamics due to averaging.
There are already examples of experiments that have demonstrated the conclusions obtained on our simple surface model in real-world systems. The reduction of resorufin to amplex red on nano-confined catalyst consisting of Pt nanoparticles sandwiched between a SiO_2 core and a mesoporous SiO_2 layer have shown that the frequency of the actual catalysis reaction in this system is increased compared to bulk Pt by a factor of nearly 10.[3] However, the overall reaction includes diffusion of the precursor to and of the product molecule away from the Pt catalyst inside the mesoporous SiO_2 layer; measurement data allowed to infer that this process limits the total turn over frequency (TOF) to approximately the ensemble value. To put it clear, the bulk measurement would have revealed that nanoparticles do not achieve enhanced reactivity, while on the SM level this conclusion was proved to be not valid. Moreover, the rate limiting mechanism could be elucidated as well, which is a prerequisite for further system improvement. Additionally, Au@mSiO_2 2D nanoplate-mediated reduction of resazurin to yield resorufin has been investigated on SMs.[4] It has been observed that the TOF decisively depends on the very location where the reaction takes place. The sequence of decreasing reactivity according to corners > edges > flat facets was certainly to be expected, but the result that a gradient along the relatively extended nanoparticle surface areas is also present must be attributed as original insight caused by the SM character of the measurement. That even one atom can influence the reactivity of surface-attached molecules has been reported for the *cis-cis* and *trans-trans* isomerization of porphycene on a Cu(100) surface, in whose vicinity deliberately copper adatoms were placed.[5] Depending on the distance of the adatom, the degree of isomerization could be tuned. Furthermore, cooperative effects within porphycene rows were observed. Since no chemical reaction between the copper adatom and the molecules took place, the observations were interpreted as tautomerization was only be governed by relatively weak, long-range forces. Thus, these last two results show that the heterogeneity of bulk materials represents a realization of various nanosystems that cannot be detected and discriminated at the level of ensemble measurements. Yet, in order to optimize these materials they need to be grasped at the SM level. However, if experimental data exist on this scale, the corresponding analysis methods must already be available. And indeed, to date various measurement tools are capable of detecting physical quantities in the SM range. Their emergence can be traced back to the development of the scanning tunneling and later the scanning force microscope, whereas the first was used in Ref. [5].[6,7] Because of the Abbe

diffraction limit, those imaging techniques, that used electron beams as mediators, in this field pioneered, e.g., with the first images of DNA molecules using transmission electron microscopy in 1956.[8] The development of various super-resolution optical methods, such as stimulated emission depletion,[9,10] total internal reflection fluorescence,[11] and photoactivated or stochastic optical reconstruction microscopy,[12,13] have now extended the SM imaging capability into the UV/VIS range; Ref.s [3, 4] listed above took advantage of these methods. Furthermore, access to the chemical structure of SMs is provided by surface-enhanced and tip-enhanced Raman spectroscopy.[14–16]

Magnetic resonance, be it nuclear magnetic (NMR) or electron paramagnetic resonance (EPR), as ubiquitous measurement methods in many areas of natural science, entered the group of analytical methods that achieve SM sensitivity only at the beginning of this decade. The corresponding sensor is a lattice impurity of diamond, the negatively charged nitrogen-vacancy (NV^-) center.[17–21] Its electronic triplet ground state and specific level transition dynamics including the electronic singlet state allow the spin state of the system to be read out by optically detected magnetic resonance (ODMR), where commonly non-resonant green laser radiation is utilized for excitation and the fluorescence response in the red area of the visible spectrum is detected.[20,21] The sensitivity, for example, to magnetic fields is provided by the magnetic moment of the $m_S = \pm 1$ spin sub-states. Since the NV^- center can also be polarized by laser irradiation to a degree above the thermal Boltzmann limit, it constitutes, at least in weak static magnetic fields, where the $m_S = \pm 1$ spin sub-state degeneracy is lifted, a two-level system (TLS) which can be coherently controlled by microwave (mw) radiation.[20–22] By doing so, a large catalogue of sensing schemes is amenable to detect static and alternating magnetic fields originating either of random (noise) processes or coherent evolution of neighboring spins. It has been developed in several branches of classical magnetic resonance and quantum sciences, and what nowadays is denoted as quantum sensing.[23]

0.1 Quantum sensing - definition

Besides a few historically preceding implementations quantum sensing is a research field that has noticeably burgeoned only recently.[20,23–25] The particularity of this scientific approach consists in elaborating the common principles of previously as distinct regarded physical apparatuses like atomic vapor cells, trapped ions, superconducting quantum interference devices, quantum dots, and solid state

spins. The perception of their diversity seemed justified all the more since they are respectively responsive to various physical quantities ranging from electric and magnetic fields, to temperature and mechanical stress. Nevertheless, being, each in its own right, quantum systems and demonstrating unparalleled pairing of sensitivity and spatial resolution compared to their classical counterparts, revealing the quantum aspect of measurement protocols seems to offer new opportunities for many branches of science. The Copernican revolution of quantum sensing is, at any rate, that the brittle nature of quantum systems which, e.g., in quantum computing has been experienced as a notorious drawback, is used as a source to gain knowledge about the influencing environment. In order to rationalize this new approach, quantum sensing resorts to adopt concepts such as quantum coherence, quantum entanglement, and the DiVincenzo criteria from parent areas of quantum science,[22] and it even capitalizes on results of well-established spectroscopic methods, e.g., NMR and EPR. However, a pivotal purpose of quantum sensing research currently exists in the development of application-confined measurement protocols and novel atomic-size quantum sensor systems.
To pursue the latter objective systematically, it is helpful to have a definition of a quantum sensor at hand, besides the concrete examples given in the preceding. In Ref. [23] a hierarchy of criteria has been developed which states the following prerequisites for a physical object to be a quantum sensor.

1. It consists of a quantum object which enables physical quantities to be measured by means of its quantized energy states.

2. The basis or the eigenstates of the quantum object can be prepared in superposition states, so that the temporal change of the phase relationship between them can be employed to infer the influencing signal source from it.

3. Real quantum superiority may be achieved when two or more quantum objects can be entangled, whereby sensitivity and precision surpassing classical limits are feasible.

The first definition is rather minimal and includes long-established techniques. For example, optical molecular spectroscopy can be included. Dye-molecules that show an altered absorption in different solvents (solvatochromism) would then be detectors for the latter. The second is more demanding since coherent control of the energy states is required. Still, widely used techniques, like NMR and EPR, are known that capitalize on this principle. The systems we investigate in this thesis operate at this quantum sensor level. Superposition states are non-equilibrium

states and their longitudinal and transversal relaxation can be phenomenologically described by time constants T_ψ. The sensitivity of a quantum sensor relies on T_ψ by $\frac{1}{\gamma\sqrt{T_\psi}}$, where γ is a signal-dependent transduction parameter.[23] Thus, it can be seen that prolonging T_ψ is a crucial step for sensor optimization.

0.2 Quantum sensing - results of previously conducted experiments

In order to provide a first overview of the detection capabilities of the NV^- center, we list experimental results of recent years focusing on the detection of spin species. Regarding stability, sensitivity, and scope of applications, the NV^- center represents an already mature quantum sensor operating at ambient conditions.[20,21,26,27] Results to probe in-bath,[28,29] few,[30] and single[31] electron as well as bath[32] and single[33–35] nuclear spins residing within the diamond matrix has been extensively reported. Sensing of paramagnetic species exterior to the diamond host has been conducted by various protocols. Because the longitudinal spin relaxation time T_1 of the NV^- center is sensitive to the presence of high spin cations (Mn^{2+}, Gd^{3+}) in the few-spin regime,[36–38] they were used as lipid bilayer embedded spin labels with a sensitivity of four Gd^{3+} spins and sub cellular resolution.[39] By designing appropriate linker molecules tethered on both, the diamond surface and the Gd^{3+} complexation agent, which are deterministically cleavable with respect to changes of pH or redox potential these quantities are measurable on the zmol range.[40] NMR experiments probing surface-related nuclear spins started with sample sizes of 10^4.[41,42] Limited through meager spectral resolution, more advanced schemes have been developed, thereby, achieving resolvable frequency values of a few kHz[43] or even arbitrarily[44,45] small. Eventually, single-spin sensitivity has been reported for protons and ^{29}Si nuclei.[46,47]

0.3 Quantum sensing - the search for new sensor implementations

In pursuit of the goal of developing new quantum sensors, the NV^- center can be seen as a benchmark. Therefore, efforts have been taken to maintain the diamond environment and to replace the impurity-atom nitrogen, for example, with silicon. This approach led to silicon-vacancy centers, which, however, possessed inferior spin properties.[48] A further solid state candidate is given by an exchange of the diamond matrix against silicon, where electron spins are generated by phosphor

doping; the electrical readout of which showed superior longitudinal relaxation times in the regime of seconds at low temperatures compared to the NV^- center ($\approx 10^{-1}$ s).[49,50]
A realization by a molecular system is conceivable with the group-V endohedral fullerenes $N@C_{60}$ and $P@C_{60}$.[51] These were originally proposed in particular as quantum bits in a possible realization of a quantum computer due to their relatively high relaxation times and potential scalability in linear arrangements.[52–54] Conversely, as shown above, the former feature is advantageous for sensing applications, too. Meanwhile, preliminary results have been reported presenting the $N@C_{60}$-mediated detection of solvent molecules and Cu^{2+} ions using ensemble EPR spectroscopy as well as the electrically detected magnetic resonance (EDMR) spectrum of a $N@C_{60}$-coupled C_{60} cation.[55–57] In contrast to the NV^- center, $N/P@C_{60}$ possess no inherent mechanism that allows for single molecule addressing. While readout using the EDMR protocol can be expected to result in a sensitivity of $< 10^3$ molecules,[58] it has very recently been demonstrated that dipolar coupling of $N@C_{60}$ to the NV^- center electron spin enables coherent addressing of a single $N@C_{60}$ molecule.[59]

0.4 Outline

The topics covered in the preceding overview serve as a guideline to this thesis insofar as we aim to investigate certain aspects of quantum sensing. The first two chapters are intended to provide an introduction. In Chapter 1 a theoretical foundation to EPR spectroscopy and concepts of quantum sensing is presented. Material and technical aspects of quantum sensor implementations, given by the $N@C_{60}$ fullerene and the NV^- center, are dealt with in Chapter 2. Chapter 3 sets out results which we obtained on bulk C_{60} cation generation - a species whose occurrence under currently proposed readout protocols for $N@C_{60}$ need to pondered as a spectroscopic contribution. Wet-chemical approaches pursued to optimize the spin properties of nanodiamond-hosted NV^- centers are demonstrated in Chapter 4. By demonstrating the feasibility of this method, particularly regarding the DAST-mediated fluorination and hydrazonation, chemical functionalization protocols may accompany to standard termination techniques in future. The topic of Chapter 5 is the detection of an electron transfer reaction between nickel bis(diphenyldithiolene) and the diamond surface on the SM level which widens the horizon of applications amenable to the NV^- quantum sensor. The conclusion of this thesis and an outlook is issued in Chapter 6.

1 Theoretical foundations of quantum sensing

Quantum mechanics is the theoretical framework of quantum sensing. Therefore, the present chapter provides the physical concepts which are necessary to get along the experimental results presented in the remainder of this work. Hereby, the leading thought will be: How can we prepare and control a quantum state to garner information on its environment that, likewise, constitutes the system to be investigated? (see Chap. 1.4) Furthermore, since predominantly electron paramagnetic resonance methods were used, their basics are briefly introduced in Chap. 1.1-1.3.

1.1 Basics of magnetic resonance

In its magnetic resonance related branches, quantum sensing relies on the fundamental property of an electron and some nuclei[1] to possess a spin which is totally determined by a quantum number J.[2] From its value an operator[3] $\underline{\hat{J}} = (\hat{J}_1, \hat{J}_2, \hat{J}_3)^{\mathrm{T}}$ can be deduced whose eigenvalue spectrum for a projection on to one of the axes is given by $m_J|_{i=1,2,3} = J, J-1, \ldots, -J$, $J \in \mathbb{Z} \cup \left\{-\frac{1}{2}, \frac{1}{2}\right\}$. Symmetry characteristics, especially the commutation relationships,[4]

$$\left[\hat{J}_i, \hat{J}_j\right]_{\forall i,j,i\neq j} = \mathrm{i}\hbar \sum \varepsilon_{ijk} \hat{J}_k \quad \text{and} \quad \left[\underline{\hat{J}}^2, \hat{J}_i\right]_{i=1,2,3} = 0; \quad \underline{\hat{J}}^2 = \hat{J}_1^2 + \hat{J}_2^2 + \hat{J}_3^2, \quad (1.1)$$

classify $\underline{\hat{J}}$ as an angular momentum operator - a circumstance, that deeply governs the underlying physics, as manifested, e.g., in spin-orbit coupling effects and spin state rotations.[60,61] Associated with the spin angular momentum operator $\underline{\hat{J}}$ is the magnetic (dipole) moment of a particle of charge q and mass m

$$\underline{\mu}_J = g\frac{q}{2m}\underline{\hat{J}} = \gamma \underline{\hat{J}}. \quad (1.2)$$

where g is a factor which is particle-dependent and $\hbar = \frac{h}{2\pi}$ is the reduced Planck constant, with $h = 6.626\,07 \times 10^{-34}$ Js. For nuclei its value depends on the inner structure of the particular isotope, however, calculations from first principles are

[1] A necessary and sufficient condition that for a nucleus holds true $J \neq 0$, is that neutron and proton number are not even at the same time.

[2] Usually, the spin quantum number J is denoted as S for an electron and I for nuclear spins.

[3] $\underline{A}^{\mathrm{T}}$ indicates the transpose of a vector, i.e $\underline{A}^{\mathrm{T}}_{ij} = \underline{A}_{ji}$

[4] ε_{ijk} represents the antisymmetric symbol which is 1 for cyclic permutations of $(1,2,3)$, -1 for those being anti-cyclic, and 0 if indexes mutually equal.

scarce. Conveniently, the gyromagnetic ratio γ is referred to as a characteristic property and experimentally determined. For an electron, to which we predominantly devote in the proceeding, its value is $g_\mathrm{e} = 2.002\,32$ reflecting the behavior of the electron under certain interaction symmetries.

1.1.1 Heuristic derivation of electron magnetic resonance in a static magnetic field

The electron as spin-possessing particle enters the experimentalists' domain when residing in a magnetic field which, firstly, may be given as time-independent $\underline{B} = (0, 0, B_3)^\mathrm{T} = (0, 0, B_z)^\mathrm{T}$. In order to achieve the main results swiftly, we proceed heuristically.[60,61] From classical electromagnetism we employ the relation $\underline{\mu} = -\nabla_{\underline{B}} E \Rightarrow E = -\underline{\mu}\underline{B}$, with the magnetic moment $\underline{\mu}$ and the energy E. Regarding an electron with mass m_e and charge $-e$, Eq. (1.2) transforms to

$$\underline{\mu}_\mathrm{e} = g_\mathrm{e}\frac{-e}{2m_e}\hat{\underline{S}} = \frac{-g_\mathrm{e}\mu_b}{\hbar}\hat{\underline{S}} = -\gamma_\mathrm{e}\hat{\underline{S}}. \tag{1.3}$$

where $\mu_b = 9.274 \times 10^{-24}\,\mathrm{J\,T^{-1}}$ is the Bohr magneton. Since for an electron $S = \frac{1}{2} \Rightarrow m_S = \pm\frac{1}{2}$, eventually, we end up on

$$E = -\underline{\mu}_\mathrm{e} \cdot \underline{B} \xrightarrow{\hat{S}_z\left|\frac{1}{2},\pm\frac{1}{2}\right\rangle = \pm\frac{1}{2}\hbar\left|\frac{1}{2},\pm\frac{1}{2}\right\rangle} E = \gamma_\mathrm{e}\hat{\underline{S}} \cdot \underline{B} = \gamma_\mathrm{e}\hat{S}_z B_z = \pm\frac{1}{2} g_\mathrm{e}\mu_b B_z, \tag{1.4}$$

thus, the magnetic field lifts the degeneracy of the spin sub levels $\left|S = \frac{1}{2}, m_s = \pm\frac{1}{2}\right\rangle$ and transition energies $\Delta E = g_\mathrm{e}\mu_b B_z$ are in the range of meV under standard EPR conditions where $B = 0.3\,\mathrm{T}$ (see Fig. 2**A**).[5]

Besides this scalar coupling another classical relation permits a glimpse into spin dynamics. Therein, the torque $\underline{D}$, which is given as the time derivative of the angular momentum $\underline{\dot{L}}$, exerted on a magnetic moment inside a magnetic field reads as $\underline{D} = \underline{\dot{L}} = \underline{\mu} \times \underline{B}$. Casting $\hat{\underline{S}}$ into this equation leaves us receiving

$$-\frac{g_\mathrm{e}\mu_b}{\hbar}\dot{\hat{\underline{S}}} = \dot{\underline{\mu}}_\mathrm{e} = \frac{g_\mathrm{e}\mu_b}{\hbar}\left(\underline{B} \times \underline{\mu}_\mathrm{e}\right), \tag{1.5}$$

where $\underline{\mu}_\mathrm{e} = (\mu_{\mathrm{e},x_\mathrm{lab}}, \mu_{\mathrm{e},y_\mathrm{lab}}, \mu_{\mathrm{e},z_\mathrm{lab}})^\mathrm{T}$ is given in lab coordinates which may correspond to the canonical basis. To solve Eq. (1.5), one conveniently changes to a

[5] For this reason, thermal polarization is meager in EPR spectroscopy. The population ratio $N_\mathrm{R} = N_{\left|S=\frac{1}{2},m_s=\frac{1}{2}\right\rangle}/N_{\left|S=\frac{1}{2},m_s=-\frac{1}{2}\right\rangle}$ scales as the Boltzmann factor $\approx 1 - \Delta E/kT \Rightarrow N_\mathrm{R} \approx 1 - 0.001$ for $B_z = 0.3\,\mathrm{T}$ and $T = 300\,\mathrm{K}$. Thus $N_{\left|S=\frac{1}{2},m_s=+\frac{1}{2}\right\rangle} \approx N_{\left|S=\frac{1}{2},m_s=-\frac{1}{2}\right\rangle}$.

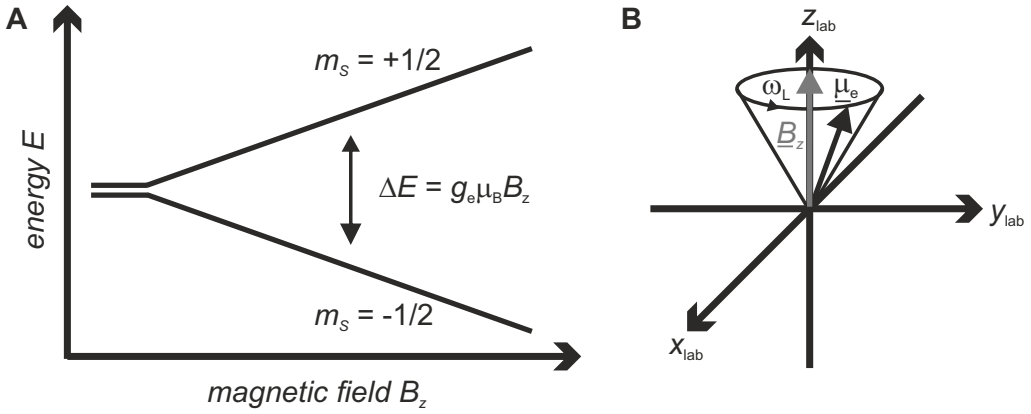

Figure 2: Interaction between the magnetic moment of an electron $\underline{\mu}_\mathrm{e}$ and a static magnetic field $\underline{B} = (0, 0, B_z)^{(\mathrm{T})}$. **(A)** Lifting of the degeneracy of spin levels, where energy splitting ΔE is proportional to the magnetic field strength, cf. Eq. (1.4). **(B)** Precession of the magnetic moment $\underline{\mu}_\mathrm{e}$ with Larmor frequency ω_L in the lab frame, cf. Eq. (1.5).

coordinate system whose unit vectors $\underline{e}_{x,\mathrm{r}}$ and $\underline{e}_{y,\mathrm{r}}$ rotate at a precession frequency ω_L, i.e. $\underline{\omega}_\mathrm{L} = (0, 0, \omega_\mathrm{L})^\mathrm{T}$, about the z_lab-axis of the lab frame. By considering the corresponding basis transformation

$$\begin{pmatrix} \underline{e}_{x,\mathrm{r}} \\ \underline{e}_{y,\mathrm{r}} \\ \underline{e}_{z,\mathrm{r}} \end{pmatrix} = \begin{pmatrix} \cos(\omega_\mathrm{L} t) & \sin(\omega_\mathrm{L} t) & 0 \\ -\sin(\omega_\mathrm{L} t) & \cos(\omega_\mathrm{L} t) & 0 \\ 0 & 0 & 1 \end{pmatrix} \begin{pmatrix} \underline{e}_{x,\mathrm{lab}} \\ \underline{e}_{y,\mathrm{lab}} \\ \underline{e}_{z,\mathrm{lab}} \end{pmatrix}, \tag{1.6}$$

we obtain for the time derivatives of the unit vectors in the rotating frame $\dot{\underline{e}}_l = \underline{\omega}_\mathrm{L} \times \underline{e}_l$, $l \in \{x, y, z\}$. Then we can calculate the evolution of the magnetic moment in the rotating frame $\underline{\mu}_{\mathrm{e,r}} = \left(\underline{e}_{x,\mathrm{r}}, \underline{e}_{y,\mathrm{r}}, \underline{e}_{z,\mathrm{r}}\right) \cdot (\mu_{\mathrm{e},x}, \mu_{\mathrm{e},y}, \mu_{\mathrm{e},z})^\mathrm{T}$ recalling Eq. (1.5)

$$\dot{\underline{\mu}}_{\mathrm{e,r}} = \frac{\mathrm{d}}{\mathrm{d}t} \begin{pmatrix} \mu_{\mathrm{e},x_\mathrm{r}} \\ \mu_{\mathrm{e},y_\mathrm{r}} \\ \mu_{\mathrm{e},z_\mathrm{r}} \end{pmatrix} + \underline{\omega}_\mathrm{L} \times \underline{\mu}_{\mathrm{e,r}}, \tag{1.7}$$

while $\frac{\mathrm{d}}{\mathrm{d}t}$ may represent the time dependency of the components of the magnetic moment within the rotating frame. Thus, we get together with Eq. (1.5)

$$\tfrac{\mathrm{d}}{\mathrm{d}t}\underline{\mu}_{\mathrm{e,r}} = \dot{\underline{\mu}}_{\mathrm{e,r}} - \underline{\omega}_\mathrm{L} \times \underline{\mu}_{\mathrm{e,r}} = \tfrac{g_\mathrm{e}\mu_b}{\hbar}\left(\underline{B} \times \underline{\mu}_{\mathrm{e,r}}\right) - \underline{\omega}_\mathrm{L} \times \underline{\mu}_{\mathrm{e,r}} = \underline{\mu}_{\mathrm{e,r}} \times \left(\tfrac{g_\mathrm{e}\mu_b}{\hbar}\underline{B} - \underline{\omega}_\mathrm{L}\right). \tag{1.8}$$

If we choose our coordinate system such that the precession frequency $\underline{\omega}_\mathrm{L} =$

$g_e \mu_b \hbar^{-1} \underline{B}$, then the velocity of the magnetic moment equals zero and $\underline{\mu}_{e,r}$ rests for any instance of time. By comparison of coordinates in Eq. (1.8) we end up with $\omega_L = g_e \mu_b \hbar^{-1} B_z$ and back transformation into the lab frame analogous to Eq. (1.6) reveals, that the x and y components of the magnetic moment $\underline{\mu}_e$ rotate with ω_L, while its z component aligned with the static magnetic field is constant (see. Fig. 2**B**).
These simple derivatives have thus provided us with two intuitions, spin states split up in static magnetic fields of strength $B_0 := B_z$ by

$$E = g_e \mu_b B_0 = \omega_0 \hbar, \tag{1.9}$$

while $\omega_0 := \omega_L$, and the system possess a B_0-dependent eigenfrequency ω_0, the Lamor frequency. Hence, we met the precondition for a resonance phenomenon.

1.1.2 Driving level transitions using alternating magnetic fields

Magnetic moment dynamics, i.e., the controlled and coherent transition between its eigenstates, is achieved by an alternating magnetic field. May this be given as

$$\underline{B}_1 = B_1 \left(\cos(\omega_1 t) \cdot \underline{e}_x + \sin(\omega_1 t) \cdot \underline{e}_y \right) \tag{1.10}$$

with B_1 the amplitude, ω_1 the angular velocity, and $\underline{e}_l$, $l \in \{x, y, z\}$ the basis vectors of the lab frame.[6] The equation of motion of $\underline{\mu}_e$ in the lab frame, in which the static magnetic field $\underline{B}$ is aligned along the z-axis and $\underline{B}_1$ rotates around it, is[60]

$$\dot{\underline{\mu}}_e = \underline{\mu}_e \times \left[\frac{g_e \mu_b}{\hbar} \left(B_0 \cdot \underline{e}_z + B_1 \cos(\omega_1 t) \cdot \underline{e}_x + B_1 \sin(\omega_1 t) \cdot \underline{e}_y \right) \right], \tag{1.11}$$

which reads as[60]

$$\begin{aligned} \dot{\underline{\mu}}_{e,r} &= \underline{\mu}_{e,r} \times \left[\left(\frac{g_e \mu_b}{\hbar} \underline{B}_0 - \omega_1 \right) \cdot \underline{e}_{z,r} + \frac{g_e \mu_b}{\hbar} B_1 \cdot \underline{e}_{x,r} \right] \\ &= \underline{\mu}_{e,r} \times \left[\Delta\omega \cdot \underline{e}_{z,r} + \frac{g_e \mu_b}{\hbar} B_1 \cdot \underline{e}_{x,r} \right], \end{aligned} \tag{1.12}$$

[6] This field can hardly be realized technically. Nevertheless, if the complex conjugated of the above given field is taken into account as well, which would correspond to a linear polarized field, in what follows a high frequency contribution of $2\omega_1$ would come up, which do not add to magnetic moment (spin) dynamics under our experimental conditions since it is far off-resonant to ω_0. It is therefore neglected in the computation, what is called rotating wave approximation.

by transforming the lab frame into a coordinate system that rotates with $\underline{B}_1$. When $\frac{\hbar}{g_e \mu_b} \Delta\omega = \frac{\hbar}{g_e \mu_b} (\omega_0 - \omega_1) \ll B_1$, which is the resonance case, the magnetic moment precess around $\underline{B}_{\text{eff}} B_1 \underline{e}_{x,\text{r}}$ in analogy to Eq. (1.5), i.e. transitions between eigenstates $\left|\frac{1}{2}, \pm\frac{1}{2}\right\rangle$ occur. Additionally, in this framework precise selection of magnetic moment energy levels can be described.[61] Therefore, a phase Φ is added to $\underline{B}_1$, which is linear polarized here, yielding $\underline{B}_1 = 2B_1 \cos(\omega_1 t + \Phi)$. Changing into the rotating frame, the components of $\underline{B}_1$ are represented by $B_{x,\text{r}} = B_1 \cos\Phi$, $B_{y,\text{r}} = B_1 \sin\Phi$ and $B_{z,\text{r}} = 0$. Solving Eq. (1.12) for the resonance case, results in $\mu_{\text{e},x} = 0$, $\mu_{\text{e},y} \propto \sin(\omega_1 t_\text{p})$ and $\mu_{\text{e},z} \propto \cos(\omega_1 t_\text{p})$, after a mw pulse of length t_p was applied. If t_p is chosen so that $\omega_1 t_\text{p} = \pi$, the lateral components of the magnetic moment are zero and $\mu_{\text{e},z} = -1$. Thus, spin state inversion was reached.[61] By applying alternating fields, phase coherence is imposed, which is discussed more detailed in Chap. 1.4.[62]

1.1.3 Incidental remarks

Up to now, the deductions made are preliminary in two ways. First, electrons are quantum objects. This means that their temporal evolution is not deterministic, as we implicitly assumed in the above derivations. Instead, the equation of motion of an electron state $|\Psi\rangle$ is given by the time-dependent Schrödinger equation

$$\frac{\mathrm{d}}{\mathrm{d}t} |\Psi\rangle = -i\hat{H}(t) |\Psi\rangle , \tag{1.13}$$

where the Hamiltonian $\hat{H}(t)$ encodes the energy of the system. If it is possible to average over the spatial coordinates, as it is the case for the free electron residing in a static magnetic field given alike to the previous chapter, the solution of Eq. (1.13) results for the spin eigenstates $\left|\frac{1}{2}, \pm\frac{1}{2}\right\rangle$ as follows (cf. Eq. (1.9))

$$\left|\frac{1}{2}, \pm\frac{1}{2}\right\rangle (t) = \pm\frac{1}{2} \exp\left(-i \cdot \frac{g_\text{e}\mu_b}{\hbar} B_0 \pm \frac{1}{2} t\right) = \pm\frac{1}{2} \exp\left(-i \cdot \omega_0 \pm \frac{1}{2} t\right). \tag{1.14}$$

The correlation of this equation of motion of a single spin with measurable quantities or observables such as the magnetic moment $\underline{\mu}_\text{e}$ is established by the computation of its expectation value $\left\langle \underline{\mu}_\text{e} \right\rangle$ according to [7]

$$\left\langle \underline{\mu}_\text{e}(t) \right\rangle = \left\langle \Psi(t) \left| \underline{\mu}_\text{e} \right| \Psi(t) \right\rangle = \int \Psi^*(t)\, \underline{\mu}_\text{e}\, \Psi(t)\, \mathrm{d}\tau. \tag{1.15}$$

[7] * indicates complex conjugation.

Solving Eq. (1.15) by using Eq. (1.13) then returns the results of Eq. (1.8) and Eq. (1.12).
The second simplification in Chap.s 1.1.1 and 1.1.2 was the assumption of a free, non-interacting electron. However, in condensed matter we very seldom observe but one magnetic moment respectively spin. Generally, a particular sample contains nuclear spins and electron spins to a certain degree. The interaction between those paramagnetic species alters the local magnetic field at the location of the spin under investigation. To take this into account, the theoretical framework of the spin Hamiltonian is used (see Chap. 1.2).
In order to unravel the probability distribution given by Eq. (1.15) in such a solid state system, many measurements have to be performed. If the system is ergodic, this can be done in two ways. Either a bulk sample is measured for which ideally is assumed that it contains many identical realizations of the species under investigation or a single representative of the system to be probed is prepared in a defined state and the probability distribution is interrogated by successive measurements. The first approach is pursued in cw-EPR spectroscopy (see Chap. 1.3), the second in NV^- center-mediated quantum sensing (see Chap. 1.4).

1.2 The spin Hamiltonian

The static spin Hamiltonian $\hat{H}_0$ allows to compute the energies of states of a paramagnetic species with effective electron spin S in its electronic ground state additional residing in the magnetic field of m nuclear spins I_k according to[61]

$$\hat{H}_0 = \hat{H}_{\mathrm{eZ}} + \hat{H}_{\mathrm{zfs}} + \hat{H}_{\mathrm{hf}} + \hat{H}_{\mathrm{nZ}} + \hat{H}_{\mathrm{nq}} + \hat{H}_{\mathrm{nn}} \tag{1.16}$$

wherein the respective terms describe the electron Zeeman interaction ($\hat{H}_{\mathrm{eZ}}$), the zero-field splitting ($\hat{H}_{\mathrm{zfs}}$), the electron-nuclear spin hyperfine coupling ($\hat{H}_{\mathrm{hf}}$), the nuclear Zeeman interaction ($\hat{H}_{\mathrm{nZ}}$), the nuclear quadrupole interaction for nuclear spins with $I > \frac{1}{2}$ ($\hat{H}_{\mathrm{nq}}$), and the nuclear spin-spin interactions ($\hat{H}_{\mathrm{nn}}$). The term spin Hamiltonian is justified by the fact that only spin coordinates are included; the spatial degrees of freedom of the wave function are taken into account by means of interaction matrices. Then Eq. (1.16) becomes

$$\hat{H}_0 = \frac{\mu_{\mathrm{b}}}{\hbar} \underline{B}^{\mathrm{T}} \underline{\underline{g}} \underline{\hat{S}} + \underline{\hat{S}}^{\mathrm{T}} \underline{\underline{D}} \, \underline{\hat{S}} + \sum_k^m \underline{\hat{S}}^{\mathrm{T}} \underline{\underline{A}}_k \underline{\hat{I}}_k + \sum_k^m \gamma_k \underline{B}^{\mathrm{T}} \underline{\hat{I}}_k + \sum_{\hat{I}_k > \frac{1}{2}} \underline{\hat{I}}_k^{\mathrm{T}} \underline{\underline{P}}_k \underline{\hat{I}}_k + \sum_{j \neq k} \underline{\hat{I}}_i^{\mathrm{T}} \underline{\underline{d}}^{(j,k)} \underline{\hat{I}}_k. \tag{1.17}$$

In this thesis we will mainly encounter the first four terms. The nuclear quadrupole interaction may be relevant for $^{14}N@C_{60}$, however, under our measurement conditions its contribution is not resolvable. We will come across nuclear spin-spin couplings when it is a matter of relaxation paths of the NV^- center. Yet, in this context a spin bath model is used which is described by ensemble parameters and not discrete interactions as they are formulated in Eq. (1.17). The nuclear Zeeman interaction will not be relevant for us, but its physical structure does not differ from that of the electron Zeeman interaction. Only the energies vary significantly due to $\frac{\gamma_e}{\gamma_k} \gtrsim 10^3$.

The **electron Zeeman interaction**, in the general case, can be expanded according to[63]

$$\hat{H}_{eZ} = \frac{\mu_b}{\hbar} B_0 \left(n_x, n_y, n_z\right) \begin{pmatrix} g_x & 0 & 0 \\ 0 & g_y & 0 \\ 0 & 0 & g_z \end{pmatrix} \begin{pmatrix} \hat{S}_x \\ \hat{S}_y \\ \hat{S}_z \end{pmatrix} = \frac{\mu_b}{\hbar} B_0 \sum_{i=x,y,z} n_i g_i \hat{S}_i, \tag{1.18}$$

where the g-matrix is in its eigenframe (g frame), $\underline{n} = (n_x, n_y, n_z)$ are the unit vectors of the eigenframe of $\underline{B}$ (lab frame). We presume a $S = \frac{1}{2}$ spin, for which the spin operator components read as $\hat{S}_i = \frac{1}{2}\hat{\sigma}_i$, given the Pauli matrices

$$\hat{\sigma}_x = \left(\begin{smallmatrix} 0 & 1 \\ 1 & 0 \end{smallmatrix}\right), \quad \hat{\sigma}_y = \left(\begin{smallmatrix} 0 & -\mathrm{i} \\ \mathrm{i} & 0 \end{smallmatrix}\right), \quad \hat{\sigma}_z = \left(\begin{smallmatrix} 1 & 0 \\ 0 & -1 \end{smallmatrix}\right). \tag{1.19}$$

Thus, inserting Eq. (1.19) into (1.18) let us garner

$$\hat{H}_{eZ} = \frac{1}{2} \frac{\mu_b}{\hbar} B_0 \begin{pmatrix} n_z g_z & 0 & n_x g_x - \mathrm{i} n_y g_y \\ 0 & 0 & 0 \\ n_x g_x + \mathrm{i} n_y g_y & 0 & -n_z g_z \end{pmatrix}. \tag{1.20}$$

Diagonalization of this equation reveals the eigenvalue spectrum for $m_S = \pm\frac{1}{2}$

$$E\left(m_s\right) = m_S \frac{\mu_b}{\hbar} B_0 \left(\sum_i n_i^2 g_i^2 \right)^{\frac{1}{2}} = m_S \frac{\mu_b}{\hbar} \left[B_0 \left(\underline{n}^T \underline{g}\right) \left(\underline{g}^T \underline{n}\right) B_0 \right]. \tag{1.21}$$

Consequently, the energy difference between both spin states can be calculated through

$$E\left(+\frac{1}{2}\right) - E\left(-\frac{1}{2}\right) = \nu_0 = \left(\left|\underline{g}^T \underline{n}\right|\right) \frac{\mu_b}{2\pi\hbar} B_0 \stackrel{!}{=} g \frac{\mu_b}{2\pi\hbar} B_0 \tag{1.22}$$

and $|\cdot|$ is the $p = 2$-norm. Both, Eq. (1.20) and Eq. (1.21), reveal that a rhombic system, where $g_x \neq g_y \neq g_z$, residing in a static magnetic field of direction $\underline{n}$ and

strength B_0 possesses six degrees of freedom. We draw some conclusions that are relevant for investigations presented in this thesis.
1. The link to Eq. (1.9) is given for $\frac{1}{3}(g_x + g_y + g_z) = g_e$ and $n_x = n_y = 0; n_z = 1$.
2. In liquids of low viscosity or for molecules whose barrier to rotation is energetically low, g-anisotropic contributions are averaged. This can be shown by transforming $\underline{n}$ into a spherical coordinate system and averaging over all angular coordinates. Correspondingly, an EPR spectrum yields $g_{\mathrm{iso}} = \frac{1}{3}(g_x + g_y + g_z)$.
3. For a spin species with g-anisotropy the magnetic field splitting becomes

$$\Delta B_{ij} = \frac{h\nu_0}{\mu_{\mathbf{b}}}\left(\frac{1}{g_i} - \frac{1}{g_j}\right), \quad i \neq j \in \{x, y, z\}\,. \tag{1.23}$$

This means that higher frequencies ν_0 allow for enhanced spectral resolution.
4. If the magnetic field direction is spatially fixed, as it is the case in our NV^- center-mediated sensing experiments, and its absolute orientation is known the effective g-factor computed from an EPR spectrum allows for elucidation of the mutual alignment of g-frame and lab frame. For this it is necessary to know the main axis entries of the g-matrix either from (single crystal) EPR measurements or by quantum chemical calculations. The most general transformation is described by three Euler angels and a set of three axises around which the rotation is accomplished.[62]
5. Deviations from the g-factor of the free electron are mediated by the spin-orbit coupling.[61] Taking this interaction into account ($\hat{H}_{LS}$), equation (1.18) reads as follows

$$\hat{H}_{\mathrm{Z}} + \hat{H}_{LS} = \frac{\mu_{\mathrm{b}}}{\hbar}\underline{B}^{\mathrm{T}}\left(\underline{\hat{L}} + g_e\underline{\hat{S}}\right) + \lambda\underline{\hat{L}}^{\mathrm{T}}\underline{\hat{S}}. \tag{1.24}$$

$\underline{\hat{H}}_{\mathrm{L}}$ is the dilated electron Zeeman term including the orbital angular momentum $\underline{\hat{L}}$ and $\hat{H}_{LS}$ accounts for spin-orbit interaction, which is quantified by the coupling constant λ. A Second-order perturbation theory solution of Eq. (1.24) results in[61]

$$\underline{\underline{g}} = g_e\mathbb{1} + 2\lambda\underline{\underline{\Lambda}} \Leftrightarrow \Lambda_{ij} = \sum_{n\neq 0}\frac{\left\langle \Psi_0 \middle| \hat{L}_i \middle| \Psi_n \right\rangle \left\langle \Psi_n \middle| \hat{L}_j \middle| \Psi_0 \right\rangle}{\epsilon_0 - \epsilon_n}, \tag{1.25}$$

with ground and nth excited state wave function Ψ_0 and Ψ_1, respectively, whose energy eigenvalues are given by ϵ_0 and ϵ_1. From this we can conclude that the closer the energies of the orbitals involved are and the larger λ is, which is proportional to the atomic number, the larger $\Delta g = g - g_e$ becomes. For this reason, heavy elements (e.g. transition metals) often exhibit $\Delta g \geq 0.1 - 1 \times 10^1$, whereas

for organic samples often holds true $\Delta g \approx 0$.[61,64]

The **electron-nuclear spin hyperfine interaction** between an electron spin S and one nuclear spin I reads according to Eq. (1.17) as $\hat{H}_{\mathrm{zfs}} = \hat{\underline{S}}^{\mathrm{T}} \underline{\underline{A}} \hat{\underline{I}}$. This can be further divided into an isotropic part (Fermi Contact interaction: $\hat{H}_{\mathrm{fc}}$) and the anisotropic electron-nuclear dipole coupling ($\hat{H}_{\mathrm{dd}}$).[61,65,66] They can be specified as follows

$$\hat{H}_{\mathrm{fc}} = -\frac{2}{3}\frac{\mu_0}{\hbar} g_{\mathrm{e}} \mu_{\mathrm{b}} \gamma_n \left|\Psi_0(0)\right|^2 = a_{\mathrm{iso}} \hat{\underline{S}}^{\mathrm{T}} \hat{\underline{I}} \tag{1.26}$$

(μ_0 is the vacuum permeability and $|\Psi_0(0)|$ the electron density of the s-orbital electron[8] at the location of the nucleus) and

$$\hat{H}_{\mathrm{dd}} = \frac{\mu_0}{4\pi\hbar} g_{\mathrm{e}} \mu_{\mathrm{b}} \gamma_n \left[\frac{\left(3\hat{\underline{S}}^{\mathrm{T}} \underline{r}\right)\left(\underline{r}^{\mathrm{T}} \hat{\underline{I}}\right)}{r^5} - \frac{\hat{\underline{S}}^{\mathrm{T}} \hat{\underline{I}}}{r^3} \right], \tag{1.27}$$

where $\underline{r}$ is the vector connecting the two spins. The interaction in equation (1.26) is dominant for electron-nitrogen nuclear spin interaction in N@C_{60}, while the electron-nuclear spin interaction of the NV^- center in the electronic ground state is determined by both parts since its electron density distribution at the location of the nitrogen atom nearly vanishes.[67]

The physical structure of equation (1.27) also applies to the coupling between two electron spins $\hat{\underline{S}}_1$ and $\hat{\underline{S}}_2$ (**electron-electron dipolar coupling**) and we take a more detailed look at it since it is not included in Eq. (1.17). We start with

$$\hat{H}_{\mathrm{edd}} = \omega_{\mathrm{edd}} \left[\frac{\left(3\hat{\underline{S}}_1^{\mathrm{T}} \underline{r}\right)\left(\underline{r}^{\mathrm{T}} \hat{\underline{S}}_2\right)}{r^5} - \frac{\hat{\underline{S}}_1^{\mathrm{T}} \hat{\underline{S}}_2}{r^3} \right], \tag{1.28}$$

where $\omega_{\mathrm{edd}} = \frac{\mu_0}{4\pi\hbar} g_{\mathrm{e},1} g_{\mathrm{e},2} \mu_{\mathrm{b}}^2$. Introducing raising and lowering operators $\hat{S}_+ = \hat{S}_x + \mathrm{i}\hat{S}_y$ and $\hat{S}_- = \hat{S}_x - \mathrm{i}\hat{S}_y$, Eq. (1.28) can be reformulated[65]

$$\hat{H}_{\mathrm{edd}} = \nu_{\mathrm{edd}} \left\{ \hat{\underline{S}}_1 \hat{\underline{S}}_2 - 3 \left[\hat{S}_{1,z} \cos\vartheta + \frac{1}{2}\sin\vartheta \left(\hat{S}_{1,+} \mathrm{e}^{-\mathrm{i}\phi} + \hat{S}_{1,-} \mathrm{e}^{\mathrm{i}\phi} \right) \right] \cdot \left[\hat{S}_{2,z} \cos\vartheta + \frac{1}{2}\sin\vartheta \left(\hat{S}_{2,+} \mathrm{e}^{-\mathrm{i}\phi} + \hat{S}_{2,-} \mathrm{e}^{\mathrm{i}\phi} \right) \right] \right\} \tag{1.29}$$

[8] Electrons in orbitals of non-vanishing orbital angluar momentum can contribute via spin polarization mechanisms.[61]

The expansion of these terms results in the so-called dipolar alphabet from which for our experimental conditions, however, solely the first term

$$A = \hat{S}_{1,z}\hat{S}_{2,z}(1 - 3\cos^2\vartheta) \Rightarrow \hat{H}_{\mathrm{edd}} = \frac{\mu_0}{4\pi\hbar} g_{\mathrm{e},1} g_{\mathrm{e},2} \mu_{\mathrm{b}}^2 \hat{S}_{1,z}\hat{S}_{2,z}(1 - 3\cos^2\vartheta) \quad (1.30)$$

is relevant.[9]
The zfs term in Eq.s (1.16), (1.17), which comes into effect for $S > \frac{1}{2}$, is discussed in Chap. 2.2.2.

1.3 Continuous wave EPR

Commonly, bulk EPR experiments are conducted on samples containing about 10^{12} electron spins. The summation of their single magnetic moments μ_i sitting in a magnetic field $|\underline{B}| = B_0$ only at $T = 0$ yields $\sum_i^N \mu_i = \mu = N\mu_i$, which states that all spins are aligned along $\underline{B}$. Since the energy difference between spin states is in the meV range (cf. footnote 5), for finite temperatures thermal induced transitions between them occur and the temperature-dependent thermal polarization for $S = \frac{1}{2}$ spins is given by[62]

$$\Delta N_{\mathrm{therm}} = N_{\left|S=\frac{1}{2}, m_s=-\frac{1}{2}\right\rangle} - N_{\left|S=\frac{1}{2}, m_s=+\frac{1}{2}\right\rangle} \approx \frac{N}{2}\frac{g_{\mathrm{e}}\mu_b B_0}{kT}. \quad (1.31)$$

Therefore, in thermal equilibrium the spin ensemble possesses a net magnetization

$$M_0 = \frac{1}{V}\Delta N_{\mathrm{therm}}. \quad (1.32)$$

1.3.1 The Bloch equations

In this ensemble limit a magnetization vector $\underline{M} = (M_x, M_y, M_z)^{\mathrm{T}}$ can be defined, which is characterized analogous to the magnetic moment regarding its dynamics in magnetic fields, i.e., it obeys the equation of motion given in Eq. (1.12). It has already been noted in Chapter 1.1.3 that its derivation was not theoretically sound since a quantum mechanical object can only be described by classical equations if the statistics of the operator spectrum are available which, however, holds true as long as $\underline{M}$ represents a pure state.[62] And indeed, for this macroscopically measurable quantity the so-called Bloch equations analogous to Eq. (1.12) were derived

[9] Further terms either induce state mixing and cause higher harmonics of small amplitude or allow for energy transfer between both spins.[65]

by *F. Bloch* in 1946 without resorting to quantum mechanical considerations.[68] They are given according to

$$\begin{aligned}
\frac{\mathrm{d}}{\mathrm{d}t}M_z &= \gamma\left(-M_x B_1 \sin(\omega t) + M_y B_1 \cos(\omega t)\right) + \frac{M_0 - M_z}{T_1} \\
\frac{\mathrm{d}}{\mathrm{d}t}M_x &= \gamma\left(-M_y B_0 + M_z B_1 \sin(\omega t)\right) + \frac{M_x}{T_2} \\
\frac{\mathrm{d}}{\mathrm{d}t}M_y &= \gamma\left(-M_z B_1 \cos(\omega t) + M_x B_1 \cos(\omega t)\right) + \frac{M_y}{T_2}
\end{aligned} \tag{1.33}$$

when the sample experiences the magnetic field $\underline{B} = (B_1\cos(\omega t), B_1\sin(\omega t), B_0)^{\mathrm{T}}$, and is thus prepared in a non-equilibrium state, and γ is the gyromagnetic ration of the spin species investigated.[62] The mw field is characterized by its power $P_{\mathrm{mw}} = B_1^2$ and frequency $\omega = 2\pi\nu$. The decay constants are phenomenologically introduced: T_1 is called longitudinal or spin-lattice relaxation time. It describes the temporal behavior of the restitution of the M_z component to the equilibrium state given by equation (1.32). The underlying mechanisms are dissipative. The coherence imposed by the oscillating field, i.e., the presence of a phase relationship between the energy basis states, also decays into equilibrium, which is determined by equation (1.6). The corresponding decay constant T_2 is called decoherence time. Under cw-EPR conditions, where ω varies slowly compared to the electron spins' Lamor precession, a steady state ansatz is valid to solve Eq.s (1.33) in the rotating frame. The solution yields for the transverse magnetization, which is the measurable quantity in a cw-EPR experiment[62]

$$\bar{M} = \frac{\gamma B_1 M_0}{\gamma^2 B_1^2 \left(\frac{T_1}{T_2}\right) + \left(\frac{1}{T_2}\right)^2 + (\omega_0 - \omega)^2}. \tag{1.34}$$

This renders a Lorentzian shaped function of linewidth

$$lw_{\mathrm{Lorentzian}} = \frac{\sqrt{1 + \gamma P_{\mathrm{mw}} T_1 T_2}}{\gamma T_2}, \tag{1.35}$$

from which equation we can deduce that the linewidth of an EPR transition is determined by both, the relaxation times, mainly T_2 which is in most condensed matter experiments the rate limiting step, and the applied mw power. Furthermore, the resonance phenomenon can be deduced from Eq. (1.34) mathematically considering that the function takes it maximum at $\omega = \omega_0$ and $\lim_{\omega\to\infty} = 0$.
We give some comments on the technical aspects of cw-EPR measurements and refer to the literature for a detailed description.[66,69] In general, in an X- or W-

band cw-EPR spectrometer, the static magnetic field is varied and the microwave frequency is kept constant to record the spectrum. The sample is located in a cavity which serves to tune the resonant circuit represented by the spectrometer so that in the non-resonant case the mw power is dissipated. In the resonant case, however, the sample absorbs mw energy, which leads to a power output in the form of mw radiation, which is registered by the phase sensitive detector. Spectra are recorded according to the lock-in principle. The static magnetic field is modulated with a frequency (typically 100 kHz). Consequently, the cw-EPR signal S_{EPR} is recorded as $\frac{\mathrm{d}}{\mathrm{d}B_0}S_{\mathrm{EPR}}$, which corresponds to the first derivative of the absorption curve.

1.4 Quantum sensing - A brief introduction

The description of a quantum sensing protocol requires a model of the sensor, which we suppose to be a Two-level system (TLS), and of the measuring process. Both is dealt with in Chap. 1.4.1 and 1.4.2, respectively.[10]

1.4.1 Two-level system

The essential concepts of quantum sensing can be exemplified with the help of an appropriate TLS whose defining characteristics are:

(1) The TLS has two eigenstates $|0_{\mathrm{TLS}}\rangle = |0\rangle = \left(\begin{smallmatrix}1\\0\end{smallmatrix}\right)$ and $|1_{\mathrm{TLS}}\rangle = |1\rangle = \left(\begin{smallmatrix}0\\1\end{smallmatrix}\right)$ with well-separated energy levels $E_{|0\rangle}$ and $E_{|1\rangle}$, where $E_{|0\rangle} < E_{|1\rangle}$, a transition energy given by $E_1 - E_0 = E_{|0\rangle\leftrightarrow|1\rangle} = h\nu_0 = \hbar\omega_0$ and a transition rate $\frac{\mathrm{d}}{\mathrm{d}t}n_{|0\rangle} = \frac{\mathrm{d}}{\mathrm{d}t}n_{|1\rangle} = \Gamma$ ($n_{|\cdot\rangle}$: state population). See Fig. 3**A**.

(2) The TLS can repeatedly be prepared, w.l.o.g., in the ground state $|0\rangle$ and it exists a physical measurement scheme to obtain its current state.

(3) Transitions between the energy levels can be induced coherently by applying time-dependent fields.

(4) The transition frequency ω_0 or the transition rate Γ changes in present of an external signal $V(t)$ which interaction is quantified by a coupling parameter $\gamma_{\mathrm{S}} = \frac{\partial^q E}{\partial V^q}$, where $q = 1, 2$ depends on the sensing scheme.

[10] Note that this chapter is mainly adapted from Ref. [23].

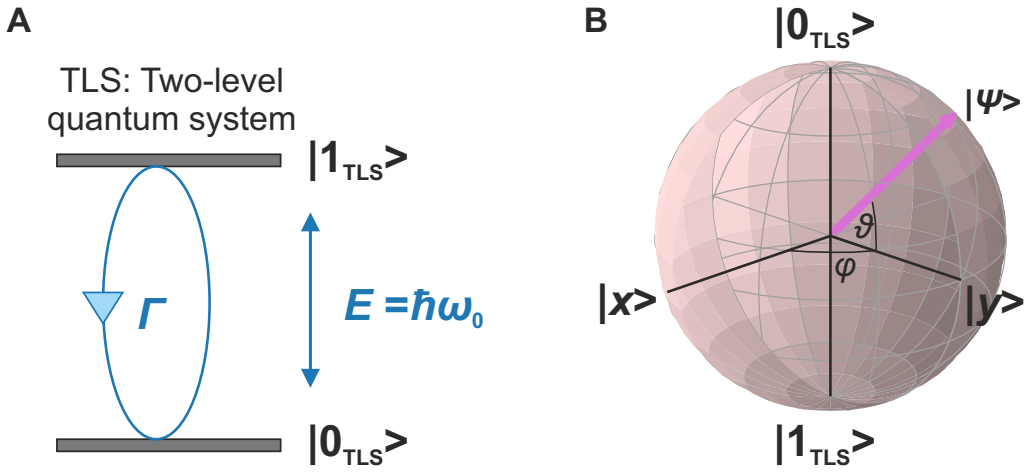

Figure 3: Representation of a Two-level system (TLS). **(A)** Two discrete energy levels are separated by energy $E = \hbar\omega_0$ and a transition rate Γ is imposed due to state mixing or alternating fields, which can couple to the TLS. **(B)** Bloch sphere representation of a TLS state $|\Psi\rangle$ (magenta arrow) in its eigenstate basis ($|0_{\mathrm{TLS}}\rangle$, $|1_{\mathrm{TLS}}\rangle$. The degrees of freedom of the TLS are given by the polar (ϑ) and azimuthal angle (φ).

An arbitrary state of the TLS is represented through $|\Psi\rangle = a\,|0\rangle + b\,|1\rangle$ with complex coefficients a, b and $|a|^2 + |b|^2 = 1$. If, for example, $a = 1$ the TLS is in one of its eigenstates. Otherwise, values of $0 < |a|^2 < 1$ indicate superpositions states. Transformation into polar coordinates under the normalization condition allows for writing the state representation up to a global phase as

$$|\Psi\rangle = \cos\left(\frac{\vartheta}{2}\right)|0\rangle + \mathrm{e}^{\mathrm{i}\varphi}\sin\left(\frac{\vartheta}{2}\right)|1\rangle = \begin{pmatrix}\cos\left(\frac{\vartheta}{2}\right)\\ \mathrm{e}^{\mathrm{i}\varphi}\sin\left(\frac{\vartheta}{2}\right)\end{pmatrix},\ 0 \leq \vartheta \leq \pi,\ 0 \leq \varphi < 2\pi. \quad (1.36)$$

The degrees of freedom of the TLS are given by the polar (φ) and azimuthal angle (ϑ). Capitalizing on the Bloch sphere visualization (see Fig. 3**B**), any state is represented by a vector $|\Psi\rangle$ of unity length and a unique set of ϑ,φ-values. Special states are given by $\vartheta = 0$ and 2π for the eigenstates and the equatorial plane is addressed by $\vartheta = \pi$.

1.4.2 Model of the measuring process

In addition to the model for the sensor, we also need one for the measurement process. This is given by the quantum sensor Hamiltonian[23]

$$\hat{H}(t) = \hat{H}_0 + \hat{H}_V(t) + \hat{H}_{\mathrm{ctrl}}(t). \tag{1.37}$$

$\hat{H}_0$ constitutes the internal static Hamiltonian, $\hat{H}_V(t)$ represents the Hamiltonian of the signal to be measured, and $\hat{H}_{\mathrm{ctrl}}$ allow appropriate control of the sensor-signal system. If $\hat{H}_0$ is known and $\hat{H}_{\mathrm{ctrl}}$ can be adapted freely, the influence of the signal Hamiltonian on the sensor states can be inferred from Eq. (1.37). The individual terms result as follows.

The **internal Hamiltonian** is the representation of the sensor in the absence of signals. Since it should be static, it is given in the energy eigenstate basis according to

$$\hat{H}_0 = E_0 |0\rangle \langle 0| + E_1 |1\rangle \langle 1| = \left(\begin{smallmatrix} E_0 & 0 \\ 0 & E_1 \end{smallmatrix}\right). \tag{1.38}$$

Coupling between the sensor and the signal $V(t)$ is encoded in the **signal Hamiltonian** which reads as

$$\hat{H}_V(t) = \frac{1}{2}\gamma_{\mathrm{S}} \left(\begin{smallmatrix} -V_{\parallel}(t) & V_{\perp}(t) \\ V_{\perp}(t) & V_{\parallel}(t) \end{smallmatrix}\right). \tag{1.39}$$

where γ_{S} is the coupling strength. From Eq. (1.39) can be deduced that $V_{\parallel}$ and $V_{\perp}$ exert a different influence on the quantum sensor. $V_{\parallel}$ causes shifts of the energy eigenstates, thereby ω_0 is changed. Off-diagonal contributions $V_{\perp}$, however, do not commute with the internal Hamiltonian and may induce level transitions. This increases the transition rate Γ. Furthermore, a distinction need to be made between coherent and noise signal sources. The former can generally be detected by a lock-in principle, while the latter is only accessible by its spectral power density.
The **control Hamiltonian** consists of a set of manipulation operations that allow the states of the TLS to be tuned to the signal to be measured. Following the naming of quantum computing, these are called quantum gates. In addition to the Pauli matrices (see Eq. (1.19)), the Hadamard gate $\frac{1}{\sqrt{2}}\left(\begin{smallmatrix} 1 & 1 \\ 1 & -1 \end{smallmatrix}\right)$ and the projection operators ($\langle 0/1| \cdot \rangle$) on the eigenvalues are important in basic approaches.

To explain the principle of a quantum measurement using the TLS we choose the example of a Ramsey measurement of a signal $V_{\parallel}$, such that $\omega = \omega_0 + \gamma_{\mathrm{S}} V_{\parallel}$ (see Fig. 4**A**).

1. The TLS is prepared in its initial state.

2. By means of a $\frac{\pi}{2}$ pulse, which corresponds to a Hadamard gate, a superposition state is accomplished

$$|\Psi_0\rangle = \frac{1}{\sqrt{2}} \begin{pmatrix} 1 & 1 \\ 1 & -1 \end{pmatrix} \begin{pmatrix} 1 \\ 0 \end{pmatrix} = \frac{1}{\sqrt{2}} \begin{pmatrix} 1 \\ 1 \end{pmatrix} = \frac{1}{\sqrt{2}} \left(|0\rangle + |1\rangle\right). \tag{1.40}$$

3. In the free precession period the state $|\Psi_0\rangle$ evolves according to Eq. (1.13), where the Hamiltonian is given as $\hat{H} = \hat{H}_0 + \hat{H}_V = \begin{pmatrix} \omega & 0 \\ 0 & \omega \end{pmatrix}$, for a period of time τ. The propagator of this evolution is given by $\hat{U}(\tau) = \exp\left(-\mathrm{i}\hat{H}\tau\right)$. Accordingly, the transformation $\hat{U}|\Psi_0\rangle$ results in the state

$$|\Psi(\tau)\rangle = \frac{1}{\sqrt{2}} \left(|0\rangle + \mathrm{e}^{-\mathrm{i}\omega\tau}|1\rangle\right), \tag{1.41}$$

   where the two eigenfunctions acquire a relative phase $\varphi = \omega\tau$ and we omit a global phase factor.

4. The second $\frac{\pi}{2}$ pulse in Fig. 4**A** creates the observable state $|\alpha\rangle$

$$|\alpha\rangle = \frac{1}{\sqrt{2}} \left(1 + \mathrm{e}^{-\mathrm{i}\omega\tau}\right)|0\rangle + \left(1 - \mathrm{e}^{-\mathrm{i}\omega\tau}\right)|1\rangle, \tag{1.42}$$

5. The resulting state is read out by a Bernoulli process, which yields the transition probability p according to

$$p = 1 - |\langle 0|\,\alpha\rangle|^2 = \frac{1}{2}\left[1 - \cos(\omega\tau)\right]. \tag{1.43}$$

6. Since we obtain in 5. a response of either 0 or 1, this specific τ step needs to be repeated until sufficient statistics are obtained.

7. If we had performed the same protocol with the same τ value without the signal and thus knew $p(\omega_0, \tau)$, we could obtain the signal $V_\parallel$ from the difference in p. However, it is commonly inferred from a protocol in which τ is incremented and the characteristic oscillation expressed in Eq. (1.43) is evaluated.[11]

The Ramsey protocol can only detect constant or signals with a frequency of $\approx \frac{1}{\tau}$. We can clarify this when we look at the phase pickup in the third protocol step. This is given by $\varphi = \int_0^\tau \gamma_S V_\parallel(t)\,\mathrm{d}t$. If $V_\parallel(t)$ oscillates fast on the

[11] In this case, $p(\omega_0)$ must be known, which is generally the case, unlike $p(\omega_0, \tau)$.

τ-timescale, it averages to zero and accordingly no phase is acquired (see Fig. 4**A**). Theoretically, we could adapt τ to any signal, but two limitations exist. For high frequencies it is given by the minimal gate length, i.e. signals oscillating at the timescale of the duration of a $\frac{\pi}{2}$ pulse manipulation are not accessible. For low-frequency signals the measurement restriction is present through the coherence decay of the superposition state, for example, by non-coherent interaction with a spin bath, which is characterized by the time constant T_2^*. For the NV^- center this is constituted by ^{13}C nuclear spin impurities in the diamond host or surface contributions.[70] Typical values we obtained range at $T_2^* = 1.5\,\mu s$ (see Chap. 2.2.3). This corresponds to roughly $7 \times 10^2\,kHz$. Yet, if we were to detect electron-electron or even electron-nuclear coupling interactions, whose energy could undercut the $1 \times 10^2\,kHz$ regime, this may not be sufficient. A variation of the $1/\tau$ filter is given by inserting a π pulse between the two $\frac{\pi}{2}$ pulses. The phase pickup is then given by $\varphi = \int_0^{\frac{\tau}{2}} \gamma_S V_\parallel(t)\,dt - \int_{\frac{\tau}{2}}^{\tau} \gamma_S V_\parallel(t)\,dt = \frac{2}{\pi}\gamma_S V_\parallel \tau \cos\alpha$, with the signal $V_\parallel \cos(2\pi\nu_{ac}t + \alpha)$ (see Fig. 4**B**). The subdivision of the free evolution period of the TLS and thus of the frequency filter also makes it possible to deliberately induce a disturbance in one of the two windows. Phase pickup in the two partial intervals then provides different values from which information about the interference can be obtained. This is the principle of NV^- center-related double electron-electron resonance (NV-DEER) spectroscopy, as it is presented in Chap. 6.5.2.2.

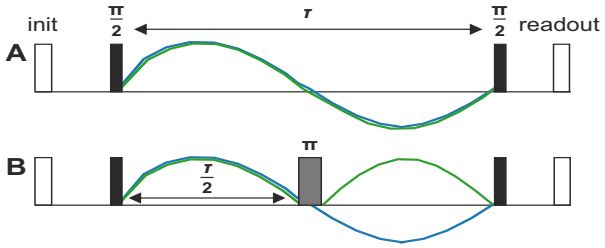

Figure 4: Example sensing schemes discussed in in the text. (A) Ramsey and (B) Hahn echo scheme. τ is a time to be incremented, $\frac{\pi}{2}$ and π are spin state operations. The blue curve corresponds to a signal to be measured and the green line indicates the corresponding phase pickup. It can be seen, that for the Ramsey scheme the phase pickup equals to zero over the investigation time τ, while the Hahn echo protocol acquires a finite value according to the area under the green curves.

It should be pointed out that the selected example of the Ramsey scheme represents the general principles of a quantum sensing protocol, which we therefore summarize again: initialization of the quantum sensor, manipulation of the spin system according to the signal source to be recorded, projection into an observable

eigenstate, probabilistic readout, repetition of the measurement to determine the underlying statistics and incrementing of a time or frequency control variable to reveal the temporal or energetic behavior of the signal.

Various measurement schemes have been developed to determine the amplitude, frequency or phase of coherent signals. Noise signals occurring from different underlying statistics can be characterized by methods that can be seen as an extension of the Hahn Echo protocol. High frequency signals can be determined by their influence on the longitudinal T_1 relaxation time. An extensive description of these methods, however, is beyond the scope of this thesis and we therefore refer to the literature.[20,23–25]

2 The material and technical aspect of quantum sensing

First, in this chapter we turn to the material aspects of quantum sensing. We introduce the endohedral fullerene N@C_{60} as a molecular system. The parent molecule, the C_{60} fullerene, has its own intriguing story that began with its discovery, published by *H. W. Kroto* et al. in 1985,[71] that intermediately climaxed again in the report on the first macroscopic production technique,[72] which made subsequent research endeavors possible at all, and that has merged into the current role of C_{60} fullerene as one of the classical nanomaterials. (see Chapt. 2.1.2). The group-V endohedral fullerene N@C_{60} as a molecular system is characterized in Chap. 2.1.3 regarding its physical and spectroscopic properties. While the NV^- center is embedded in a diamond host, its local structure justifies considering it as a quasi-molecule. With this model the most important properties, which are also exploited in this work in connection with its detection properties, can be explained; this is done in Chap. 2.2. Some of the material characteristics of the diamond host are discussed in Chapter 2.3. The supplementary (Chap. 2.4) elucidate the details of the ODMR setup used.

2.1 Atomic nitrogen encapsulating C_{60} fullerene - a molecular system

2.1.1 Definitions and nomenclature

Fullerenes are allotropes of carbon. They feature a closed spheroid cage structure which can be constructed through a cover of the spherical surface by regular polygons. The vertices of the polygons are occupied by carbon atoms, whereas the edges correspond to C−C σ bonds. Stability considerations and deductions from graph theory imply as a necessary condition, for classical fullerenes to be Archimedean solids built from twelve pentagons and $N = \nu^g/2 - 10$ hexagons, where $\nu^g \geq 20$ is the number of C atoms.[73–75] Experimental results exist for $\nu^g = 20$, 36, 60, 70, 76, 78, 82, 84, 90, 94, 96.[71,76–80]

Current recommendations of the International Union of Pure and Applied Chemistry (IUPAC)[12] of naming the chemical compounds represented by $\nu^g = 60$ and $\nu^g = 70$ is $(C_{60} - I_h)$ [5, 6]fullerene and $\left(C_{70} - D_{5h(6)}\right)$ [5, 6]fullerene, respectively.[81]

[12] The nomenclature $(C_{\nu^g} - pg)$ $[X, Y]$ fullerene states the number of C atoms ν^g, the point group pg and the ring size X and Y of the rings constituting the chemical compound. The name buckminister fullerene is chosen to esteem the architect *R. Buckminster Fuller*.[73]

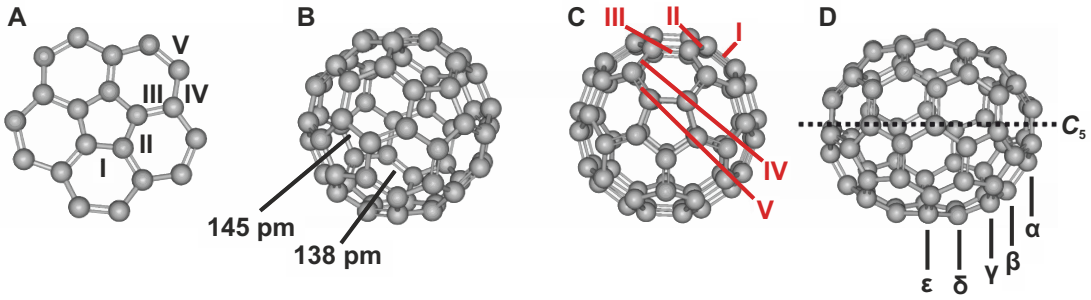

Figure 5: Schematic drawings of **(A)** corannulene, **(B)** C_{60} fullerene, and C_{70} fullerene **(C)** alongside the C_5 symmetry axis and **(D)** perpendicular to it. Latin numbers indicate bonds, greek letters classes of equivalent carbon atoms regarding their chemical shift.

In this work, C_{60} fullerene and C_{70} fullerene synonymously is used.

Fullerenes, enclosing a atom, ion, molecule or cluster are named endohedral fullerenes.[82] Regarding the intercalated species it can be distinguished between endohedral mono, di, and trimetallo fullerenes as well as main-group metal cluster, noble gas, and non-metal fullerenes.[51]
Herein, we are not pursuing the recommendation of IUPAC to name a fullerene $(C_{\nu^g} - PG)\,[X, Y]$ intercalating a species S according to $(C_{\nu^g} - PG)\,[X, Y]$ fullerene *incar* species, and to denote it $i\mathrm{S}[C_{60} - I_h]$.[81] Instead, the $S@C_{\nu^g}$ nomenclature commonly found in literature is used.

2.1.2 Material properties and production of C_{60} and C_{70} fullerenes

The C_{60} fullerene comprises a molecule that in ideal approximation is represented by a truncated icosahedron. This Archimedean solid consists of $\nu^g = 60$ vertices, $f = 32$ surfaces and $e = 90$ edges.[13] Its point group I_h is of order 120, therefore, it is commonly referred to as a highly symmetrical molecule (cf. Fig. 5**B**).[14]
Besides the forecast of the C_{60} fullerene by *E. Osawa*, which was influenced by the curved spherical cap-like structure of corannulene (Fig. 5**A**), various experimental results corroborate this appellation.[80,83] For example, X-ray crystallographic investigations on an osmylated C_{60} derivative and on C_{60} crystallized from benzene as well as gas-phase electron diffraction studies have been shown little deviation from the I_h symmetry.[84–86] Further agreement has been obtained by ^{13}C NMR

[13] In general applies Euler's polyhedron formula: $\nu^g + f - 2 = e$.[75]
[14] Note, that the octahedron point group O_h is of order 48.

spectroscopy. The data provide but one signal in the field area of non-protonated aromatic carbon, therefore, demonstrating the equivalence of the carbon atoms. Furthermore, the results allow to draw predictions with respect to bond distances, van der Waals (vdW) radii, and the binding topology.

1. 5-membered rings are mutually separated by 6-membered rings.
2. Single (145 pm) and double bonds (138 pm) alternate. Additionally, 5-membered rings are solely built from single bonds.
3. The vdW diameter, the vdW surface, and the vdW volume are, respectively:[15] $d_{\mathrm{vdW,C_{60}}} = 0.95\,\mathrm{nm}$, $S_{\mathrm{vdW,C_{60}}} = 3.5\,\mathrm{nm}^2$, $V_{\mathrm{vdW,C_{60}}} = 0.45\,\mathrm{nm}^3$.[87,88]

Additional characteristics of the C_{60} fullerene are its comparatively high electron affinity and polarizability which were measured to be $W_{\mathrm{A}} = 2.65\,\mathrm{eV}$ (gaseous phase) und $\alpha_{\mathrm{C_{60}}} = 82.7 \times 10^{-30}\,\mathrm{m}^3$, respectively.[89,90]
The chemical structure of the C_{70} fullerene as it is available from quantum chemical calculations and X-ray crystallography experiences a symmetry breaking compared to the C_{60} fullerene.[91,92] The corresponding point group is D_{5h} where the C_5 symmetry axis centrally intersects the polar 5-membered rings (cf. Fig. 5**C** und **D**). ^{13}C NMR measurements reveal five signals which are assigned to equivalence classes α - ε shown in Fig. 5**D**.[93,94] Thereby annihilating the bonding alternation of the C_{60} fullerene crystal structure analysis, unveils eight distinct bond distances. However, it is still possible to allocate them into a single ($142 - 146\,\mathrm{pm}$) and a douple bond regime ($137 - 138\,\mathrm{pm}$).[92] Fig. 5**A**&**C** draws an analogy between the binding topology of corannulene and the C_{70} fullerene. Hence, the latter one can be interpret as a fusion of two corannulene units which are linked via a sliver of 5- and 6-membered rings. Due to lowered curvature, this intermediate part of the C_{70} molecule represents an area of increased vdW interaction.[95] The molecular size of the C_{70} fullerene can be estimated by the following vdW values:[16] $S_{\mathrm{vdW,C_{70}}} = 3.8\,\mathrm{nm}^2$ and $V_{\mathrm{vdW,C_{70}}} = 0.54\,\mathrm{nm}^3$.[87,88] The polarizability is given as $\alpha_{\mathrm{C_{70}}} = 102 \times 10^{-30}\,\mathrm{m}^3$, therefore, the ratio of the corresponding quantities for C_{70} and C_{60} is calculated to $\alpha_{\mathrm{C_{70}}}/\alpha_{\mathrm{C_{60}}} = 1.23$.[96]

The electrochemistry of fullerene anions has been widely studied, which was supported by the easy preparative accessibility of the reduction protocols, such as the use of alkali and alkaline earth metals, organometallic and BH_3compounds,

[15] The given values assume a vdW radius of carbon of 0.147 nm.[87]
[16] Cf. footnote 15.

and electrosynthesis, as well as their relative stability, at least of low-oxidized fullerenes.[97] All intermediates of the single electron reduction cascade up to the hexaanion could be characterized with respect to their reduction potential.[98] Of practical significance are the solid state properties of C_{60} anion salts, which can form ferromagnetic and superconducting phases, the latter being observed for Cs_2RbC_{60} up to a temperature of 33 K.[99] Eventually, technical demonstration of a single C_{60} molecule transistor possessing superconductivity has been reported.[100] The use of [6, 6]-phenyl-C−61-butyric acid methyl ester in organic solar cells is based on the low reduction potential of the corresponding C_{60} derivative insofar as it acts as an electron acceptor.[101]

In contrast to the C_{60} anion, the corresponding cations are less in focus both, in terms of research results and possible applications, which is mainly related to their chemical instability. This thesis deals with their generation and spectroscopic investigation in Chapter 3.

In addition to the charged species, neutral C_{60} fullerenes are also the subject of current research, due to their unparalleled chemical composition of spherical geometry, full sp^2 carbon coverage and high molecular volume. One feature resulting from this is its low solubility leading to so called solvophobic solvation.[88] With relatively weak C_{60} solvent molecule interactions occurring, which corresponds to a low solvation enthalpy, the negative solvation entropy becomes determining and the Gibbs solvation energy $\Delta_{\text{solv}}G^\circ = \Delta_{\text{solv}}H^\circ - T\Delta_{\text{solv}}S^\circ$ becomes positive.[17] As a consequence, cluster, aggregate, and nanocrystal formation can be observed in a large number of particular solvents. This circumstance was used to produce a variety of one-, two, and three-dimensional confined nanostructures using crystallization methods; a technical application given by a field-effect transistor was also presented.[102,103] In life sciences the chemical orthogonality as well as the electrochemical properties have lead to investigations in terms of C_{60} as, e.g., radical scavenger, drug delivery agent, antibiotic for Gram-positive bacteria, and component of a glucose biosensor.[104]

Krätmscher et al. reported the first production protocol to obtain macroscopic amounts of C_{60} and C_{70}.[72] This process bases on resistive heating of graphite electrodes under a helium atmosphere. Currently, two production techniques are employed: the evaporation of graphite in the arc and combustion of toluene or tetralin.[105,106] While in the former case yields of $5 - 12\,\%$ related to C_{60} and C_{70} are accessible the combustion method earns $1\,\%$. Yet, the latter one capitalizes

[17] For Tetralin, for example, there is: $\Delta_{\text{solv}}H^\circ = 197\,\text{kJ mol}^{-1}$, $\Delta_{\text{solv}}S^\circ = -208\,\text{kJ mol}^{-1}$ at 298 K and 1013 mbar.[88]

on lower an energy consumption and its scalability.[106] Common to all those production techniques a crude mixture of C_{60}, C_{70}, higher fullerenes and amorphous carbon is garnered. Accordingly, purification and component-wise separation is crucial, especially, since total synthesis protocols aiming to produce fullerenes still remains elusive due to low yields.[107,108]

2.1.3 Material properties and production of N@C_{60} fullerene

The $^{14}N@C_{60}$ molecule[18] consists of a C_{60} fullerene and a nitrogen atom which is preserved in its $^4S_{3/2}$ electronic ground state and resides in the very center of the fullerene cavity (see Fig. 6).[19] Such a molecular system is particularly remarkable because otherwise atomic nitrogen can only be observed as short-living species under very harsh conditions, for example in discharge experiments.[110]

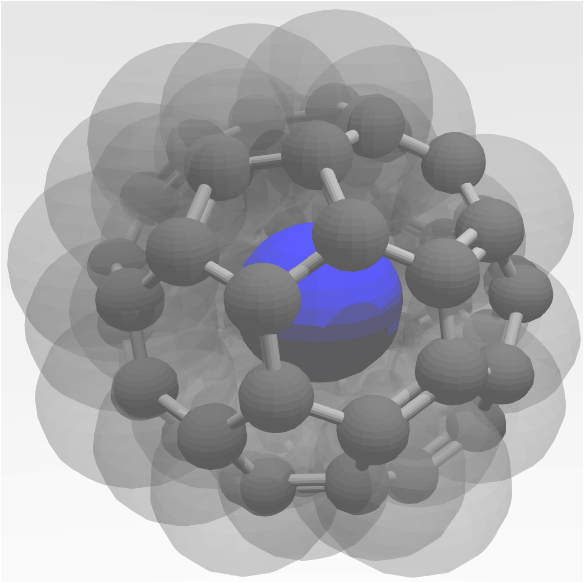

Figure 6: Molecular structure of N@C_{60} showing the nitrogen atom (blue) with vdW diameter $D_{\mathrm{vdW}} = 3.1\,\text{Å}$, the fullerene cavity ($D_{\mathrm{vdW}} = 4.4\,\text{Å}$), and the C_{60} fullerene ($D_{\mathrm{vdW}} = 9.5\,\text{Å}$), when transparent spheres indicate $D_{\mathrm{vdW}} = 2.9\,\text{Å}$ of carbon (grey).[87,109]

The paramagnetic $S = 3/2$ spin ground state of the endohedral nitrogen atom has been substantiated by EPR spectroscopy.[111,112] Especially, the observed narrow linewidth in the µT range or, conterminously, the long relaxation times which for $T_2 = 120(10)\,\mu\text{s}$ suggest a natural linewidth even lower, was traced back to a purely isotropic system (see Chap. 2.1.4 for more details). Quantum chemical calculations resulted in a global energy minimum when the nitrogen atom is located in the center of the C_{60} fullerene cavity.[113] The activation energy for the process of nitrogen extrusion was calculated to be $\approx 2\,\text{eV}$.[114]

[18] In the remainder of this work, we suppress the specification of the nitrogen isotope since all experiments were carried out with ^{14}N implanted material.

[19] Accordingly, neither bond formation nor charge transfer occurs between the C_{60} fullerene and the nitrogen atom.

A comparison of the UV/VIS spectra of C_{60} and $N@C_{60}$ shows no significant deviation in the extinction values over the spectral range of $\lambda = 200 - 700\,\mathrm{nm}$ (λ: wavelength).[115] The thermal stability of $N@C_{60}$ was discussed over a longer period of time.[116,117] Recent studies show that $N@C_{60}$ decomposes under ambient conditions in solid state with a time constant of about 38 weeks.[57] Thermal stress increases the decay rate.[118] However, stabilization is possible under protective atmosphere.[57]

A. Weidinger et al. developed two processes for producing $N@C_{60}$: the ion implantation and the glow discharge method.[119] The former was used in the context of this work and is described below. An extended description is given in [57].

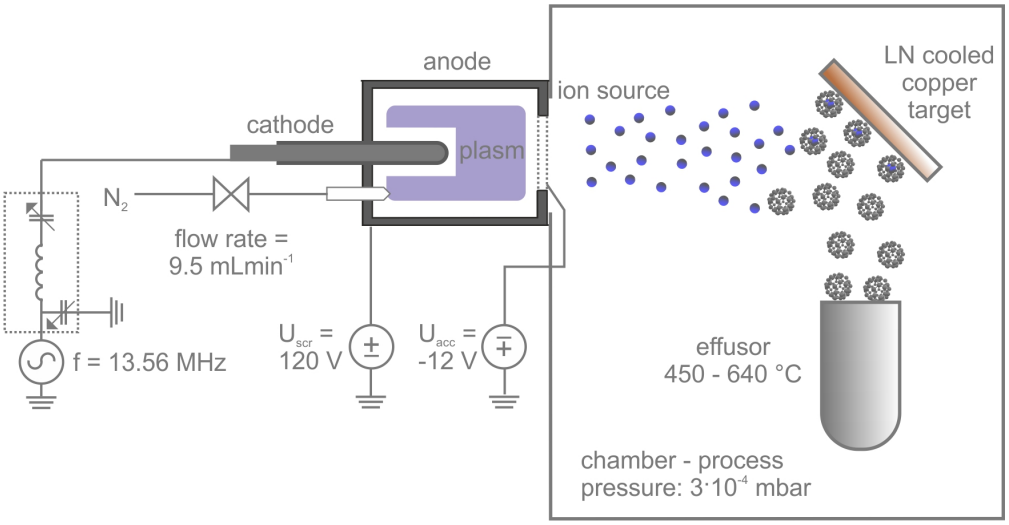

Figure 7: Schematic drawing of the implantation setup denoting standard process parameters. See text for details.

The capacitive-coupled high frequency (13.56 MHz) ion source is fed with a constant volume flow $\dot{V}_{N_2}$ of nitrogen (see Fig. 7). In the ignited plasma, N^+ ions are generated by collisional ionization with electrons accelerated in an alternating electric field. These ions are extracted by ion optics into the chamber with the energy $e\,(U_{\mathrm{plasm}} + U_{\mathrm{scr}} + U_{\mathrm{acc}})$, whereby the latter two contributions are adjustable. A certain proportion of the ions integrate into the fullerenes which are present before and on the target. These are synchronously sublimated in the process from a resistively heated effusor. The target is a liquid nitrogen-cooled, rotatable, double-sided copper plate construction located in a 45°-geometry in the idealized trajectories of both $N@C_{60}$ precursors. To increase the mean free path

of the nitrogen ions, the plant is operated under reduced pressure. After the implantation process is completed, the target is ejected. The raw material forms a layer few micrometers thick on the copper plates, which is collected by scraping. In addition to fullerenes and endohedral fullerenes, it contains insoluble material (fullerene fragments and polymers). The ratio of $N@C_{60}$ to C_{60} is about 1×10^{-4}. Since a 80 : 20 mixture of C_{60} and C_{70} is used in the current process control, an appropriate processing is necessary. To separate C_{60} / $N@C_{60}$ from C_{70} / $N@C_{70}$, higher fullerenes, and non-fullerene by-products, purification by filtering and plug-filtration[120] is conducted. Eventually, enrichment of $N@C_{60}$ towards C_{60} is accomplished by high pressure liquid chromatography (HPLC). This method capitalizes on the small difference in polarizability of the two species to separate them via molecular interactions with a pyrene-functionalized column bed (COSMOSIL Buckyprep, Nacalai Inc.).

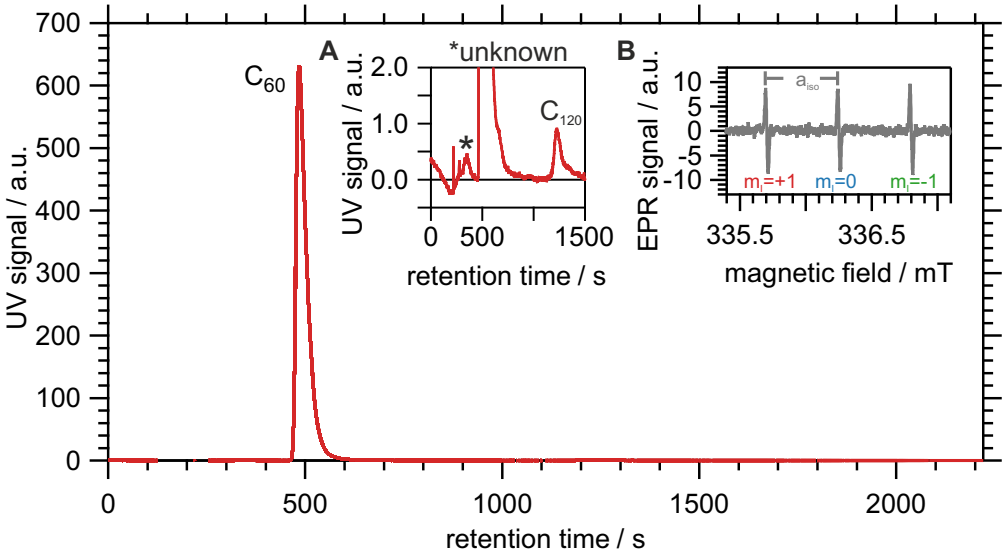

Figure 8: Example results of $N@C_{60}$ analysis. HPLC Chromatogram, recorded with calibrated UV/ VIS detector, shows mainly C_{60} which is identified due to characteristic retention time of 485 s. Inset **(A)**: Contamination by unknown species and C_{120} amounts to 0.5 %. Inset **(B)** Overview EPR spectrum reveals characteristic hyperfine splitting (see Chap. 2.1.4). Quantification is accomplished by double-integrating one hyperfine line and determining $N@C_{60}$ according to Eq.(4.1) using TEMPO as spin standard.

The C_{60} / $N@C_{60}$ content is characterized by an analytical HPLC protocol utilizing an UV detector which was calibrated against a C_{60} standard. The amount of $N@C_{60}$ is determined using X band cw-EPR spectroscopy (with standard param-

eter mw power $P_{\mathrm{mw}} = 10\,\mu\mathrm{W}$, modulation amplitude $B_{\mathrm{mod}} = 0.01\,\mathrm{mT}$, binning $0.01\,\mathrm{mT/bin}$, sweep rate $0.13\,\mathrm{mT/s}$. Spin counting is enabled by TEMPO calibration. An example analysis outcome for the material used in the experiments for single N@C_{60} molecule readout yields a purity of 99.5 % with C_{120} as main impurity, a filling factor of 1.0×10^{-4}, i.e., the ration of N@C_{60} particles per total fullerene particle content, and a hyperfine coupling strength of 15.8(1) MHz (see Fig. 8).[59]

2.1.4 N@C_{60} fullerene as quantum sensor

The effective electron ground state $S = \frac{3}{2}$ spin Hamiltonian of N@C_{60} taking solely isotropic coupling to the ^{14}N nuclear spin ($I = 1$) into account reads as

$$\underline{\hat{H}}_0 = \frac{\mu_{\mathrm{b}}}{\hbar} g_{\mathrm{iso}} B_z \hat{S}_z + a_{\mathrm{iso}} \hat{S}_z \hat{I}_z, \tag{2.1}$$

where $g_{\mathrm{iso}} = 2.002\,04(4)$ has recently be determined with high precession and $a_{\mathrm{iso}} = 0.56(1)\,\mathrm{mT}$.[118,121] Thus, the state energies can be computed according to

$$\langle S, m_s| \otimes \langle I, m_I| \underline{\hat{H}}_0 |S, m_s\rangle \otimes |I, m_I\rangle = \frac{\mu_{\mathrm{b}}}{\hbar} g_{\mathrm{iso}} B_z m_S + a_{\mathrm{iso}} m_S m_I \tag{2.2}$$

and the corresponding term diagram is given in Fig. 9. An example spectrum emphasizing the hyperfine splitting by a_{iso} is exhibited in Fig. 8 - inset **B**.

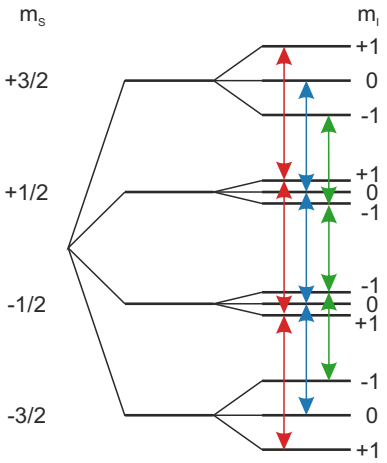

Figure 9: N@C_{60} spin level diagram, see Eq. (2.2).

Most of the results obtained in this thesis are covered by this simple model. Corrections such as the full development of the hyperfine matrix leading to second order energy terms as large as 930 µT, zero-field splitting contributions, and nuclear Zeeman interaction cannot be resolved with our EPR spectrometer.[122] Following the remarks in Chapter 1.2 on electron-spin-spin coupling, secular terms of this dipolar interaction should lead to additional terms $\frac{\mu_0 g_1 g_2 \mu_{\mathrm{b},1} \mu_{\mathrm{b},2}}{4\pi\hbar} \frac{1}{r_{12}^3} m_{S_1} m_{S_2} (1 - 3\cos^2\theta)$ for spins S_1 and S_2. Whether these can be observed for the C_{60} cation-N@C_{60} system in bulk EPR measurements is discussed in Chap. 3.

Next, we briefly comment on the potential utilization of endohedral group-V fullerenes as quantum sensors. While the requirements for temperature

and pressure sensing protocols have been reported as well,[123,124] we are concentrating here on the detection of magnetic fields. From early studies on the line broadening of N@C_{60} in dependence of its concentration in powder samples it could be concluded that it is sensitive to environmental spins due to dipolar interactions.[125] An extension of this approach has been demonstrated on C_{60}/ N@C_{60} nanostructures, whereby a change of the N@C_{60} linewidth was concluded by the degree of solvent and thus simultaneously proton intercalation into the fullerene host crystal.[55] By functionalizing N@C_{60} with permethylated β-cyclodextrin, its water-solubility could be achieved. Subsequently, experiments were conducted in polar solvents of increasing Cu^{2+} concentration which found its manifestation in a linearly increasing linewidth of N@C_{60}.[56] These two approaches rely on the coherent manipulation of ensemble spins using bulk EPR. The underlying physical mechanism is the influence of the spin bath onto the decoherence time T_2. To give a rough estimation for requirements of observing dipol-dipol interaction between N@C_{60} and a $S = \frac{1}{2}$ species as resolvable spectroscopic feature with our EPR spectrometer, we assume a splitting two times the linewidth, which results in nearly $50\,\mu\mathrm{T} = 1.4\,\mathrm{MHz}$ for N@C_{60}. Since $E^{\mathrm{dip}}_{\mathrm{N@C_{60}}-S=1/2} \approx \frac{52\,\mathrm{MHz}}{r^3\,\frac{1}{\mathrm{nm}^3}}$ the distance between both spins need to be $r \lesssim 3\,\mathrm{nm}$.

Regarding their sensitivity, EDMR- and ODMR-assisted protocols range in the small ensemble and single molecule regime, respectively.[57–59] For the latter, NV^- center-mediated addressing of a N@C_{60} molecule at cryogenic temperatures recently has been reported. Its T_2 decoherence time was measured as longer as $1\,\mu\mathrm{s}$, where the T_2 time of the specific NV^- imposed restrictions on the full determination. However, even with this estimated value, there is an improvement in frequency resolution to below 1 MHz. If we take a bulk value of T_2 from the literature, which was obtained at diluted ^{15}N@C_{60} and resulted in $190\,\mu\mathrm{s}$, the sensing radius would be extended to $\approx 20\,\mathrm{nm}$.[126]

A full discussion of the possibilities of N@C_{60} to act as a quantum sensor on the single molecule level leads beyond the scope of this thesis. However, the use of the full Hilbert space, especially including the ^{14}N nuclear spin, which naturally has relaxation times in the $\mathrm{ms} - \mathrm{s}$ range, seems to be auspicious, in particular, since dynamic decoupling sequences acting on the electron spin as well as the coherent state transfer between electron and nuclear spin has already been demonstrated on bulk samples.[122,126]

Finally, it should be noted that group-V endohedral fullerenes are also promising from a chemical point of view, since they possess a defined surface compared to nanodiamonds, for example. This is accessible by a variety of synthetic ap-

proaches, such as thermal and photochemical cycloadditions as well as nucleophilic additions.[127]

2.2 The diamond hosted NV^- center - a quasi-molecular system

The NV^- center is a diamond lattice impurity whose electronic states can be derived by considering it as a quasi-molecule energetically embedded within the diamond band structure. Specific electronic interactions cause the spin levels $|m_S = 0\rangle$ and $|m_S = \pm 1\rangle$ to exhibit different transition dynamics, which concurrently lead to different fluorescence behavior (see Chap. 2.2.1). Since the axial-symmetrical NV^- center has a spin triplet ground state a characteristic response to static (Chap. 2.2.2) and alternating magnetic fields (Chap. 2.2.3) can be observed.

2.2.1 Optical properties of the NV^- center

Hosted in an all-carbon diamond crystal, the NV^- center comprises a substitutional nitrogen atom and a neighboring vacancy.[128,129] The defective lattice decoration breaks down the translational symmetry of the diamond $Fd\bar{3}m$ space group and leaves the C_{3v} point group as an adequate description of the local impurity structure, that is constituted by one nitrogen and three covalently unsaturated carbon atoms in a tetrahedral arrangement (see Fig. 10**A**).
In general, the C_3 symmetry axis of the NV^- center is aligned along the four diagonals ($\langle 111\rangle$, $\langle 1\bar{1}\bar{1}\rangle$, $\langle \bar{1}1\bar{1}\rangle$, $\langle \bar{1}\bar{1}1\rangle$) of the diamond structure in either direction which results in four different orientation classes regarding vectorial interactions (see the four orange sticks in Fig. 10**B** which represent one orientation of the NV^- axis, respectively).[130]
In terms of its global energy the NV^- center lies within the diamond band gap between the valence band (VB) and the conduction band (CB).[129] Therefore, it can be interpret as a quasi-molecule and the nitrogen (σ_N) as well as three carbon (σ_1, σ_2, σ_3) dangling bonds may linearly combined according to[20] $a_1' = \sigma_N - \Lambda'(\sigma_1 + \sigma_2 + \sigma_3)$, $a_1 = \Lambda(\sigma_1 + \sigma_2 + \sigma_3) + \sigma_N$, $e_x = \frac{2\sigma_1 - \sigma_2 - \sigma_3}{\sqrt{6}}$, and $e_y = \frac{\sigma_2 - \sigma_3}{\sqrt{2}}$ to result in four symmetry-adapted molecular orbitals (MOs).[19,128] In its negative charge state six electrons occupy these MOs. Due to Coulomb interactions

$$\left|{}^3A_2\right\rangle = |e_x e_y - e_y e_x\rangle \otimes \begin{Bmatrix} |+1\rangle \\ |0\rangle \\ |-1\rangle \end{Bmatrix} = |E_0\rangle \otimes \begin{Bmatrix} |+1\rangle \\ |0\rangle \\ |-1\rangle \end{Bmatrix} \tag{2.3}$$

[20] Λ and Λ' are factors that take mixing between the dangling bond orbitals into account.

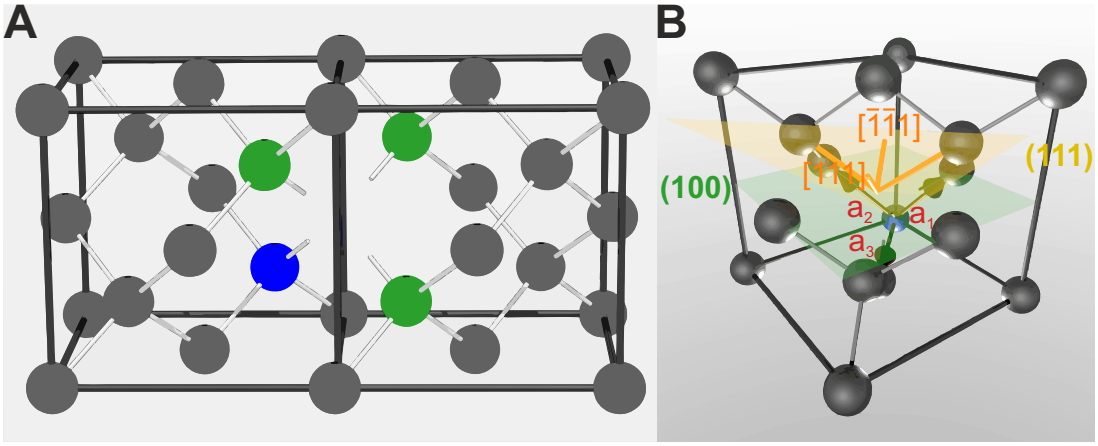

Figure 10: (A) Diamond lattice structure (gray spheres) hosting a NV^- center which consists of a carbon-substituting nitrogen atom (blue) and three carbon atoms surrounding a lattice vacancy. **(B)** NV^- center aligned along the [111] axis. a_i (red) represents the primitive basis vectors of the face centered cubic lattice, while the basis is constituted by the nitrogen atom (blue) and the vacancy. Furthermore, two characteristic crystals planes (100) and (111) are depicted as well as potential NV^- center symmetry axis orientations [111], [$\bar{1}\bar{1}$1], [1$\bar{1}\bar{1}$], and [$\bar{1}$1$\bar{1}$], where the last two are not assigned.

the electronic ground state, whose spin degrees of freedom constitute a triplet spin state: $|S=1, m_S=+1\rangle =: |+1\rangle$, $|S=1, m_S=0\rangle =: |0\rangle$ and $|S=1, m_S=-1\rangle =: |-1\rangle$, is lowest in energy, and thus constitutes the highest occupied molecular orbital (HOMO) (Fig. 11**A**).[19,128,129] Because of the axial symmetry of the NV^- center the degeneracy of the spin triplet states is lifted by dipolar spin-spin interaction, where the electronic ground state zero field splitting parameter is $D = 2\pi \cdot 2.87\,\text{GHz}$ in the absence of crystal strain (Fig. 11**B**).[129] The first excited electronic state $|^3\text{E}\rangle$ (lifetime $\tau_{|^3\text{E}\rangle} \approx 25\,\text{ns}$) is attainable by non-resonant laser excitation at $\lambda_{\text{exc}} = 520\,\text{nm}$ into phonon sidebands (green arrows in Fig. 11**B**) under preservation of the spin angular momentum number m_S. Concerning relaxation, however, there is a strong dependency on m_s due to spin dependent intersystem crossing (ISC) into the singlet state $|^1\text{A}_1\rangle$ whose lifetime is given by $\tau_{|^1\text{A}_1\rangle} \approx 250\,\text{ns}$, and is thus comparatively longer than $\tau_{|^3\text{E}\rangle}$. While for the $|0\rangle$ spin state the ISC coupling strength is two orders of magnitude lower as for the $|\pm1\rangle$ spin states (upper black dash-dotted arrows in Fig. 11**B**) it preferentially decays via photon emission in the visible area at $\lambda_{\text{em}} \approx 637 - 850\,\text{nm}$ (red arrows in Fig. 11**B**). Contradictorily, in the limit of many excitation cycles the $|\pm1\rangle$ spin states

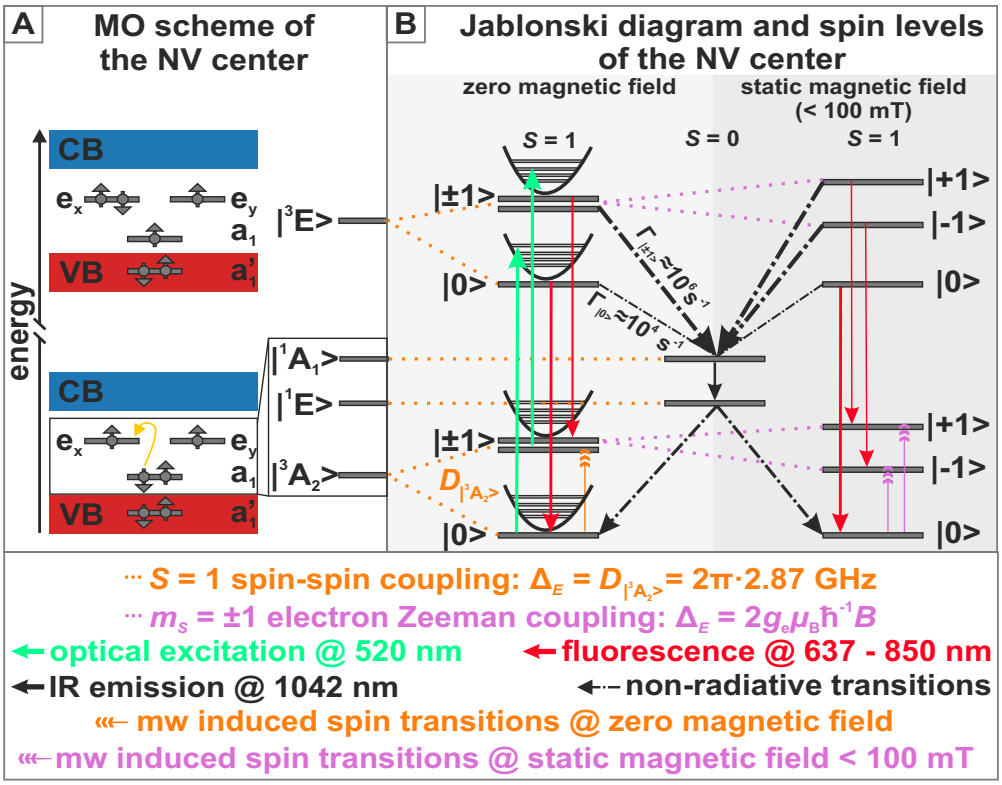

Figure 11: **(A)** Energy level scheme of C_{3v} symmetry-adapted MOs of electronic ground and excited state. States denoted with small letter are given in spatial coordinates, those with capital letter additionally include spin degrees of freedom. **(B)** Jablonski diagram of NV^- center electronic level transitions. Dotted lines depict degeneracy lifting interactions, single-headed arrows represent optical, three-headed mw induced transitions. Intersystem crossing relaxation is indicated by dash-dotted arrows.

more often pass to the singlet manifold to eventually decay predominantly in the electronic ground state $|E_0\rangle \otimes |0\rangle$. Since the IR emission of the singlet state relaxation $\lambda_{|^1\mathrm{E}\rangle \to |^1\mathrm{A}_1\rangle} = 1042\,\mathrm{nm}$ commonly is not detected, and therefore does not contribute to the overall photon count, per unit time less photons are emitted on this relaxation pathway because of $\tau_{|^3\mathrm{E}\rangle}/\tau_{|^1\mathrm{A}_1\rangle} < 1$. Thus, counting photons in a period of time, which is comparable to the singlet state lifetime, allows for spin state discrimination and spin state readout (see Fig. 21**B**).
Additionally, the fact that independent of the initial state the final state of one excitation cycle predominantly is given by the $|E_0\rangle \otimes |0\rangle$ state leads to a non-thermal polarization, which can reliably be prepared by driving the electronic transitions

for a time longer than any state lifetime. The NV center is in an equilibrium state then whose lifetime is mainly determined by the $\tau_{|^3\mathrm{E}\rangle}$ state (see Chap. 2.4.2).

2.2.2 The response of the NV$^-$ center to static magnetic fields

The sensitivity of the NV$^-$ center to a magnetic field $\underline{B} = B_0\,(\sin\vartheta\cos\varphi, \sin\vartheta\sin\varphi, \cos\vartheta)^{\mathrm{T}}$ can be deduced from its ground state spin Hamiltonian given in the Zeeman basis

$$\hat{H}_0 = D_x\hat{S}_x^2 + D_y\hat{S}_y^2 + D_z\hat{S}_z^2 + \gamma_{e,\mathrm{NV}}\underline{B}\cdot\underline{\hat{S}} \tag{2.4}$$

where we neglect hyperfine and far-reaching dipolar coupling terms.[21] Herein, $\underline{\hat{S}} = \left(\hat{S}_x, \hat{S}_y, \hat{S}_z\right)^{\mathrm{T}}$ is the vector spin operator, whose components are given by $\hat{S}_x = \sqrt{2}^{-1}\left(\begin{smallmatrix}0&1&0\\1&0&1\\0&1&0\end{smallmatrix}\right)$, $\hat{S}_y = \left(\sqrt{2}i\right)^{-1}\left(\begin{smallmatrix}0&1&0\\-1&0&1\\0&-1&0\end{smallmatrix}\right)$, and $\hat{S}_z = \left(\begin{smallmatrix}1&0&0\\0&0&0\\0&0&-1\end{smallmatrix}\right)$. The gyromagnetic ratio of the NV$^-$ center γ_e^{NV} is determined by the g-factor $g_e^{\mathrm{NV}} = 2.0028$.[129] Note that the zero field splitting (zfs) matrix is formulated in its eigenframe $\underline{D} = \left(\begin{smallmatrix}D_x&0&0\\0&D_y&0\\0&0&D_z\end{smallmatrix}\right)$ and that the orientation of the magnetic field $\underline{B}$ in respect to the NV$^-$ center symmetry axis is formulated in spherical coordinates, where ϑ and φ are the canonical angles. The expansion of Eq. (2.4) results in

$$\hat{H}_0 = \begin{pmatrix} D_z+\frac{D_x+D_y}{2} & 0 & \frac{(D_x-D_y)}{2} \\ 0 & D_x+D_y & 0 \\ \frac{(D_x-D_y)}{2} & 0 & D_z+\frac{D_x+D_y}{2} \end{pmatrix} + \gamma_e^{\mathrm{NV}} \begin{pmatrix} B_0\cos\vartheta & \frac{B_0\sin\vartheta\mathrm{e}^{-\mathrm{i}\varphi}}{\sqrt{2}} & 0 \\ \frac{B_0\sin\vartheta\mathrm{e}^{\mathrm{i}\varphi}}{\sqrt{2}} & 0 & \frac{B_0\sin\vartheta\mathrm{e}^{-\mathrm{i}\varphi}}{\sqrt{2}} \\ 0 & \frac{B_0\sin\vartheta\mathrm{e}^{\mathrm{i}\varphi}}{\sqrt{2}} & -B_0\cos\vartheta \end{pmatrix}. \tag{2.5}$$

Let us consider the zfs term first. Since $\underline{D}$ merely stems from dipol-dipol electron interaction, it is traceless ($D_z = -\left[D_x + D_y\right]$), and new parameters D, E can be introduced. For them applies: $D = D_{zz} - \frac{1}{2}\left(D_x + D_y\right)$ and $E = \frac{1}{2}\left(D_x - D_y\right)$. In the absence of lattice distortion or electric fields (for bulk diamond NV$^-$ centers $E \approx 0$ holds true on the $D = 2\pi \cdot 2.870\,\mathrm{GHz}$ scale) we come upon the NV$^-$ center as an ideal uni-axial system. Therefore $D_x = D_y$, and E vanishes. Because we are solely interested in transitions between different spin states we can set the zero point of energy to $0 \stackrel{!}{=} -\frac{2D}{3}$. Eventually, we have

$$\hat{H}_0 = \begin{pmatrix} D & 0 & 0 \\ 0 & 0 & 0 \\ 0 & 0 & D \end{pmatrix} + \gamma_e^{\mathrm{NV}} \begin{pmatrix} B_0\cos\vartheta & \frac{B_0\sin\vartheta\mathrm{e}^{-\mathrm{i}\varphi}}{\sqrt{2}} & 0 \\ \frac{B_0\sin\vartheta\mathrm{e}^{\mathrm{i}\varphi}}{\sqrt{2}} & 0 & \frac{B_0\sin\vartheta\mathrm{e}^{-\mathrm{i}\varphi}}{\sqrt{2}} \\ 0 & \frac{B_0\sin\vartheta\mathrm{e}^{\mathrm{i}\varphi}}{\sqrt{2}} & -B_0\cos\vartheta \end{pmatrix}. \tag{2.6}$$

[21] In our cw-ODMR experiments this is justified due to power broadening. In pulse experiments mw excitation frequencies can be applied which are centered in a way that the hyperfine interaction-related manifolds are effectively degenerated.

This can be further simplified to[22]

$$\hat{H}_0 = \begin{pmatrix} D + \gamma_e^{\mathrm{NV}} B_0 & 0 & 0 \\ 0 & 0 & 0 \\ 0 & 0 & D - \gamma_e^{\mathrm{NV}} B_0 \end{pmatrix} \tag{2.7}$$

if we presuppose that the magnetic field and the NV^- axis coincide ($\vartheta, \varphi \stackrel{!}{=} 0$). In this way, we can reproduce the level scheme in Fig. 12**A**. For example, when taking the Zeeman basis in vector representation $\langle 1, +1| = (1, 0, 0)$, $|1, +1\rangle = \begin{pmatrix} 1 \\ 0 \\ 0 \end{pmatrix}$, $\langle 1, 0| = (0, 1, 0)$, $|1, 0\rangle = \begin{pmatrix} 0 \\ 1 \\ 0 \end{pmatrix}$, we may get

$$\Delta E_{|1,+1\rangle \leftarrow |1,0\rangle} = \left| \langle 1, +1| \hat{H}_0 |1, +1\rangle - \langle 1, 0| \hat{H}_0 |1, 0\rangle \right| = \left(2\pi \cdot D + \gamma_e^{\mathrm{NV}} B_0 \right). \tag{2.8}$$

We now return to the general case, where $\vartheta, \varphi \neq 0$ and $E \neq 0$ (Eq. (2.5)). The first inequality points out that $\underline{B}$ and the symmetry axis of the NV^- center are no longer aligned. Yet, since in our experiments we apply only slight static magnetic fields of $\approx 10\,\mathrm{mT}$, the inequality $\gamma_e^{\mathrm{NV}} B_0 \ll 2\pi \cdot D$ is still valid and the the NV^- axis remains the quantization axis of the lab frame. Consequently, the Zeeman basis still provides good eigenfunctions, yet, the eigenvalues change (see Fig. 12**C**). Additionally, due to the off-diagonal parameter E in the zfs term, the degeneracy of the $|1, \pm 1\rangle$ states is lifted even in zero field (see Fig. 12**B**, where $B_x, B_y = 0$).

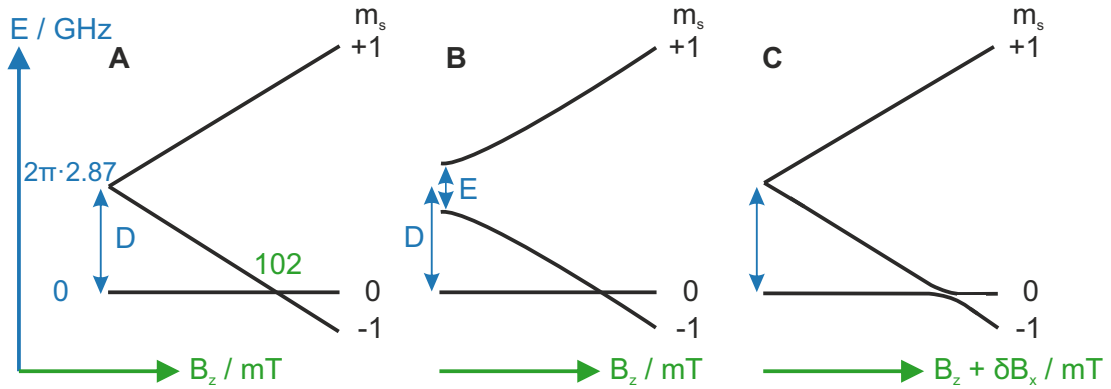

Figure 12: NV^- center response to static magnetic fields when **(A)** NV^- center and B_z axis are co-aligned, **(B)** crystal strain or electric fields are present ($E \neq 0$), and **(C)** slight misalignment between B_0 and NV^- center axis. Adapted from Ref. [70].

[22] Note that in the nomenclature of Chap. 1.4.2 this constitutes the internal Hamiltonian.

In this case, the tilting of B against the NV$^-$ center axis (Δ_{NVB}) and the effective magnetic field strength projected onto the the NV$^-$ center axis ($B_{0\|\mathrm{NV}}$) can be calculated according to[131]

$$\Delta_{\mathrm{NVB}} = \frac{7D^3 + 2(\omega_1+\omega_2)\left[2(\omega_1^2+\omega_1^2) - 5\omega_1\omega_2 - 9E^2\right] - 3D(\omega_1^2+\omega_2^2-\omega_1\omega_2+9E^2)}{9(\omega_1^2+\omega_2^2-\omega_1\omega_2-D^2-3E^2)} \tag{2.9}$$

$$B_{0\|\mathrm{NV}} = \frac{\hbar}{\mu_b g_{\mathrm{e}}^{\mathrm{NV}}}\sqrt{\frac{1}{3}(\omega_1^2+\omega_2^2-\omega_1\omega_2-D^2)} - E^2. \tag{2.10}$$

Fig. 13 depicts example cw-ODMR measurements on a single NV$^-$ center. The measurement protocol is designed that the laser continuously excites electronic transitions, and according to Chap. 2.2.1 an equilibrium state is constituted, which results in an average photon count rate. Additionally, mw radiation is applied whose frequency is swept. If the resonance condition in Eq. (2.8) is met, where $B_0 = 0$ for the moment, mw induced spin transitions into the $|\pm1\rangle$ spin state take place. Thus, enhanced ISC relaxation occurs, which causes a dip in the photon count rate signal. Its frequency is given by $\nu = 2.8717(5)$ GHz. In a magnetic field of 9.23(1) mT the degeneracy of the $|\pm1\rangle$ spin state is split (see Eq. (2.7)) and two signals become visible. The frequency difference results in $2\frac{g_{\mathrm{NV}}\mu_b}{h}B_{0\|\mathrm{NV}} = 503.7(3)$ MHz.

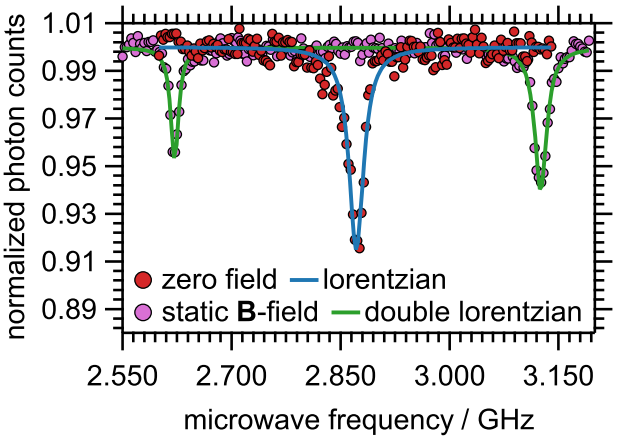

Figure 13: cw-OMDR spectra at zero magnetic field (red) and with applying a magnetic field of 9.23(1) mT (magenta). The fit functions are given.

The full Hamiltonian of a NV$^-$ center with ^{15}N nuclear spin contains additional terms of the electron-nuclear hyperfine interaction, which, however, can not be seen in the spectra in Fig. 13. This is due to line broadening caused by the laser and mw irradiation. A classical description refers to the Bloch equations (see Eq. (1.35)), which need to be adopted for both excitation processes. Semi-classical approaches utilize specific evolution equations and take relaxation parameters into account via decoherence contributions.[132] It is possible to resolve, e.g., the hyperfine coupling

to ^{15}N and diamond-inherent ^{13}C nuclear spins by lowering the laser and mw power, but this also reduces the signal intensity. A second approach consists of pulsed ODMR measurement schemes, which project the interaction between the electron spin and magnetic fields on the phase relationship of its basis states. These will be discussed next.

2.2.3 Basic NV$^-$ center pulse experiments

In the previous chapter we provided the static or internal Hamiltonian of the NV$^-$ center in line with our experiments. According to Chap. 1.4.2 we additional require a control Hamiltonian. To induce transitions between spin sublevels and thereby manipulate state populations, mw radiation, whose $\underline{B}_1$ field vector is orientated perpendicular with respect to the NV$^-$ center symmetry axis, is therefore applied. If $\underline{B}_1 \parallel x$ and linearly polarized, the corresponding Hamiltonian reads as[61,70]

$$\hat{H}_1 = 2\Omega_x \cos(\omega_{\mathrm{mw}} t)\, \hat{S}_x = \frac{1}{\sqrt{2}} \left[\Omega_+ \begin{pmatrix} 0 & \mathrm{e}^{-\mathrm{i}\omega_{\mathrm{mw}} t} & 0 \\ \mathrm{e}^{\mathrm{i}\omega_{\mathrm{mw}} t} & 0 & \mathrm{e}^{-\mathrm{i}\omega_{\mathrm{mw}} t} \\ 0 & \mathrm{e}^{\mathrm{i}\omega_{\mathrm{mw}} t} & 0 \end{pmatrix} + \Omega_- \begin{pmatrix} 0 & \mathrm{e}^{\mathrm{i}\omega_{\mathrm{mw}} t} & 0 \\ \mathrm{e}^{-\mathrm{i}\omega_{\mathrm{mw}} t} & 0 & \mathrm{e}^{\mathrm{i}\omega_{\mathrm{mw}} t} \\ 0 & \mathrm{e}^{-\mathrm{i}\omega_{\mathrm{mw}} t} & 0 \end{pmatrix} \right], \quad (2.11)$$

wherein the two right terms correspond to the decomposition of a linearly polarized field into a clockwise and counterclockwise rotating component. We transform Eq. (2.11) into the rotating frame and apply the rotating wave approximation which yields

$$\hat{H}_1^{\mathrm{I}} = \begin{pmatrix} \Delta_+ & \frac{\Omega_+}{\sqrt{2}} & 0 \\ \frac{\Omega_+}{\sqrt{2}} & 0 & \frac{\Omega_+}{\sqrt{2}} \\ 0 & \frac{\Omega_+}{\sqrt{2}} & \Delta_+ \end{pmatrix}, \quad (2.12)$$

with the Rabi frequency $2\Omega_x = \Omega_+ =: \Omega = \gamma_{\mathrm{e}}^{\mathrm{NV}} B_1$, where B_1 is the mw amplitude, and $\Delta_\pm = 2\pi D \mp \gamma_e B_0 - \omega_{\mathrm{mw}}$ accounts for detuning of the mw frequency. The off-diagonal elements in Eq. (2.12) cause spin state transitions, whose rate is determined by the mw field strength B_1. The following experiment shows this very obvious.

Rabi oscillation measurement From now on all experiments are conducted in an external static magnetic field of $B_0 \approx 10\,\mathrm{mT}$. Therefore, the $m_S = \pm 1$ states are well separated (see Fig. 13) and we can address a specific transition, in the following we take the one at 2.6216(3) GHz, which corresponds to

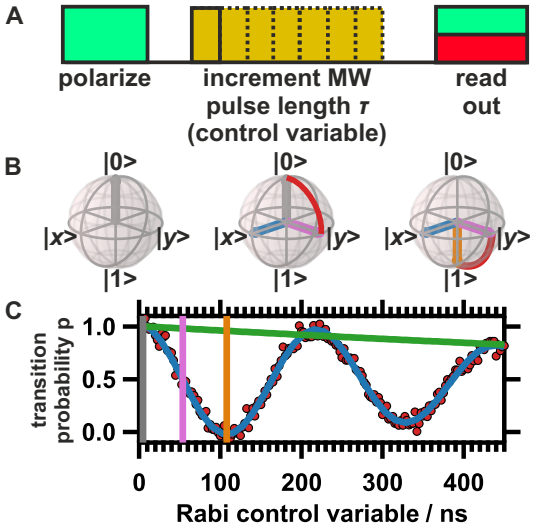

Figure 14: Rabi oscillation measurement. **(A)** Pulse scheme including initialization, mw pulse incrementation, and read out. **(B)** Evolution of the spin state on the Bloch sphere in the resonant case. $\underline{B}_1$ (blue) is aligned along $|x\rangle$. Note, that for the pseudo-TLS in the text $|1\rangle = |-1\rangle$. The color code of the state vector indicates specific time values, given in: **(C)** Characteristic example measurement. Magenta line represents length of the $\frac{\pi}{2}$, orange line of the π pulse. Green line indicates rotating frame relaxation T_ρ.[23]

the $|-1\rangle \leftrightarrow |0\rangle$ transition. By doing so, we can neglect the $|+1\rangle$ state and consider the approached submanifold as pseudo-TLS, which is given by $\hat{H}_0^{\mathrm{sb}} = \left(\begin{smallmatrix} 0 & 0 \\ 0 & \Delta_+ \end{smallmatrix}\right)$. We assume zero detuning, i.e., $2\pi D - \gamma_e^{\mathrm{NV}} B_0 = \omega_{\mathrm{mw}}$.[23] Accordingly, the state vector rests in the rotating frame and the Bloch sphere representation is adoptable. Furthermore, transverse mw radiation of strength B_1 is applied, which provides the control Hamiltonian according to $\hat{H}_{\mathrm{ctrl}}^{\mathrm{Isb}} = \begin{pmatrix} 0 & \frac{\Omega_+}{\sqrt{2}} \\ \frac{\Omega_+}{\sqrt{2}} & 0 \end{pmatrix}$. Consequently, the sensor Hamiltonian $\hat{H}$ reads the same as the control part $\hat{H}^{\mathrm{Isb}} = \begin{pmatrix} 0 & \frac{\Omega_+}{\sqrt{2}} \\ \frac{\Omega_+}{\sqrt{2}} & 0 \end{pmatrix}$. The time evolution of this system according to Eq. (1.13) is governed by the propagator $\hat{U}(t) = \exp(-i\hat{H}t)$ which reveals $|\alpha\rangle = \frac{1}{2}\left(1 + \mathrm{e}^{-\mathrm{i}\Omega t}\right)|0\rangle + \frac{1}{2}\left(1 - \mathrm{e}^{-\mathrm{i}\Omega t}\right)|1\rangle$, where $|0\rangle$, $|1\rangle$ are the pseudo-TLS eigenstates (see Fig. 14**B**). This describes an oscillating behavior of the basis states in presence of a transvere mw field; e.g., if t is chosen that $\frac{1}{2}\frac{th}{\gamma_e^{\mathrm{NV}}\mu_{\mathrm{b}}B_1} = \pi$, the pseudo-TLS is in its eigenstate $|-1\rangle$. After readout we obtain for the transition probability $p = 1 - |\langle 0\,|\alpha\rangle|^2 = \sin^2\left(\frac{\Omega t}{2}\right)$ (see Fig. 14**C**). In the general case the Rabi equation becomes

$$p = \left(\frac{\Omega}{2\Omega_\Delta}\right)\sin^2\left(\frac{\Omega_\Delta}{2}t\right) \tag{2.13}$$

with a slight detuning $\Omega_\Delta = \sqrt{\Omega^2 + \Delta_+^2}$. Since the B_1 amplitude can be assumed to follow a $\propto \frac{I_{\mathrm{a.c.}}}{d}$ dependency (Biot-Savart law), with $I_{\mathrm{a.c.}}$ is the alternating current applied to the mw antenna (for technical details see Chap. 2.4) and d is the distance between the NV^- center and the mw antenna, its value need to be

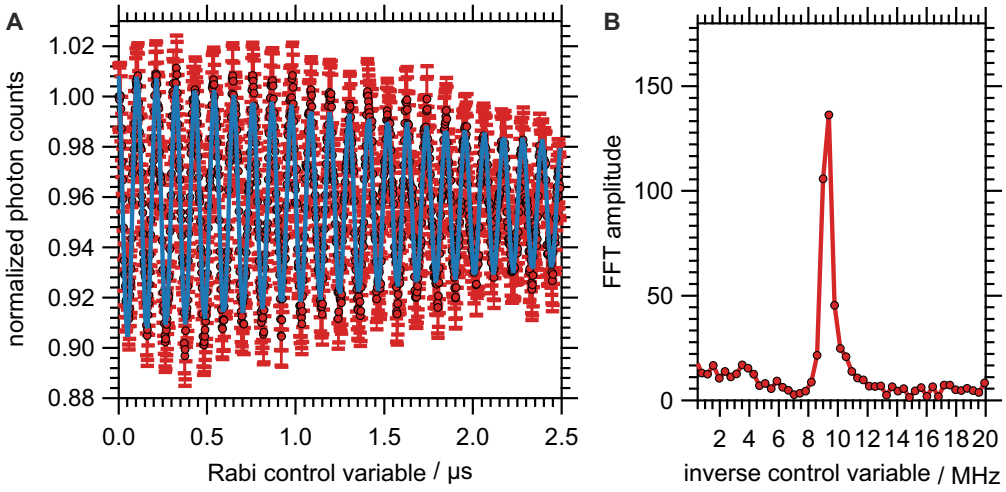

Figure 15: Rabi oscillation measurement on a single bulk NV^- center. **(A)** Data (red) and single-tone sinusoidal fit with mono-exponential decay function (blue). Values of the fit parameters are given in the text **(B)** Corresponding FFT analysis reveals a single-tone Rabi frequency of $\Omega = 2\pi \cdot 9.4\,\mathrm{MHz}$.

determined anew for each center. In Fig. 15 a Rabi measurement on the NV^- center used as sensor in Chap. 5 is demonstrated.[23] The data show single-tone oscillation with frequency $\Omega = 2\pi \cdot 9.4\,\mathrm{MHz}$. This corresponds to a π pulse length of 54 ns and $\frac{\pi}{2}$ pulse length of 27 ns. The rotating frame decay constant is given by $T_\rho = 3.3(1)\,\mu\mathrm{s}$. The Rabi contrast amounts to $\approx 10\,\%$. With the time values in our hands, which are necessary to generate maximum state superposition ($\frac{\pi}{2}$ pulse) or spin state inversion (π pulse), we come to further pulse measurement protocols.

Pulsed ODMR spectroscopy refers to rotating frame detuning. The measurement protocol includes a π pulse which is applied after laser polarization (for technical details see Chap. 2.4). The carrier frequency ω_{mw} of this pulse is swept and state inversion occurs in analogy to Eq. (2.13) if the detuning is minimal, i.e., the resonance condition is met.
Fig. 16 shows an example measurement. In contrast to the cw-ODMR experiment (cf. Fig. 13), a distinct splitting of the signal can be observed which is due to electron-^{15}N nuclear hyperfine interaction. To ease the derivations in Chap. 2.2.2, we neglected this contribution to the internal NV^- center Hamiltonian. However, it can be taken into account by a isotropic factor $a_{\mathrm{iso,NV}}$, which can be deduced

[23] Note that all measurements presented in this chapter were recorded on the same NV^- center, i.e., the sensor utilized in Chap. 5.

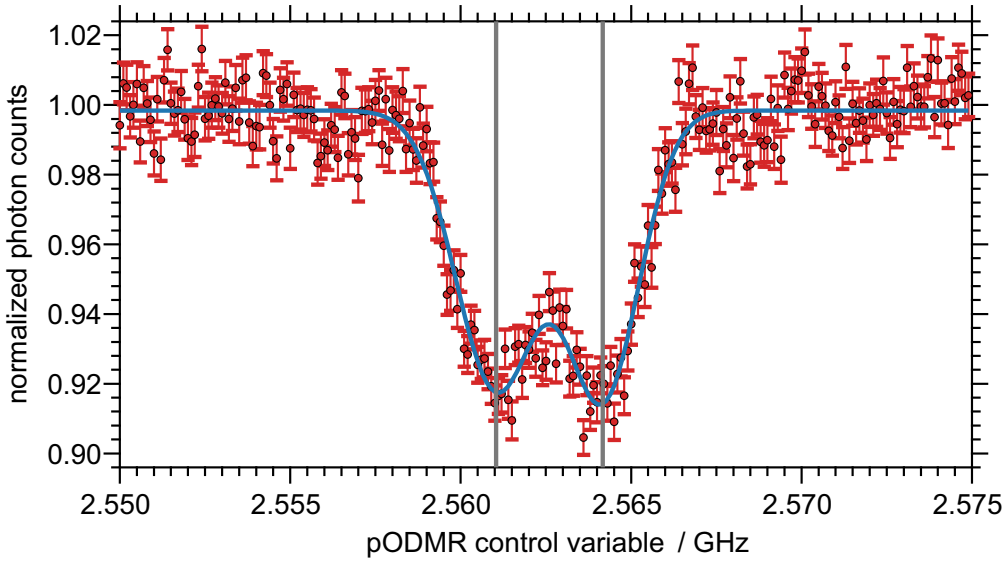

Figure 16: Pulsed OMDR measurement of the $|0\rangle \leftrightarrow |-1\rangle$ transition (red). Hyperfine splitting due to ^{15}N nuclear spin is clearly visible and amounts to 3.13(9) MHz. The blue line is a double-Lorentzian fit whose minima are indicated by gray lines.

from the hyperfine matrix $\underline{\underline{A}}$ in its eigenframe, and for ^{15}N ($I = \frac{1}{2}$) is given by $a_{\mathrm{iso,NV}} = 3.03\,\mathrm{MHz}$.[70] In analogy to Eq. (1.30) the eigenvalues have to be expanded by a term $a_{\mathrm{iso,NV}} m_I m_S$ (secular approximation). From our measurement we obtained $a_{\mathrm{iso,NV,exp}} = 3.13(9)\,\mathrm{MHz}$, which is in good accordance.

Ramsey measurement, which has already been introduced in Chap. 1.4, was conducted since pulsed ODMR spectroscopy still exhibit line broadening effects caused by the mw radiation. In contrast, the Ramsey protocols is solely limited by T_2^*.
The pulse pattern is designed as $\frac{\pi}{2} - \tau - \frac{\pi}{2}$, sandwiched between spin state polarization and readout (cf. Fig. 4**A**). The carrier frequency of the $\frac{\pi}{2}$ pulse was set to $\omega_{\mathrm{mw}} = 2\pi \cdot 2.558\,\mathrm{GHz}$ hence we excited the spectrum in Fig. 16 off-resonant. This allowed us to unravel the full hyperfine spectrum of the $|-1\rangle \leftrightarrow |0\rangle$ spin transition by incrementing τ.[21] Thereby, we could confirm the observation of the pulsed ODMR spectrum, namely the expected coupling to the ^{15}N nucleus. However, due to reduced linewidth an additional interaction presumably with a far-located ^{13}C nucleus could revealed. The corresponding interaction frequencies are noted in Fig. 17.

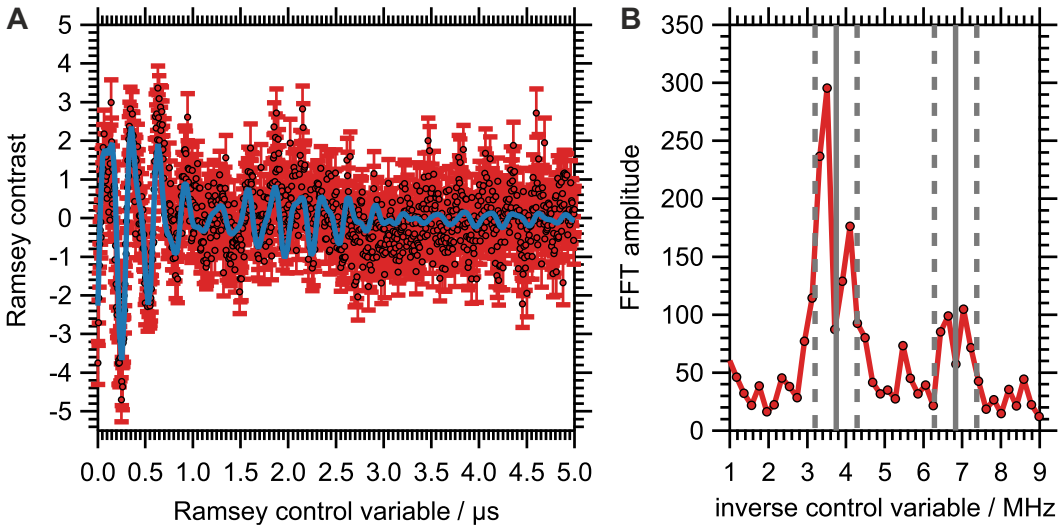

Figure 17: Ramsey measurement on single bulk NV^- center. (A) Data (red) are fitted by a four-tone sinusoidal with mono-exponential decay factor (blue line). T_2^* is given by 1.48(9) µs. **(B)** Corresponding FFT analysis reveals coupling to ^{15}N with $a_{\mathrm{iso,NV,exp}} = 3.1(2)$ MHz (solid gray lines) and presumably to a far-located ^{13}C nucleus quantified by a coupling strength of 0.6(2) MHz (dashed gray lines).

We mentioned in Chap. 2.2.2, footnote 21, that by exiting the $|-1\rangle \leftrightarrow |0\rangle$ spectrum in its very center, we effectively drive one transition despite its distinct hyperfine pattern. That this is indeed the case, we can confirm by inspection of the Rabi oscillation in Fig. 15, which was recorded after the elucidation of the hyperfine spectrum presented here. Therein, only one spin state transition frequency occurs. Otherwise, if several resonances are present, beating of the Rabi oscillation can be observed due to different detuning contributions in Eq. (2.13) of the particular hyperfine levels.

Hahn echo measurement relies on the $\frac{\pi}{2} - \frac{\tau}{2} - \pi - \frac{\tau}{2} - \frac{\pi}{2}$ pulse sequence depicted in Fig. 4**B**, whereby the control variable τ is incremented. Since we already discussed its frequency locking capability, we restrict us here to the report of the experimental finding, which is exhibited in Fig. 18. To mitigate the influence of competing, spin non-dependent relaxation processes on our experimental outcome, we conducted the measurements using a differential protocol, whereby we addressed both spin state populations by either applying a $\frac{\pi}{2}$ or $3\frac{\pi}{2}$ pulse as projection operation (see Fig. 18**A**) as it is discussed in more detail in Chap. 4.6.6. The FFT analysis of both traces reveals qualitatively comparable frequencies,

namely $\nu_1 = 0.1(1)\,\mathrm{MHz}$, $\nu_2 = 0.04(1)\,\mathrm{MHz}$, $\nu_3 = 1.50(2)\,\mathrm{MHz}$. The first two contributions probably stem from frequency uptake of the Lamor precession of nuclear spins, which under our experimental conditions are given in the kHz range. The high frequency FFT signal is caused by electron spin echo envelope modulation due to magnetic field misalignment and coupling to a nuclear spin.[133]

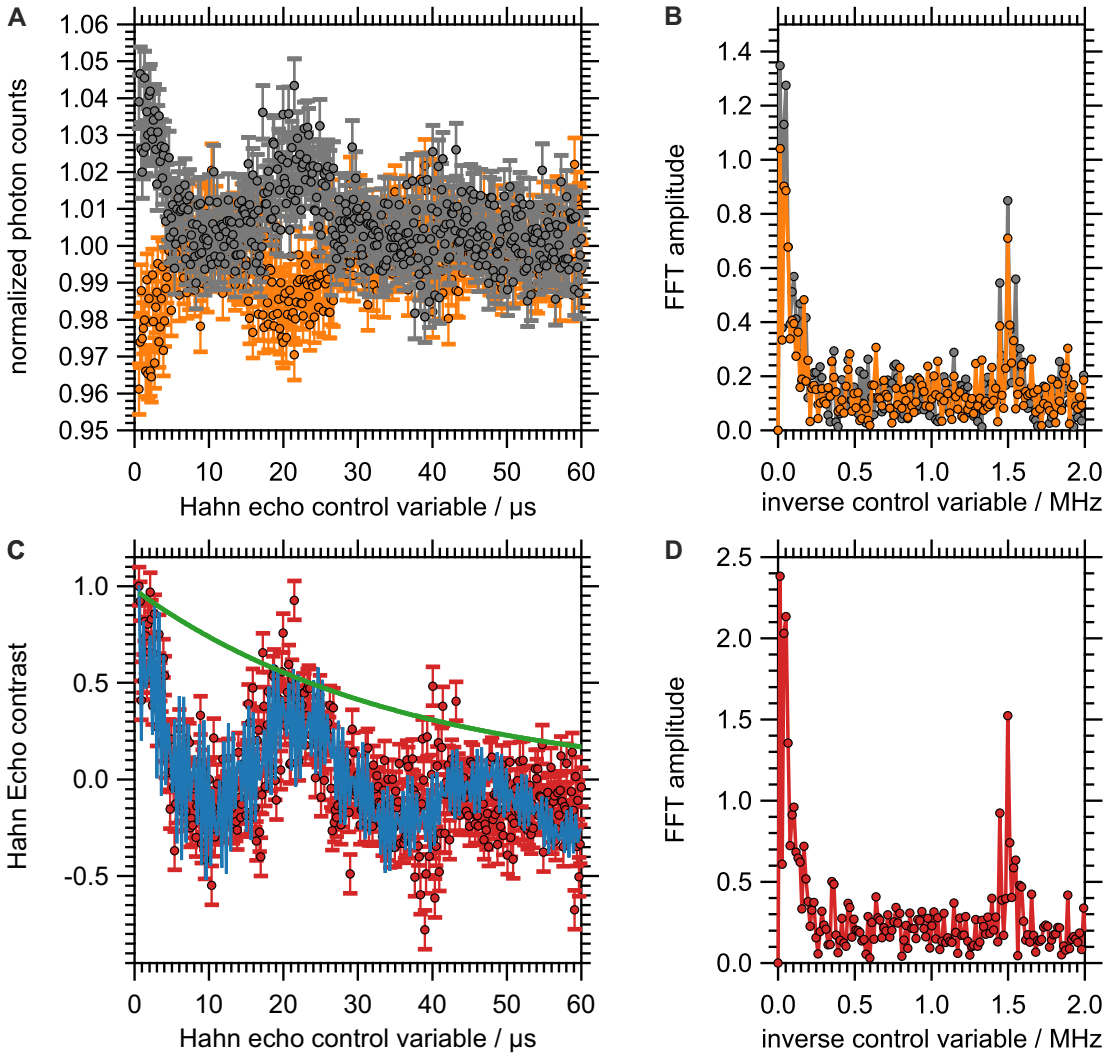

Figure 18: Hahn Echo measurement on a single bulk NV^- center. **(A)** $|0\rangle$ (gray) and $|-1\rangle$ (orange) projection measurement. **(B)** Corresponding FFT analysis. **(C)** Contrast data set, obtained by subtraction of both time traces in **(A)**. The blue line is a four-tone sinusoidal with mono-exponential decay factor whose contribution is indicated by the green line. The T_2 decoherence time amounts to $43.3(8)\,\mu\mathrm{s}$ **(D)** FFT analysis of **(C)**.

This mechanism depends non-trivial on the nuclear Lamor frequency, the degree of misalignment in terms of off-diagonal B-field contributions and the hyperfine coupling matrix. Probably, the cause is to be seen in the ^{15}N nuclear spin, since we could not observe a strongly coupled ^{13}C nucleus. Note that this frequency component can be seen in all measurements on this specific NV^- center. Note that the signals symmetrically located around $\nu_3 = 1.50(2)\,\mathrm{MHz}$ at $\nu = 1.45(2)\,\mathrm{MHz}$ and $\nu = 1.55(2)\,\mathrm{MHz}$ are sidebands. They originate from non-synchronous sampling of the $\nu_3 = 1.50(2)\,\mathrm{MHz}$ ESEEM frequency. The decay constant of the echo envelope is given as the T_2 decoherence time whose value is $43.3(8)\,\mu\mathrm{s}$.

2.3 Remarks on diamond - the matrix of the nitrogen-vacancy center

Diamond is an allotrope of carbon, which forms a regular space structure, commonly referred to as diamond lattice, of tetrahedrally coordinated atoms, that has $\mathrm{F4_1/d\,\bar{3}\,2/m}$ symmetry. Besides the translational elements, the rotation-reflection axis $\bar{3}$ gives rise to the C_{3v} subgroup, which describes the local symmetry of the NV center. The spacial pattern of carbon atoms can be described either by non-primitive base vectors (a_1, a_2, a_3) and a corresponding two atom base located at $(0,0,0)$ and $\frac{a_0}{4}(1,1,1)$, respectively, or two inter-penetrating face-centered cubic (fcc) lattices which are mutually shifted by $(1,1,1)$ and $\frac{a_0}{4}(1,1,1)$ along the body diagonal. The latter description reveals a conventional cubic unit cell that contains $(4 + 6 \cdot \frac{1}{2} + 8 \cdot \frac{1}{8} = 8)$ atoms where the lattice constant is given to be $a_0 = 3.57\,\text{Å}$ (see Fig. 19).[109]

This specific arrangement of relatively strong C−C bonds (bond length: 154 pm, binding energy: 348 kJ/mol)[109] formed by sp^3 hybridized carbon atoms results in material properties that are often unparalleled by competing substances in the particular fields. Diamond surpasses due to its hardness (Knoop hardness: $57 - 104\,\mathrm{GPa}$; cf. cubic boron nitride 45 GPa, silicon carbide 32 GPa)[134] and thermal conductivity ($2000\,\mathrm{W/m/K}$) all other materials.[135–137] The optical transparency of pure diamond ranges from $0.250 - 2.5\,\mu\mathrm{m}$ caused by two- and three phonon absorption processes on the upper and an allowed indirect electronic transition on the lower limit, additionally leading to its characterization as wide bandgap semiconductor at room temperature.[135,137] Possessing a refractive index of $n_{405\,\mathrm{nm}} = 2.46$, the critical angle of total internal reflection for the diamond-air-interface is lowered to 23° compared to 43° in the crown glass-air system.[135] Diamond shows strong resilience against oxidation processes, attack of hydrofluoric

acid and fouling caused by organic chemicals.[135,138–140]
The production of artificial diamonds essentially involves two processes: High pressure-high temperature (HTHP) synthesis and chemical vapor deposition (CVD). The HPHT method reproduces the conditions of the thermodynamic stability of the diamond phase by using pressures of $\approx 15\,\mathrm{GPa}$ and temperatures of $> 3000\,\mathrm{K}$ on graphite precursors.[137] In addition, catalysts, e.g., FeN or Fe-Ni alloy may be used, which lower the aforementioned parameters.[141,142] The nitrogen content is relatively high due to the production process ($\approx 50\,\mathrm{ppm}$), however, it can be reduced by using getter materials as group III elements or titanium.[142] CVD growth relies on a seed layer since it is a epitaxial technique.[137] In the past, diamond was the necessary choice which imposed size restrictions. Meanwhile hetero-epitaxially grown Ir/metal-oxide/Si substrates could also be used as seed layers, where size limitation is overcome[143] The growth process consists of the plasma-mediated generation of hydrogen radicals which react with methane in a radical reaction.[144] The latter absorb on the seed layer. This method allows control of diamond contamination. Therefore, diamond with low impurities are available, e.g., for nitrogen values below 1 ppb can be achieved. Conversely, desired hetero-layers can be intentionally introduced into the diamond crystal (δ-doping).[145]

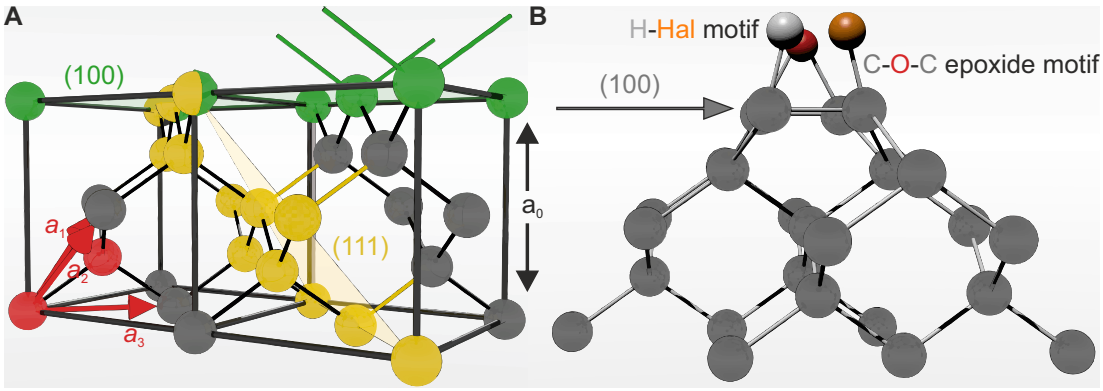

Figure 19: (A) Diamond structure of tetrahedrally coordinated carbon atoms where two conventional unit cells with lattice constant $a_0 = 3.57\,\text{Å}$ containing eight atoms, respectively, are shown. The crystallographic unit vectors a_1, a_2, a_3 and the two-atom base are displayed in red. Colored faces correspond to either the (100) (green) or the (111) (yellow) surface. Potential surface atoms and dangling bonds are demonstrated in the corresponding color. **(B)** Schematic drawing of a possible reconstruction of the (100) surface showing a (2x1)-superstructure. Two motifs of saturate surface dangling bonds are shown. Color code: oxygen (red), hydrogen (white), halogen (orange).

The properties of different diamond facets varies significantly from each other. For example, the oxidation rate of the (111) surface is 7.5 times higher than of the (100) surface. The increased stability of the latter is also reflected in the cleavage energy.[137] In addition, the number of unsaturated bonds per carbon atom differs. Figure 19**A** shows the (100) surface in green and the (111) in yellow. It can be seen that for the former each carbon atom has two dangling bonds, for the latter only one. This has an influence on possible surface reconstructions and the subsequent chemical termination. Fig. 19**B** depicts an example reconstruction of the (100) diamond surface. The presented epoxide motif, for example is hardly achievable for the (111) facet. This will be of relevance in Chap. 4. In Chap. 5 we obtain from experimental data strong evidence that the diamond surface can act as a reducing agent. One indicator for this is its electron affinity, which also depends on the surface termination and the particular facet. In the literature we find the following values: 100-(1×1), keto-terminated gives 3.91 eV; 100-(1×1), ether-terminated 1.7 eV; 100-(1×1), H-terminated -1.96 eV; 110-(1×1), H-terminated -2.41 eV.[146] Finally, atomic force microscopy measurements have shown that on the scale of few nanometers the diamond surface possesses terraces and step edges in the range of several Å. This illustrates that averaged parameters, as they are mentioned in the beginning of this section, in this size domain can only be used to a limited extent.[147]

In this section we have largely referred to the properties of bulk diamond. The characteristics of nanodiamond are discussed in connection with the experiments in Chapter 4.

2.4 Supplementary

Here, we describe in detail the home-built ODMR setup and data processing of pulsed experiments used in this thesis (see Chap. 2.4.1). The normalization procedure of single photon emitter measurements is explained in Chap. 2.4.2.

2.4.1 ODMR setup

Optically detected magnetic resonance experiments were conducted at room temperature and ambient conditions using **1.** a home-built confocal microscopy setup provided with **2.** a pulsed microwave generating and applying unit and **3.** a permanent magnet. Elucidation of the particular elements of the setup are explained in the following with reference to Fig. 20.

1. Optical path: A 520 nm pulsed laser (**1**Laser, Swabian Intstruments) beam is widened via a telescope arrangement (**2**T) and an adjustable pinhole (**3**P), passed along to a wavelength-discriminating dichroitic mirror (**5**DM) using mirror **4**M, reflected there and, eventually, guided into either an oil immersion objective (NA = 1.42, Olympus) or air objective (NA = 0.9, Olympus), both denoted as **7**Obj, to give a focus volume at the sample site of approximately 0.25 µm^3. Correspondingly, under stable conditions laser power densities of $0.003 - 33\,\mathrm{W/\mu m^3}$ are obtainable. The objective can be scanned by virtue of a piezo stage (**6**, piezosystem jena) with a step size below its resolution limit. The emissive radiation is collected via the very same objective, transmitted through the aforementioned dichroic mirror, optically $\lambda \geq 650$ nm-longpass-filtered (**8**OF), focused via fish-eye lens **9**L on

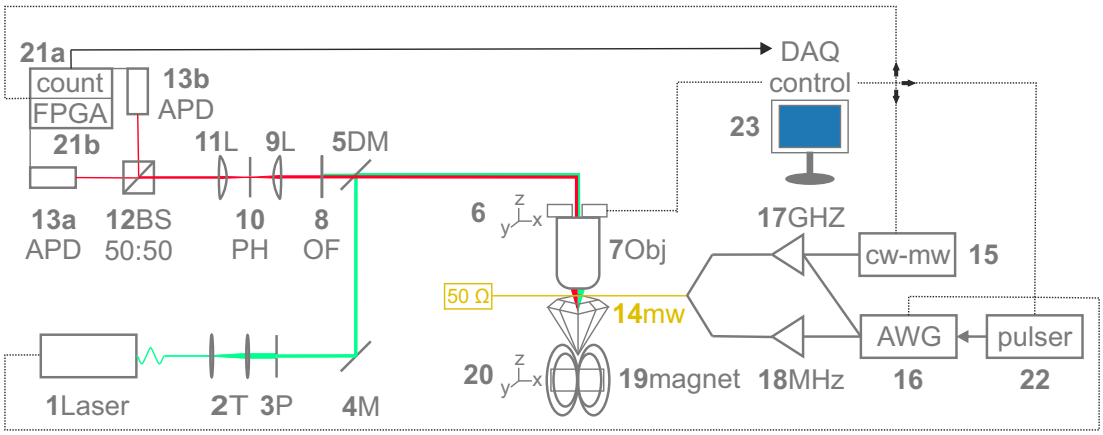

Figure 20: Schematic drawing of the ODMR setup. The particular elements are explained in the text.

a 50 µm pinhole (**10**PH) to suppress background photons, widened using fish-eye lens **11**L, and detected in a Hanbury Brown and Twiss arrangement, consisting of a 50 : 50 beamsplitter (**12**BS) and two avalanche photodiodes (**13a**APD & **13b**APD, Excelitas; dark count rate below 25 counts/s).
2. Microwave path: Application of microwaves is achieved by a 20 µm copper wire antenna which is soldered on a PCB-based waveguide structure and positioned onto the substrate using a manually adjustable stage (**14**mw). As a microwave source serves for continuous wave cw-ODMR experiments a GHz signal generator (**15**, APSIN 6010, Anapico) and for pulsed experiments an arbitrary waveform generator (**16**, AWG70002A, 8 GS/s, Tektronix). GHz signals are amplified to 42 dBm (**17**GHz, AS0104-30/17, Milmega), MHz signals to 40 dBm (**18**MHz, ZHL-42W, Minicircuits). The microwave circuit is impedance matched by a 50 Ω terminating resistor.
3. Static magnetic field: To lift the $m_S = \pm 1$ degeneracy of the NV^- center and the $m_S = \pm\frac{1}{2}$ degeneracy of dark spin species a permanent magnet (**19**magnet, material: NdFeB, magnetic remanence $1.29 - 1.32$ T) is used. The alignment of the magnetic field vector and the NV center axis as well as magnetic field strength adjustment is achieved through moving the magnet with a xyz-micrometer stage (**20**). Magnetic field calibration is conducted by cw-ODMR experiments.
For recording fluorescence scans and cw-ODMR spectra, timing of the particular components, i.e. piezo scanner position, laser, mw generator, was realized with by a I/O data acquisition modul (**21a**, NI 6323, National Instruments).
Pulsed experiments were timed by the AWG, photon counting was achieved by a field programmable gate array (FPGA) counter (**21b**, TimeTagger20, Swabian Instruments) which was also used for coincidence measurements. For heterodyne detection of alternating magnetic fields an additional external oscillator is required. For this reason, a second timing device (**22**, Pulse Streamer, Swabian Instruments) can be implemented.
Experimental control of the setup and data acquisition is accomplished by a modified version of the Python based software suite Qudi (**23**).[148]

Next, we want to address pulsed measurement data acquisition and processing, whereas we take a Rabi oscillation measurement as guideline (see Fig. 21).
Spin state oscillation is induced by mw pulses of increasing duration. Therefore, the centerpiece of this protocol is an incrementation sequence of the mw pulse length (control variable τ), where $\tau_{\text{start}} = 2.5$ ns and $\Delta t_{\text{mw}}(\tau) =: \tau = 2.5$ ns (Fig. 21**A**). After $40 \cdot \tau$ the length of the mw pulse amounts to $\Delta t_{\text{mw}}(\tau) = 102.5$ ns.

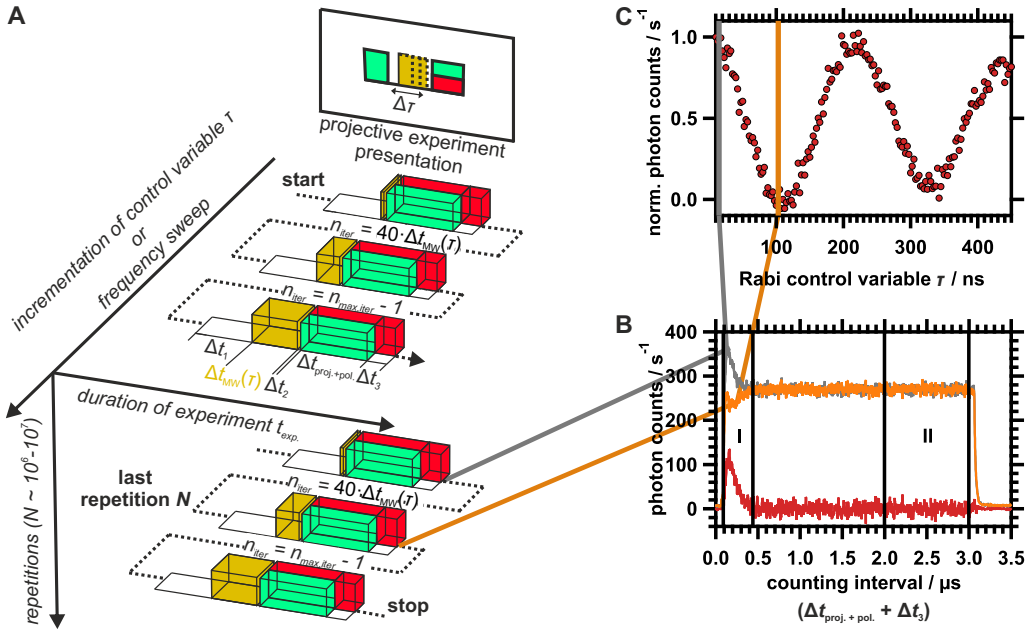

Figure 21: **(A)** Representation of the pulse scheme of a Rabi oscillation measurement. Laser pulses are given in green, counting intervals in red, and mw pulses in yellow. **(B)** Outcome of counting for two selected incrementing traces indicated by gray and orange line. The red graph is the difference of gray and orange counting trace.**(C)** Data set after normalization. See text for details.

One iteration sequence run ends after $n_{\mathrm{iter}} = 180$ incrementation steps which corresponds to a mw pulse length of duration $\Delta t_{\mathrm{mw}}(\tau) = 452.5\,\mathrm{ns}$. This spin control part is sandwiched between a waiting time $\Delta t_1 = 1.5\,\mu\mathrm{s}$, which serves to provide a complete singlet state relaxation, and the readout sequence. The latter consists of pulse ring down time Δt_2 (20 ns for GHz and 40 ns for MHz pulses), parallel laser illumination and photon counting for $\Delta t_{\mathrm{proj.+pol.}} = 3\,\mu\mathrm{s}$ and subsequent dark counting for $\Delta t_3 = 500\,\mathrm{ns}$. Pulse experiments are designed in such a way that spin state polarization of a particular iteration is made available by the laser pulse of the preceding iteration. The triplet electron excited state lifetime is in the range $10 - 20\,\mathrm{ns}$. Thus, in the information encoding time interval of roughly 400 ns (see Fig. 21**B**) on average approximately $20 - 40$ photons are emitted. However, due to the radiation characteristics of the NV^-center, loss of photons at the diamond-air interface and technical reasons the effective value is by factor 100 lower. To enhance the signal-to-background ratio $N = 10^4 - 10^7$ repetitions of one iteration sequence are recorded. Fig. 21**B** shows two example counting traces after $\approx 1.5 \times 10^5$ repetitions. From these counting traces, the measurement

results are generated as a plot of the transition probability in dependency of τ, by calculating the mean value over the range marked as I in Fig. 21**B**. The standard deviation thereby obtained is the 1σ uncertainty interval for the respective data point. In order to take account of any changes in the optical path, the mean values are normalized to the photon count rate of region II of the respective count trace, which corresponds to the equilibrium emission of the NV center. Accordingly, the outcome in Fig. 21**C** is gained.
The control variable of a pulse experiment can be of very different nature. For spectra recording it means to sweep the carrier frequency, in spin-locking experiments it defines the bandwidth. Accordingly, the data are presented with the neutral term control variable, usually extended by the name of the actual experiment.

2.4.2 Identifying a NV^- center as single-photon emitter - Data processing

In contrast to classical, non-coherent light sources, a small ensemble of single photon emitters is characterized by the fact that its Second-order autocorrelation function (see Fig. 22)[149]

$$g^{(2)}_{\text{corr}}(\tau) = \frac{P_2(t_0 + t_1|t_0)}{P_1(t_0)}, \tag{2.14}$$

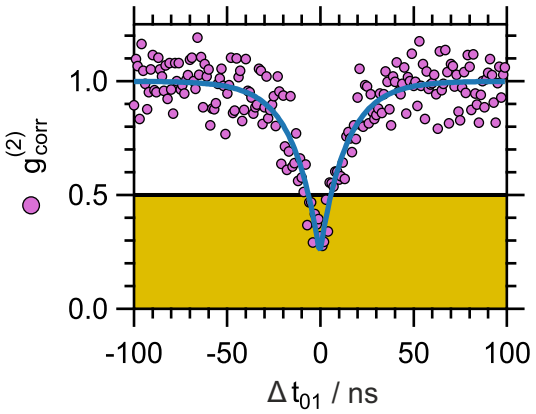

Figure 22: Second-order autocorrelation function $g^{(2)}_{\text{corr}}$ of a single photon emitter

which states the conditional probability of measuring a photon at time t_1 when the previous count event took place at time t_0, for $\Delta t_{01} = t_1 - t_0 \to 0$ has a minimum (see Chap. 4.6.6 for further details in the context of the NV^- center hosting NDs). $P_1(t_0)$ normalizes this distribution by the average photon count rate at t_0.
The basis of the technical realization to test the probability distribution given in Eq. (2.14) is the Hanbury Brown and Twiss arrangement of two APDs and the FPGA fast counting modul (time resolution: 3 ps). The latter provides a correlation class, where photon counting signal

of both APDs can serve either as start or stop event. By dividing a given interrogation time into equally spaced time bins, the FPGA detects the duration between each start and stop event and accumulates it into a histogram, whereby inversion in time corresponds to APD inversion regarding their start/ stop character. An example histogram is given in Fig. 23**D** in which events are counted that obey $\Delta t_{01} = t_0 - t_1$ and time resolution is 1 ns.
However, this histogram is corrupted by background and dark photon counts, and an appropriate correction procedure is required.[150,151] Therefore, a fluorescence map of the NV^- center under investigation is recorded (see Fig. 23**A**). From this the background fluorescence level B and the NV^- center signal strength Sg are inferred, which here results in $B = 7411\,\mathrm{ms}^{-1}$ and $Sg = 10\,637\,\mathrm{ms}^{-1}$.

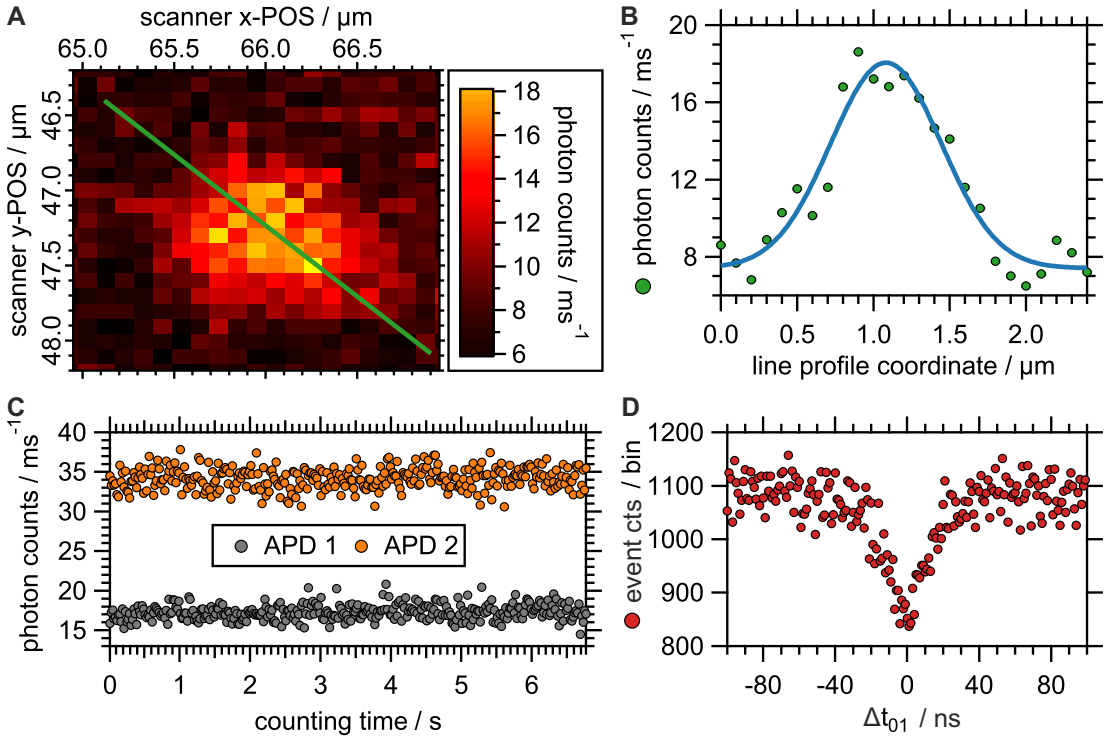

Figure 23: Data processing of single photon emitter identification. **(A)** High-resolved fluorescence map of NV^- center. **(B)** Fluorescence profile along the green line given in **(A)** Data points (green) are fitted with a Gaussian function wich full width at half maximum results in $5.1(4) \times 10^2$ nm. **(C)** Time trace of the average count rate of both APDs. **(D)** Histogram of events which obey $\Delta t_{01} = t_0 - t_1$ (bin size: 1 ns).

Additionally, the average photon emission of the NV^- center has to be taken into

account, which is determined from APD-dependent time traces (see Fig. 23**C**) recorded prior to Second-order autocorrelation measurement (denoted as C_{APD1} and C_{APD2}), as well as the measurement conditions, i.e. the duration of event counting D_{t} and the bin width b_{w}. For the data set to obtain $g^{(2)}_{\mathrm{corr}}$ in Fig. 22 these are given by $C_{\mathrm{APD1}} = 17\,300\,\mathrm{ms}^{-1}$, $C_{\mathrm{APD2}} = 34\,100\,\mathrm{ms}^{-1}$, $D_{\mathrm{t}} = 1925\,\mathrm{s}$, and $b_{\mathrm{w}} = 1 \times 10^{-9}\,\mathrm{s}$.
Eventually, we carried out the following computation, when cts_{e} means event counts (see Fig. 23**D**):

$$cts_{\mathrm{e,norm}}(\Delta t_{01}) = \frac{cts_{\mathrm{e}}(\Delta t_{01})}{C_{\mathrm{APD1}} C_{\mathrm{APD2}} D_{\mathrm{t}} b_{\mathrm{w}}}$$

and

$$g^{(2)}_{\mathrm{corr}}(\Delta t_{01}) = \frac{cts_{\mathrm{e,norm}}(\Delta t_{01}) - (1-\zeta^2)}{\zeta^2},$$

while $\zeta = \frac{Sg}{Sg+B}$. Accordingly, we end up with the data set in Fig. 22.
The analysis of this particular measurement using a mono-exponential model reveals a decay constant of 19.4(5) ns which is consistent with previous measurements.[149] The underlying model of the fit function is a three-level system in which one excited state lifetime is significantly shorter than that of the other (see Chap. 2.2.1).[149]

3 Bulk investigation of the cationic spin environment of N@C_{60} ions

Since experimental results have recently been obtained, demonstrating the readout of the spin state of N@C_{60} at the few and single molecule level, the spin characteristics of the charged species of the fullerene host, which concurrently possess a radical character, are also becoming the focus of attention. For example, they may constitute a potential source of interference in future quantum sensing experiments. An undoubted clarification of their spectroscopic signature is therefore highly desired.
In the following chapter we thoroughly re-investigated the C_{60} cation generation on a Fe^{3+}-loaded zeolite support, which represents a literature-known approach using bulk EPR spectroscopy as well as nitrogen sorption and X-ray diffraction (XRD) measurements. An adapted protocol of this method allowed us to accurately determine the g-factor of C_{60}^{+} using an internal N@C_{60} standard. Furthermore, the g-factor of C_{70}^{+} and $(C_{60})_2O_2^{2\bullet}$, which can occur as permanent or transient impurities of C_{60} fullerenes, was determined. By adopting Ce^{4+} as an oxidizing agent, we succeeded in significantly reducing the temperature required for thermal activation of the oxidation reaction; thus shifting C_{60} cation generation into the stability regime of N@C_{60}. With this result we aimed to detect bulk coupling spectra between C_{60}^{+} and N@C_{60} by means of EPR spectroscopy.

3.1 Introduction

Unlike their negatively charged counterparts fullerene cations (e.g. C_{60}^{+}) are less prominent in research and application.[24] Mainly due to relatively high reactivity in condensed matter, synthesis and stabilization of those species are challenging, whereby nucleophilic addition reactions are at the front of quenching mechanisms.[152] Consequently spectroscopic data are scarce. Especially EPR parameters (g-factor, linewidth) seem to depend greatly on the chosen method of cation preparation.[97] Nevertheless, there is a growing interest in charged fullerene species within several research fields. For organic solar cells the role of fullerene ions as intermediates in charge carrier transport has been discussed.[153] Similarly, the potential application of endohedral group-V fullerenes, as qubits or as molecular

[24] C_{60} has a 5-fold degenerated HOMO.[152] The removal of an electron simultaneously causes the generation of a radical species. However, we suppress this in the designation and write C_{60}^{+} instead of $C_{60}^{\bullet+}$.

Table 1: Reports on C_{60} cation generation and corresponding g-factor and linewidth parameter lw (adapted from [152]). DCM: dichloromethane, $[CB_{11}H_6Cl_6]^-$: hexachlorocarborane, TPP: triphenylpyrylium tetrafluoroborate, ODCB: o-dichlorobenzene, C_{60}^*: photoexcited C_{60} fullerene.

#	protocol	g-factor	lw / mT	Ref.
1	conc./ fuming H_2SO_4	2.0030	2.5/ 0.2	[155]
2	disproportionation of C_{60}^*	2.0024	0.05	[160]
3	$SbCl_5$ in DCM	$2.0023 - 2.0029$	$0.15 - 0.20$	[156]
4	HY zeolite	$2.0033 - 2.0047$	$0.3 - 1.1$	[158]
5	Fe^{3+}-exchanged NaY	2.0025	1.2	[159]
6	$[C_{60}]^+[CB_{11}H_6Cl_6]^-$	2.0022	0.3	[152]
7	C_{60}^* using TPP in ODCB	2.0021	0.08	[161]
8	conc. H_2SO_4	$1.9034 - 2.0863$	$0.47 - 0.87$	[157]

quantum sensors,[52,57,59,154] requires identification of competing radical derivatives, namely C_{60} cations and C_{60} anions. Because we will concentrate on C_{60} cations in the following, Table 1 lists literature protocols that report on their generation. These can be roughly divided into three classes: the utilization of a chemically active oxidizing agent such as sulfuric acid and antimony pentachloride,[155–157] methods applying chemical inactive oxidizing agent realized, for example, by sterically demanding anions, such as the $[CB_{11}H_6Cl_6]^-$ anion, or zeolites,[152,158,159] and the generation of transient species by photo-excitation and subsequent disproportionation, whereby the stability of the C_{60} cation may also depend on the solvent used.[160,161]

Because of the simple synthetic accessibility and the assumed inertness of the zeolite matrix, we decided to re-examine the literature protocol in Ref. [159].

3.2 Revision and utilization of C_{60} cation-generating literature protocol

First of all, the preparative procedure in Ref. [159] is briefly reported: zeolite NaY (see Chap. 3.5.2) was activated by heating in an oven at 500 °C for 6 hours in air. To prepare the Fe^{3+}-exchanged sample, 1.0 g of dried NaY was suspended in 20 mL of acetonitrile (MeCN) to which $46.2 - 139$ mg of $Fe(ClO_4)_3 \cdot 6\,H_2O$ was added. This mixture was stirred for 0.5 hours. The Fe^{3+}-exchanged zeolite (FeY) was then filtered and evacuated at r.t.; 180 mg of dried FeY sample and 3.0 mg

of C_{60} powder were homogenized and transferred into an EPR tube, which was evacuated for 12 hours at r.t. and sealed off. Thereafter, the EPR tube was placed in an oven at 420 °C for 3 hours. The spectroscopic parameters of the corresponding EPR measurement is given in Tab. 1. Further observations, that are presented in Ref. [159], were the increase of the C_{60}^+ signal with increasing mass used of oxidizing agent precursor $Fe(ClO_4)_3 \cdot 6\,H_2O$ and EPR signal quenching using perylene.[25] At temperatures below 420 °C no C_{60}^+ generation could be observed. Finally, the assumption was made that during the oxidation process the diffusion of C_{60} molecules into the supercage structures of zeolite takes place (see Chapt. 3.5.2), which would lead to squeezing of the the fullerene cage. Accordingly, the I_h symmetry may be reduced, which would have effects on the EPR spectrum (e.g., anisotropic g-factor, g-factor shift due to modified spin-orbit coupling).
To test the last-mentioned presumption we firstly investigated the Fe^{3+}-exchanged zeolite material regarding its thermal behavior. Therefore, we prepared samples according to literature using 139.4 mg $Fe(ClO_4)_3 \cdot 6\,H_2O$, but without adding C_{60} powder. The results of the study are presented in detail in Chap. 3.5.3. They suggest that at a reaction temperature of 420 °C the crystalline structure of the zeolite material partially collapses and the oxidation reaction effectively may take place on an amorphous support. However, hints are present that alternative mesoporous structures emerge which may impose restrictions regarding the availability of oxidation sites.
Next, we evaluated the capability of the protocol to produce C_{60} cations. We added 12.6 mg C_{60} powder to 180 mg of a Fe^{3+}-zeolite sample[26] and proceeded according to the literature. We recorded a full range and a high-resolved EPR spectrum, which are shown in Fig. 24**A**&**B**. Both measurements clearly exhibit a signal that is not present in the absence of C_{60}. In addition, compared to the EPR spectrum of pure FeY, the iron-indicating signal at $g = 4.3$ is suppressed (see Fig. 34). This means that the reaction $Fe^{3+} + C_{60} \rightarrow Fe^{2+} + {C_{60}}^+$ was completed successfully. From the high-resolution EPR spectrum (24**B**) we obtained: $g = 2.0029(2)$ and a Voigtion linewidth $lw_{\mathrm{Voigtian}} = 0.51(1)$ mT.
If the linewidths in Table 1 are inspected, it becomes apparent that, apart from the approach using concentrated sulphuric acid, the zeolite method exhibits the highest values. We assumed that this was due to dipolar coupling between cations. In order to verify this assumption, it may be suitable to carry out a series of ex-

[25] It should be noted that the authors did not present a numerical value of the linewidth of C_{60}^+ in their publication, but it can be estimated from the measurement data, which was done in Ref. [152], from which we adopted the corresponding value in Tab. 1.
[26] All FeY samples used in this work were prepared using 139(1) mg $Fe(ClO_4)_3 \cdot 6\,H_2O$.

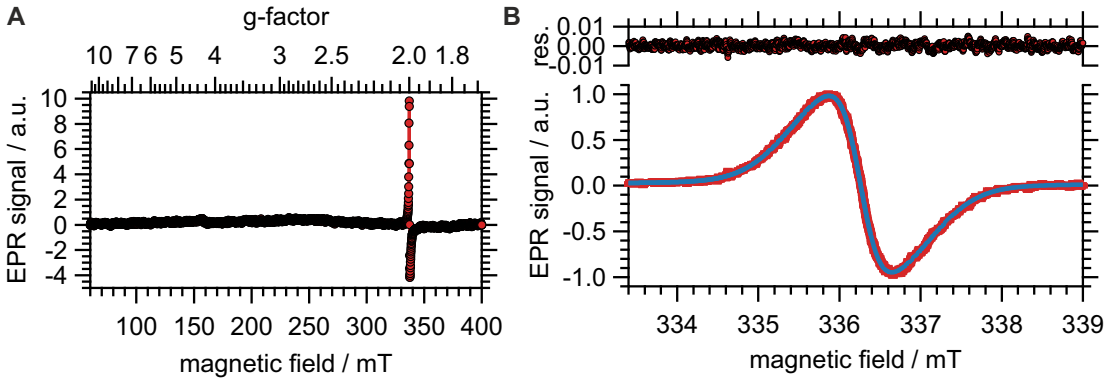

Figure 24: EPR spectra of C_{60}^{+} obtained according to the protocol presented in Ref. [159]. **(A)** Full range and **(B)** high-resolved measurement revealing $g = 2.0029(2)$, $lw_{\mathrm{Lorentzian}} = 0.57\,\mathrm{mT}$, and $lw_{\mathrm{Gaussian}} = 0.13\,\mathrm{mT}$. Measurement parameters in **(A)**: mw power $P_{\mathrm{mw}} = 100\,\mu\mathrm{W}$, modulation amplitude $B_{\mathrm{mod}} = 0.1\,\mathrm{mT}$, resolution $R = 0.1\,\mathrm{mT/bin}$, sweep rate $\dot{B} = 1.3\,\mathrm{mT/s}$; in **(B)**: $P_{\mathrm{mw}} = 10\,\mu\mathrm{W}$, $B_{\mathrm{mod}} = 0.01\,\mathrm{mT}$, $R = 0.01\,\mathrm{mT/bin}$, $\dot{B} = 0.13\,\mathrm{mT/s}$.

periments in which the C_{60} mass is increased. Provided that there is an infinite oxidation agent-loaded zeolite reservoir and a homogeneous C_{60} distribution of constant thickness, this would lead to an enhanced radical density and hence to an increasing electron spin-spin coupling due to its $\frac{1}{r^3}$ dependence. In order be able to make reliable statements about this, the influence of the measurement conditions on the linewidth, namely power broadening effects, need to be tested first.
For this reason, we prepared a sample containing 180 mg FeY and 40 mg C_{60} powder and conducted EPR measurements at varying mw excitation power. The EPR signals obtained were best fitted using a Voigtian profile, as it is the case for the measurement depicted in Figure 24**B**. However, the homogeneous linewidth is theoretically determined by a Lorentzian shaping function. Thus, we solely evaluated this contribution for the determination of the intrinsic linewidth $lw_{\mathrm{Lorentzian,intr.}}$. The corresponding data are presented in Fig. 25**A**. They reveal the typical function of a power broadened EPR signal, whereby a global minimum is reached for low power values. The quantitative relationship is given by[69]

$$lw_{\mathrm{Lorentzian}} = \frac{1}{\gamma_{C_{60}^{+}} T_{2,C_{60}^{+}}} \sqrt{1 + \gamma_{C_{60}^{+}} P_{\mathrm{mw}} T_{1,C_{60}^{+}} T_{2,C_{60}^{+}}} \tag{3.1}$$

with $lw_{\mathrm{Lorentzian}}$ is the observed Lorentzian linewidth at mw power P_{mw} and $T_{1,C_{60}^{+}}$, $T_{2,C_{60}^{+}}$ are defined in analogy to Eq. (1.35) in Chap. 1.3. Refering to Eq.

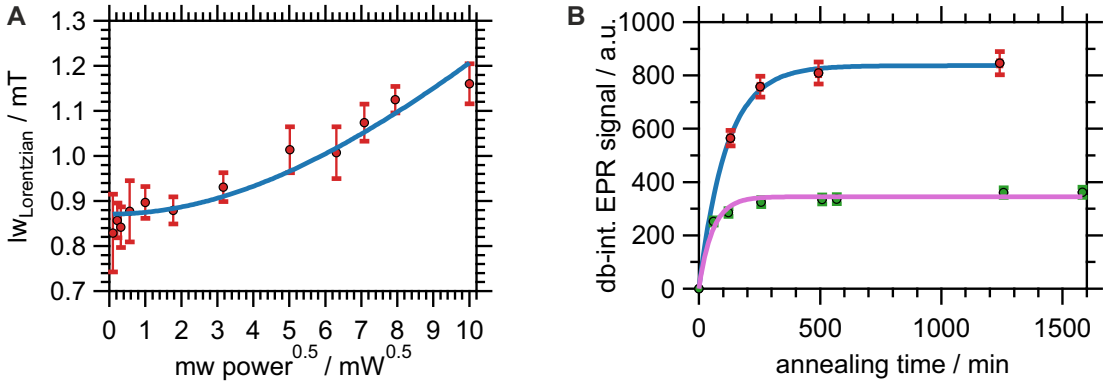

Figure 25: (A) Power broadening measurement on C_{60}^+. The EPR signal is given by a Voigtian line shape over the full mw power range (see text). Data (red) show the deconvoluted Lorentzian-shaped homogeneous linewidth at half maximum as a function of the square root of the mw excitation power $\sqrt{P_{\mathrm{mw}}}$. Blue line is a fit according to Eq. (3.1). **(B)** Kinetic measurements of the generation of C_{60}^+ (red) and C_{70}^+ (green) at 420 °C. Blue and magenta line indicate First-order saturation kinetic, respectively, with generation constants $\tau_{C_{60}^+} = 114(1)$ min and $\tau_{C_{70}^+} = 57(7)$ min.

(3.1), we fitted the data set and obtained as intrinsic linewidth $lw_{\mathrm{Lorentzian,intr.}} = \lim_{P_{\mathrm{mw}}\to 0} lw_{\mathrm{Lorentzian,app.}} = 0.868(5)$ mT (see Fig. 25**A**). Accordingly, we obtain $T_{2,C_{60}^+} = 6.54(4)$ ns from Eq. (3.1), which is noticeably shorter than reported in literature ($T_2 \approx 300$ ns).[162] Despite this deviation, it remains an important result that a non-power-broadened determination of the linewidth is possible using a mw power of 0.01 mW. Therefore, we prepared samples which contained a varying

Table 2: Dependency of the C_{60}^+ linewidth on the loading ratio R[l]. η is a linear factor, when the EPR lineshape is given by a pseudo-Voigtian profile $V(B)$ according to $V(B) = \eta \cdot L(B) + (1-\eta) \cdot G(B)$, where $L(B)$ and $G(B)$ denote the corresponding Lorentzian and Gaussian function, respectively.

R	g-factor	$lw_{\mathrm{Lorentzian}}$ / mT	T_2 / ns	η
0.22	2.0030(2)	0.86	6.5	0.57
0.07	2.0030(2)	0.51	11	0.85
0.04	2.0030(2)	0.47	12	1
0.02	2.0031(2)	0.34	17	1

mass of C_{60} powder ($m_{C_{60}}$) at constant mass of FeY (m_{FeY}). Consequently, the ratio $R^{l} = \frac{m_{C_{60}}}{m_{FeY}}$ is given in Tab 2, where concurrently the results of the investigation are presented. As previously assumed, a clear reduction in linewidth with decreasing $m_{C_{60}}$ can be stated. At the same time, the Lorentzian character η of the EPR signal increases. This indicates that the interaction between adjacent C_{60} radical cations is the determining factor for the linewidth and thus the T_2 time. If the values in Table 2 are extrapolated to infinite spin dilution ($R^{l} \to 0$), a linewidth of 0.33 mT results. With the exception of the protocols in Tab. 1, which generate cations by photoexcitation, this value is in good agreement with the remaining methods.
Since one of our objectives aimed to measure N@C_{60}-C_{60}^{+} dipolar coupling spectra, it seemed recommended to investigate the generation kinetics of the C_{60} cations. For this purpose we produced a C_{60} and for comparison a C_{70} sample with $R^{l} = 0.04$ and measured the EPR signal as a function of the annealing time. The results are shown in Fig. 25**B**. Both time curves can be modeled with a First-order saturation kinetic, i.e. a mono-exponential function with time constants $\tau_{C_{60}^{+}} = 114(1)$ min and $\tau_{C_{70}^{+}} = 57(7)$ min. It is remarkable that the reaction rate of the oxidation of C_{60} is twice as high as that of C_{70}. The reduction potentials of both substances determined in solution by cyclic voltammetry are almost identical.[152] Further investigations have to reveal which effects are involved.

Having largely characterized the literature protocol through the preliminary investigations, we were able to generate reproducible fullerene cation signals. Next, we aimed to determined the g-factor of C_{60}^{+}, C_{70}^{+} and $C_{120}O_2{}^{2\bullet}$ with high accuracy. Hence, we decided to apply N@C_{60} as internal standard whose g-factor currently was determined with high precession to $g = 2.002\,04(4)$.[121] Note that we assume the uncertainty of our measurement to be determined by the B-field sweep accuracy of our spectrometer, which we determined to be 0.01 mT.
The addition of the biradical oxygen species to this study is due to the fact that it occurs ubiquitously in C_{60} powder under ambient conditions. Already in previous studies on the stability of N@C_{60} we could observe its occurrence.[118] The corresponding reaction pathway is $2\,C_{60} + O_2 \to C_{120}O_2{}^{2\bullet} \to 2\,C_{60}O$. The identification of the reaction product can be carried out by qualitative HPLC analysis via the detection of its absorption in the UV range.
We prepared a C_{60} and a C_{70} FeY sample with $R^{l} = 0.04$. The reference spectrum of the $C_{120}O_2{}^{2\bullet}$ radical we obtained on C_{60} powder which was stored under air for a longer period of time (> 4 weeks). The superposition spectrum of C_{60}^{+} and

Table 3: High-accurate g-factor determination of fullerene-related radical species using N@C_{60} as spin standard. The obtained linewidth parameters of N@C_{60} are in the range of $lw_{\mathrm{Lorentzian}} = 8.6 - 9.7\,\mu\mathrm{T}$ and $lw_{\mathrm{Gaussian}} = 9.4 - 11.8\,\mu\mathrm{T}$, respectively.

species	g-factor	$lw_{\mathrm{Lorentzian}}$ / mT	lw_{Gaussian}	spectrum in Fig. 26
C_{60}^{+}	2.00302(4)	0.549	0.171	**CI&CII**
C_{60}^{+}	2.00298(4)	0.206	0.189	**B**
C_{70}^{+}	2.00258(4)	0.341	0.149	**D**
$C_{120}O_2{}^{2\bullet}$	2.00233(4)	0.0690	0.0566	**A**
$C_{120}O_2{}^{2\bullet}$	2.00239(4)	0.0684	0.0552	**B**

$C_{120}O_2{}^{2\bullet}$ was recorded after an annealing time of 2 hours, the spectra of pure C_{60} and C_{70} after an annealing time of 6 hours, respectively. Note that in contrast to the coupling experiments presented below N@C_{60} is fixed outside the EPR tube and is not admixed with the sample inside (see Chap. 3.5.1).
The experimental findings are depicted in Fig. 26, whereby the $C_{120}O_2{}^{2\bullet}$ reference spectrum can be found in Fig. 26**A**, the C_{60}^{+} and $C_{120}O_2{}^{2\bullet}$ superposition spectrum in Fig. 26**B**, the C_{60}^{+} spectrum in Fig. 26**CI&CII**, and the C_{70}^{+} spectrum in Fig. 26**D**. All data sets were modeled using the MATLAB based EasySpin software suite, which provides a least-squares fitting algorithm.[163] Thereby, the g-factor of N@C_{60} was set to $g = 2.002\,04$, its hyperfine splitting constant to $a_{\mathrm{iso}} = 15.6\,\mathrm{MHz}$ and the linewidth was left unrestricted in both, its Lorentzian and Gaussian contribution. The particular radical species was included with its g-factor, Lorentzian, and Gaussian linewidth. The corresponding fits can be seen in Fig. 26; the resulting parameters are listed in Tab. 3. From this it can be concluded that the three species are spectroscopically well separated provided sufficient spectral resolution. A comparison of the spectroscopic data of the C_{60} cation generation methods 1,2,6 and 7 in Tab. 1 with those for $C_{120}O_2{}^{2\bullet}$ in Tab. 3 suggests that the above-mentioned methods detected the biradical oxygen species rather than C_{60}^{+}. Therefore, it seems advisable to revise these methods with regard to the data obtained here. Additionally, this implies that the aforesaid value of $T_2 = 300\,\mathrm{ns}$ is doubtful since it was obtained on C_{60} powder.[162]

All g-factor values gathered with X band EPR spectroscopy are isotropic. To unravel a possible anisotropy, higher spectral resolution is required. This is achieved when the EPR spectra are recorded under W band spectrometer conditions, which operates at a frequency of 95 GHz. Due to $\nu = g\mu_{\mathrm{b}}h^{-1}B$ this allows to split the

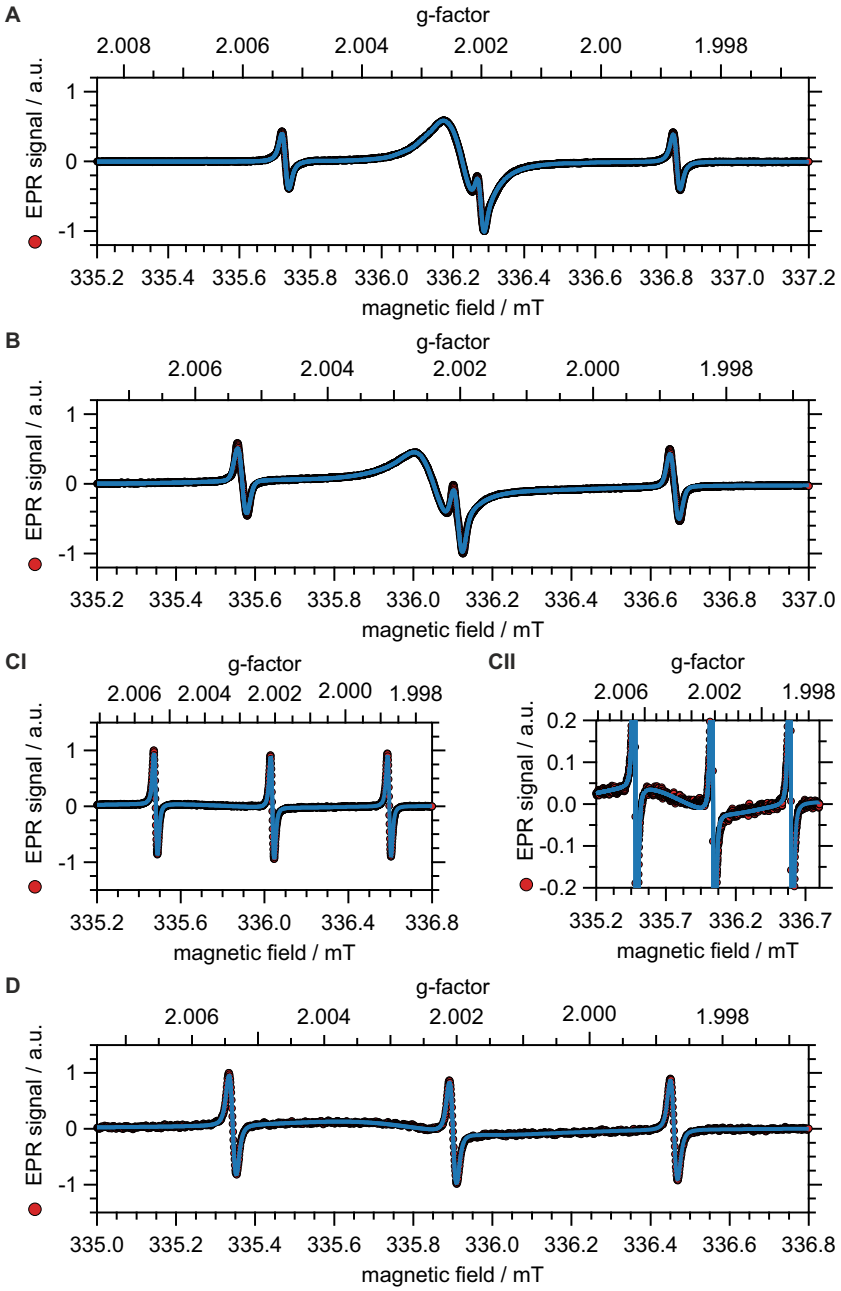

Figure 26: High-accuracy g-factor determination of fullerene-related radical species using N@C_{60} as spin standard. EPR spectrum of **(A)** $C_{120}O_2{}^{2\bullet}$ obtained on C_{60} powder, **(B)** C_{60}^+ and $C_{120}O_2{}^{2\bullet}$ generated by FeY-mediated oxidation, and **(CI)** C_{60}^+ generated by FeY-mediated oxidation. **(CII)** Same as **(CI)**; the scaling is appropriately adjusted to emphasize the C_{60}^+ signal. **(D)** EPR spectrum of C_{70}^+ generated by FeY-mediated oxidation. Blue lines are fits according to the model described in the text. All EPR spectra were recorded at X band frequency with parameters: $P_{\mathrm{mw}} = 10\,\mu\mathrm{W}$, $B_{\mathrm{mod}} = 0.01\,\mathrm{mT}$, $R = 0.01\,\mathrm{mT/bin}$, $\dot{B} = 0.13\,\mathrm{mT/s}$.

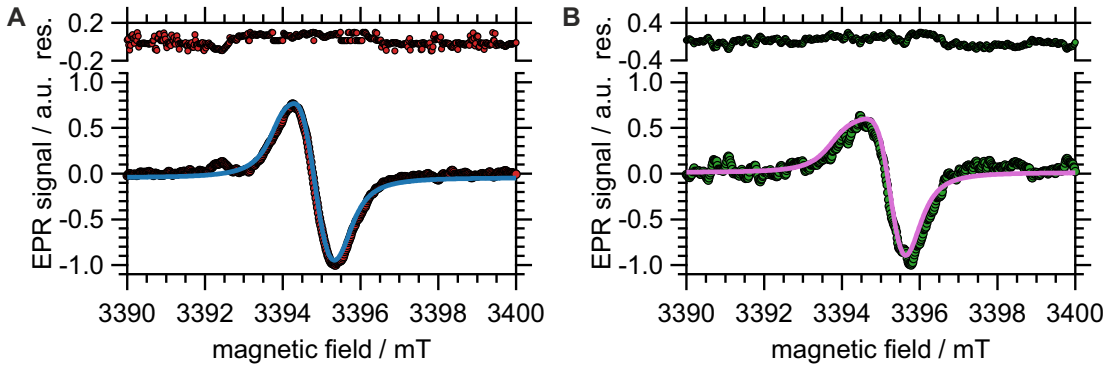

Figure 27: W band EPR spectra of **(A)** C_{60}^+ (red) and **(B)** C_{70}^+ (green). The blue and magneta line are fit models explained in the text.

Zeeman energy terms more strongly (see Eq. (1.23)).
We prepared a C_{60} and a C_{70} sample with $R^{\text{l}} = 0.2$ since we aimed to yield a high signal-to-noise ratio (Due to technical reasons, compared to X band EPR spectroscopy, the total amount probed in a W band spectrometer is significantly smaller). The annealing time amounted to 6 hours. The data sets obtained are presented in Fig. 27. Especially the C_{70}^+ signal shows a deviation form the ideal Lorentzian shape indicating anisotropic contributions. To evaluate this quantitatively we fitted the data with a model that includes full potential g-factor anisotropy ($g_x \neq g_y \neq g_z$) and the presence of $C_{120}O_2{}^{2\bullet}$. Thus, we obtained for C_{60}^+

$$g_x = 2.0028(2);\ g_y = 2.0029(2);\ g_z = 2.0046(2); g_{\text{iso}} = 2.0034(2)$$

and for C_{70}^+

$$g_x = 2.0022(2);\ g_y = 2.0027(2);\ g_z = 2.0034(2); g_{\text{iso}} = 2.0028(2).$$

Note that the values are shifted upwards compared to the X band data. However, the W band spectrometer was not frequency-calibrated, which may cause this systematic error. Nevertheless, the values for $\Delta g_{\text{iso},C_{60}^+C_{70}^+,\text{X band}} = \Delta g_{\text{iso},C_{60}^+C_{70}^+,\text{W band}}$ are the same for both measurement methods within the given error limits and accuracies. Regardless of this, both spectra have a g-factor anisotropy, with C_{60}^+ having an axial symmetry and C_{70}^+ a rhombic symmetry. Since we can mainly exclude structural restrictions imposed by the zeolite host due to our preliminary investigations, we trace this observation back to a Jahn-Teller distortion of the cationic fullerene cage, which has already been reported for C_{60} anions.[164]

3.3 Advancement of the literature protocol

Although the method presented in the previous chapter is well suited to generate fullerene cations, it does not allow for measuring coupling spectra between $N@C_{60}$ and C_{60}^+. The generation time constant for C_{60}^+ was evaluated to be $\tau_{C_{60}^+} = 114(1)\,\text{min}$ at 420 °C, yet, the thermal stability of $N@C_{60}$ under this conditions is less than 5 minutes. Thus, this protocol does not enable us to generate a sufficient amount of both spin species at the same time. Without going too deeply into electrochemical thermodynamics, the reason for the high temperature that must be present when using Fe^{3+} as oxidizing agent is the low reduction potential of the reaction $Fe^{3+} + e^- \rightarrow Fe^{2+}$ ($E^0 = 0.771\,\text{V}$).[109] With the corresponding value for the C_{60} fullerene oxidation of $E^0_{C_{60}} = 1.3\,\text{V}$,[165] the result of the Gibbs free energy of the reaction is $\Delta G = 0.53F > 0$ (F: Faraday constant), which characterizes it as thermodynamically unfavorable. The increase in temperature changes the effective reduction potential E^{eff} of both species according to the Nernst equation $E^{\text{eff}} = E^0 + \frac{R}{F}T \ln \frac{a_{\text{ox}}}{a_{\text{red}}}$ (R: ideal gas constant, $a_{\text{ox/red}}$: thermodynamic activity of the corresponding species), which scales only with $9 \times 10^{-5}\,\text{K}^{-1}$. Therefore, further parameters have to be considered, such as the temperature dependence of the thermodynamic activity of the redox species (cf. the temperature-dependent position dynamics of Fe^{3+} in Chap. 3.5.3) or kinetic effects, such as radical diffusion within the fullerene layer.

A facile way to circumvent elevated temperatures in comparison to the $N@C_{60}$ stability is to implement an oxidizing agent with a higher reduction potential. We relied on Ce^{4+} for two reasons. First, it is reported $E^0_{Ce^{4+}/Ce^{3+}} = 1.72\,\text{V}$, which is noticeably higher than the corresponding value for C_{60}. Second Ce^{4+} is EPR silent, while the reduced species Ce^{3+} possesses a reported g-factor of $g = 0.7963 - 1.266$;[166] thus, no interference within our detection area is to be expected.

We carried out the experiments with two different Ce^{4+} compounds, namely ceric ammonium nitrate (CAN) and ceric sulfate. The first substance, a mature oxidizing agent widely used in organic chemistry,[167] has already been applied in the context of zeolite systems and its capability to catalyze the synthesis of 1H-tetrazoles and 1,8-dioxo-octahydroxanthenes has been reported.[168,169] The preparation of CAN- (CANY) and $Ce(SO_4)_2$ (CeY)-loaded zeolite Y is described in Chap. 3.5.1. In contrast to previous experiments on FeY we chose $N@C_{60}$ powder as fullerene material with a filling factor of 5×10^{-4} to monitor the $N@C_{60}$ stability. However, technically the sample preparation was as before, where $R^{\text{l}} = 0.04$.

We start with the discussion of the CAN-loaded zeolite Y (CANY) experiment. It

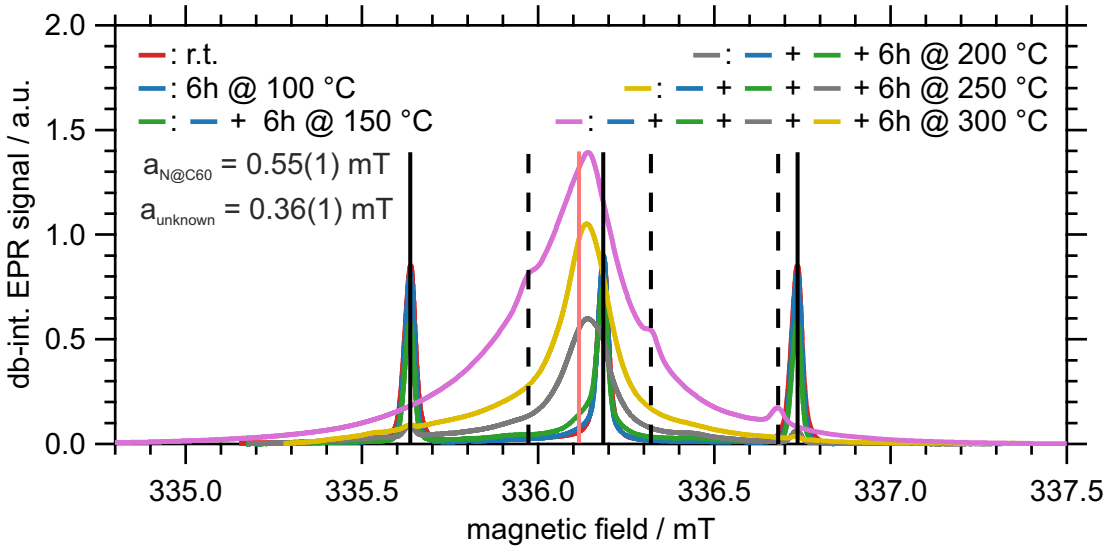

Figure 28: X band EPR monitoring of C_{60}^{+} generation in the presence of N@C_{60} using CAN-loaded zeolite Y. The corresponding annealing time is given. $a_{N@C_{60}}$ is the isotropic hyperfine coupling constant of the N@C_{60} spectrum (solid black lines) and $a_{unknown}$ the assumed hyperfine coupling constant of the spectrum of an unknown species (dashed black lines). The broad signal is due to C_{60}^{+}. The coral line indicates $C_{120}O_2^{2\bullet}$. Measurement parameters: $P_{mw} = 10\,\mu W$, $B_{mod} = 0.01\,mT$, $R = 0.01\,mT/bin$, $\dot{B} = 0.13\,mT/s$.

was designed to heat the sample at a certain temperature for 6 hours and record an EPR spectrum. The temperature was then increased by 50 °C and this process was repeated until 300 °C was reached. The data set is shown in Fig. 28. As expected, the N@C_{60} signal decreases with continuous annealing time. The signal, which indicates $C_{120}O_2^{2\bullet}$, increases up to a temperature of 150 °C and is abstinent at higher temperatures. The formation of the C_{60} cation commences even at 100 °C, in contrast to 480 °C using the Fe^{3+} catalyst; the signal dominates the spectrum for temperatures equal or above 200 °C.

Remarkably, after a heating the sample up to 300 °C, the emergence of a new signal with a pronounced structure can be observed. Its g-factor is $g = 2.0017$ and the coupling constant is $a = 0.36(2)\,mT$. We believe that this spectrum is a fullerene adduct,[170] which is formed at elevated temperatures either by the addition of ammonia or nitrate. An inspection of the literature shows that nitrogen-centered and particular aniline-type radicals exhibit g-factors which are in the area of the C_{60} cation and additionally possess higher hyperfine coupling constants in the range of 1 mT.[171,172] However, EPR experiments conducted on irradiated KCN-doped KCl

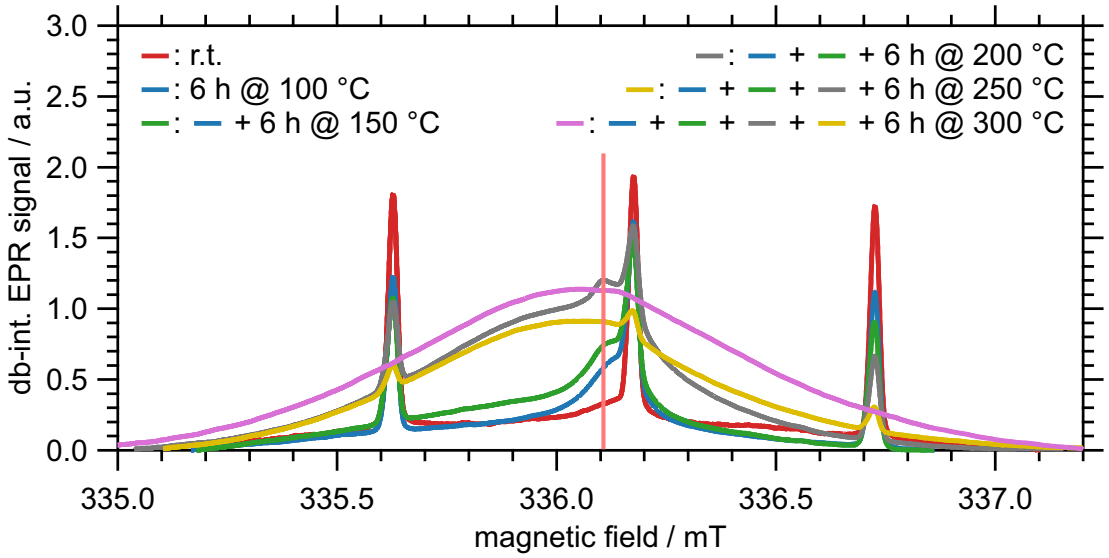

Figure 29: X band EPR monitoring of C_{60}^{+} generation using $Ce(SO_4)_2$-loaded zeolite Y (CeY). The corresponding annealing time is given. The broad signal is due to C_{60}^{+}. The coral line indicates $C_{120}O_2^{2\bullet}$. Measurement parameters: $P_{mw} = 10\,\mu W$, $B_{mod} = 0.01\,mT$, $R = 0.01\,mT/bin$, $\dot{B} = 0.13\,mT/s$.

single crystals revealed for $CNO^{2-/-}$ radicals values which fit to our observation, namely $g = 2.0015$ and $a_{iso,CNO^{2-/-}} = 0.47\,mT$.[173] The corresponding reaction mechanism would mimic a thermally induced aromatic nitration. Although this observation seems interesting and requires further investigation, it constituted a drawback for us because the adduct EPR spectrum should make the deconvolution of a C_{60}^{+}-N@C_{60} coupling spectrum more difficult.

Therefore, we continued the investigation on $Ce(SO_4)_2$-loaded NaY (CeY) whose preparation is described in Chap. 3.5.1. The sample was prepared with $R^{l} = 0.04$. The outcome of the temperature-dependent measurements are demonstrated in Fig. 29, whereby the control of the experiment was the same as for CANY. The qualitative behavior of the sample is comparable to the CANY results: $C_{120}O_2^{2\bullet}$ is thermally unstable, but persits up to a temperature of 200 °C. Remarkably, even at r.t. its signal is clearly pronounced. N@C_{60} decomposes and is absent at temperatures above 250 °C. However, the generation of the C_{60} cation slightly commences at ≈ 100 °C and its occurrence can be deemed secured for temperatures of 150 °C.

Encouraged by these results, we tried to prepare a sample from which we expected to measure the bulk coupling spectrum of C_{60} cations and N@C_{60}. We proceeded as

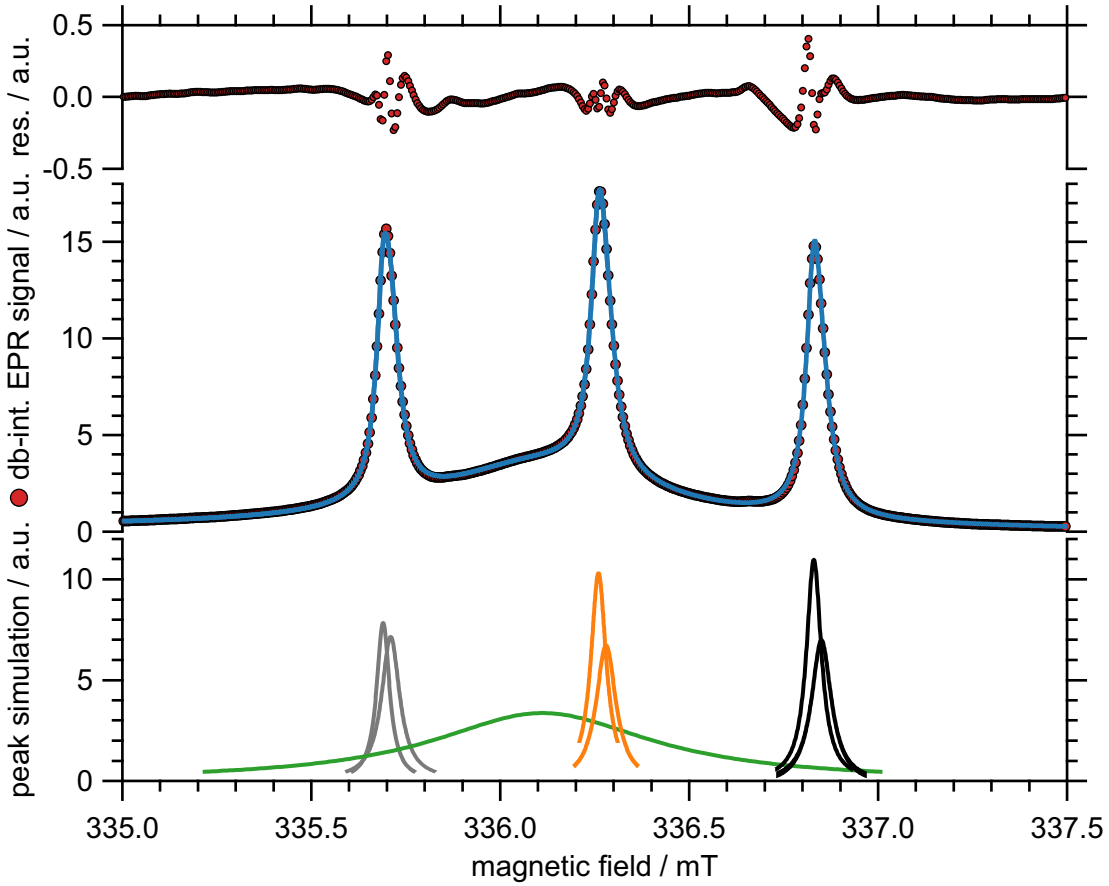

Figure 30: Double-integrated X band EPR spectrum of C_{60}^+/ N@C_{60} sample (red, middle graph). The lower graph depicts signals used to deconvolve the experimental data. The blue line is the corresponding sum fit function. Measurement parameters: $P_{\mathrm{mw}} = 10\,\mu\mathrm{W}$, $B_{\mathrm{mod}} = 0.01\,\mathrm{mT}$, $R = 0.01\,\mathrm{mT/bin}$, $\dot{B} = 0.13\,\mathrm{mT/s}$.

follows. First we prepared a CeY-C_{60} powder sample with $R^{\mathrm{I}} = 0.04$ and annealed it for 6 hours at 250 °C to produce C_{60}^+. Subsequently, we opened the EPR tube, removed the solid and added 2.7 mg N@C_{60} powder with a filling factor of 2×10^3. Then, we transferred this mixture in an EPR tube, evacuated for 12 hours and sealed it. Eventually, we heated the sample at 250 °C for 2 hours. The resulting X band EPR spectrum is depicted in the middle graph in Fig. 30.
The expected signals from C_{60}^+ and N@C_{60} are clearly visible. A comparison between this spectrum and those measured on CANY and CeY, respectively, apparently shows that the C_{60} cation signal is higher with factor 3 regarding the signal maximum and the N@C_{60} signal is is higher with factor 30 probably due to consecutive experiment control. No additional structure because of dipolar cou-

pling can be identified. However, when fitting the data by a Voigtian function for C_{60}^+ and three Lorentzian functions to take the N@C_{60} signal into account, we observed noticeable malapproximation. Contrarily, the allowance of two Lorentzian functions per hyperfine line resulted in the best fit, whose particular contributions are shown in Fig. 30 (lower graph). The splitting amounts to 0.02 mT or 6×10^2 kHz. Considering Eq. (1.30) this results in a C_{60}^+-N@C_{60} distance of ≈ 5 nm. Additionally, we computed the surface area under the EPR signals and evaluated it according to the TEMPO calibration. The result gives a number of 1×10^{15} for both spin species. The total amount of molecules in the sample is $\frac{0.0047\,\mathrm{gmol}}{720\,\mathrm{g}} \cdot 6.0 \times 10^{23}\,\mathrm{mol}^{-1} = 1 \times 10^{18}$. This means that on about every 500th molecule sits a spin species. We make a very simple estimation. First, we suppose full homogenization, i.e. C_{60}^+ and N@C_{60} spin species alternate. Further, we assume that a C_{60} cation sits in the middle of a cube with an edge occupation of $(500)^{\frac{1}{3}} = 8$ C_{60} molecules. The next-neighboring N@C_{60} spin species is located on one of the edges. With the vdW diameter of C_{60} of 1 nm the edge length of the cube is calculated to 8 nm. Thus, the distance between the center C_{60}^+ and an N@C_{60} molecule is given by $4 - 14$ nm depending on the exact location on the edge. Thus, the result of the distance from the coupling measurement and the spin count evaluation are in the same range. Nevertheless, the measurement result and the corresponding analysis must be described as preliminary. Due to the lack of a clear coupling pattern, the evaluation is not very reliable. The adding of signals generally leads to better data approximation (see Chap. 4.6.3). Furthermore, the evaluation implies that each N@C_{60} molecule couples to a C_{60} cation. In general it can be expected that there is a superposition of uncoupled and coupled spin species for both, C_{60}^+ and N@C_{60}. This is not considered here.
However, it should be noted that an improvement was achieved by modifying the literature protocol using $Ce(SO_4)_2$. Because it is now possible to generate C_{60}^+ in the stability range of N@C_{60}. In addition, there is potential for improvement of the method. N@C_{60} material with a higher filling factor can be used, which increases the initial spin density of this material. Beyond, pulsed EPR measurements can be performed on this system. With this method the width of the EPR signal is not limited by Eq. (1.35), but by the T_2 decoherence time.

3.4 Conclusion

To conclude this chapter we recall its most crucial results. We have revised a literature-known protocol - the oxidation of C_{60} on Fe^{3+} exchanged zeolites - which

determined a g-factor of 2.0025 for C_{60}^+. First, we investigated the thermal behavior of the zeolite matrix and found that it is not structurally stable under the presence of thermal load and Fe^{3+} ions. Therefore, the crystallinity and the specific structure probably do not play a role in the oxidization mechanism.
After successfully reproducing the generation of the C_{60} cation, linewidth studies showed that its value is narrower than reported in the literature and is presumably caused by dipolar interaction at high C_{60} mass load. The newly determined value is in agreement with other methods.
Using N@C_{60} as spin standard, we were able to determine the g-factor of C_{60}^+, C_{70}^+, and $C_{120}O_2{}^{2\bullet}$ with high precision. We obtained $\bar{g}_{C_{60}^+} = 2.003\,00(3)$, $g_{C_{70}^+} = 2.002\,58(4)$, and $\bar{g}_{C_{120}O_2{}^{2\bullet}} = 2.002\,36(3)$. Thus, the three spin species are spectroscopically well resolvable. Additionally, using W band EPR spectroscopy we could demonstrate g-factor anisotropy for both, C_{60}^+ and C_{70}^+, whereby the first turns out to be an axial system, the latter a rhombic system. We attribute this reduction in symmetry to a Jahn-Teller distortion, which is also reported for C_{60}^-.
By using Ce^{4+} instead of Fe^{3+} as oxidizing agent, we were able to reduce the thermal demand of the oxidation reaction by about 200 °C for the $Ce(SO_4)_2$ protocol. Thus we reach the range of relative stability of N@C_{60}. We applied a consecutive experiment approach of first generating C_{60}^+ separately and adding N@C_{60} subsequently to obtain a system which exhibits a C_{60}^+-N@C_{60} coupling spectrum. The outcome is ambiguous. However, the comparison of the results of the signal deconvolution and the simple calculations based on spin counting revealed to be in the same range.
In summary, we expect that especially the $Ce(SO_4)_2$ zeolite system is asking for further investigation. Besides the already obtained spectroscopic data regarding the g-factor characteristics of the fullerene cations, optimizations of the Ce^{4+} system can lead to bulk EPR data for dipolar coupling between C_{60} cations and other spin species, especially N@C_{60}. These can be used to interpret measurement results obtained on more complex measurement systems, such as single molecule detection using ODMR.

3.5 Supplementary

3.5.1 Methods

EPR spectroscopy
X band EPR spectra were obtained using a Magnettech Miniscope MS 400 spectrometer. The measurement parameters are specified together with the presentation of the respective measurement data.
Calibration g-factor calibration was realized by 1. measuring the spectrum of a manganese(II) standard embedded in a zinc sulfide crystal for whose third hyperfine line is known $g_{\mathrm{std,\,3.\,HF}} = 2.0267(2)$ or 2. using $N@C_{60}$ as internal standard ($g = 2.002\,04(4)$).[121] In the second case, $N@C_{60}$ powder of filling factor 4×10^{-4} was glued on the sealed side of the EPR tube. Measurements were carried out beforehand on samples containing $N@C_{60}$ inside and outside the EPR tube, where no spectroscopic difference between the respective EPR spectra could be observed. Spin counting was enabled by TEMPO calibration. See Chap. 4.6.1.
W band EPR spectra were recorded in the group of Prof. Steinhoff at the Universität Osnabrück on a home-built EPR spectrometer which operates at 95 GHz. The measurements were conducted by Elena Bondarenko.
Fitting of EPR signals were carried out using MATLAB based EasySpin software which provides a least-squares fitting algorithm.[163]

Nitrogen sorption measurements were performed with a Porotec Surfer device at 77 K on dried samples. Before any measurement, the samples were outgassed at 250 °C for 10 hours. The nitrogen sorption measurements were carried out by Maximilian Münzner and Alexander Grimm at the Universität Leipzig. To obtain the pore size distribution the adsorption branch of the BET isotherm was used with the method of Barrett, Joyner and Halenda (BJH)[174] or a DFT approach.[175] For the analysis, the program ASiQwin from Quantachrome Instruments was used.

XRD measurements on zeolite, Fe^{3+}/ C_{60} loaded zeolite, and calcinated zeolite powder samples were conducted on a Panalytical X'pert diffractometer (Cu Kα radiation, 2θ step size: 0.033°) by Christian Hohmann at the Universität Osnabrück.

C_{60} and $N@C_{60}$ powder was obtained with 99.5 % purity from $N@C_{60}$ enrichment process conducted in our group (see Chap. 2.1.3). All other chemicals used were purchased from commercial suppliers and used without further purification steps.

Sample preparation CAN: $(NH_4)_2[Ce(NO_3)_6]$-loaded zeolite Y (CANY) was prepared under slight modifications according to literature.[168] 0.740 g of CAN was dissolved in 30 mL of acetone, and 500 mg dried NaY was added. This suspension was stirred until complete dryness. Subsequently, heating in a furnace over night at 80 °C was carried out (yield: 98 %). $Ce(SO_4)_2$: 0.299 g of $Ce(SO_4)_2$ was dissolved in 10 mL of H_2SO_4 (10 vol%), 1.003 g dried NaY was added and the suspension was stirred over night at 70 °C until complete dryness. The solid was washed three times with ultrapure water and dried over night in a furnace at 80 °C (yield: 95 %).

3.5.2 Brief remarks about zeolites

Silicates are intermolecular condensation products of monosilicic acid $Si(OH)_4$, the monomeric unit of which is given by $[SiO_4{}^{4-}]$ tetrahedra. They form a rich system of compounds, which is caused by the multitude of linking possibilities of the $[SiO_4{}^{4-}]$ units and is realized in zero- (neosilicates), one- (inosilicates), two-dimensional (phyllosilicates) and three-dimensional silicate structures (tectosilicates).[177] An additional source of variability is provided in that during the condensation reaction oxygen bonded M-units (M−O; M = Be, B, Al) can replace the silicon ions, which leads to beryllosilicates, borosilicates, and aluminosilicates.

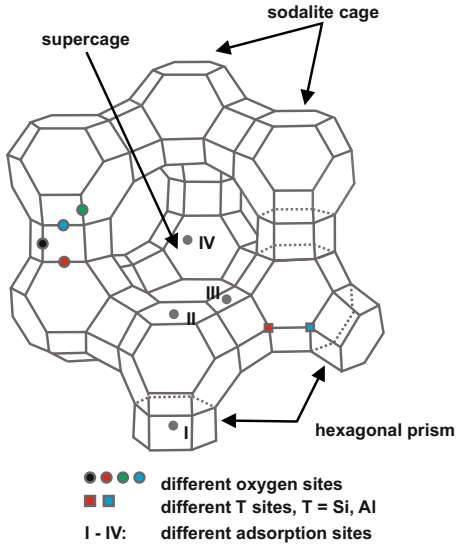

Figure 31: Schematic drawing of NaY zeolite. Nodes represents either Si or Al, edges −Si−O−Al/Si bonding motifs.[176].

Zeolites are tectosilicates composed of corner-sharing $[SiO_4{}^{4-}]$ and $[AlO_4{}^{5-}]$ tetrahedra. Their composition is governed by the Löwenstein's rule, which states that the lowest Si/Al ratio is equal to one. Accordingly, there are no Al−O−Al structural motifs. The presence of aluminum induces negative adsorption sites, which are saturated by cations. The general unit cell formula is given by $M^{n+}_{\frac{i}{n}}[(AlO_2^-)_i(SiO2)_j]_k \cdot mH_2O$, with M be the charge-balancing cation and i, j, k, m are stoichiometric coefficients. The variety of structural richness can be deduced from that currently 225 framework structures are known. Zeolites have a wide range of industrial applications: as acidic or redox catalysts, especially in petrochemistry, as gas separators due to the sieve effect of their porous structure

and as ion exchangers because of their negative adsorption sites.[178]
We used zeolite NaY or Faujasite ($Na_2Ca[Al_2Si_4O_{12}]_2 \cdot 12H_2O$) as precursor in this work. Its crystal structure is, like diamond, in the cubic space group $F4_1/d\,\bar{3}\,2/m$, which can be seen in Fig. 31 with the sodalite cages playing the role of the carbon atoms. The pore structure is mainly characterized by supercages with a diameter of 1.2 nm which are connected by windows with a diameter of 0.8 nm.[176]

3.5.3 Characterization of thermal behavior of Fe^{3+} loaded faujasite

In order to separate the impact on the zeolite crystallinity of the different processes that take place before and during the thermally induced oxidation reaction

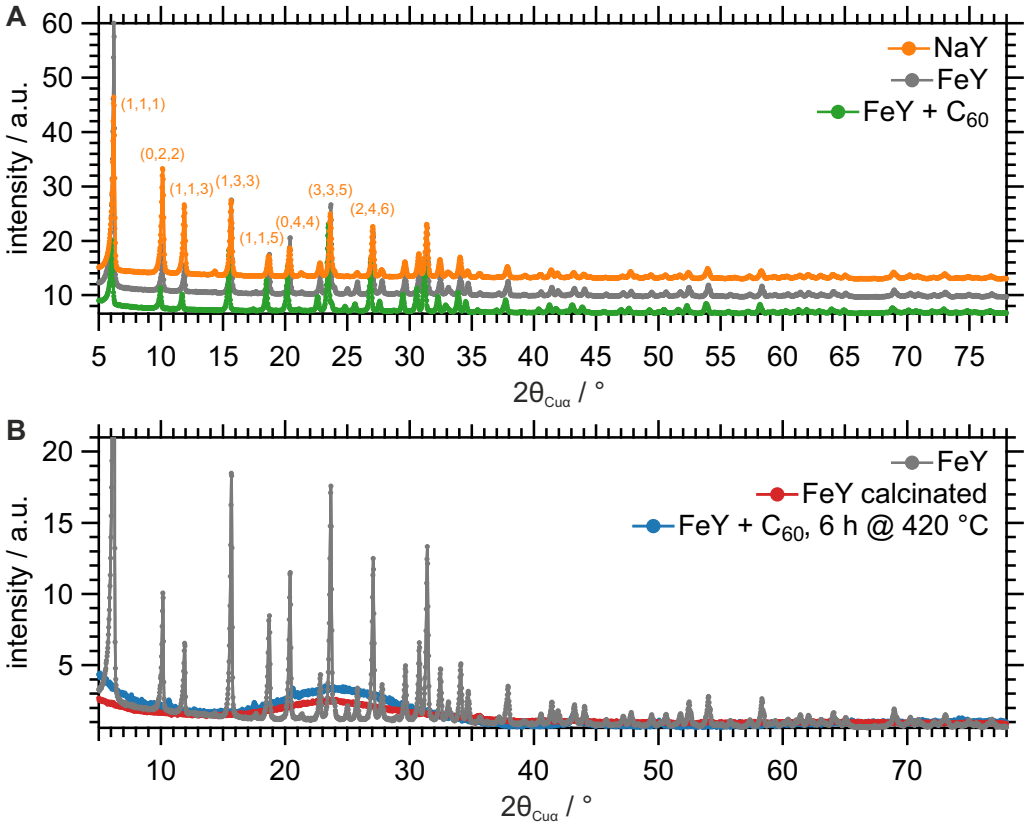

Figure 32: XRD measurements on different intermediates of FeY-mediated C_{60} oxidation. **(A)** Diffraction pattern of dried NaY (orange), FeY (gray) and C_{60}-loaded FeY (green). The assignments were achieved according to literature.[179] Offsets are chosen for clarity of representation. **(B)** Diffraction pattern of FeY (gray) prior to annealing (same as in **(A)** and given for comparison), of FeY after annealing for 3 hours at 637 K, and of C_{60}-loaded FeY after annealing.

of C_{60} on zeolite-supported Fe^{3+}, we performed XRD measurements of particular intermediate steps of the literature protocol in Ref. [159]. Fig. 32 summarizes the results obtained. A quantitative analysis of the data would include the use of Rietveld refinement, however, this is beyond the scope of this discussion. We proceed qualitatively.
Fig. 32**A** depicts the diffraction patterns of dried NaY, FeY, and C_{60}-loaded FeY. The peak positions for the former are compared with selected literature values, whereby good agreement could be found. Both, the wet-chemical ion exchange of sodium against iron and the addition of C_{60} powder, have no influence on the crystallinity. The slight offset between the respective powder diffraction data is global and cannot be reliable attributed to a modification of the zeolite structure, for example, a shrank lattice constant, without further analysis; a changed incidence angle of the Cu Kα radiation would lead to the same result.
The annealing of FeY at temperatures $> 420\,°C$ either as a calcination step without C_{60} powder or in its presence, i.e. according to the conditions existing during the oxidation reaction, cause a collapse of the crystal structure. This is indicated in the XRD data by broad, unstructured features which only have isolated Bragg peaks.
It is noteworthy that the zeolite structure of NaY is thermally stable (see Fig. 32)**A**, while the exchange with Fe^{3+} ions results in a mostly amorphous material at elevated temperatures.

An important method to characterize porous materials is the physiosorption of gases.[180,181] The basic idea is to characterize the surface of a solid by the amount of adsorbed gas molecules. A technical realization to determine this quantity consists in measuring the change of pressure associated with this process in an exactly known volume below the saturation pressure ($p/p_0 < 1$) of the gas used. The characteristic pressure response of a sample to a discrete change of the added gas volume is mapped in the adsorption isotherm. If the desorption of the adsorbable gas is monitored as well, the full hysteresis of a physiosorption isotherm is obtained. Its particular shape is mainly determined by the pore size distribution of the material investigated and the corresponding physical mechanisms (micropore filling, capillary condensation, multilayer adsorption). A commonly accepted hierarchy of pore types is given according to: macropores (pore diameter $D_p > 50\,\mathrm{nm}$), mesopores ($D_p = 2 - 50\,\mathrm{nm}$), and micropores ($D_p < 2\,\mathrm{nm}$).[181]
The investigations of a large number of systems have led to certain classes of isotherms representing the different pore sizes, whereby eight types are currently

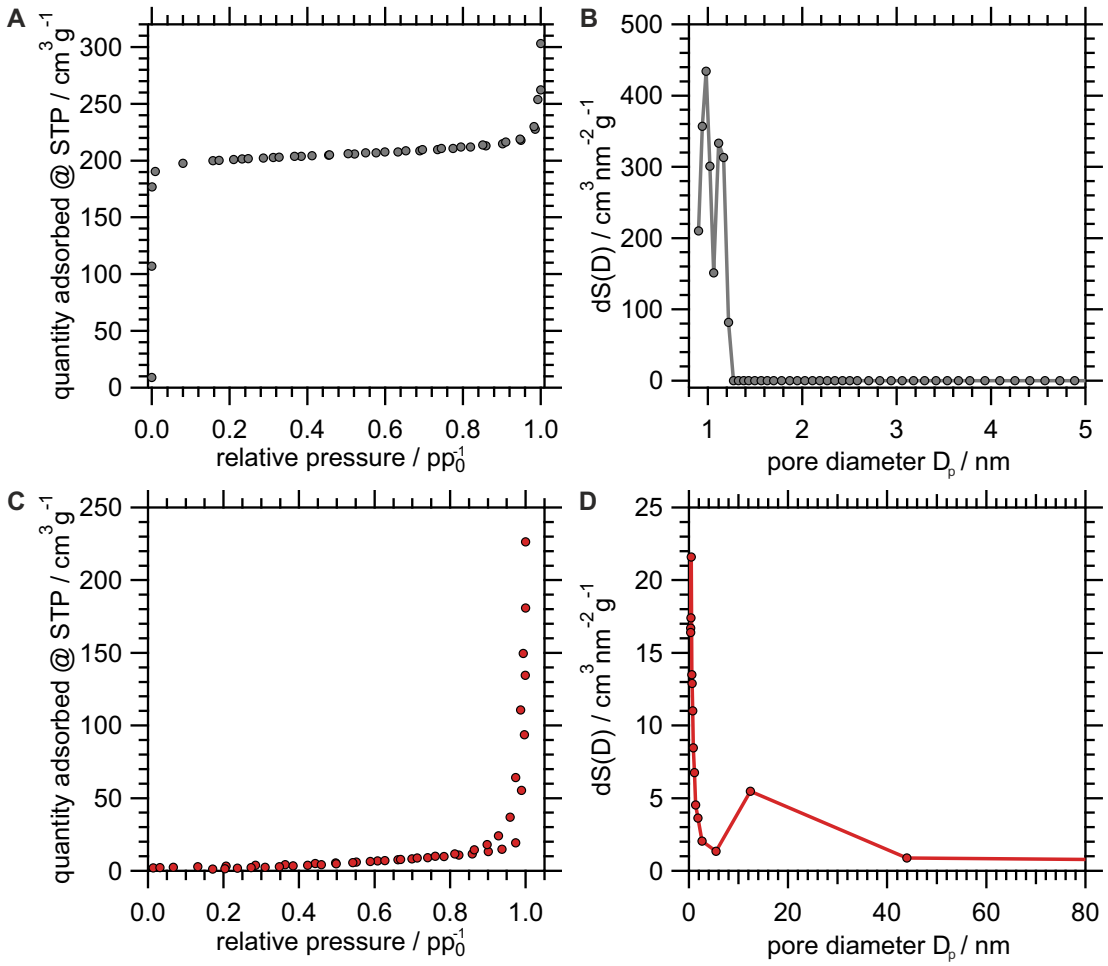

Figure 33: Nitrogen sorption measurements on FeY (red, upper row) and calcinated FeY (gray, lower row). **(A)** Nitrogen sorption type-I isotherm of FeY, which represents a microporos material. **(B)** Corresponding pore diameter distribution. **(C)** Nitrogen sorption isotherm (superposition of type III and V) of calcinated FeY, which represents a meso- or macroporos material. **(D)** Corresponding pore diameter distribution. The classification of isotherms was taken from literature.[181]

distinguished in the literature.[181] The calculation of the pore diameter distribution and the effective surface area of a material depends on these classes. For macro- and mesoporous systems the BET method is widely used,[174] microporous systems are evaluated by DFT methods.[175]

We now turn to the measurement findings, which are presented in Fig. 33. Two samples were investigated, namely FeY (Fig. 33**A**&**B**) and calcinated FeY (Fig. 33**C**&**D**). The first sample shows the typical type-I isotherm of a microporos ma-

terial. The calculated pore diameter distribution reveals two maxima at 0.98 nm and 1.2 nm, which confirms the structural information in Chap. 3.5.2 well. The specific surface area is given by $637\,m^2g^{-1}$, which value is in good accordance to literature.[182] After the calcination process, i.e. annealing the sample at 420 °C for 3 hours, the shape of the isotherm significantly changed. It is best described by a superposition of a type-III and type-V isotherm. The first is appropriate to describe macro- or nonporous systems, the latter holds for mesoporous materials. Accordingly, the computed pore diameter distribution is altered. The global maximum is reached for $D_p \to 0$, whereas a second broad contribution of pore diameters in the range of $6-44$ nm is present. Furthermore, the specific surface area is reduced to $11.9\,m^2g^{-1}$. This strongly indicates a mainly nonporous material.

Fe $3d^5$ high spin cations ($^6S_{\frac{5}{2}}$) are EPR active. The ground state spin Hamiltonian $\hat{H}_0 = g\mu_b \underline{B}\,\underline{\hat{S}} + D\left[\hat{S}_z^2 - \frac{1}{3}S(S+1)\right] + E\left[\hat{S}_x^2 - \hat{S}_y^2\right]$ gives rise to different signals. In zeolite systems the following has been observed: 1. in a total-symmetric environment, i.e. in octahedral complexes, $D = 0$, $E = 0$ and hence isotropic signals appear at $g \approx 2.0$; 2. $D \neq 0$, $D \gg 0$, and $E = 0$ (axial symmetry) anisotropic signals are present at $g_\parallel = 2.0$ and $g_\perp = 6.0$; 3. If $D = 0$, $E \neq 0$, which is

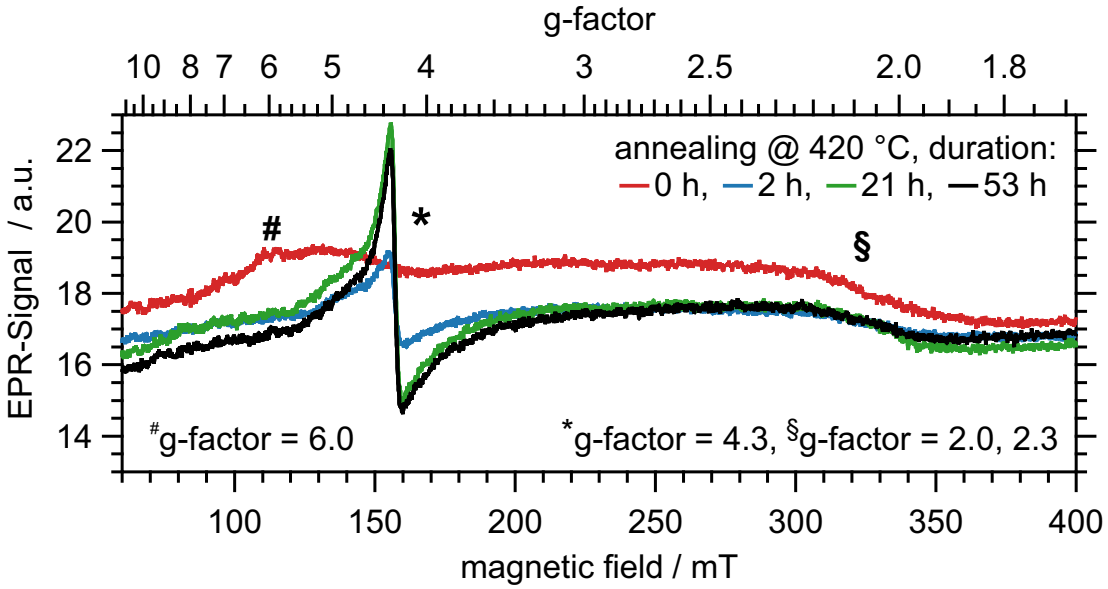

Figure 34: EPR monitoring of FeY calcination process. EPR spectra were recorded at the annealing conditions mentioned. Offset of the EPR spectrum prior to heating is chosen for clarity of representation.

the case for tetrahedral (C_{3v}) and distorted octahedral (D_{2h}) coordination environment, $g = 4.3$.[183] The last case was attributed to zeolite skeleton-coordinated Fe^{3+} preceded by an Al^{3+} exchange.[184] An additional signal source is constituted by iron oxides, which are detectable at $g = 2.3$.[185]
We performed temperature-dependent EPR measurements on FeY to test the transitions between the differently coordinated Fe^{3+} species. The outcome is shown in Fig. 34. Prior to the calcination step a slightly pronounced signal at $g = 6.0$ and a broad one at $g = 2.0$ can be noticed. Upon heating the sample, a prominent signal at $g = 4.3$ comes to the fore, which seems to saturated for long annealing times. While the signal at $g = 6.0$ vanishes, the one at $g = 2.0$ remains apparently unchanged.
The observations are largely in accordance with the literature.[184,185] While Fe^{3+} is located in axial symmetry at the negatively charged adsorption sites before annealing (case 2), the input of thermal energy leads to an $Fe^{3+} \rightarrow Al^{3+}$ exchange and thus to the inclusion of the Fe^{3+} ions in the zeolite structure.

In summary, we conclude that the annealing process leads to a strong reduction of the crystallinity of the zeolite material regardless of the presence of C_{60} fullerenes. Thus, thermally induced diffusion of fullerenes into supercage structures of the zeolite can be excluded almost completely. It is also questionable whether the mesoporous structures created by the annealing process cause restrictions, such as the blocking of oxidation sites, since their size is on average significantly greater than the vdW diameter of C_{60} and C_{70} (see Chap. 2.1.3).

4 Chemical surface functionalization as a route for optimizing the spin properties of NV^- centers in nanodiamond

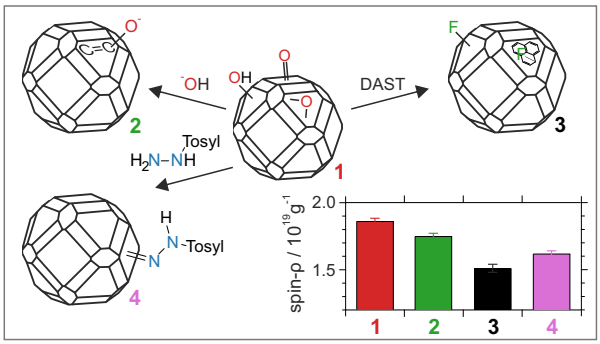

From the perspective of recent proof-of-principle demonstrations nanodiamond augurs fruitful applications, for example as drug delivery agent, confined electrode material, and, if it hosts negatively charged nitrogen-vacancy (NV^-) centers, as bio-compatible fluorescence label or nanoscale detector of magnetic, electric, temperature, and concentration fields. For any of such utilization comprehensive chemical control over the diamond surface properties is highly desired. In particular for NV^- center-based sensing schemes, the charge state stability and intrinsic spin noise level are decisively influenced by different surface parameters (e.g., defects, functionalization). However, the very nature of interdependencies remains opaque and is, now more than ever, under debate, recently sparked through both, experimental and theoretical work.

Especially against the background of the latest research results we hypothesize that the established post-synthesis treatment protocols need to be reconsidered and therefore present novel wet-chemical approaches which aim to partially saturate surface-related dangling bonds by fluorination, nitrogenation, and base-mediated surface homogenization. Electron paramagnetic resonance (EPR), infrared, and X-ray photoelectron spectroscopy enables us extensive ensemble characterization of the nanodiamond material produced. Our best result obtained for the fluorination protocol, for which spectroscopic data indicates an unexpected weakened covalent carbon-fluorine binding state, amounts to a 19% reduction in surface spin density compared to pristine laser-ablated starting material. Additionally, conducting optically detected magnetic resonance measurements on few-nanodiamond clusters before and after base-treatment, enables us to correlate EPR average values and T_1 relaxation times of ensembles containing approximately 30 NV^- centers. Therefore, we propose the presented methods as relatively modest approaches as opposed

to previously reported surface termination protocols. In general, we assume tailored chemical functionalization schemes might help to target the nanodiamond surface issue successfully.

The following part of this thesis is currently in preparation for publication in a peer-reviewed journal: R. Wieczorek, J. M. Kurzhals, K. Küpper, W. Harneit, Reducing the spin noise of nitrogen-vacancy centers by partial saturation of nanodiamond surface dangling bonds using wet-chemical approaches, in preparation.

4.1 Introduction

Addressing the relevance of chemical control over the surface properties of nanodiamond (ND), we should carefully discern two different objectives. One of them is currently pursued mainly in life sciences and can be characterized in such a way that the diamond surface serves as a platform that can be expediently modified to perform different tasks,[186–189] e.g., cell membrane targeting by non-covalent biotinylation,[190] non-viral gene delivery by poly-cationic polyethylendiimine-ND assembles,[191] and enhanced bactericidal activity due to oxygen termination of the ND surface.[192] The second approach is based on the ability of the diamond lattice to host defects, most prominently the negatively charged nitrogen-vacancy (NV^-) center, whose properties can be exploited to use ND as optical markers or sensors, e.g., for magnetic, electric, temperature and concentration fields.[193–195] The fluorescence stability and sensitivity of the latter is delicately influenced by the diamond surface, so that it can rather be regarded as a source of interference. The full development of the potential of ND will, however, be the combination of both research branches resulting in a bio-relevant tool whose activity can be simultaneously monitored at the sub-cellular level.[189] Despite the progress that has been made in recent years, both accesses to the diamond surface and the associated methods are faced with their own difficulties. Additionally, an integration of them does not simplify the situation, at any rate, because the solutions of one are not necessarily beneficial to the other. To illustrate this in more detail we may regard two examples.
In an early study, which has impressively demonstrated the possibilities of applying NV^- center hosting ND in biological research, non-detonation ND clusters with average size of 140 nm were incubated into living human HeLa cells.[196] Subsequently, in-cell tracking of the ND position and its rotational orientation over a period of hours could be accomplished as well as magnetic noise sensing based on

T_2 decoherence time measurements, which is a prerequisite for advanced detecting of biological processes.[23] However, when aiming to utilize ND as sensor for such events, which are located inside the cell nucleus, their size need to be quite smaller than that of the ND in the aforementioned experiment, namely in the range of a few nanometer, in order to be internalized in this particular compartment.[197,198] Yet, such diminution in ND diameter elicit severe drawbacks regarding its detection performance, e.g., due to $NV^- \longrightarrow NV^0 + e^-$ charge dynamics. Since harvesting of the information encoded in the NV^- center spin level populations occurs via optical addressing with wavelengths exciting both charge species, NV^0 center emission causes more copious background noise, thereby extending required measurement time.[199] Furthermore, laser illumination may spur the reduction process by photoexcitation.[200,201] Frequently, surface termination has been attributed as a crucial factor because of electron acceptor states, which lead to an upwards bending of the NV^- center band above the Fermi level in case of a negative electron affinity of the surface, e.g., for H-functionalization.[202,203] However, for shallow NV^- centers charge state conversion in the dark has been reported as well.[204,205] This has an even more critical influence on quantum sensing schemes compared to increased background noise, as the acquisition of the signal fields to be measured is realized through detection of population differences owing to changes in the phase relationship of the NV^- center eigenstates in the (non-illuminated) free evolution periods of the total spin Hamiltonian.[23] Additional kinetics altering level populations may thus corrupt measurement outcomes, which was indeed demonstrated; mitigating protocols have been developed, however, they will also extend measurement time.[205]

If we now move to the domain of biological application of ND, covalent and non-covalent binding of drug molecules often takes place via activated carbon moieties.[206–208] Although the functionalization of ND on non-activated C−H bonds, e.g., by means of the Suzuki cross-coupling reaction, has been presented, contamination by transition metal traces can not be excluded in such processes, which can influence the toxicity and the magnetic properties of the spin bath.[209] Thus, surface terminations such as alcohols, ketones, carboxylic acids, carboxylic acid esters, and ethers are often the means of choice in current research. In fact, considerable efforts have been taken to homogenize the ND surface with respect to these carbon bonding patterns, whereby, e.g., air-oxidization proved to be most efficient in generating a highly carboxylic acid-functionalized ND surface.[210–212] It constitutes a versatile precursor for further functionalizations, e.g. due to reduction, amidation, esterification and (subsequent) polymer-coating, the latter both,

in non-covalent approaches via electrostatic interaction and preparative "grafting to" designs, e.g. for PEGylation.[186,206,213–215] With the help of these methods, for example, the increased delivery of nucleus-targeting peptides could be demonstrated, provided that the ND carriers were prepared by coating with a cationic peptide shell.[216] Furthermore, the carboxylated ND surface has been attributed a role of its own right in a study that investigated its possible use as a nanocarrier drug delivery system using antibiotics and demonstrated their controllable release.[217] Especially in the last report, the predominantly COOH-terminated surface showed superior characteristics. If the release kinetic of drugs is to be monitored in future experiments assisted by NV^- centers, the implementation of which has already been successfully demonstrated by means of T_1 relaxometry experiments using Gd^{3+} spin labels,[36,39,40] this surface termination may, however, prove to be disadvantageous. Thus, a theoretical investigation demonstrates that a homogeneous coverage with only one C−O functionality results either in sub-bandgap image states or energetically deep in the bandgap localized acceptor states.[218] While commonly a positive electron affinity (PEA) of the surface, which leads to a downward bending of valence and conduction band, is generally considered to be NV^- center stabilizing, it has been shown that for the termination with the highest PEA, namely with fluorine, bleaching can nevertheless be observed.[219] This could also be explained in the aforementioned study by acceptor levels near the conduction band.[218] Furthermore, it has been suggested that oxygen and even fluorine surface decoration may not be the best choice in terms of bandgap trap state intrusion but substitutional nitrogen, a termination hardly to achieve by chemical approaches.[220,221] Very recently, the ubiquitous C=C bond motif on the diamond surface has been identified as an electron trap.[222] Moreover, using *ab initio* calculations and an electrostatic model, it could be revealed that hydrogen passivated ND possess atom-like so called surface bound states unparalleled by its bulk counterpart,[223] which emphasizes that solid state models are often not strictly valid on the range of ND. So, it is recognizable that surface functionalization reactions have to be designed carefully to contribute both, the demands of application and of sensor stability.

We used the above-mentioned considerations as a starting point for our investigations. From these we first derived two possible approaches to reduce the spin density on the ND surface, and thus to increase the sensitivity of the NV^- center either by changing the relative energy state of sp^2 carbon bonds or by separating their presumably conjugated bonding pattern. We assumed that we could realize the first access by treating ND with a strong base. Furthermore, we hypothesized

to get a handle on the second approach employing DAST-mediated fluorination. Eventually, the Bamford-Stevens olefination appeared to us as a promising protocol due to a hydrazone intermediate, which renders a C=N-motif. We suspected that this would result in a reduction of the surface spin density either because the imine or aziridine binding structure is somewhat analogous to substitutional nitrogen termination or because surface stabilization occurs through N $\longrightarrow$ O exchange. For subsequent thermal decomposition of the hydrazone intermediate we expected surface homogenization that might also have a lower radical species density compared to previous hydrogenation reports.

4.2 Results of the functionalization protocols

4.2.1 Treatment with strong bases

The treatment of ND with strong bases is a simple wet-chemical method, which we conducted by refluxing a suspension of 2 M NaOH and laser-ablated ND (RayND) material for six hours followed by a purification and drying procedure (see Chap. 4.6.2). We chose this ND material for all functionalization protocols due to its ready availability and its properties comparable to those of detonation ND (DND), except for the ODMR experiments where we used milled ND (mND) due to their higher content of NV^- centers (see the SI.S6 and below). As the first investigation method, we relied on infrared (IR) spectroscopy, which is particularly suitable for distinguishing between different carbon bonding motifs. The results can be seen in Figure 35, where additionally the IR spectrum of the pristine RayND material is shown for comparison. (IR spectra presented in the main text are given moreover in Chap. 4.6.2 with full assignment of all observable absorption bands and the literature used for interpretation).

First, we address the common features of both spectra as they will prove to be only slightly changing for the outcome of each of the functionalization protocols. The adsorption of water is indicated by a broad stretching mode absorption band at $\tilde{\nu} \approx 3400\,\mathrm{cm}^{-1}$ and the corresponding deformation mode peak at $\tilde{\nu} \approx 1630\,\mathrm{cm}^{-1}$. At $\tilde{\nu} = 1559\,\mathrm{cm}^{-1}$ and $\tilde{\nu} = 1540\,\mathrm{cm}^{-1}$ there are specific weak and narrow IR bands referring to the diamond core and nitrogen impurities. The range from $\tilde{\nu} \approx 1700 - 1800\,\mathrm{cm}^{-1}$ indicates carbonyl functionalities. The exact position within this range allows to make more accurate statements about the chemical environment of the C=O group. Here, the rule applies that the more pronounced its double bond character, the higher the wavenumber. Thus, carboxylic anhydrides, esters, and lactones are at the upper limit

of the range, ketones at the lower.[224] In general, a superposition of signals of these different functionalities can be expected.[225] Hydrogen surface termination is detectable either as usually weak signal at $\tilde{\nu} \approx 1457\,\mathrm{cm}^{-1}$ ($C(sp^2)-H$) or as a broad absorption band at $\tilde{\nu} \approx 1100\,\mathrm{cm}^{-1}$ ($C(sp^3)-H$), where both are caused by deformation vibrations.[226] However, further studies have claimed for the latter signal additional assignments, namely N-defect centers in the diamond core, $-NO_2$ and $-SO_2OH$ binding motifs and $\delta-CCC$ vibrations.[227–229] We follow Ref. [226], yet, other sources may contribute to the signal as well. However, their very chemical nature left them unaffected by our functionalization protocols.

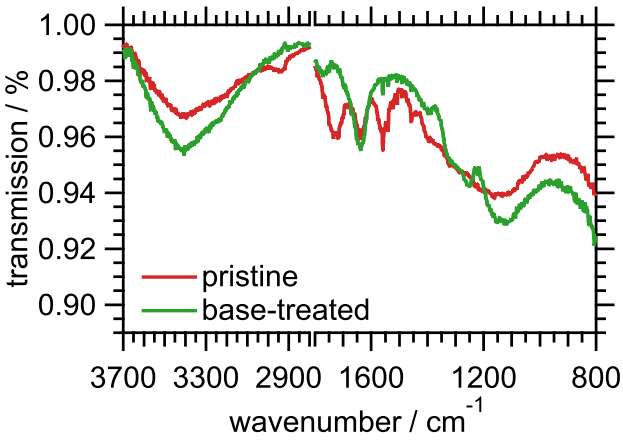

Figure 35: IR spectra of pristine (red) and base-treated (green) RayND.

With these remarks we now turn to the differences of the IR spectra of pristine and base-treated RayND. Three observations are concise. First, after base treatment the broad signal at $\tilde{\nu} = 1550\,\mathrm{cm}^{-1}$ diminishes, yet, the aforementioned narrow and characteristic signals in this area remain. The former has been ascribed to the carboxamide functionality, so that it is plausible that harsh basic conditions led to cleavage of the $C-NH_2$ bond.[230] Second, more relevant to us a shift of the C=O peak to higher wavenumbers can be seen ($\tilde{\nu}_{\mathrm{prist}} = 1718\,\mathrm{cm}^{-1}, 1733\,\mathrm{cm}^{-1} \rightarrow \tilde{\nu}_{\mathrm{base}} = 1771\,\mathrm{cm}^{-1}$), which is coincident with its decrease. The position of the IR absorption band of the carbonyl group on the C(100) (1×1) reconstructed surface was measured to be $\tilde{\nu} = 1731\,\mathrm{cm}^{-1}$, in good agreement with the value we obtained for the pristine RayND, while the signal at $\tilde{\nu} = 1718\,\mathrm{cm}^{-1}$ may be due to C=O contributions from other diamond surface facets.[231] The increase in the wavenumber under the influence of NaOH indicates the formation of conjugated binding structures or the presence of electron-releasing substituents on the carbonyl carbon, in short, the formation of (α,β-unsaturated) carboxylic anhydrides or strained ring structures such as lactones.[230] Third, a signal at $\tilde{\nu} = 1255\,\mathrm{cm}^{-1}$ comes to the fore which may be assigned to ether or alcohol moieties containing α,β-unsaturated carbon ($C(sp^2)-OC(sp^3)$ / $HOC(sp^2)-H$)).[224] This consists a pivotal outcome which, e.g., is not present for

Table 4: Results of the deconvolution procedure of high-resolved C 1s XPS spectra of listed protocols. The attributed functionalities are given with their areas $A_{(\cdot)}$ in %. Explanations for ascertaining the Akaike weight w_{Akaike} can be found in Chap. 4.6.3.

protocol	$A_{\text{C(sp}^2\text{)}}$	$A_{\text{C(sp}^3\text{)}}$	$A_{\text{C-O}}$	$A_{\text{C=O}}$	$A_{\text{C-F}}$	w_{Akaike}
pristine	0.6(4)	93(3)	1(1)	5(1)	-	0.73
base-treated	6(2)	85(2)	5(1)	4(1)	-	1
hydroxylated	13(3)	82(3)	3(1)	1.3(4)	-	1
fluorinated	2.7(5)	90(3)	4.5(8)	2(1)	0.03(3)	0.84
de-hydrazonated	1.6(3)	96(1)	1.2(5)	1.5(3)	-	0.99

the prominently employed acid-assisted wet-oxidizing protocol (see Fig. 37). It may be helpful to corroborate this finding by inspecting the X-ray photoelectron spectroscopy (XPS) results with respect to the high-resolved C 1s spectra. Initially, we faltered in terms of obtaining reliable fits, since the signals of C(sp^2) and C−O motifs are weak in our measurements. Therefore, we applied a fit procedure which capitalizes on insights gained in information theory, especially in model selection theory. An elucidation of this procedure is given in the Chap. 4.6.3 where the high-resolved C 1s spectra are presented with their respective deconvolution. In Tab. 4 we list the corresponding results. As can be seen in comparison between pristine and base-treated RayND material, for the latter the proportion of sp^2 and oxygen-bonded sp^3 carbon is significantly increased which qualitatively fits well with the IR analysis. In short, IR and XPS characterization of base-treated RayND reveals a surface decoration where strained lactones and enol motifs play a crucial role. A continuative discussion of this will be given along with the results of the EPR measurements (see Chap. 4.3).

4.2.2 DAST-mediated fluorination

The next functionalization approach we want to focus on is the diethylaminosulfur trifluoride (DAST)-mediated fluorination.[232,233] Being a mature protocol in organic chemistry, it is capable to react with oxygen containing groups like alcohols, aldehydes, ketones, carboxylic acides, and lactones.[234] We are concentrating here on the substitution of hydroxyl and carbonyl groups. Fig. 36**A** illustrates the mechanism for the S_N2-type nucleophilic substitution on DAST **AI** forming an alkoxy-(*N*,*N*)-diethylaminosulfur difluoride intermediate **AII**, whose existence

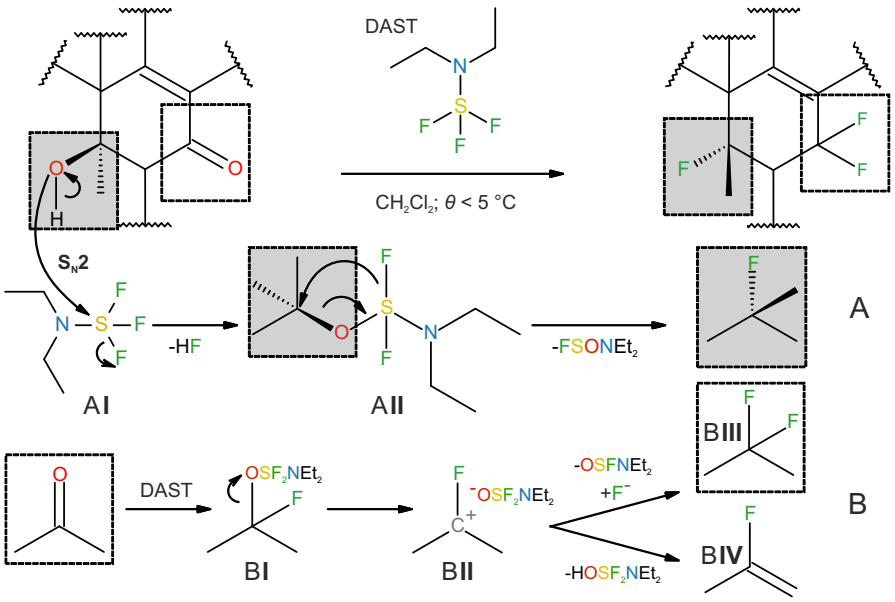

Figure 36: DAST-mediated fluorination; see text for details.

is deduced from ^{19}F NMR spectroscopy.[234] However, as can be inferred from elimination and rearrangement reactions observed, the latter, e.g., for borneol, carbenium ions might appear as intermediates and a more S_N1-like reaction process may occur.[233] The carbonyl replacement under DAST conditions has been proposed to start with hydrofluoric acid-catalyzed generation of the α-fluoro alcohol intermediate **BI**. The subsequent transfer of a further fluoride ion can take place as S_N2-controlled or - as shown in Scheme 36 - as S_N1 process, eventually affording the difluoro compound **BIII**. Again, the presence of carbenium ions can lead to rearrangement and elimination reactions, resulting in vinyl fluorides **BIV**, however, solvent effects are also decisive here.[234]

We designed the DAST-mediated fluorination of RayND to utilize acid-treated RayND as a precursor for borane-tetrahydrofuran ($BH_3 \cdot THF$)-assisted reductive hydroxylation in anticipation of obtaining a predominant C−OH surface coverage that would then be used in the fluorination reaction. Employing $BH_3 \cdot THF$ as reduction agent for oxygen-containing functional groups, is a widely used method in organic chemistry.[235] Furthermore, this protocol has also been successfully applied to ND - both studies reported a decrease of the intensity of the carbonyl IR band in wake of the reaction.[225,236] Yet, our observations are somewhat different (see Chap. 4.6.2). Fig. 37 depicts the corresponding IR spectra. The acid-treated ND precursor material shows, as expected, a C=O vibration band

at $\tilde{\nu} = 1764\,\mathrm{cm}^{-1}$. After the reduction was carried out, a feature-rich spectrum is visible which, however, is dominated by an IR band at $\tilde{\nu} = 1730\,\mathrm{cm}^{-1}$, but also shows signals in the area of the alkyl-C−H ($\tilde{\nu} \approx 2857 - 2960\,\mathrm{cm}^{-1}$) and C−OC/H ($\tilde{\nu} = 1018 - 1261\,\mathrm{cm}^{-1}$) stretching vibrations. We interpret these findings as follows. At first it can be held that a partial reduction has taken place. The alkyl-proton as well as the ether-/ alcohol-related IR bands are to be understood very well according to the transformation: C=O ⟶ H-C-OH. The unexpected carbonyl band of nominally reductively hydroxylated RayND shows a downward shift in energy compared to the starting material. Possible assignments are in particular carboxylic acid esters, unstrained cyclic lactones, and ketones.[224] The justification for their appearance is somewhat puzzeling against the background of the smooth transformation in Ref. [225, 236]. However, it is known that there are decisive differences between different carbonyl functionalities regarding the reactivity against $BH_3\cdot$THF according to the following order: carboxylic acid > aldehyde > ketone > alkene > ester ≈ lactone.[235,240,241] Hence, the reduction would rather have taken place at the first representatives of this hierarchy, while at the same time carbonyl group homogenization had taken place to the advantage of carboxylic acid esters and lactones. Additionally, it should be emphasized, that $BH_3\cdot$THF can serve not solely as an O- but also as a C-reducing agent in the meaning of the reaction −HC=CH− + BH_3 ⟶ $-H_2C-C(BH_2)H$, the so-called Brown hydroboration.[242] Without discussing the full scope of this preparative technique, prominent in particular for obtaining alcohols from alkenes under basic oxidative conditions, it should be mentioned here as a competitive reaction, lowering the effective O-reduction agent concentration, especially since we were able to find a signal indicative to boron in the overview XPS spectrum of hydroxylated RayND (see the Chap. 4.6.2). The acid cleavage of the C-B bond, which we conducted by

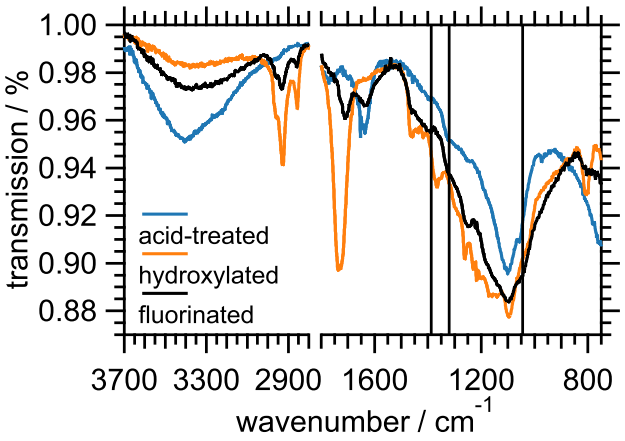

Figure 37: IR spectra of acid-treated (blue), hydroxylated (orange), and fluorinated (black) RayND. Black lines indicate C−F-specific IR absorption bands.[237–239]

the subsequent quenching of the reaction mixture, leads to C-H bonds and therefore does not represent an explanatory argument for the C=O signal.[235] It should also be noted that studies on the ring opening of epoxides, which are commonly known as a widespread motif on the diamond surface, with $BH_3 \cdot THF$ have shown that sterically hindered derivatives react only slightly and with pronounced rearrangement of the molecular structure.[243] This richness of possible surface termination functionalities makes it difficult to give a rigorous reasoning for the incomplete reduction without further experimental investigations.
Despite only partially hydroxylated, there were two motivations why we still considered the obtained RayND material as appropriate for further use in the DAST protocol. First, the high-resolution C 1s XPS spectrum (see Tab. 4) confirms the necessary prerequisites, namely the presence of C−O and C=O functionalities. The also clear amount of sp^2 carbon, the largest value of all investigated samples, we attribute to surface reconstruction following the hydroxylation, which is accompanied by the variety of aforementioned reaction pathways. Especially rearrangement reactions, a phenomenon well known in organic chemistry but less investigated for ND, may be a plausible mechanism for this. Second, DAST fluorination accepts hydroxyl as well as carbonyl groups and both reaction pathways lead to the desired C-F termination.
The concrete implementation of DAST-mediated fluorination was conceived by us on the basis of a report on fluorination of diamondoid fluorides (see Chap. 4.6.2).[238] The inspection of the IR spectrum of the gained RayND material re-

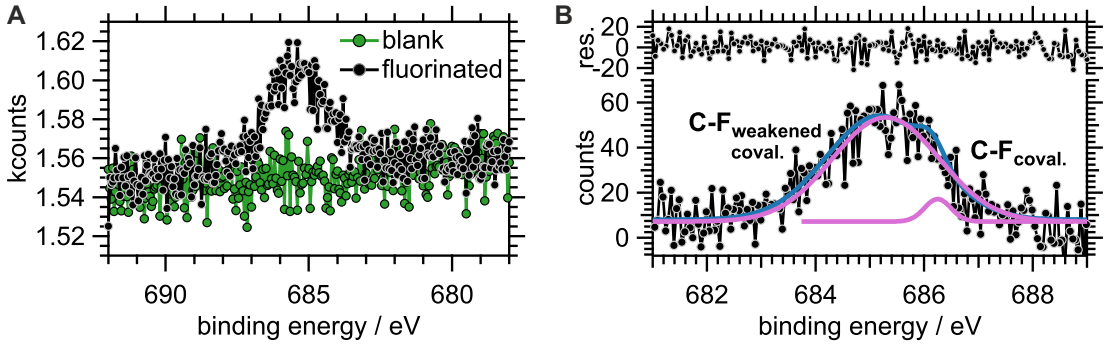

Figure 38: (A) High-resolved F 1s XPS spectrum (black) of fluorinated RayND in comparison to expected blank spectrum (green) of base-treated RayND. **(B)** Deconvolution of high-resolved F 1s XPS spectrum revealing binding energies (BE) of $BE_{\mathrm{C-F_{weakened\,coval.}}} = 685.3(3)\,\mathrm{eV}$ and $BE_{\mathrm{C-F_{coval.}}} = 686.3(3)\,\mathrm{eV}$, while $BE_{\mathrm{C(sp^3)}} = 285.0(3)\,\mathrm{eV}$ was determined.

veals in addition to the signals coined by the hydroxylation reaction in the areas of the C(sp^3)−H ($\tilde{\nu} = 2860 - 2956\,cm^{-1}$) and C=O group ($\tilde{\nu} = 1710\,cm^{-1}$) vibrations, a reduced pronunciation in the area of the ether/ alcohol excitation modes. However, this is precisely where the signals of a possible C-F functionalization are expected, of whose we have found in accordance with the literature: $\tilde{\nu} = 1387\,cm^{-1}$ ((m, $\nu-$ C(sp^3)−F)), $\tilde{\nu} = 1320\,cm^{-1}$ ((sh, $\nu-$ C(sp^3)−F)), and $\tilde{\nu} = 1045\,cm^{-1}$ ((sh, $\nu-$ C(sp^2) −F)).[237–239] In addition, we investigated the fluorinated RayND material using XPS. The corresponding F 1s spectrum is shown in Fig. 38. First, it should be pointed out that it provides a distinct fluorine signal, while the blank sample (base-treated RayND) is silent in this area (Fig. 38**A**). A quantitative evaluation of the associated binding energy (BE) gives 685.3(3) eV and 686.3(3) eV (Fig. 38**B**), when a deconvolution of the signal is performed taking the sp^3 carbon signal at 285.0(3) eV as a reference point (see Chap. 4.6.3). We want to take a closer look at these values by comparing them with available literature data. The report most comparable to our approach also deals with the fluorination of ND by a wet-chemical method. However, it is designed for carboxylic surface functionalities whose Ag^{2+} salts are decarboxylated in a catalytic cycle under the formation of a carbon radical and in which F−TEDA$^+$$BF_4^-$ acts both as a fluorine transfer agent and as a redox catalyst.[244] According to this procedure a successful fluorination of ND could be accomplished and the corresponding F 1s XPS spectrum led to a binding energy of 687.3 eV, thus, a significant offset has to be stated in comparison with our findings. Values from other reports referring to the fluorination of diamond can be divided into two categories. The values for ND were found at higher binding energies, viz. 686.6 eV and 689.2 eV in Ref. [245] and 687.5 eV in Ref. [246]. With reference to the literature on graphite fluorides, in particular, these values are regarded as proof of a covalent C−F bond.[247–250] However, if we consult the literature on the fluorination of bulk diamonds, we find lower values for the binding energy in comparison, namely 685 eV, 685.5 eV, 685.1(1) eV and 685.8 eV,[251–254] which correspond to our values. An exception is given in Ref. [255] with 687 eV. Yet, the very nature of the C−F bond is only little discussed in most of the previous reports. Merely Ref. [251], wherein a SF_6 plasma was used, deduced fluorine doping of the uppermost 15 to 20 atomic layers forming C−F chains, which interpretation could be substantiated because of subsequent acid treatment. Thereby, the F 1s signal was reduced as well as shifted upwards in energy (287.2 eV), a clear indication of a change of the chemical environment. However, if we relate again to the literature on graphitic fluorides, we find values in this binding energy regime for fluorine-deficient phases (e.g., C_4F).[248–250] In-

terestingly, the exact type of the carbon-fluorine binding was long under debate in this field.[256] Recently, models have been established which, in accordance with experimental studies, assume a weakened covalence due to hyperconjugation.[257] This leads to a delocalization of the electrons constituting the C-F bond across the neighboring carbon p_z orbitals. This concept enables to embed tetrahedral ($C(sp^3)-F$) bonds into the sp^2 bonding pattern of the surrounding graphite layer. If we follow this approach, it means that employing DAST-mediated fluorination, we decorate the sp^2-carbon areas previously created by hydroxylation locally with fluorine. The outcome of the C 1s XPS spectrum, which shows a significant decrease of the corresponding signal, is in agreement with this (Tab. 4).

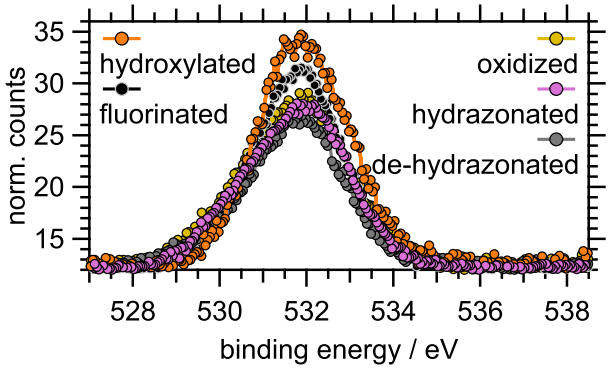

Figure 39: High-resolved O 1s XPS spectra of selected functionalization protocols applied on RayND. Normalization was performed by means of the corresponding C 1s signal surface area.

According to the mechanism in Fig. 36, DAST-mediated fluorination is also expected to reduce surface bonded oxygen. Whether this actually took place can not be decided on the basis of the C 1s XPS data due to the large uncertainties of the values. However, in Fig. 39 for the O 1s signals normalized to the surface area of the corresponding C 1s signals a decrease in transition from the hydroxylated to the fluorinated RayND is observable. Nevertheless, we leave it at this qualitative evaluation, since a quantitative statement is hardly possible due to surface-adsorbed water (cf. the IR spectra). The finding of the reduced O 1s signal can also be explained by the fact that the fluorinated surface is more hydrophobic and therefore binds less water. In summary, however, we can state that we were able to achieve successful wet-chemical fluorination using the DAST protocol.

4.2.3 Bamford-Stevens reaction

The last functionalization approach we want to present is the Bamford-Stevens olefination, for which the mechanism of the reaction under protic conditions is illustrated in Fig. 40 depicting as special case the chemical substances used by us.[258,259] The first reaction step includes the nucleophilic attack of the *p*-

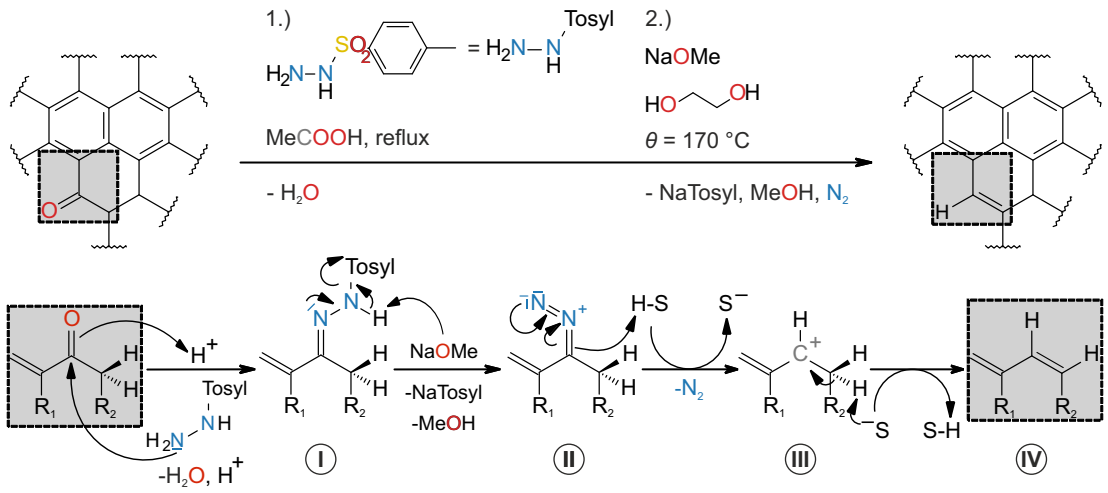

Figure 40: Bamford-Stevens olefination under protic conditions.

toluenesulfonyl hydrazide-NH_2 group at the carbonyl carbon which after de-hydration leads to the stable hydrazone 40**I**. The hydrazone intermediate is N−H-deprotonated through base catalysis (NaOMe) and transformed into a diazoalkane 40**II** by elimination of the *p*-toluenesulfinate anion ($Tosyl^-$). The H-donor capability of protic solvents (S-H: $HOCH_2CH_2OH$) allows the decomposition of nitrogen at elevated temperature, leading to a carbocation 40**III** which stabilizes to an alkene by deprotonation 40**IV**. Variations of the reaction design include the utilization of aprotic solvents or alkyllithium reagents (Shapiro reaction), thereby changing the regioselectivity of the chemical transformation and allowing for a wide range of ketone and aldehyde substrates to be reduced.[260] We contrived a three-step reaction protocol: oxidation using $K_2Cr_2O_7$, hydrazonation with *p*-toluenesulfonyl hydrazide, which we were especially interested in due to the formed −C=N− moiety, and de-hydrazonation using ethylene glycol as protic solvent and applying elevated temperature (see the SI.S2 for experimental details).

The $K_2Cr_2O_7$-mediated oxidation proceeded as expected as can be infered from the IR spectrum (Fig. 41). A broad C=O IR signal centered at $\tilde{\nu} = 1785\,\mathrm{cm}^{-1}$ indicates carboxylic anhydrides, carboxylic acids and strained lactones, where the condensed or dehydrated systems may have been caused by the presence of sulfuric acid.

The subsequent hydrazonation could also be successfully confirmed by IR spectroscopy, insofar as narrow bands not otherwise observable occurred (Fig. 41). We identified them as molecular-like vibration modes since they are not broadened as it is typically the case for the surface-related signals, however, a detailed discussion

on this topic is presented in the SI.S2. Eventually, the thermal decomposition of the hydrazone, i.e. the de-hydrazonation, is cleary visible in the IR spectrum which mimics the one of pristine RayND, somehow (Fig. 41). To put this in concrete terms: Both spectra show a signal for alkyl groups $\tilde{\nu}_{\mathrm{HC(sp^3)-H,pristine}} = 2932\,\mathrm{cm}^{-1}$ vs. $\tilde{\nu}_{\mathrm{HC(sp^3)-H,de\text{-}hydrazon.}} = 2941\,\mathrm{cm}^{-1}$, the C=O vibration is comparable and located at the lower limit of the carbonyl range $\tilde{\nu}_{\mathrm{C=O,pristine}} = 1718\,\mathrm{cm}^{-1}, 1733\,\mathrm{cm}^{-1}$ vs. $\tilde{\nu}_{\mathrm{C=O,de\text{-}hydrazon.}} = 1740\,\mathrm{cm}^{-1}$, and the ether/ alcohol area reveals little pronunciation. Inspection of the C 1s XPS data can confirm this conclusion. Tab. 4 clarifies that except for carbonyl group termination both RayND materials surpass the other samples with respect to the $C(sp^3)$ signal and possess the lowest contribution of sp^2 carbon and sp^3 oxygen. Regarding the C=O surface load, the Bamford-Stevens protocol can additionally suppress it, so that it is reasonable to refer to it as wet-chemical H-termination approach.

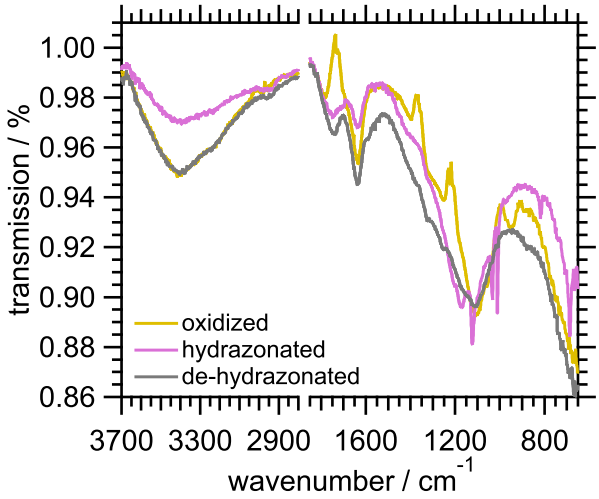

Figure 41: IR spectra of oxidized (yellow), hydrazonated (magenta), and de-hydrazonated (gray) RayND.

Since in the course of the Bamford-Stevens protocol nitrogen is deliberately supplied to and detached from the RayND material, the high-resolved N 1s XPS spectrum should epitomize a good indicator of the chemical transformations done. Fig. 42 depicts a comparison of the spectra obtained for the RayND products after each reaction step. It can be seen that at least two signals at $BE \approx 399\,\mathrm{eV}$ and $BE \approx 402\,\mathrm{eV}$ are present and that their intensity qualitatively renders the nitrogen surface load expected for the particular reaction. We tried to receive a more quantitative result by normalizing the signals by using the surface area of the corresponding C 1s signals as weight. Yet, because of varying linewidths the differences between the signal amplitudes at $BE \approx 399\,\mathrm{eV}$ were too meager to get clear findings.

Therefore, we decided to deconvolve the signals in order to obtain reliable quantities for the binding energy and surface area values. The outcome of this procedure is shown in Fig. 43**A-C**, where the main components at 398.9 eV and 402.2 eV are depicted; hydrazonated RayND reveals an additional signal at 400.4 eV. First,

we discuss the obtained binding energies and corresponding assignments. The attribution of the main components was discussed controversially and we briefly present the possible interpretations. On carbon nitride compounds, the peak at $BE = 398.9\,\text{eV}$ was associated with C−N bond motifs of low coordination number.[261,262] This means that nitrogen is either sp or sp^2 hybridized as well as at least one of the neighboring atoms, which can be carbon or nitrogen. The value was also found on nitrogen-terminated diamond surfaces, and was associated with C≡N, C=N binding patterns and amine functionalities.[263] Additionally, on aziridine-functionalized multiwalled carbon nanotubes the signal was clearly attributed to the aziridine environment.[264] The chemical correspondence to the 402.2 eV signal was seen on carbon nitride systems in quaternary nitrogen, i.e. ammonium and tetraalkyl-ammonium groups.[262] On the other hand, N-O units have also been argued by authors who investigated nitrogen doped diamond-like carbon films.[265] In Ref. [263], the peak is identified with inelastic scattering processes, which are associated with an interband transition loss of the N 1s main signal at 400.0 eV constituting a minor contribution to our findings. At least, the signal we obtained for hydrazonated RayND at 400.4 eV can be identified as sp^2 hybridized nitrogen with three neighbors,[261] sp^2 carbon layer substituting nitrogen,[262] and carbamate moieties (−N−COO−).[264] The summary of these various assignments prompted us to make the following assumptions: 1. The signal at 402.2 eV is not affected by our functionalization protocols, since under their conditions quaternary or O-bound nitrogen is chemically relatively stable. 2. The signals at 398.9 eV and 400.4 eV indicate changes in the chemical surface binding motifs, as they represent hydrazone, imine, nitrile, and possibly amine groups. This implies for a quantitative evaluation that the area of the total N 1s XPS signal is composed of a constant ($BE = 402.2\,\text{eV}$) and a variable part ($BE = 398.9\,\text{eV}$ for oxidized and de-hydrazonated and $BE = 398.9\,\text{eV} + 400.4\,\text{eV}$ for hydrazonated RayND).

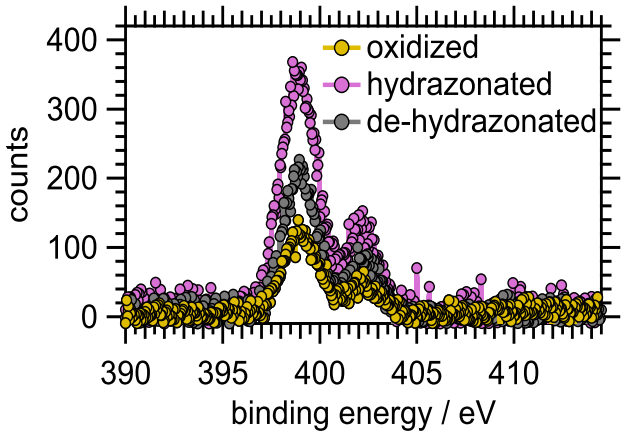

Figure 42: High-resolved N 1s XPS spectra of RayND products of the Bamford-Stevens protocol.

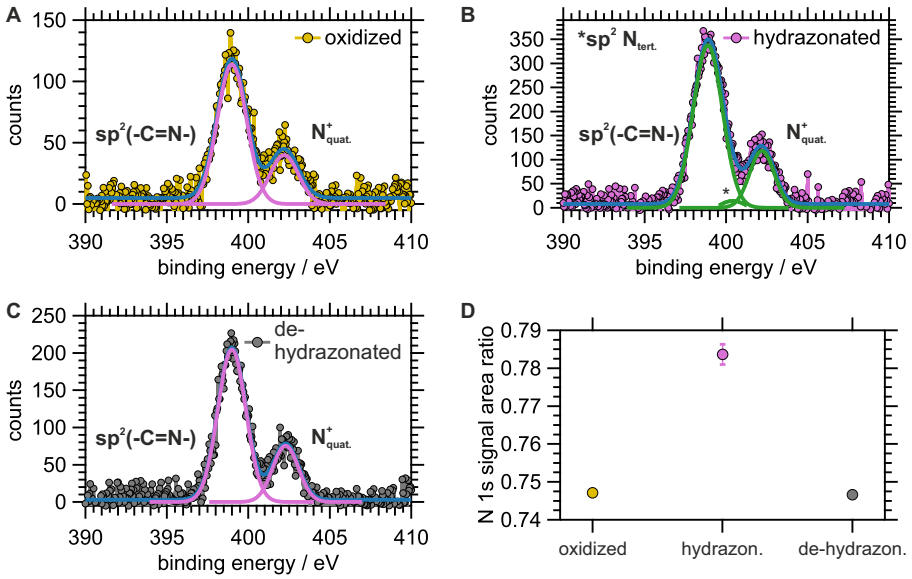

Figure 43: Deconvolution of the N 1s XPS spectra of (A) $K_2Cr_2O_7$-oxidized, (B) hydrazonated, and (C) de-hydrazonated RayND. (D) Ratio of the 398.9 eV ((A) & (C)) or 398.9 eV + 400.4 eV signal surface area (B) compared to the total N 1s signal surface area.

Accordingly, we evaluated the data and the result is shown in Fig. 43**D**. It can be seen that the relative amount of the functionalization-relevant signal is significantly higher for hydrazonated RayND according to the expectations. Taking the high-resolution O 1s XPS signals normalized to the area of the C 1s signal as a soft indicator, we can state with Fig. 39 that the signal is largest for oxidized RayND, decreases for hydrazonated and reaches the lowest intensity for hydrogen termination. These findings are plausible when considering the influence of both the amount of oxygen decoration of the surface and its hydrophilicity together. The former is highest for the oxidized RayND, the hydrazonation protocol reduces C-O binding motifs, but is still hydrophilic. On the other hand, RayND of the last step of the Bamford-Stevens olefination protocol has the lowest proportion of oxygen termination and is also hydrophobic.
In sum, we can say that by IR and X-ray photoelectron spectroscopy we were able to characterize the first implementation of Bamford-Stevens olefination on ND sufficiently with regard to its individual intermediate stages. The results are consistent and offer promising nanodiamond surface termination, especially with the hydrazone intermediate.

4.3 Results of EPR spectroscopy

After presenting the three functionalization approaches, we now focus on the radical species content each of the corresponding intermediates possess. Thereby, electron paramagnetic resonance (EPR) spectroscopy is the natural means of choice for bulk investigations. For this purpose, we prepared samples with mass m_{RayND} given in Tab. 5. Fig. 44 shows the obtained double-integrated EPR spectra which are normalized to unity mass in mg. All of them are centered around $g = 2.0028(2)$, which is in good agreement with literature.[266–269] Based on the signal of pristine RayND, it can be seen that three methods, namely oxidation using $K_2Cr_2O_7$, oxidizing acid treatment, and reductive hydroxylation lead to an increase in the signal surface area, while H-termination by de-hydrazonation, base treatment, hydrazonation and fluorination reduce it. However, it is known from thorough studies on DND material that the EPR signal at $g \approx 2.0028(2)$ is caused by two species differing in their physical environment.[245,268,270–272] One is constituted by lattice impurities residing in the diamond core which were identified as P1 center due to its hyperfine coupling pattern.[269] The second is related to carbon-inherent radicals which stem from dangling bonds. Their exact location is somewhat under debate, with particular arguments being put forward for their embedding in the uppermost (graphitic) surface layers or a location between C (sp^3) diamond core and partially C (sp^2) reconstructed surface layers.[272] Nevertheless, only the second spin species is accessible to our functionalization protocols, while

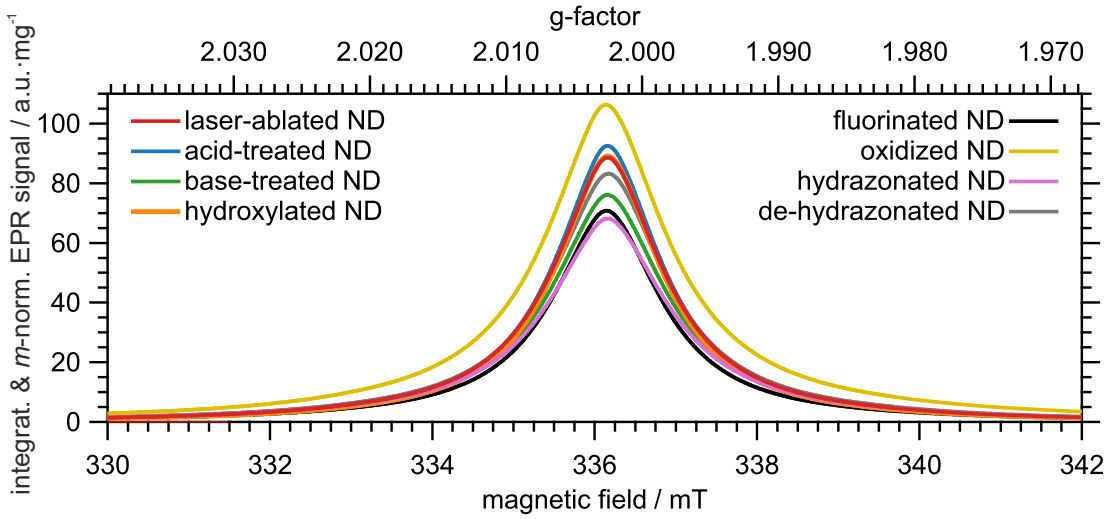

Figure 44: Double-integrated EPR signals (normalized per unit weight) of given functionalization protocols conducted on RayND.

Table 5: Parameters, viz., lorentzian linewidth $lw_{\mathrm{lor,db}}$, strain Hamiltonian $H_{\mathrm{str.,db}}$, and weight w_{db}, obtained from the two-spin model fit (see Chap. 4.6.4) to EPR signals of the listed RayND protocols and calculation of the dangling bond spin density $\rho_{\mathrm{sp,db}}$ by means of the surface area below the integrated total spin EPR signal A_{EPR} (see Fig. 45) and the probed RayND mass m_{RayND} whose error is ± 0.3 mg.

protocol	A_{EPR} a.u.	m_{ND} mg	$lw_{\mathrm{lor,db}}$ mT	$H_{\mathrm{str.,db}}$ MHz	w_{db} %	$\rho_{\mathrm{sp,db}}$ mg^{-1}
RayND	$2.13(6) \times 10^{17}$	11.0	1.01	0.01	96.6	$1.86(2) \times 10^{16}$
RayND SAS	$2.29(7) \times 10^{17}$	12.1	0.99	0.09	96.6	$1.77(2) \times 10^{16}$
acid-treated	$2.20(7) \times 10^{17}$	11.2	0.95	7.73	96.1	$1.89(2) \times 10^{16}$
base-treated	$1.91(6) \times 10^{17}$	11.1	1.03	0.17	97.7	$1.69(2) \times 10^{16}$
hydroxyl.	$2.09(6) \times 10^{17}$	11.3	0.94	7.78	96.0	$1.78(2) \times 10^{16}$
fluorinated	$1.06(3) \times 10^{17}$	5.9	0.97	5.03	97.1	$1.51(3) \times 10^{16}$
oxidized	$1.70(5) \times 10^{17}$	6.3	1.10	0.05	97.2	$2.68(5) \times 10^{16}$
hydrazon.	$1.06(4) \times 10^{17}$	8.4	1.07	0.17	97.2	$1.62(2) \times 10^{16}$
de-hydrazon.	$9.14(27) \times 10^{16}$	4.9	1.03	0.01	97.5	$1.82(4) \times 10^{16}$

the diamond core-dependent P1 centers should be stable across chemical processes. Finally, in order to be able to link the results presented here with the extensive research catalogue compiled at DND, we compared our starting material of laser-ablated RayND with common detonation DND (see Chap. 4.6.2) and found that the mass spin density for both materials is comparable and the slight deviation is within the scope of the literature.[187]

To be able to separate the dangling bond contribution from the one of the P1 centers, we fitted our EPR data with a two-spin model using the EasySpin software package (see Chap. 4.6.4).[163] For the P1 signal a g-factor of $g_{\mathrm{P1}} = 2.0028(2)$, lorentzian linewidth of $lw_{\mathrm{lor,P1}} = 0.35(5)$ mT and strained Hamiltonian parameter with value $H_{\mathrm{str.,P1}} = 0.095(30)$ MHz taking anisotropic hyperfine interactions into account was fixed, while the regression parameters of the dangling bond (db) signal were let unrestricted. Accordingly, we obtained the values for $lw_{\mathrm{lor,db}}$ and $H_{\mathrm{str.,db}}$ given in Tab. 5 (Note that the g-factors of the P1 and db spectrum deviated by a maximum of ± 0.0001 for each sample. Therefore, they are not listed here, but given in Chap. 4.6.4). Additionally, we received from the fit the proportion that both spectra had of the total EPR signal; in Tab. 5 they are noted as w_{db}. Multiplying these weights by the double-integrated EPR sig-

nal A_{EPR}, which was normalized to m_{RayND}, we were able to calculate the surface spin mass density, which is given as $\rho_{\mathrm{sp,db}}$ in Tab. 5. The results are depicted in Figure 45 as bar chart. Before we examine the results of the wet-chemical functionalization protocols presented above, we first want to determine a comparative value resulting from the self-assisted ultrasonication deaggregation (SAUD) procedure.[188,273] It is often evoked that ND undergoes severe aggregation, reasons for which have been explained by condensation reactions, size-dependent effects and surface potentials.[188,206,274] Various procedures to remedy this shortcoming have been developed (see Ref. [188] for an overview), whereby the SAUD process used here is appealing due to its simplicity and absence of residues. It is a common strategy in several branches of chemistry to kinetically stabilize radical species by steric hindrance;[275] ND agglomerates are a natural realization of this principle, so breaking up the ND clusters and increasing the chemically accessible surface area seems to be a primary method of reducing surface-related spin density. Our results show that this is indeed the case (see SI.S2), because, as can be seen from Table 5 and Figure 45, the dangling bond spin density decreases by 5(1) %. Thus, we discuss in the following the different protocols with respect to this SAUD-threshold. The best result we achieved by DAST-mediated fluorination yielded a relative reduction of 15(2) %, followed by the hydrazonation step of the Bamford-Stevens protocol with 9(1) %. The base treatment resulted in 5(1) % relative reduction. Hydroxylation and the de-hydrazonation step reveal comparable results within 3σ uncertainties, while oxidization either by acid-treatment or $K_2Cr_2O_7$-assisted reveals an increase of 7(3) % and 51(4) %, respectively.
Remarkably, with exception of the base treatment, the oxygen-termination pro-

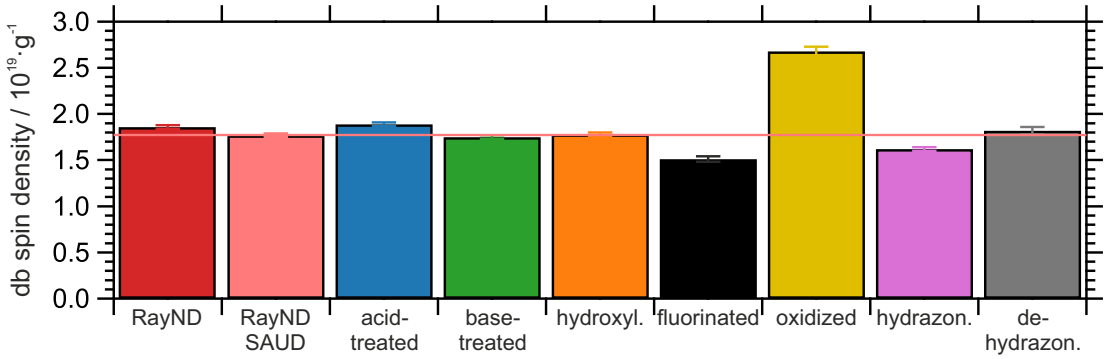

Figure 45: Bar chart of dangling bond spin density (normalized per unit weight) for the protocols listed. The coral-colored line represents deagglomeration (SAUD) threshold.

tocols all show increased surface radical load. Theoretical investigations in Ref. [218] comparing different surface terminations have revealed that main/ full coverage with −OH, −COOH, dense C−O−C, and C=O functionalities induce either surface image states or deep-level acceptor states. While concentrating on ionization processes and proposing different mechanisms for their appearance, the explanations given can heuristically also be adopted to radical species generation, when corresponding surface-related traps near NV^- excited states are assumed. Taking the reductive hydroxylation, it is according to our experimental findings additionally accompanied by significant generation of sp^2 carbon which may provide such surface defect states.[222]

The H-termination accomplished by the de-hydrazonation step of the Bamford-Stevens protocol has not led to a reduction in surface spin density. Thus, it must be concluded that the expectation the reaction may yield a low-radical but hydrogen functionalized surface due to the beforehand correspondingly prepared hydrazone-decoration has not fulfilled. Whether a less demanding reaction control, such as thermally induced de-nitrogenation, for example by using the Shapiro protocol, which takes place at low temperatures and without the formation of a carbenium intermediate, produces a different result, should be tested experimentally.[259]

In order to find explanations for the reduction of $\rho_{\mathrm{sp,db}}$ due to the DAST-mediated fluorination approach, we first rely on Ref. [222] in which experimental and theoretical evidence has been provided that C=C binding motifs cause Fermi level pinning below the NV^- states thus creating surface-related acceptor states even at a coverage as low as 0.003 %. Our spectroscopic analysis of the corresponding RayND products fits well in this argumentation. While the hydroxylated precursor possessed a high surface sp^2 carbon load, the fluorination produced its decline, the C−F binding situation resulted as a weakened covalent interaction intersecting $C(sp^2)$ segments. Carbon-inherent radical species stability on a localized level is commonly discussed according to two prerequisites : sterical hindrance and resonance due to enlarged π bond systems,[276] the latter of which is reduced by our approach. Theoretical investigations usually emphasize that the high Pauling electronegativity of the fluorine atom causes a PEA of the diamond surface or, equivalently, a downward band bending of NV^- center states below the Fermi level, which leads to its charge stabilization.[146,277] Yet, another quantum mechanical computation approach has elucidated that (2×1):F (001) reconstructed surfaces also introduce localized surface states near the conduction band.[218] Future experiments are necessary to scrutinize the different proposed effects. Some concluding remarks: 1. An EPR study on DND fluorinated in the F_2/H_2 gas

stream at elevated temperatures (470 °C) reports a double increase in surface spin density $\rho_{\mathrm{sp,db}}$, presumably due to the harsh reaction conditions.[245] 2. Whereas for acid-treated and hydroxylated RayND we trace back the large values of the strain Hamiltonian $H_{\mathrm{str.,db}}$ (Tab. 5) to either strain or enhanced spin-orbit coupling due to sp^2 hybridization,[222] in case of the fluorination product we assume dipolar interactions caused by the introduced ^{19}F nuclear spin. 3. By changing the surface spin density according to the results presented, we modulate the NV^- center spin-bath as well. Accordingly, we expect a prolongation of the T_2 spin decoherence time due to altering the spectral noise density $S_i(\omega) = 2B_i^2(t)\frac{\tau_c}{1+\omega 2\tau_c^2} = \frac{1}{T_2}$, with $B_i(t)$ as the variance of the i-spatial component of fluctuating spin-bath magnetic field and τ_c as its correlation time, of the spin-bath in two ways: the suppression of high-frequency noise caused by electron-electron coupling $\approx 52\,\mathrm{MHz}$ towards lower frequency noise in the kHz range and the lowering of the quantity of $B_i(t)$ which depends on $\rho_{\mathrm{sp,db}}$.[278] However, the proof of this assumption is left to future experiments.

Turning to the second best result, the hydrazone-functionalized RayND, less literature is available for rationalization of the results. Although studies on substitutional nitrogen termination are available, which also suggest advantageous properties with respect to minimal band gap intrusion, this does not fully reflect our functionalization conditions.[220,221] If we nevertheless refer to Ref. [220] the band structure of (001) (2×1):N/H diamond surface reconstruction is calculated there, whereby the result were obtained that the surface states penetrate only 0.2 eV into the bandgap - correspondingly, a high stabilization of NV^- centers is given. Conversely, potential electron traps which can form radical states are energetically high and thus rarely populated. The surface reconstruction presented in Ref. [220] is locally built from pyrrolidine units. We may have been capable of chemically generating these through the hydrazonation protocol by the nucleophilic attack of the p-toluenesulfonyl hydrazide-NH_2 group at an ubiquitous C−O−C surface motif leading to an O $\longrightarrow$ N exchange. At the molecular level, this would correspond to a chemical reaction of tetrahydrofuran with hydrazine, which is very unlikely. However, due to the increased strain within the cyclic structures of the diamond surface reconstruction, this could be possible, nonetheless. A further explanation for reduction of surface spin density is the formation of aziridine at the expense of oxirane moieties, for which spectroscopic evidence in the high-resolved O 1s XPS spectrum is qualitatively given (see Fig. 39). This process is known as an intermediated in the proposed mechanism of the chemical reduction of graphite oxide using hydrazine hydrate.[279] We assume the aziridine motif to be more stable

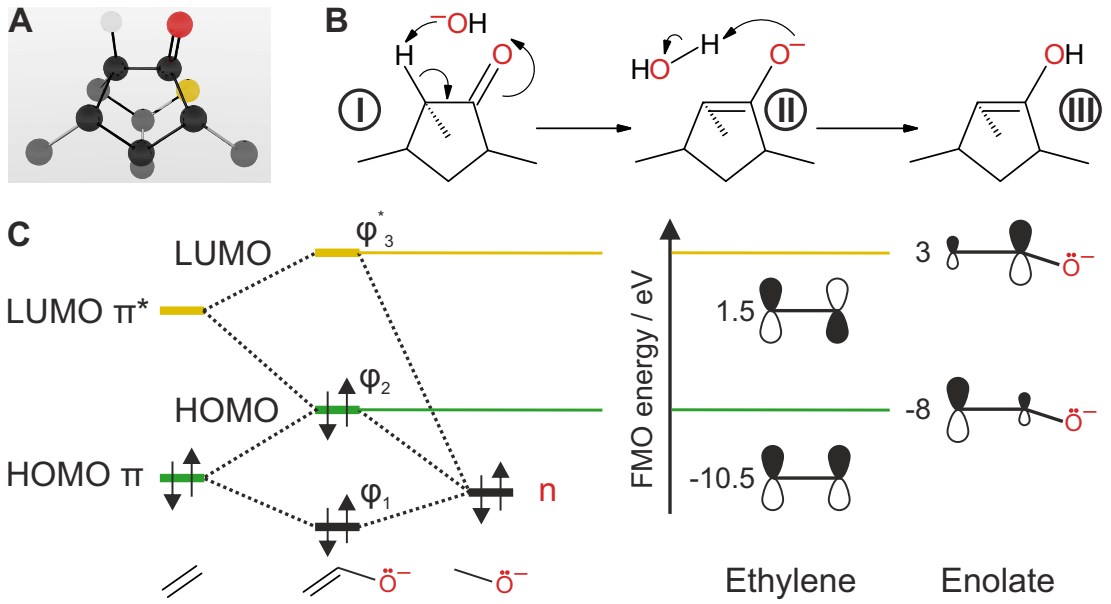

Figure 46: (A) Diamond (100)-surface reconstruction showing hydrogen (white) and carbonyl (red) functionality accompanied by an anionic carbon (yellow). (B) Projection of the black-colored 5-membered carbon ring shown in (A), which undergoes base catalyzed enolate formation (II) and enolization (III). (C) Qualitative frontier molecular orbital (FMO) scheme of the ethylene oxide anion derived from the MOs of its sub-moieties (left). Estimated FMO energies according to Ref. [281] (right).

compared to the oxygen analogue due to decreased electronegativity of the nitrogen atom which, e.g., hampers nucleophilic attack and subsequent ring opening. Since for oxiranes, for that kind of reactions radical-type mechanisms are known, we therefore mask a potential route for electron spin generation.[280]
Concerning the base treatment, which gave only a slight reduction in the dangling bond spin density, the spectroscopic results seem to impede a concise explanation since otherwise as spin generating interpreted features appear in the C 1s XPS spectrum, namely C(sp^2) and C−O motifs. We propose a mechanism that refers to the enolate formation of a carbonyl compound. Fig 46(A) shows a section of the (2x1):O/H surface reconstruction of the (100) diamond surface. (B) shows the corresponding projection on a 5-membered ring chemical structure. The deprotonation of moiety **I** by the hydroxyl ion is described by the equilibrium constant $K = 10^{\mathrm{p}K_{\mathrm{a,I\text{-}H}} - \mathrm{p}K_{\mathrm{a,H-OH}}}$ of the reaction $\mathbf{I}{-}\mathrm{H} + \mathrm{OH}^- \rightleftharpoons \mathbf{I}^- + \mathrm{H}{-}\mathrm{OH}$ and $\mathrm{p}K_\mathrm{a}$ is the acid dissociation constant as a quantitative measure of the strength of an acid, whereby holding true: the stronger the acid the lower its $\mathrm{p}K_\mathrm{a}$. For cyclohexanone

pK_a = 17.8(1.5) is documented;[282] thus, due to enhanced ring strain and attached methyl groups the value should be lower for cyclopentanone derivative **I**; we assume it to equal the value of water. Than we have $K = 1$ and both states **I** and **II** are equally likely. From basic MO theory we adopt the scheme in Fig. 46(C), which represents intermediate **II**. On the left side a qualitative scheme is shown, which elucidates the generation of the MOs of C=C−O^- by linear combination of the MOs of ethylene and of one non-bonding orbital of the σ bonded oxygen anion. On the right side energy estimations according to Ref. [281] are given. The crucial outcome of this simple model is that the energy of the HOMO and LUMO level of the enolate are shifted upwards with respect to unfunctionalized C=C bonds. Since in Ref. [222], which was already mentioned in the discussion of the DAST-protocol, C=C acceptor levels are calculated to be roughly 1 eV below the NV^-/NV^0 band, the estimated rise in the LUMO energy of 1.5 eV for the oxygen-conjugated C=C bond may be sufficient to lessen electron spin trapping and NV^- center oxidization. However, the proposed mechanism solely generates new C=C bonds and does not affect existing ones. To find an explanation here, we hypothesize that base-catalyzed (Favorski rearrangement), thermally induced (Claisen rearrangement) rearrangement reactions or,[260] e.g., thermally allowed [2 + 2] two-step ionic or radical-type cycloadditions provoke C=C binding homogenization towards conjugated systems like Fig. 46**II**,[283] which are stabilized with respect to their total energy. In order to verify the model, which is only heuristically based here, experimental data can be gathered under reaction control using stronger bases, which should lead to a more powerful effect if the equilibrium would then have to lie more on the side of the enolate, and rigorous quantum-chemical calculations can be called in.

4.4 Results of ODMR measurements

To corroborate the results of the bulk EPR measurements on the few-digit ND level, we additionally performed NV^- center-based ODMR experiments. For this, we chose higher-quality milled ND (mND), which we obtained as ultrapure water-based slurry (weight concentration 1 g/L). Due to its one-step design and preparative straightforwardness we singled out the base protocol. EPR monitoring (see Chap. 4.6.6) according to the procedure presented beforehand, revealed $\rho_{sp.,db} = 9.5(9) \times 10^{14}\,mg^{-1}$ for as-received and $\rho_{sp.,db} = 8.0(4) \times 10^{14}\,mg^{-1}$ for base-treated mND material. Thus, on the mg-scale both, RayND and mND, show comparable results regarding dangling bond spin density reduction (see Chap.

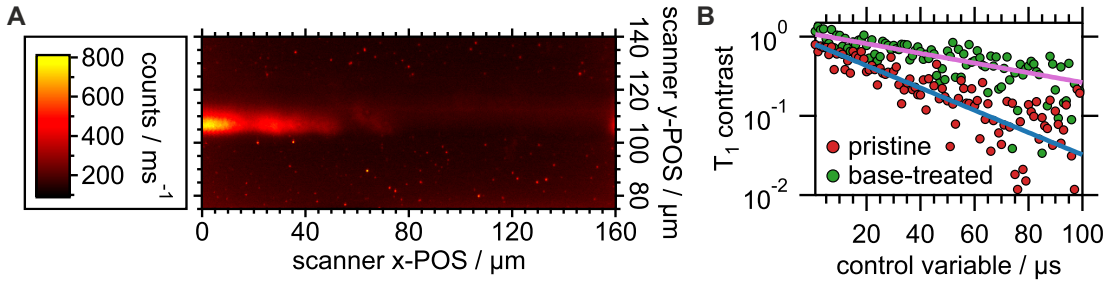

Figure 47: **(A)** Example fluorescence scan of mND prepared sample. The bright line in the middle epitomizes the mw antenna. **(B)** Example T_1 measurement outcome for both, pristine (red) and base-treated (green) mND. The blue and magenta colored line is a mono-exponential fit, respectively. The control variable is a progressing waiting time after polarization of the NV^- center in the $|0\rangle$ state.

4.6.6 for calculation). Sample preparation prior to ODMR investigation included the transfer of mND into *iso*-propanol phase (see Chap. 4.6.6), which allows for a swifter evaporation of the suspension agent. To receive an appropriate mND cluster separation, we additionally diluted the *iso*-propanol-based suspension by a factor of 1 : 1000. Eventually, we drop-casted 3 µl on a NV-silent bulk-diamond substrate for sample preparation.
An example fluorescence scan is depicted in Fig. 47**A**, where well-separated spots, which correspond to mND clusters, in the vicinity of the mw antenna can be seen. We randomly selected nine of those to perform the ODMR experiments. These were designed in such a way that we first recorded Second-order autocorrelation functions that gave us an average amount of NV^- centers per cluster of about 30 (see Chap. 4.6.6) Then, we recorded cw-ODMR spectra and performed spin state rabi oscillation measurements to obtain the microwave pulse lengths necessary for relaxation time measurements (see Chap. 4.6.6). The determination of the longitudinal spin T_1 relaxation time indicating the time constant with which the spin system polarized in an non-equilibrium state relaxes back into the equilibrium, was conducted as a differential protocol (see Chap. 4.6.6). An example outcome of the T_1 measurements on as-received and base-treated mND is depicted in Fig. 47**B**, where clearly can be seen that base-treatment prolongs the longitudinal relaxation time. The statistical evaluation over the nine measurements performed is given in Fig. 48**A**. From this we can deduce that the median of the distribution of T_1 values for as-received mND is 32 µs (25th percentile: 16 µs, 75th percentile: 43 µs) and for base treated 71 µs (25th percentile: 57 µs, 75th percentile: 98 µs).
The evaluation under the assumption of a normal distribution with 1σ uncertainty

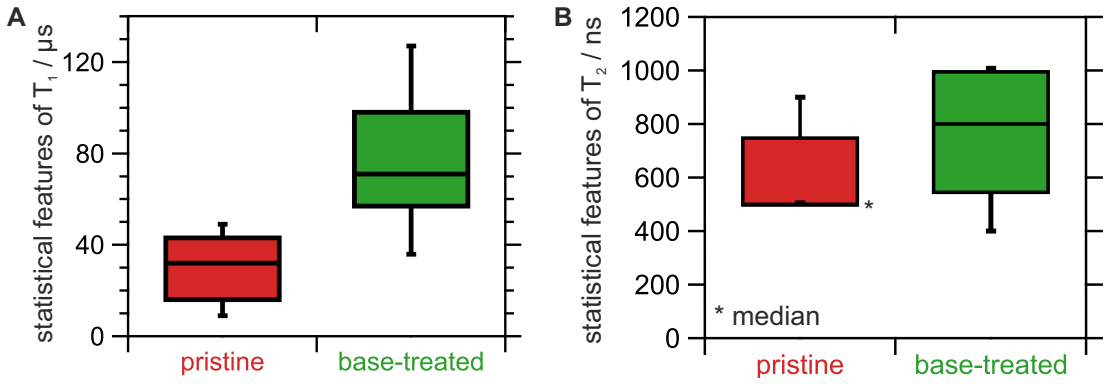

Figure 48: Box plot representation of **(A)** T_1 and **(B)** T_2 measurements on mND; lower and upper whiskers represent 10th and 90th percentile, respectively.

limits yields for pristine mND 30(14) µs and for base-treated 76(28) µs. Within these statistical uncertainties it can be stated that base treatment of mND enhances the T_1 relaxation time approximately by a factor of 2. Although this result is of practical importance, especially since we have selected the one with the lowest surface spin density reduction from the functionalization protocols and the fluorination or hydrazonation suggest an even more significant prolongation of the T_1 relaxation time, we have to state that we can not safely identify the underlying mechanism. Concretely, whether it renders a pure spin-related process due to changing the spin-bath properties, or whether underlying ionization kinetics partially govern the measurement outcome. The discussion hereto is given in the SI.S6.

The Hahn echo related T_2 decoherence time was obtained also using an differential pulse scheme. The corresponding data sets are presented in Chap. 4.6.6, while Fig. 48**B** depicts the evaluated distributions. It can be seen that the base treatment has only a minor influence on this parameter, which is also statistically hardly reliable. However, a plausible explanation for this is that the T_2 decoherence time is limited more by the interaction with mND core-inherent spin sources (such as nuclear spins: ^{14}N, ^{13}C) than with the high-frequency surface electron spin-bath.[278] The median of the T_2 distribution for pristine mND is given by 500 ns and for base-treated by 800 ns, values which are expected from the literature.[284]

4.5 Conclusion

We draw a twofold conclusion from our experimental observations. First, we were able to present two novel functionalization protocols for ND, namely DAST-

mediated fluorination and the Bamford-Stevens olefination. This may be relevant for different research fields, especially since the surface decoration is only partial, except for the de-hydrazonation step, and thus the O-termination preferred in life sciences applications is still present. Our second focus was on whether it is possible to reduce surface spin density using wet-chemical approaches. For this purpose, we examined all protocols including their intermediate stages using EPR spectroscopy. In fact, we were able to identify three reactions that led to a significant reduction even below the deagglomeration threshold given by the SAUD technique, namely DAST-mediated fluorination, hydrazonation and base treatment. We presented first explanations to rationalize the results. For the base treatment protocol, we were able to confirm the results of the bulk EPR studies at the few-digits ND level. The corresponding ODMR measurements revealed a prolongation of the longitudinal T_1 relaxation time after performing this chemical process.
In summary we propose, that more in-depth investigations including the optimization of the protocols presented may help to stabilize NV^- centers in ND and lower surface-related spin-bath contributions, thereby improving the sensing capabilities of ND in future experiments.

4.6 Supplementary

4.6.1 Spectroscopic methods

IR spectroscopy Infrared spectra were recorded on a Bruker Vertex 70 spectrometer equipped with a diamond ATR unit. Internal CO_2 background correction was used. To enhance signal-to-noise ratio, every spectrum is a sum-up of eight measurement runs.
For analysis, the region of $\tilde{\nu} = 1800 - 2800\,\mathrm{cm}^{-1}$ was omitted due to incomplete background correction therein.

XPS measurements were performed by Dr. K. Küpper at the Universitat Osnabruck employing a PHI Versaprobe III spectrometer equipped with a monochromatic Al Kα, micro-focused scanning X-ray source. For the current measurements the X-ray beam size was set to 100 µm. To compensate for charging effects a dual beam charge neutralization method was used. Calibration was performed according to the position of the C1s line. General survey and high-resolution spectra of elements were recorded.

EPR spectroscopy EPR spectra were obtained using a Magnettech Miniscope MS 400 spectrometer, applying the following measurement parameters: mw power $P_{\mathrm{mw}} = 10\,\mu\mathrm{W}$, modulation amplitude $B_{\mathrm{mod}} = 0.01\,\mathrm{mT}$, resolution $0.01\,\mathrm{mT/bin}$, sweep rate $0.13\,\mathrm{mT/s}$.
***g*-factor calibration** was realized by measuring the spectrum of a manganese(II) standard embedded in a zinc sulfide crystal for whose third hyperfine line is known $g_{\mathrm{std,\ 3.\ HF}} = 2.0267(2)$. When additionally recording the microwave frequency of the EPR signal both, for the standard ν_{std} and the sample ν_{pr}, computation of the apparent g-factor scale is accomplished through:

$$g_{\mathrm{pr}} = \nu_{\mathrm{pr}} \cdot g_{\mathrm{std,\ 3.\ HF}} / \nu_{\mathrm{std,\ 3.\ HF}}.$$

Spin counting was enabled by TEMPO calibration. Measuring the EPR signal (measurement conditions: microwave power $P_{\mathrm{mw,std}}$, modulation amplitude $B_{\mathrm{mod,std}}$, temperature T_{std}) of an amount of the TEMPO standard for which the number of spins N_{std} is known and determining the surface area under its EPR absorption curve A_{std}, in addition with its g-factor g_{std}, spin quantum number S_{std}, and multiplicity M_{std}, we obtain the number of spins inside a bulk sample

N_{pr} according to[69]

$$N_{\mathrm{pr}} = \frac{A_{\mathrm{pr}}}{A_{\mathrm{std}}} \cdot \sqrt{\frac{P_{\mathrm{mw,std}}}{P_{\mathrm{mw,pr}}}} \cdot \frac{B_{\mathrm{mod,std}}}{B_{\mathrm{mod,pr}}} \cdot \frac{g_{\mathrm{std}}}{g_{\mathrm{pr}}} \cdot \frac{T_{\mathrm{pr}}}{T_{\mathrm{std}}} \cdot \frac{S_{\mathrm{pr}}\left(S_{\mathrm{pr}}+1\right)}{S_{\mathrm{std}}\left(S_{\mathrm{std}}+1\right)} \cdot \frac{M_{\mathrm{pr}}}{M_{\mathrm{std}}} \cdot N_{\mathrm{std}} \quad (4.1)$$

where the quantities referring to the sample (index "pr") have the same meaning as for the standard. Since the EPR signal is influenced not only by apparent factors but also by intrinsic properties, e.g., saturation effects, unresolved dipolar coupling to nuclei and electrons, a quantitative evaluation must nevertheless be carried out with caution. However, these contributions to the EPR signal are taken into account by fitting the EPR spectra with a two-spin model (see Details on EPR data measurements) which is supported by previous experimental results. For more detailed investigations, in particular, to validate the absolute spin density values given in the main text, it would be advisable to use a ND sample as a reference, whose spin number was determined by complementary methods (e.g., SQUID), yet, a method which was not available to us. The specification of the errors of the quantitative EPR measurements is based on repetitive measurements on TEMPO samples which gave a 3σ standard deviation of 3 %.

ODMR measurements Optically detected magnetic resonance (ODMR) experiments were conducted at room temperature and ambient conditions using a home-built confocal microscopy setup provided with a pulsed microwave generating and applying unit and a permanent magnet. For details see Chap. 2.4.1.

4.6.2 Synthesis protocols and material characterization

All chemicals were purchased from commercial suppliers and used without further purification steps. Solvents were of analytical grade quality and stored under protective atmosphere.

Laser-ablated nanodiamond material (RayND, average grain size: 4.0 – 5.0 nm) was received as powder from Ray Techniques Ltd.
The pre-characterization was performed by IR, XPS and EPR spectroscopy, which yielded the following results.
ATR-FTIR[27] (cf. Fig. 49):[226] $\tilde{\nu}\,(\mathrm{cm}^{-1})$ = 3412 (br, $\nu-$ O−H), 2932 (br, $\nu-$ HC(sp^3)−H), 1733 (s, $\nu-$ C=O), 1718 (s, $\nu-$ C=O), 1647 (s, $\delta-$ O−H of $\mathrm{H_2O_{ads.}}$),

[27] IR assignments include the following prominent nomenclature: (br) broad, (sh) shoulder, (s) strong, (m) medium, (w) weak, (ν) stretching vibration, (δ) bending vibration.

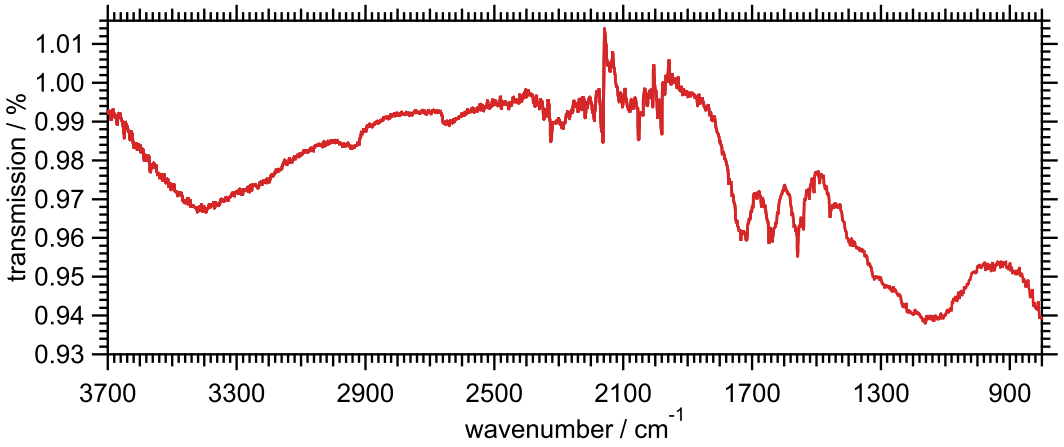

Figure 49: Infrared spectrum of laser-ablated RayND. Except apparatus-internal CO_2 background correction no data processing was carried out. Signals between $\approx 2300 - 1950\,\mathrm{cm}^{-1}$ are measurement artifacts because of incomplete CO_2 compensation.

1637 (s, $\delta-$ O$-$H of $H_2O_{ads.}$), 1559 (s, N defects), 1540 (s, lattice absorption), 1507 (m, lattice absorption), 1457 (sh, $\delta-$ HC(sp^2)$-$H), 1376 (sh, $\delta-$ O$-$H), 1320 (sh, $\delta-$ O$-$H), 1286 (sh, $\nu-$ C(sp^2)$-$OC(sp^3)), 1217 (sh, $\nu-$ C(sp^2) $-$OC(sp^3) / HOC(sp^2)$-$H), 1162 (w, $\nu-$ C(sp^3)$-$OC(sp^3) / HOC(sp^2)$-$H), 1137 ($\delta-$ C(sp^3) $-$H).

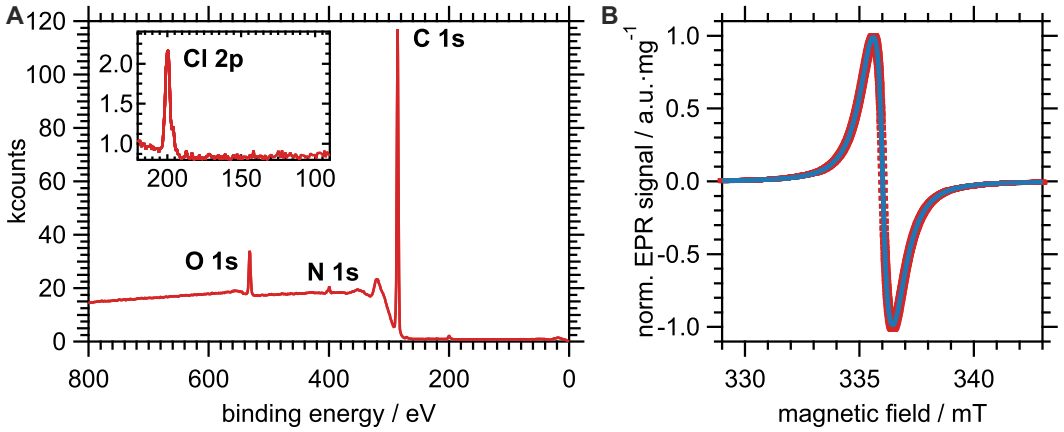

Figure 50: **(A)** Overview XPS spectrum of pristine RayND. All relevant signals are displayed and assigned. **(B)** EPR spectrum of pristine RayND (red). The blue line corresponds to the two-spin model fit revealing the values: $g_{P1} = 2.0028$, $lw_{lor,P1} = 0.38\,\mathrm{mT}$, $H_{str.,P1} = 0.01\,\mathrm{MHz}$, $w_{P1} = 0.75$; $g_{db} = 2.0028$, $lw_{lor,db} = 0.01\,\mathrm{mT}$, $H_{str.,db} = 0.01\,\mathrm{MHz}$, $w_{db} = 18$ (cf. Chap. 4.6.4 for details).

Overview XPS data of pristine laser-ablated RayND shows signals of carbon, oxygen, nitrogen and chlorine, the latter presumably being caused by the purification process of the provider. The parameters of the deconvoluted EPR signal are given in Fig. 50.

Milled nanodiamond material (NDNV40nmLw10ml, average size: $35-40\,\mathrm{nm}$) was obtained as slurry (mass concentration: $1\,\mathrm{mg\,mL^{-1}}$) in DI water from Adámas Nanotechnologies, Inc. Due to the low material availability, only EPR characterization was performed. The data are presented below (see Chap. 4.6.6).

General neutralization, purification, and drying procedure (0)
Upon completion of the particular reaction, the reaction mixture was cooled to r.t. Then, the suspension was centrifuged, the supernatant discarded, and Milli-Q water added. Thereafter, the residuum was slurried by means of an ultrasonic bath. This procedure was repeated until the supernatant exhibited a pH value of 7. Subsequently, the neutralized suspension was evaporated to dryness by means of a rotary evaporator and kept under vacuum for approximately 2 hours ($p \leq 13\,\mathrm{mbar}$). Eventually, the solid was dried in a drying oven at 150 °C for at least 12 hours.

Oxidizing acid treatment of RayND (1)
1.000 g RayND was poured into 30 mL of a 1 : 1 : 1 (volume ratio) mixture of $HClO_4$ (70%), HNO_3 (64-66%), and H_2SO_4 (96%), refluxed for 6 hours and, purified according to 4.6.2.**(0)**. Yield: 93 %.

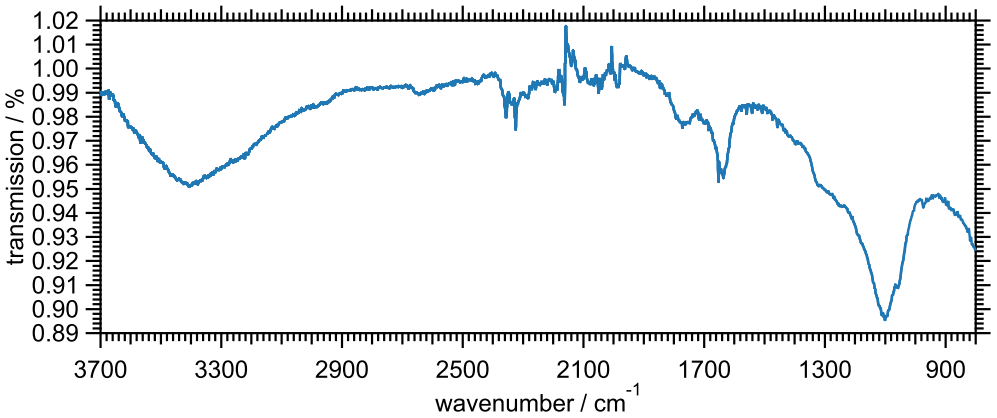

Figure 51: Infrared spectrum of acid-treated RayND. Except apparatus-internal CO_2 background correction no data processing was carried out. Signals between $\approx 2300-1950\,\mathrm{cm^{-1}}$ are measurement artifacts due to incomplete CO_2 compensation.

ATR-FTIR (cf. Fig. 51):[226] $\tilde{\nu}\,(\mathrm{cm}^{-1}) = 3405$ (br, $\nu-$ O−H), 1764 (s, $\nu-$ C=O), 1635 (s, $\delta-$ O−H of $H_2O_{ads.}$), 1559 (w, N defects), 1541 (w, lattice absorption), 1457 (sh, $\delta-$ HC(sp^2)−H), 1323 (sh, $\delta-$ O−H), 1245 (sh, $\nu-$ C(sp^2)−OC(sp^3) / HOC(sp^2)−H), 1101 (br, $\delta-$ C(sp^3)−H), 1057 (sh, $\nu-$ C(sp^2)−Cl), 957 (w, $\delta-$ H−C(sp^2)−C(sp^2)−H).
No XPS data are available for acid-treated RayND. The EPR signal deconvolution is presented in Chap. 4.6.4, Fig. 66.

Base treatment of RayND (2)
0.150 g of RayND was added to 20 mL of 2 M NaOH. The suspension was refluxed for 6 hours and purified according to 4.6.2.**(0)**. Yield: 92 %.
ATR-FTIR (cf. Fig. 52):[226] $\tilde{\nu}\,(\mathrm{cm}^{-1}) = 3407$ (br, $\nu-$ O−H), 1771 (s, $\nu-$ C=O), 1638 (s, $\delta-$ O−H of $H_2O_{ads.}$), 1559 (w, N defects), 1540 (w, lattice absorption), 1457 (sh, $\delta-$ HC(sp^2)−H), 1388 (sh, $\delta-$ O−H), 1323 (sh, $\delta-$ O−H), 1255 (m, $\nu-$ C(sp^2)−OC(sp^3) / HOC(sp^2)−H), 1222 (sh, $\nu-$ C(sp^2)−OC(sp^3) / HOC(sp^2)−H), 1119 (br, $\delta-$ C(sp^3)−H).

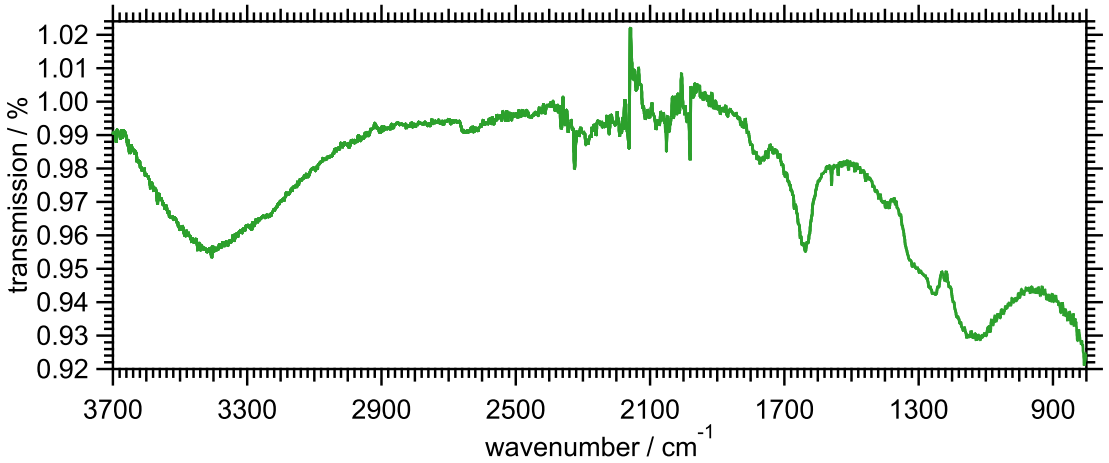

Figure 52: Infrared spectrum of base-treated RayND. Except apparatus-internal CO_2 background correction no data processing was carried out. Signals between $\approx 2300 - 1950\,\mathrm{cm}^{-1}$ are measurement artifacts because of incomplete CO_2 compensation.

The overview XPS data of the base-treated RayND shows an additional signal indicative of silicon. This may be due to the harsh basic conditions during refluxing, which may cause silicon oxide to dissolve in the form of anions (e.g., $[SiO(OH)_3]^-$) and, eventually, precipitate onto RayND. The parameters of the deconvoluted EPR signal are given in Fig. 53.

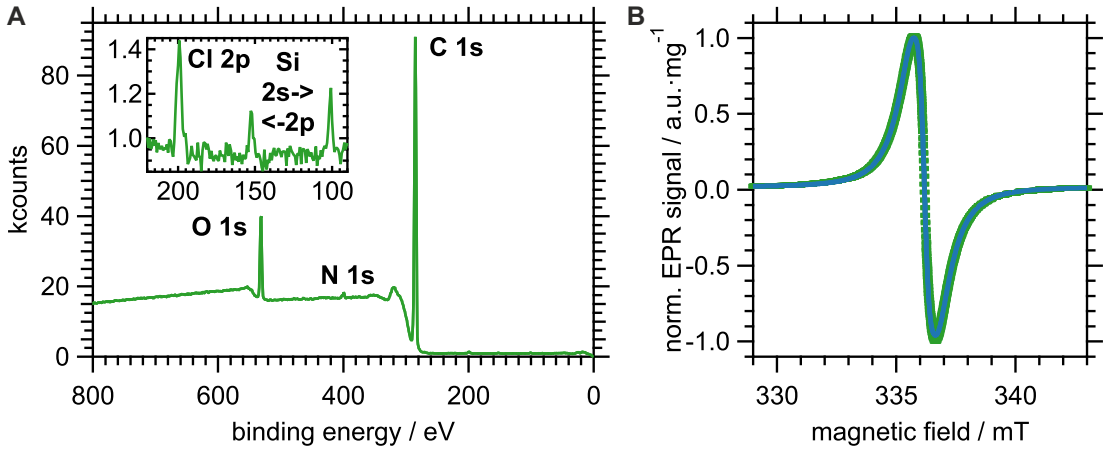

Figure 53: **(A)** Overview XPS spectrum of base-treated RayND. All relevant signals are displayed and assigned. **(B)** EPR spectrum of base-treated RayND (green). The blue line corresponds to the two-spin model fit revealing the following values: $g_{P1} = 2.0026$, $lw_{lor,P1} = 0.32\,mT$, $H_{str.,P1} = 1.7\,MHz$, $w_{P1} = 0.17$; $g_{db} = 2.0026$, $lw_{lor,db} = 1.03\,mT$, $H_{str.,db} = 0.17\,MHz$, $w_{db} = 7.3$ (cf. Chap. 4.6.4 for details).

Reductive hydroxylation of RayND (3)

Reductive hydroxylation of acid-treated RayND was performed under modified conditions of literature procedure.[236] 0.500 g of **(1)** was taken up in 40 mL THF

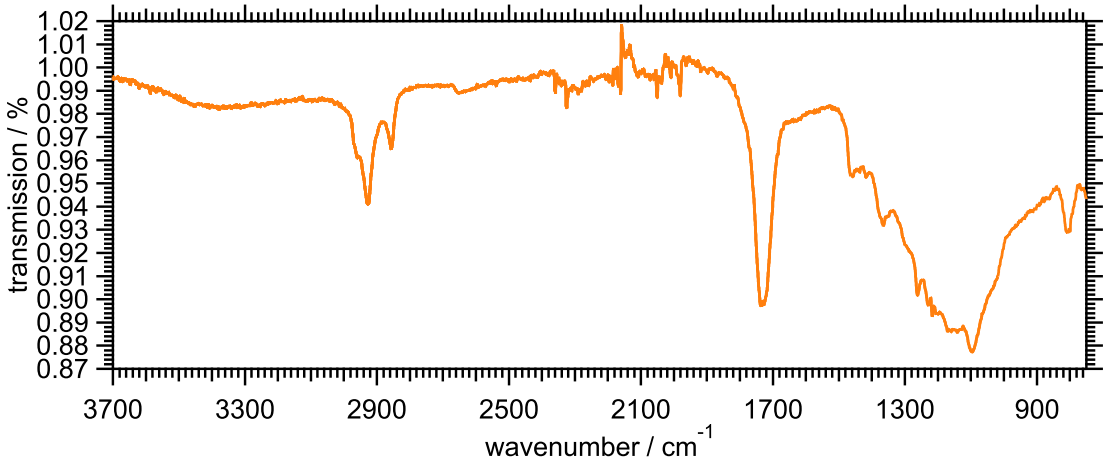

Figure 54: Infrared spectrum of hydroxylated RayND. Except apparatus-internal CO_2 background correction no data processing was carried out. Signals between $\approx 2300 - 1950\,cm^{-1}$ are measurement artifacts due to incomplete CO_2 compensation.

and 5 mL of 1 M BH_3·THF was added dropwise. The suspension was refluxed for 12 hours, additional 15 mL THF and 2 mL of 1 M $BH_3 \cdot$ THF were supplemented and refluxing was completed within further 12 hours. After cooling to r.t., the reaction mixture was hydrolysed with 50 mL HCl and purified according to 4.6.2.**(0)**. Yield: 80 %.

ATR-FTIR (cf. Fig. 54):[225,226] $\tilde{\nu}\,(\mathrm{cm}^{-1})$ = 3392 (br, $\nu-$ O−H), 2960 (s, $\nu-$ HC(sp^3)−H), 2928 (s, $\nu-$ HC(sp^3)−H), 2857 (s, $\nu-$ HC(sp^3)−H), 1730 (s, $\nu-$ C=O), 1461 (sh, $\delta-$ C(sp^2)−H), 1418 (w, $\delta-$ O−H), 1366 (m, $\delta-$ O−H), 1300 (sh, $\delta-$ O−H), 1261 (m, $\nu-$ C(sp^2)−OC(sp^3)), 1229 (sh, $\nu-$ C(sp^2)−OC(sp^3) / HOC(sp^2)−H), 1218 (sh, $\nu-$ C(sp^2)−OC(sp^3) / HOC(sp^2)−H), 1128 (br, $\delta-$ C(sp^3)−H), 1099 (m, $\nu-$ C(sp^3)−OH), 1018 (sh, $\nu-$ C(sp^3)−OH), 806 (m, $\delta-$ HCC(sp^2)−C(sp^2)CH / $[\mathrm{C_{arom.}}-\mathrm{C_{arom.}}]_n$ / $\mathrm{C_{oxirane}}-\mathrm{C_{oxirane}}$).

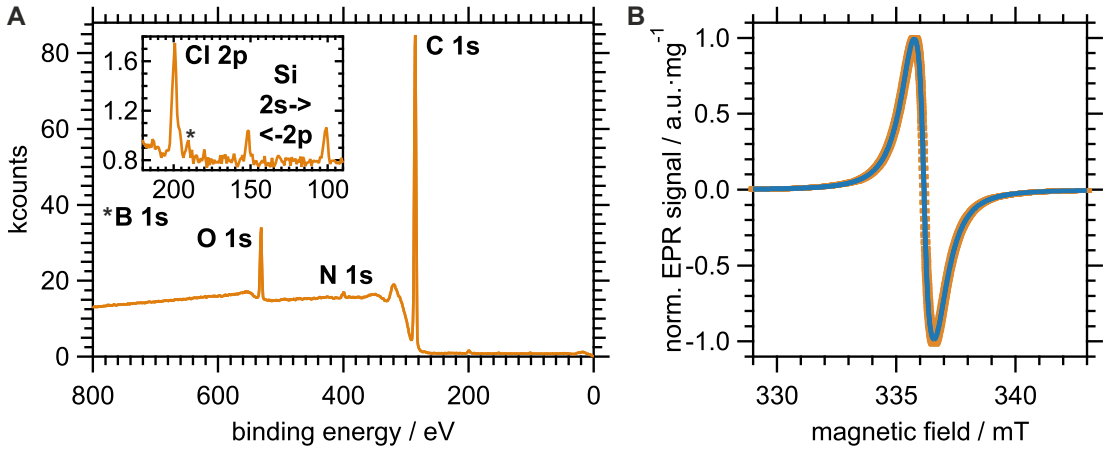

Figure 55: (A) Overview XPS spectrum of hydroxylated RayND. All relevant signals are displayed and assigned. **(B)** EPR spectrum of hydroxylated RayND (orange). The blue line corresponds to the two-spin model fit revealing the following values: $g_{\mathrm{P1}} = 2.0027$, $lw_{\mathrm{lor,P1}} = 0.35\,\mathrm{mT}$, $H_{\mathrm{str.,P1}} = 0.01\,\mathrm{MHz}$, $w_{P1} = 0.21$; $g_{\mathrm{db}} = 2.0026$, $lw_{\mathrm{lor,db}} = 0.94\,\mathrm{mT}$, $H_{\mathrm{str.,db}} = 7.8\,\mathrm{MHz}$, $w_{\mathrm{db}} = 4.9$ (cf. Chap. 4.6.4 for details).

The reductive hydroxylation by means of $BH_3 \cdot$ THF has its counterpart in the overview XPS spectrum by the newly added signal that indicates boron. The cause of the occurrence of silicon is unclear. Perhaps the starting material, i.e. the acid-treated RayND, which, however, was not monitored by XPS, was already contaminated. Otherwise, acid quenching is also a possible reason. The parameters of the deconvoluted EPR signal are given in Fig. 55.

Fluorination of RayND (4)

DAST-mediated fluorination of hydroxylated RayND nanodiamond was performed under modified conditions of literature procedure which reports the preparation diamondoid fluorides.[238] 0.100 g of **(3)** in 20 mL DCM was cooled in an ice bath ($\vartheta < 5\,°C$). 0.30 mL DAST was added dropwise and the reaction mixture was stirred for 2 hours under continuous cooling. Subsequently, the suspension was quenched with 150 mL saturated $NaHCO_3$ and 20 mL DCM was added. The aqueous phase was extracted twice with 20 mL DCM. The combined organic phases were washed with Milli-Q water three times and dried over anhydrous Na_2SO_4. DCM was removed under reduced pressure. The resulting residue was taken up in Milli-Q water and purified according to 4.6.2.**(0)**. Yield: 80 %.

ATR-FTIR (cf. Fig. 56):[226,238,239,285] $\tilde{\nu}\,(cm^{-1})$ = 3400 (br, $\nu-$ O−H), 2956 (br, $\nu-$ HC(sp^3)−H), 2929 (br, $\nu-$ HC(sp^3)−H), 2860 (br, $\nu-$ HC(sp^3)−H), 1710 (s, $\nu-$ C=O), 1638 (s, $\delta-$ O−H of $H_2O_{ads.}$), 1559 (s, N defects), 1540 (w, lattice absorp- tion), 1459 (w, $\delta-$ C(sp^2)−H), 1405 (w, $\delta-$ O−H), 1387 (m, $\nu-$ C(sp^3)−F), 1368 (w, $\delta-$ O−H), 1320 (sh, $\nu-$ C(sp^3)−F), 1245 (sh, $\nu-$ C(sp^2)−OC(sp^3) / HOC(sp^2)−H), 1221 (sh, $\nu-$ C(sp^2)−OC(sp^3) / HOC(sp^2) −H), 1218 (sh, $\nu-$ C(sp^2)−OC(sp^3) / HOC(sp^2)−H), 1100 (br, $\delta-$ C(sp^3)−H), 1045 (sh, $\nu-$ C(sp^2) −F).

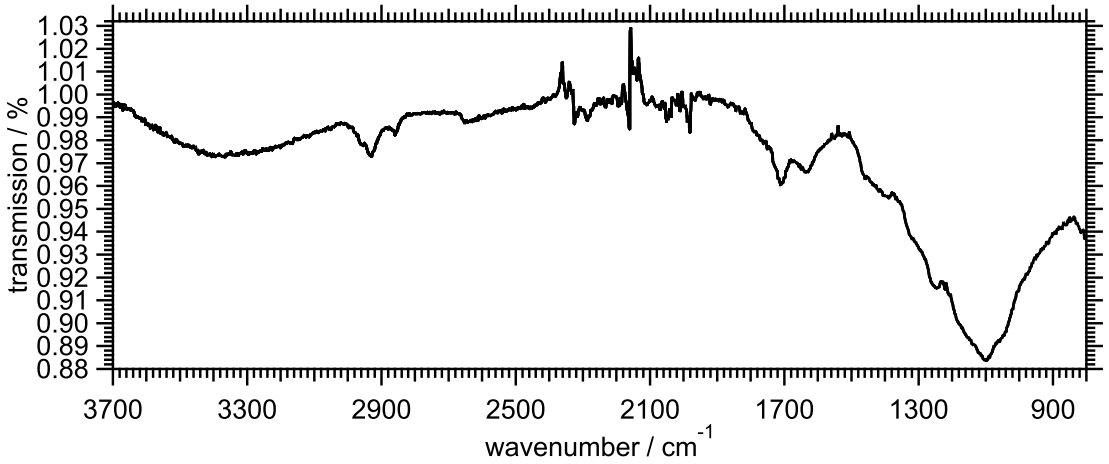

Figure 56: Infrared spectrum of fluorinated RayND. Except apparatus-internal CO_2 background correction no data processing was carried out. Signals between $\approx 2300 - 1950\,cm^{-1}$ are measurement artifacts because of incomplete CO_2 compensation.

With two exceptions, the XPS overview spectrum of fluorinated RayND mimics that of the hydroxylated ones, while here, however, the origin of silicon can be

traced back to the presence of hydrofluoric acid (see Fig 36). The sulfur indicating signal may refer to the uncleaved intermediate Fig. 36**AII** or not thoroughly washed out desiccant. The expected fluorine signal can also be seen in the overview spectrum, but will be discussed in more detail in Chap. 4.2.2. The parameters of the deconvoluted EPR signal are given in Fig. 57.

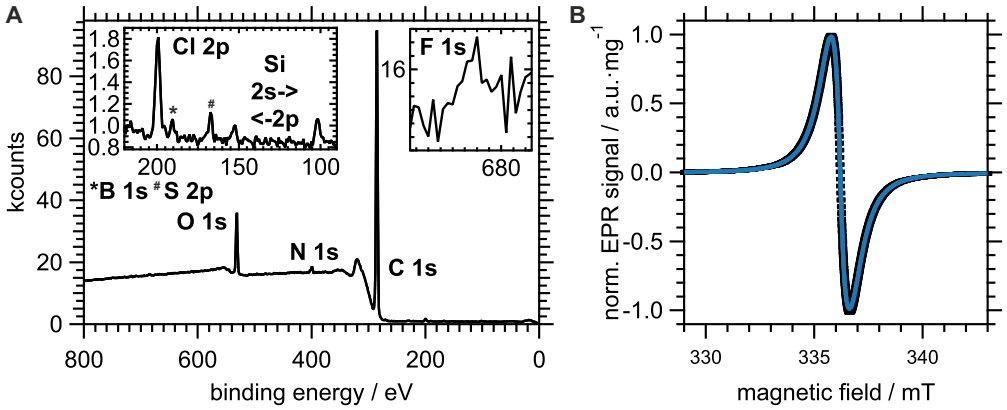

Figure 57: **(A)** Overview XPS spectrum of fluorinated RayND. All relevant signals are displayed and assigned. **(B)** First derivative EPR spectrum of fluorinated RayND (black). The blue line corresponds to the two-spin model approximation revealing the following values: $g_{\mathrm{P1}} = 2.0026$, $lw_{\mathrm{lor,P1}} = 0.35\,\mathrm{mT}$, $H_{\mathrm{str.,P1}} = 0.09\,\mathrm{MHz}$, $w_{P1} = 3.19$; $g_{\mathrm{db}} = 2.0026$, $lw_{\mathrm{lor,db}} = 0.97\,\mathrm{mT}$, $H_{\mathrm{str.,db}} = 5.0\,\mathrm{MHz}$, $w_{\mathrm{db}} = 105$ (cf. Chap. 4.6.4 for details).

Oxidization of RayND using $K_2Cr_2O_7$ (5)

250 mg of **(1)** was suspended in 20 mL diethyl ether. A solution of 19 g $K_2Cr_2O_7$ in 20 mL of Milli-Q water and 3 mL of H_2SO_4 was added dropwise while the temperature was halted below 20 °C. Then, the reaction mixture was stirred for 12 hours and purified according to 4.6.2.**(0)**. Yield: 73 %.

ATR-FTIR (cf. Fig. 58):[226] $\tilde{\nu}\,(\mathrm{cm}^{-1}) = 3405$ (br, $\nu-$ O−H), 3214 (br, $\nu-$ OCO −H), 1785 (s, $\nu-$ C=O), 1635 (s, $\delta-$ O−H of $H_2O_{\mathrm{ads.}}$), 1559 (w, N defects), 1395 (m, $\delta-$ O−H), 1310 (m, $\delta-$ O−H), 1253 (m, $\nu-$ $C(sp^2)$−$OC(sp^3)$), 1221 (sh, $\nu-$ $C(sp^2)$−$OC(sp^3)$ / $HOC(sp^2)$−H), 1102 (br, $\delta-$ $C(sp^3)$−H), 1057 (sh, $\nu-$ $C(sp^2)$/ (sp^3)−$OC(sp^3)$ / $HOC(sp^2)$−H), 944 (w, $\delta-$ $HCC(sp^2)$−$C(sp^2)H_2$).

The oxidizing agent $K_2Cr_2O_7$ is represented by the signals of chromium and one of its main impurities, molybdenum. The sulfur signal may indicate sulfuric acid esters that are known to attach to C=C bonds by the mechanism of electrophilic addition. The parameters of the deconvoluted EPR signal are given in Fig. 59.

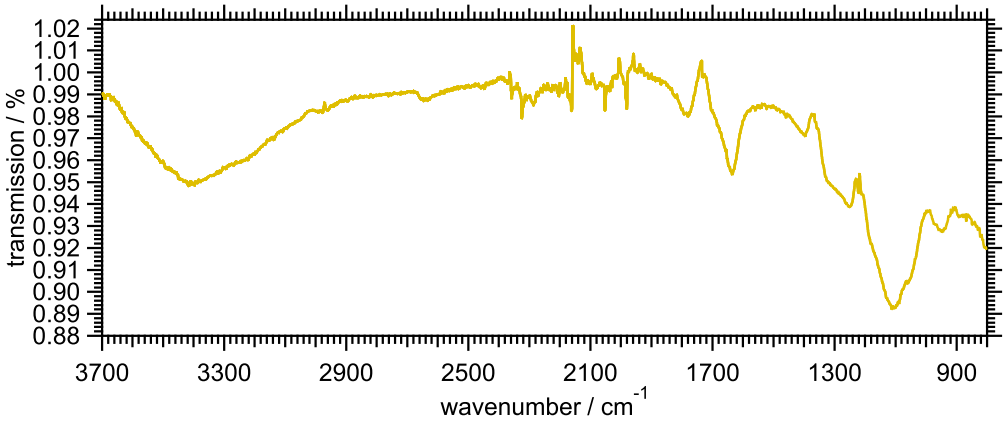

Figure 58: Infrared spectrum of oxidized RayND. Except apparatus-internal CO_2 background correction no data processing was carried out. Signals between $\approx 2300 - 1950\,\mathrm{cm}^{-1}$ are measurement artifacts due to incomplete CO_2 compensation.

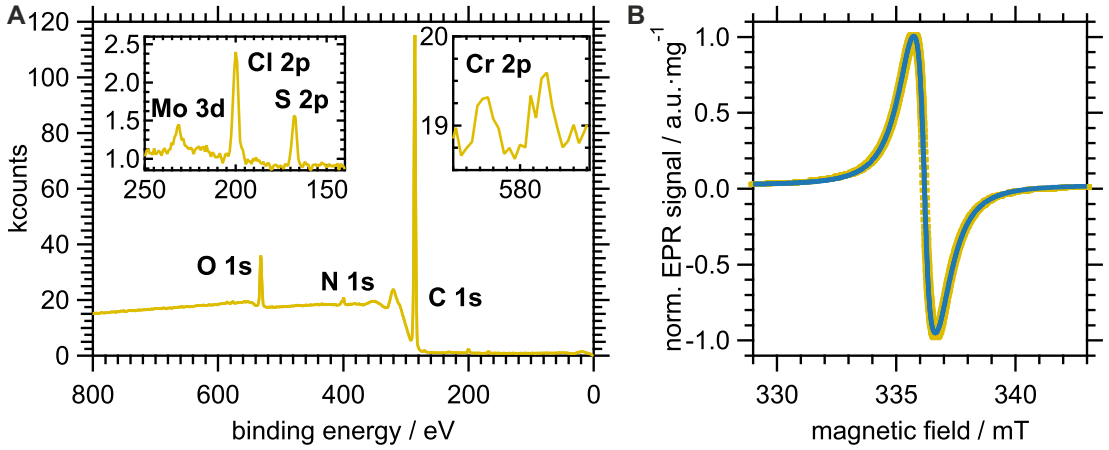

Figure 59: **(A)** Overview XPS spectrum of $K_2Cr_2O_7$-oxidized RayND. All relevant signals are displayed and assigned. **(B)** EPR spectrum of $K_2Cr_2O_7$-oxidized RayND (yellow). The blue line corresponds to the two-spin model approximation revealing the following values: $g_{\mathrm{P1}} = 2.0026$, $lw_{\mathrm{lor,P1}} = 0.36\,\mathrm{mT}$, $H_{\mathrm{str.,P1}} = 0.01\,\mathrm{MHz}$, $w_{P1} = 0.87$; $g_{\mathrm{db}} = 2.0027$, $lw_{\mathrm{lor,db}} = 1.10\,\mathrm{mT}$, $H_{\mathrm{str.,db}} = 0.05\,\mathrm{MHz}$, $w_{\mathrm{db}} = 30.0$ (cf. Chap. 4.6.4 for details).

Hydrazonation of RayND nanodiamond (6)

100 mg of **(5)** was suspended in 6 mL of concentrated acetic acid in the process holding the temperature of the mixture above 60 °C. 186.3 mg of *p*-toluenesulfonyl hydrazide was dissolved in 4 mL of ethanol (95%) at elevated temperature ($\vartheta >$ 70 °C) and added to the ND suspension. The mixture was stirred under reflux for

12 hours and purified according to 4.6.2.**(0)**. Yield: 70 %.
ATR-FTIR (cf. Fig. 60):[226] $\tilde{\nu}\,(\mathrm{cm}^{-1})$ = 3392 (br, $\nu-$ O−H), 2947 (br, $\nu-$ HC(sp^3)−H), 1748 (s, $\nu-$ C=O), 1636 (s, $\delta-$ O−H of $\mathrm{H_2O_{ads.}}$), 1559 (w, N defects), 1458 (sh, $\delta-$ HC(sp^2)−H), 1416 (sh, $\delta-$ O−H), 1327 (sh, $\delta-$ O−H), 1201 (w, $\nu-$ C(sp^2)−OC(sp^3)), 1140 (br, $\delta-$C(sp^3) −H).

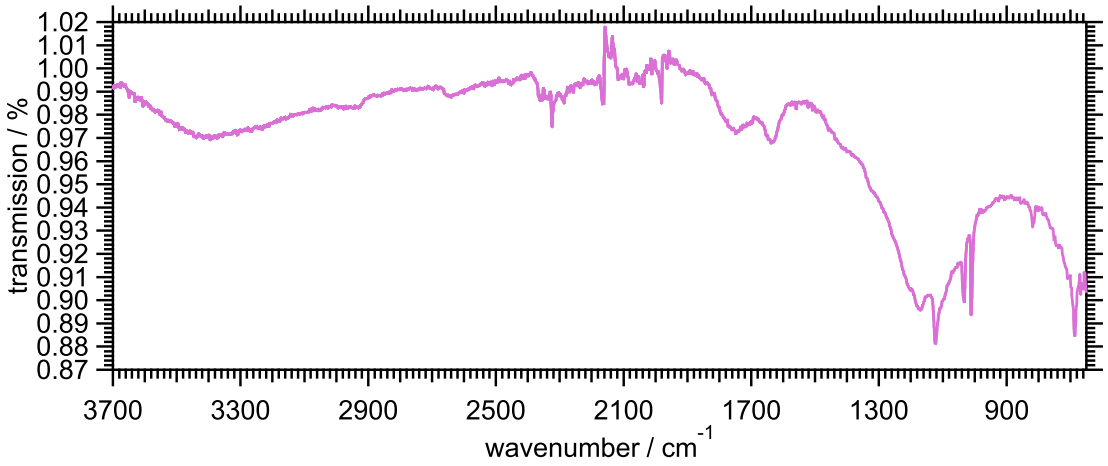

Figure 60: Infrared spectrum of hydrazonated RayND. Except apparatus-internal CO_2 background correction no data processing was conducted. Signals between $\approx 2300 - 1950\,\mathrm{cm}^{-1}$ are artifacts because of incomplete CO_2 compensation.

The remaining IR bands (cf. Fig. 60) are pronounced and narrow which was not observed for any of the other spectra. We ascribe this particular feature to *p*-toluenesulfonyl hydrazide-related molecular-like vibration modes, however, an interpretation is not straightforward. When comparing the obtained values (see Tab. 6) with those measured on free *p*-toluenesulfonyl hydrazide,[286] noticeable shifts in the respective wavenumbers may be identified which might stem from diamond surface-hydrazone interactions. This may also cause the absorption ($Abs = 1 - transmission$) to significantly differ between diamond-tethered and free *p*-toluenesulfonyl hydrazide - the strongest absorption occurs for the former at $\tilde{\nu} = 1012\,\mathrm{cm}^{-1}$ ($Abs_{\mathrm{exp.}} = 3.4\,\%$), for the latter at $\tilde{\nu} = 816\,\mathrm{cm}^{-1}$ ($Abs_{\mathrm{free}} = 77\,\%$). Yet, the signal at $\tilde{\nu} = 1032\,\mathrm{cm}^{-1}$ can not be rationalized by means of the free-molecule spectrum, whatsoever.
Therefore, we propose a second scenario, which is supported by Ref. [287] where IR spectra of methyl aziridine-2-carboxylate are reported (see Tab. 6.$\tilde{\nu}_{\mathbf{aziridine}}$). In contrast to terminate as a hydrazone, the nucleophilic attack of the amine functionality can also lead to an aziridine motif. When additionally nearest-neighboring to an ester group which is ubiquitous on the diamond surface (cf.

Table 6: Assignment of doubtful IR bands of hydrazonated RayND. $\tilde{\nu}_{\text{exp.}}$ are experimental data, $\tilde{\nu}_{\text{free}}$ data from Ref. [286] for *p*-toluenesulfonyl hydrazide, and $\tilde{\nu}_{\text{aziridine}}$ data of methyl aziridine-2-carboxylate from Ref. [287] with the corresponding assignment. In parentheses the baseline-corrected transmission intensity (Abs / %) of a particular IR band is noted. Note, that the differences of transmission intensities between our values and the molecular spectrum ("free") are caused by different measurement conditions. Wavenumbers $\tilde{\nu}$ are given in cm^{-1}.

$\tilde{\nu}_{\text{exp.}}$ ($Abs_{\text{exp.}}$)	$\tilde{\nu}_{\text{free}}$ (Abs_{free})	$\tilde{\nu}_{\text{aziridine}}$	assignment
1171 (0.60)	1186 (70)	1176	$\delta - \text{C(sp}^3\text{)}-\text{H}$
1123 (2.0)	1157 (25)	1144	$\delta - \text{HC}_{\text{aziridine}}-\text{H}$
1032 (1.8)	-	1031	$\nu - \text{C(sp}^3\text{)}-\text{O}$
1012 (3.4)	1018 (77)	1012	$\nu - \text{C(sp}^3\text{)}-\text{O}$
818 (1.0)	816 (16)	815	$\text{C}_{\text{aziridine}}-\text{C}_{\text{aziridine}}$
686 (2.8)	690 (55)	678	$\delta - \text{CC(sp}^2\text{)}=\text{O}$

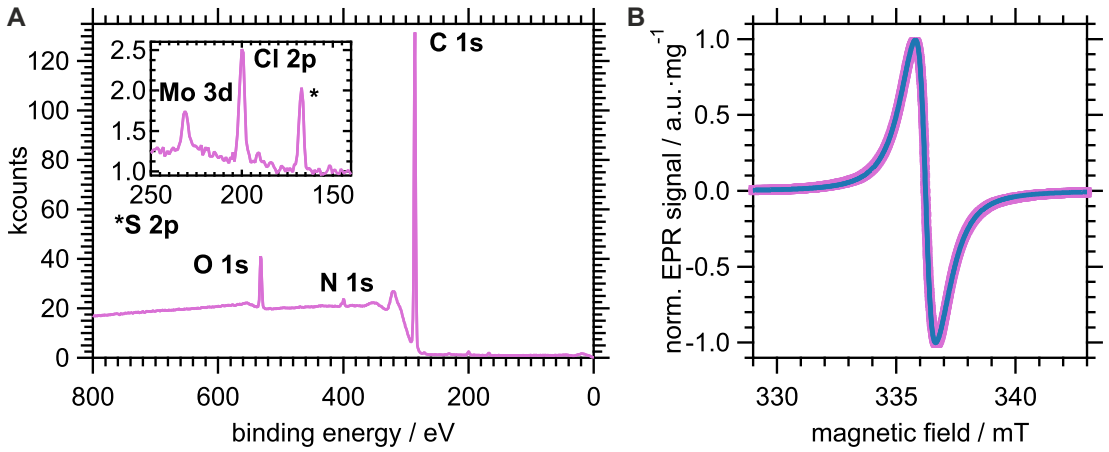

Figure 61: (A) Overview XPS spectrum of hydrazonated RayND. All relevant signals are displayed and assigned. **(B)** EPR spectrum of hydrazonated RayND (magenta). The blue line corresponds to the two-spin model approximation revealing the following values: $g_{\text{P1}} = 2.0026$, $lw_{\text{lor,P1}} = 0.36\,\text{mT}$, $H_{\text{str.,P1}} = 0.09\,\text{MHz}$, $w_{P1} = 1.6 \times 10^4$; $g_{\text{db}} = 2.0025$, $lw_{\text{lor,db}} = 1.07\,\text{mT}$, $H_{\text{str.,db}} = 0.17\,\text{MHz}$, $w_{\text{db}} = 5.5 \times 10^3$ (cf. Chap. 4.6.4 for details).

signal at $\tilde{\nu} = 1201\,\text{cm}^{-1}$), the situation investigated in [287] is met, in analogy. Thus, all IR bands can be assigned in good agreement, since the difference between $\tilde{\nu}_{\text{exp.}} = 1123\,\text{cm}^{-1}$ and the corresponding values of $\tilde{\nu}_{\text{aziridine}}$ can be elucidated by the fact, that the $\delta - \text{HC}_{\text{aziridine}}-\text{H}$ vibration mode of ethyl aziridine-2-carboxylate

probably corresponds to $\delta-\mathrm{CC_{aziridine}}-\mathrm{H}$ for diamond-tethered *p*-toluenesulfonyl hydrazide. This $\mathrm{H}\rightarrow\mathrm{C}$ substitution notoriously causes a decrease in the value of the particular wavenumber.[224]
The XPS overview spectrum only shows a change in the minor species to the extent that the chromium signal is no longer detectable, whereas in contrast the molybdenum signal is still present, possibly a consequence of its higher hardness according to the HSAB theory.[288] The nitrogen signal important for this protocol is discussed in Chap. 4.2.3. The parameters of the deconvoluted EPR signal are given in Fig. 61.

De-hydrazonation step of Bamford-Stevens olefination on RayND (7)
10 mL of ethylene glycol and 90 mg sodium methoxide were added to 40 mg of **(6)**. The suspension was stirred at a bath temperature of 170 °C for 12 hours and purified according to 4.6.2.**(0)**. Yield: 60 %.
ATR-FTIR (cf. Fig. 62):[226] $\tilde{\nu}\,(\mathrm{cm^{-1}})$ = 3397 (br, $\nu-$ O−H), 2941 (br, $\nu-$ HC($\mathrm{sp^3}$)−H), 1740 (s, $\nu-$ C=O), 1636 (s, $\delta-$ O−H of $\mathrm{H_2O_{ads.}}$), 1595 (sh, $\nu-$ C($\mathrm{sp^2}$) −C($\mathrm{sp^2}$)), 1558 (w, N defects), 1540 (w, lattice absorption), 1457 (sh, $\delta-$ HC($\mathrm{sp^2}$) −H), 1375 (sh, $\delta-$ O−H), 1321 (w, $\delta-$ O−H), 1251 (w, $\nu-$ C($\mathrm{sp^2}$)−OC($\mathrm{sp^3}$)), 1221 (sh, $\nu-$ C($\mathrm{sp^2}$) −OC($\mathrm{sp^3}$) / HOC($\mathrm{sp^2}$) −H), 1110 (br, $\delta-$ C($\mathrm{sp^3}$) −H), 1007 (w, $\delta-$ HCC($\mathrm{sp^2}$)−C($\mathrm{sp^2}$)$\mathrm{H_2}$ / $\mathrm{C_{aziridine}}$ −$\mathrm{C_{aziridine}}$).

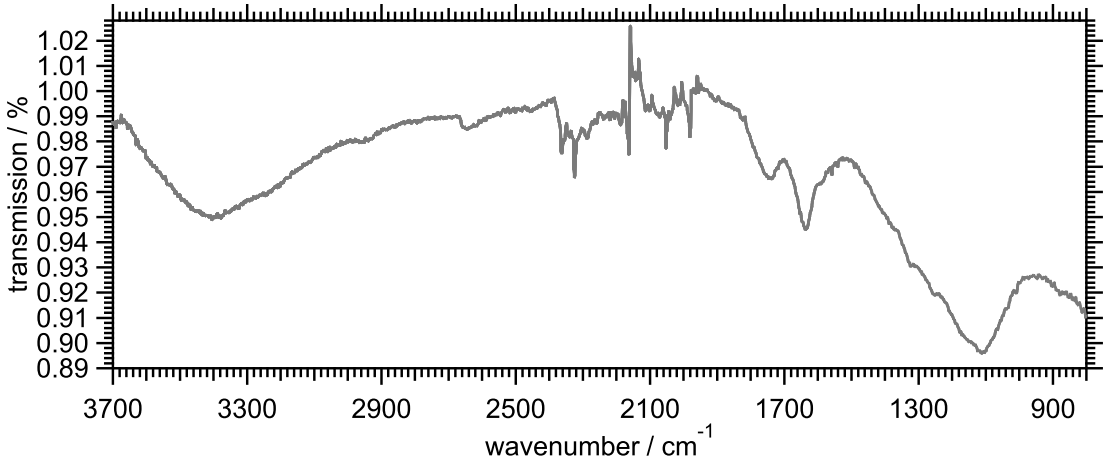

Figure 62: Infrared spectrum of de-hydrazonated RayND. Except apparatus-internal $\mathrm{CO_2}$ background correction no data processing was conducted. Signals between $\approx 2300-1950\,\mathrm{cm^{-1}}$ are artifacts because of incomplete $\mathrm{CO_2}$ compensation.

With the final step of the Bamford-Stevens protocol, the XPS overview spectrum has been reduced to the four elements carbon, oxygen, nitrogen and chlorine, as

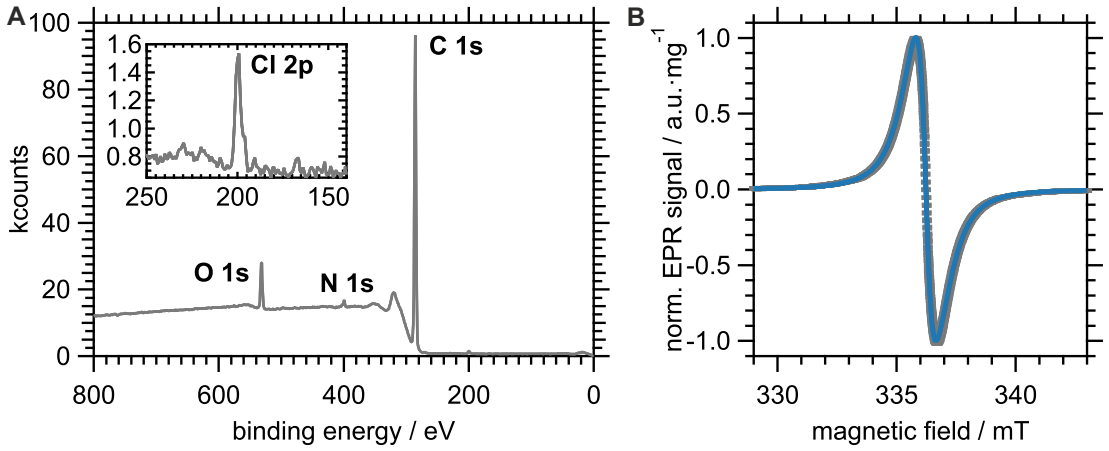

Figure 63: (A) Overview XPS spectrum of de-hydrazonated RayND. All relevant signals are displayed and assigned. **(B)** EPR spectrum of de-hydrazonated RayND (gray). The blue line corresponds to the two-spin model approximation revealing the following values: $g_{\mathrm{P1}} = 2.0026$, $lw_{\mathrm{lor,P1}} = 0.34\,\mathrm{mT}$, $H_{\mathrm{str.,P1}} = 0.1\,\mathrm{MHz}$, $w_{P1} = 3.4$; $g_{\mathrm{db}} = 2.0025$, $lw_{\mathrm{lor,db}} = 1.03\,\mathrm{mT}$, $H_{\mathrm{str.,db}} = 0.01\,\mathrm{MHz}$, $w_{\mathrm{db}} = 1.3 \times 10^2$ (cf. Chap. 4.6.4 for details).

it is in the case of the pristine RayND. The parameters of the deconvoluted EPR signal are given in Fig. 63.

Self-assisted ultrasonication deaggregation of RayND (8)

Self-assisted ultrasonication deaggregation (SAUD) of RayND was conducted according to literature.[273] 100 mg of RayND in a mixture with 4 g NaCl was thoroughly ground by hand and added to 8 mL ultrapure water. The suspension was sonicated for 2 hours. Subsequent purification included three times alternating centrifugation and washing of the residuum (50 mL ultrapure water) and final drying under reduced pressure ($p \leq 13\,\mathrm{mbar}$) for 2 hours as well as in the oven at 150 °C for 12 hours. 12 mg of the dried SAUD-processed RayND was transferred into an EPR tube for measurements. Evaluation of the obtained data is shown in Fig. 64**A**,**B** and Tab. 2 in the main text.

EPR measurements on detonation ND

Liquid-assisted pulsed laser ablation is a relatively new method to synthesize ND.[289–291] As noted in the main text many studies on radical states in ND have been carried out on detonation ND (DND), which are available since the 1960's ([206] and references therein). Therefore, we have found it useful to compare the

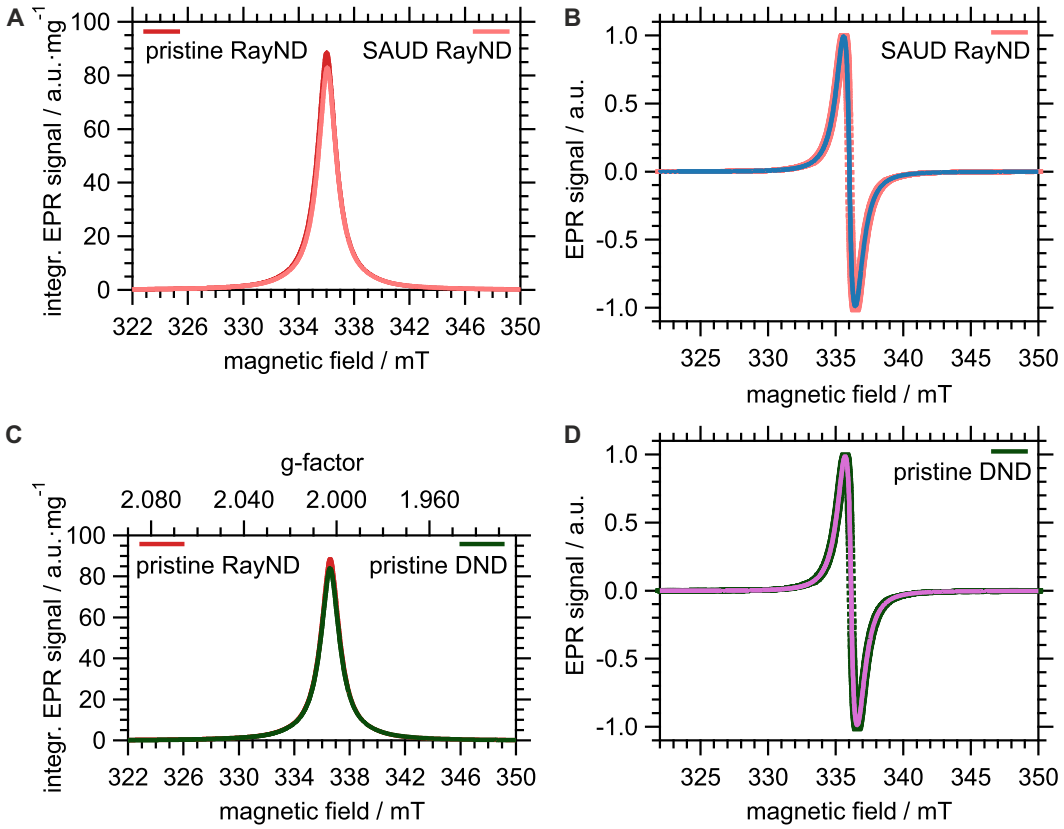

Figure 64: **(A)** Comparison of the double-integrated EPR signal (normalized per unit weight) of pristine RayND (red) and SAUD-processed RayND (coral). **(B)** Deconvolution of the EPR signal (coral) of SAUD-processed RayND by means of the two-spin model (blue line) which reveals $g_{\mathrm{P1}} = 2.0029$, $lw_{\mathrm{lor,P1}} = 0.35\,\mathrm{mT}$, $H_{\mathrm{str.,P1}} = 0.10\,\mathrm{MHz}$, $w_{P1} = 0.38$; $g_{\mathrm{db}} = 2.0029$, $lw_{\mathrm{lor,db}} = 0.99\,\mathrm{mT}$, $H_{\mathrm{str.,db}} = 5.5\,\mathrm{MHz}$, $w_{\mathrm{db}} = 10.8$. **(C)** Comparison of the double-integrated EPR signal (normalized per unit weight) of pristine RayND (red) and pristine DND (dark green). **(D)** Deconvolution of the EPR signal (dark green) of pristine DND by means of the two-spin model (blue line) which reveals $g_{\mathrm{P1}} = 2.0028$, $lw_{\mathrm{lor,P1}} = 0.23\,\mathrm{mT}$, $H_{\mathrm{str.,P1}} = 0.19\,\mathrm{MHz}$, $w_{P1} = 0.29$; $g_{\mathrm{db}} = 2.0028$, $lw_{\mathrm{lor,db}} = 1.04\,\mathrm{mT}$, $H_{\mathrm{str.,db}} = 0.01\,\mathrm{MHz}$, $w_{\mathrm{db}} = 4.8$.

RayND we used with DND on the basis of EPR measurement in order to determine whether the results presented here can also be applied to this material.
4.6 mg of as-received, non-functionalized, graphite and metal-free DND (RT-DND, average grain size: $3 - 6\,\mathrm{nm}$, Ray Techniques Ltd.) was transferred into an EPR tube without further purification. The measurement outcome is depicted in Fig. 64**C**,**D**. The obtained signal, double-integrated and normalized per unit weight,

reveals a total spin density of $1.9(1) \times 10^{16}\,\mathrm{mg}^{-1}$ and, after employing the two-spin model to set apart the surface dangling bond contribution, $1.80(9) \times 10^{16}\,\mathrm{mg}^{-1}$. Thus, according to the surface dangling bond density RayND, where we obtained $\rho_{\mathrm{sp,db}} = 1.86(2) \times 10^{16}\,\mathrm{mg}^{-1}$, and DND show comparable results as well as their spectral parameters.

4.6.3 Details on XPS data deconvolution

The evaluation of the C 1s XPS spectra turned out to be difficult because the signals of the C(sp^2), C−O, C=O, and potential C−F moieties showed significantly lower intensity compared to the diamond C(sp^3) signal, for which reason, e.g., no specific features could be observed. Because of that, the fit results initially proved to be unstable against minor changes in the statistical degrees of freedom. We therefore decided to evaluate the data using a process of consecutive signal adding that employs the residual sum of squares (RSS, which in our case equals χ^2 due to weighting factor 1) as well as the Second-Order Akaike decision criterion ($\mathrm{AIC_c}$) as figure of merit.
If we take the addition of signals for a certain carbon binding pattern C−Het, which we do not know *a priori* to be actually present in our sample, as forming a new model, we face the problem that, in general, model fitting goodness increases with the number of degrees of freedom and we meet the model selection problem. In this context, Akaike was able to show that the maximum of the empirical log-likelihood function $\ln(\mathcal{L}(\theta|y))$ of given data y and a parameter θ to be estimated is an upward biased estimator for the expectation of the Kullback-Leibler information, which is a measure of the directed distance between the (infinitely) parametrized reality and a arbitrary model, where the correction factor k depends on the number of degrees of freedom of the chosen model.[292,293] With this result he derived the so-called Akaike's information criterion (AIC)

$$\mathrm{AIC} = -2\ln(\mathcal{L}(\theta|y)) + 2k. \tag{4.2}$$

that makes it possible to quantify different models which, when possessing the same probability density, are totally determined by the number of their statistical parameters k, while the best model excelling by a minimal AIC.

We now turn to the computation aspects of the AIC theory,[293] and we first note

that we utilized the Second-Order AIC (AIC_c)

$$AIC_c = -2\ln(\mathcal{L}(\theta|y)) + 2k + \frac{2k\,(k+1)}{n-k-1}. \tag{4.3}$$

which includes an additional correction term for small sample sizes n ($n \approx k$). Assuming that our data are normally distributed, equation (4.3) results in:

$$AIC_c = n\ln\left(\frac{\chi^2}{n}\right) + 2k + \frac{2k\,(k+1)}{n-k-1}. \tag{4.4}$$

After determining the AIC_c value of each fit according to equation (4.4), we calculated the distance between the best model $\min\{AIC_{c,i}\}$ and all i models $AIC_{c,i} \in \{AIC_{c,i}\}$

$$\Delta_i = AIC_{c,i} - \min\{AIC_{c,i}\}. \tag{4.5}$$

The advantage of AIC theory is that it offers, by means of the likelihood $\mathcal{L}(g_i|y)$, given the data y and the estimated model g_i, which is characterized by its parameters k_i,

$$\mathcal{L}(g_i|y) \propto \exp\left(-\frac{\Delta_i}{2}\right) \tag{4.6}$$

and the Akaike's weights

$$w_i = \frac{\mathcal{L}(g_i|y)}{\sum_{l=1}^{|\{AIC_{c,i}\}|}\mathcal{L}(g_l|y)}\ , \tag{4.7}$$

the possibility to obtain the probability or evidence that the best model is reliably stated so.

With these preliminary remarks we now proceed to the explanation of our procedure to fit the C 1s XPS data, whereas referring to the particular iterations given in Tab. 7.

1. First, we pre-set a Gaussian function with the literature value of the binding energy (BE) of (sp^3) carbon in diamond (285 eV) as its center.[294] The following fitting was done under full relaxation of all regression parameters (7.**1**).

2. Subsequently, all potential carbon binding motives were added separately to this (sp^3) carbon signal, whereby the value of the corresponding binding energy was set to its literature value corrected, if necessary, by the deviation of the carbon signal from 285 eV, and constrained to ±0.5 eV (7.**2-4**). Full

relaxation was conceded to the remaining regression parameters. Note that this step was only performed for fluorinated RayND (Table 8) also for C−F.

3. By selecting the best two results of the two-signal iteration regarding the obtained χ^2 and AIC_c values, respectively, a new fit with the same constraints as in 2. was accomplished each time (7.**5**).

4. Then the remaining signals were successively added and a fit was performed until all signals were taken into account. Only for binding energies, restrictions within the ±0.5 eV limit were given (7.**6**).

Table 7: Deconvolution procedure of the C 1s high-resolved XPS spectrum of pristine RayND. For a particular fit iteration, the area A below a certain signal is listed that indicates the given functionality, which is identified by its binding energy $BE_{(\cdot)}$ in units of eV. Furthermore, the χ^2 fit residuals, the number of parameters j of the fit model and the AIC_c (Eq. (4.3)) can be found. The uncertainties in the binding energies amount to 0.3 eV. The expression "no conv." means that the fit did not converge within the constraints specified for $BE_{(\cdot)}$.

iteration	$BE_{C(sp^2)}$ / A / 10^2	$BE_{C(sp^3)}$ / A / 10^4	BE_{C-O} / A / 10^2	$BE_{C=O}$ / A / 10^3	BE_{C-F} / A / 10^2	χ^2 / 10^6	j	AIC_c
1		285.4 2.30(1)				4.46	5	2396
2		285.4 2.284(7)		288.1 1.03(7)		0.835	8	1995
3	284.4 2(5)	285.4 2.24(3)				3.98	8	2374
4		no conv.	no conv.					
5	284.4 3.3(9)	285.3 2.23(1)		288.1 1(1)		0.907	11	2022
6	284.4 2(1)	285.3 2.20(4)	286.3 4(2)	287.9 1.2(3)		0.308	14	1766
7	284.6 3(2)	285.3 2.18(1)	286.1 4(2)	287.8 1.0(7)	289.2 2(5)	0.302	17	1768

5. Finally, Akaike's weights w_i were calculated from the corresponding $AIC_{c,i}$ values using the method described above where the number of regression parameters k and the number of data points $n = 241$ were taken into account.

This fitting was performed for the C 1s XPS spectra of pristine, base-treated, hydroxylated, fluorinated and de-hydrazonated RayND. The results can be found in Tab. 4 in the main text and in Fig. 65, which also shows the fit residuals and

Table 8: Deconvolution procedure of the C 1s high-resolved XPS spectrum of fluorinated RayND. For a particular fit iteration, the area A below a certain signal is listed that indicates the given functionality, which is identified by its binding energy $BE_{(\cdot)}$ in units of eV. Furthermore, the χ^2 fit residuals, the number of parameters j of the fit model and the Second-Order Akaike information criterion AIC_c can be found. The uncertainties in the binding energies amount to 0.3 eV. The expression "no conv." means that the fit did not converge within the constraints specified for the binding energy.

iteration	$BE_{C(sp^2)}$ / A / 10^3	$BE_{C(sp^3)}$ / A / 10^4	BE_{C-O} / A / 10^2	$BE_{C=O}$ / A / 10^2	BE_{C-F} / A / 10^2	χ^2 / 10^6	j	AIC_c
1		285.1 2.481(6)				1.52	5	2117
2		285.1 1.483(6)		288.1 1.4(3)		1.33	8	2092
3	284.0 1.7(7)	285.2 1.28(7)				1.09	8	2043
4		285.0 1.448(6)	286.0 2.8(3)			0.818	8	1974
5		no conv.			no conv.			
6	284.1 4(1)	285.1 1.39(1)	286.0 2.7(3)			0.511	11	1867
7	284.1 2.1(7)	285.0 1.37(2)	286.0 3(2)	287.6 3(1)		0.217	14	1667
8	284.2 4.1(6)	285.0 1.34(3)	285.9 6(1)	287.6 4(1)	289.2 4(3)	0.208	17	1664

Table 9: Deconvolution procedure of the C 1s high-resolved XPS spectrum of de-hydrazonated RayND. For a particular fit iteration, the area A below a certain signal is listed that indicates the given functionality, which is identified by its binding energy $BE_{(.)}$ in units of eV. Furthermore, the χ^2 fit residuals, the number of parameters j of the fit model and the Second-Order Akaike information criterion AIC_c can be found. The uncertainties in the binding energies amount to 0.3 eV. The expression "no conv." means that the fit did not converge within the constraints specified for the binding energy.

iteration	$BE_{C(sp^2)}$ / A / 10^2	$BE_{C(sp^3)}$ / A / 10^4	BE_{C-O} / A / 10^2	$BE_{C=O}$ / A / 10^2	BE_{C-F} / A / 10^2	χ^2 / 10^6	j	AIC_c
1		285.6 1.366(4)				0.778	5	1955
2		285.6 1.367(3)		288.4 1.7(3)		0.584	8	1893
3	284.8 2.4(4)	285.6 1.337(6)				0.468	8	1839
4		no conv.	no conv.					
5	284.8 2.3(3)	285.6 1.340(5)		288.4 1.4(2)		0.309	11	1746
6	284.8 2.2(4)	285.6 1.32(1)	286.5 1.6(7)	288.3 2.0(4)		0.286	14	1734

assignment of the particular signals.

In addition, the results for the three samples in which two Akaike's weights w_i were not equal to zero, namely pristine, fluorinated, and de-hydrazonated RayND, are presented below. Tab.s 7 - 9 show the results of the consecutive approximation procedure. The corresponding computations according to the AIC theory can be found in Tab.s 10 - 12.

Here we present a short discussion on these three cases, which was omitted in the main text.

As can be seen in Table 7, iteration 7, we considered a C−F functionality in the fit, which is, however, not to be expected for pristine RayND material. But we decided to take this step in order to have a reference for the approximation of the

Table 10: Second-Order AIC analysis of the fit models of the C 1s XPS spectrum of pristine RayND. The entry iteration refers to Tab. 7 as well as AIC_c. The remaining values are calculated according to Eq.s (4.5) - (4.7) given above.

iteration	AIC_c	Δ_i	$\mathcal{L}_i$	w_i / %
1	2396	630	0	0
2	1995	230	0	0
3	2374	609	0	0
4	2022	256	0	0
5	1766	0	1	73.98
6	1768	2	0.3516	26.02

Table 11: Second-Order AIC analysis of fit models of the C 1s XPS spectrum of fluorinated RayND. The entry iteration refers to Tab. 8 as well as AIC_c. The remaining values are calculated according to Eq.s (4.5) - (4.7) given above.

iteration	AIC_c	Δ_i	$\mathcal{L}_i$	w_i / %
1	2177	453	0	0
2	2092	428	0	0
3	2043	379	0	0
4	1974	310	0	0
5	1867	310	0	0
6	1867	203	0	0
7	1667	3	0.1955	16.35
8	1664	0	1	83.65

Table 12: Second-Order AIC analysis of fit models of the C 1s XPS spectrum of de-hydrazonated RayND. The entry iteration refers to Tab. 9 as well as AIC_c. The remaining values are calculated according to Eq.s (4.5) - (4.7) given above.

iteration	AIC_c	Δ_i	$\mathcal{L}_i$	w_i / %
1	1955	222	0	0
2	1893	159	0	0
3	1839	106	0	0
4	1746	12	0.002291	0.2286
5	1734	0	1	99.77

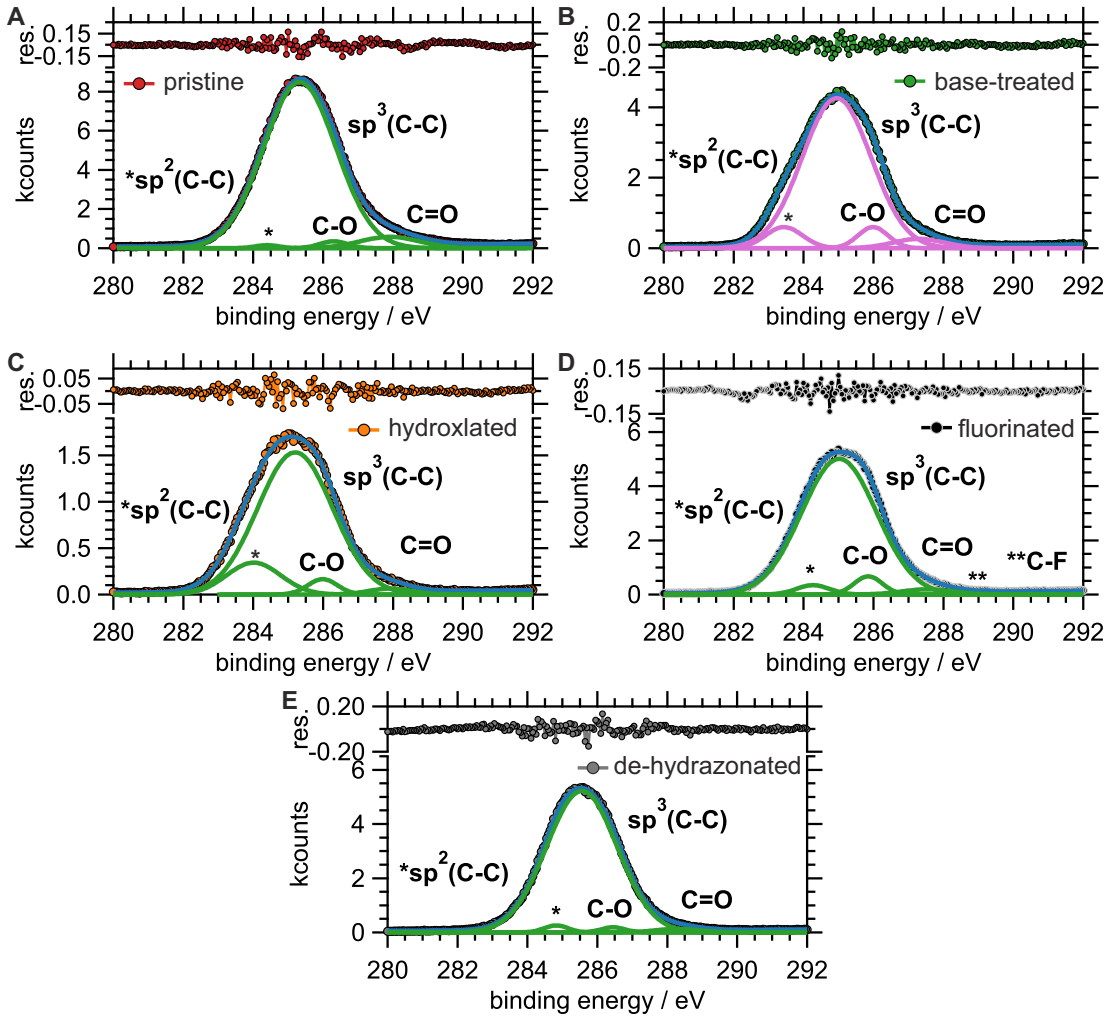

Figure 65: Result of the deconvolution of high-resolved C 1s XPS spectra of **(A)** pristine, **(B)** base-treated, **(C)** hydroxylated, **(D)** fluorinated, and **(E)** de-hydrazonated RayND. The fit residuals are shown in units of the XPS signal.

C 1s signal of the fluorinated sample (see Tab. 8). The deliberately added signal reduces the evidence of the approximation in iteration 6, which only includes the expected C−Het motifs (see Tab. 10). This agrees with the remark made at the beginning that the addition of - here concretely - Gaussian functions increases the figure of merit. However, the potency of the AIC method becomes obvious here, since the fit residue decreases due to the inclusion of the C−F signal, but AIC_c now has a larger value due to the increase in the fit parameters which, eventually, lower its evidence. Therefore we decided to apply the model according to iteration

6 to characterize the pristine RayND sample.
The AIC evaluation of the fluorinated RayND (see Tab. 8) shows 16.35% probability for the fit without C−F signal and correspondingly 83.65% for the fit when the one is taken into account. With this uncertainty in view, we have discussed the model from iteration 8 in the main text, especially since the F 1s XPS signal also indicates a C-F bond.
The deconvolution procedure of the C 1s XPS spectrum of the de-hydrazonated RayND sample indicates a low probability of less than 1 % for the model that omits the C-O bonding motifs (see Tab. 9 and Tab. 12). This result led us to deem the outcome of iteration 5 to be extremely unlikely and to discuss only the model of iteration 6 in the main text.
Finally, it should be noted that the evaluation of AIC_c values does not make a statement about the absolute probability of a model, but solely compares models against one another. Our modeling was done entirely with Gaussian-shaped functions. It is known, however, that in many cases line broadening mechanisms exist in XPS spectroscopy, which make their description by more intricate functions necessary, e.g. sums or products of Lorentzian and Gaussian functions of different weighting or even asymmetric line shapes.[295,296] In addition, we did not include C−N bonds in the deconvolution of the C 1s spectra, which is due to the fact that the intensity of the O 1s signal in the XPS overview spectra is always clearly larger than that of the N 1s signal. Therefore, the results of our AIC_c analysis must eventually be considered with respect to these model limitations.

4.6.4 Details on EPR measurements

Spectral simulation and deconvolution of EPR signals was conducted by the MATLAB based EasySpin software suite, which provides a least-squares fitting algorithm.[163] Thereby, we consistently employed matrix diagonalization for spectrum simulation and the Nelder/Mead downhill simplex method for fit optimization.
The relaxation of an ensemble of spins in a pure state, i.e., all spins are exposed to the same magnetic field and have an identical Hamiltonian, is described by a Lorentzian function whose linewidth lw_{lor} is determined by the applied microwave power B_1 and the ensemble-bath coupling strength Γ: $lw_{\mathrm{lor}} \propto B_1\Gamma$.[66] However, interactions in solid state between various kinds of spins additionally residing in locally different environments imposed by the host lift the magnetic field homogeneity. Since the underlying coupling mechanisms are often weak, they are spectroscopically not resolvable and contribute to the linewidth which is of Gaussian shape due to the underlying distribution of coupling parameters.

Phenomenological Lorentzian linewidth shaping is called homogeneous and Gaussian inhomogeneous line broadening, and to allow for both, their convolution, the Voigtian linewidth profile, can be used. So far, all interactions were assumed to be isotropic. If this condition is no longer fulfilled, statistical assumptions about the distribution of the Hamiltonian parameters are required to correctly describe the linewidth, which is summarized under the term strain.[297,298] EasySpin offers the possibility to include anisotropic hyperfine splitting by using a regression parameter called Hstrain which we adopted here and which we refer to as $H_{\mathrm{str.}}$.
We considered this procedure to be justified on the one hand because the approximation by means of Voigtian functions turned out to be unsatisfactory. On the other hand ND forms a highly anisotropic material regarding both its structure and spin impurities. For the latter, reports are available on the P1 center as well as dangling bond spins.[28,266,268]

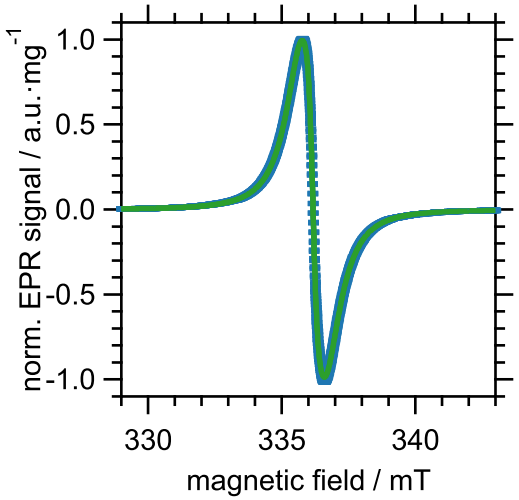

Figure 66: EPR signal of acid treated RayND (blue) and two-spin model fit (green) revealing the following values: $g_{\mathrm{P1}} = 2.0026$, $lw_{\mathrm{lor,P1}} = 0.35\,\mathrm{mT}$, $H_{\mathrm{str.,P1}} = 0.10\,\mathrm{MHz}$, $w_{P1} = 0.70$; $g_{\mathrm{db}} = 2.0026$, $lw_{\mathrm{lor,db}} = 0.95\,\mathrm{mT}$, $H_{\mathrm{str.,db}} = 7.73\,\mathrm{MHz}$, $w_{\mathrm{db}} = 17.5$.

We now turn to our fitting procedure. As mentioned in the main text, we assumed a two-spin model to approximate EPR signals in which one species is identified with diamond core-inherent spin impurities, mainly P1 centers, and the second corresponds to surface-related radical species denoted as dangling bond spins. Additionally, we neglected effects of the functionalization protocols on the diamond core. Thus, we fixed the parameters of the modeled P1 center spectrum at g-factor $g_{\mathrm{P1}} = 2.0026(2)$, Lorentzian linewidth $lw_{\mathrm{lor,P1}} = 0.35(5)\,\mathrm{mT}$ and strain broadening $H_{\mathrm{str,P1}} = 0.095(30)\,\mathrm{MHz}$ (The numbers in parentheses denote the range in which variation of the parameter was allowed for least-squares regression.), which values we inferred from the unconstrained fit of the EPR spectra of pristine RayND ($g_{\mathrm{P1}} = 2.0028$, $lw_{\mathrm{lor,P1}} = 0.37\,\mathrm{mT}$,$H_{\mathrm{str,P1}} = 0.12\,\mathrm{MHz}$) and acid-treated RayND (see Fig. 66). The dangling bond contribution of the EPR

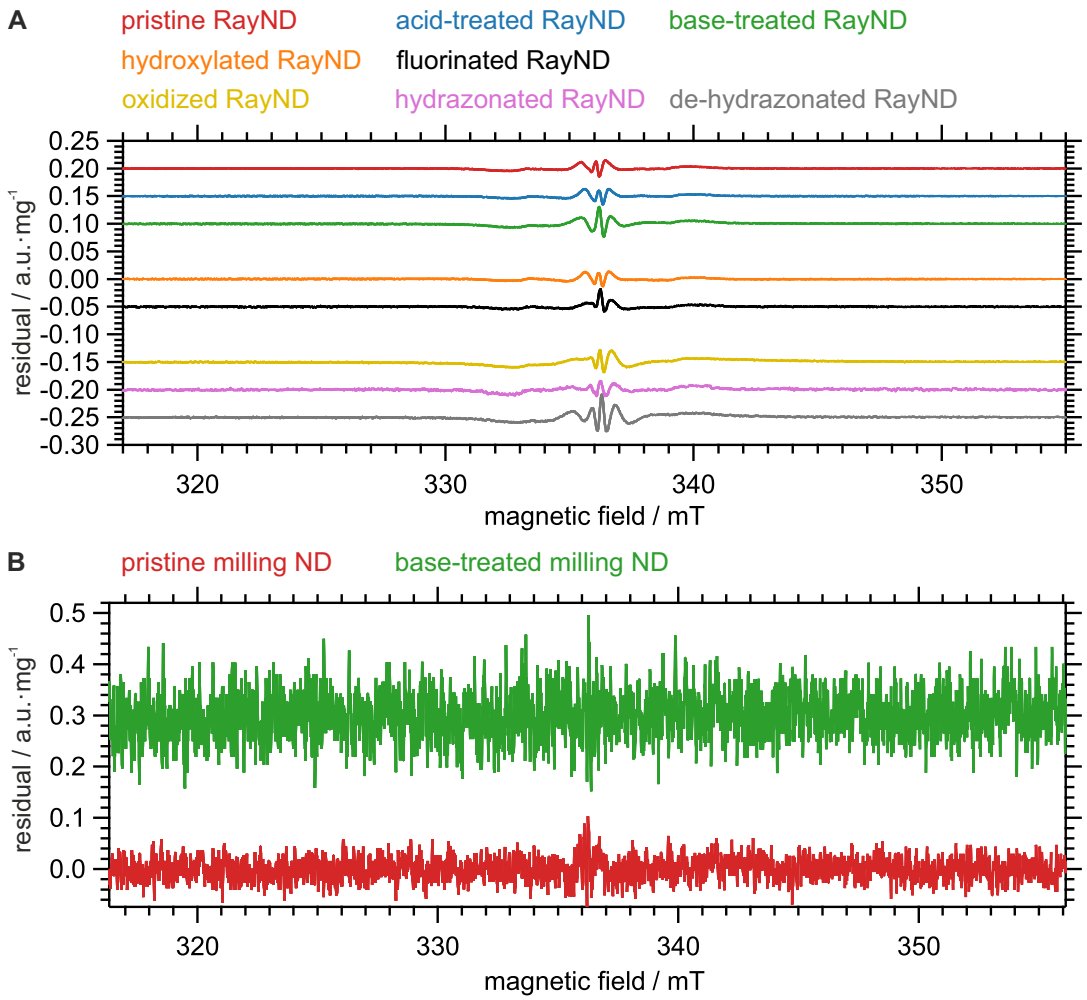

Figure 67: Residuals of EPR fit model for EPR measurements on **(A)** laser-ablated RayND material and **(B)** milled NDs. Offsets are chosen for clarity of representation. Color code corresponds to the one used to display the EPR measurements.

spectrum was fitted with regression parameters g_{db}, $lw_{\mathrm{lor,db}}$, and $H_{\mathrm{str,db}}$ that all were let unrestricted. Additionally, we obtained the weighting factors of the P1 (w_{P1}) and the dangling bond (w_{db}) spectrum. Finally, we want to address the accuracy of the chosen fit model. Fig. 67 shows the residuals of the fitting process for both materials, i.e., laser-ablated RayND and milled mND. The particular residuals reveal comparable patterns of deviation: outer inflection points as well as the inner one and both extrema give rise to minor approximation. However, if the area under the absolute value of the residual amplitude is determined, the

value for the sample with the largest deviation (RayND after de-hydrazonation) is $9\,\mathrm{a\,u}\cdot\mathrm{mg}^{-1}$. In relation to the total area of the integrated EPR signal (see Fig. 44), this leads to a fraction of 9×10^{-4}. Therefore, we consider the model used suitable for relative spin density quantification.

4.6.5 Estimation of dangling bond spin density per particle and square nanometer

In the following we give an estimation of the average number of surface radicals/ spins per particle and per nm^2, where we assumed that ND are separated into single-digit particles, i.e., no agglomeration occurs. Furthermore, we supposed spherical shape of the ND and a mass density of $\rho_m = 3\,\mathrm{g cm}^{-3}$.[267] Thus we could calculate the spin density per particle $\rho^{\mathrm{part.}}_{\mathrm{sp,db}}$ according to $\rho^{\mathrm{part.}}_{\mathrm{sp,db}} = \rho^{V}_{\mathrm{sp,db}}\cdot V_{\mathrm{ND}}$, where $\rho^{V}_{\mathrm{sp,db}} = \rho_m\cdot\rho_{\mathrm{sp,db}}$ and $V_{\mathrm{ND}} = \frac{4}{3}\pi r^3_{\mathrm{ND}}$. The values for the mass dangling bond spin density $\rho_{\mathrm{sp,db}}$ of RayND are given in Tab. 2 in the main text and the values for mND are presented in the next section as well as in the main text. Additionally, they are noted in Tab. 13, in which the computation results are also listed. Finally, we calculated the dangling bond surface area spin density $\rho^{A}_{\mathrm{sp,db}} = 4\pi r^2_{\mathrm{ND}}$, which is also shown in Tab. 13. The estimation of the particular dangling bond densities are in good accordance with Ref. [267], when especially

Table 13: Spin density per particle and per nm^2 of RayND and mND, while $r_{\mathrm{RayND}} = 2.5\,\mathrm{nm}$ and $r_{\mathrm{mND}} = 20\,\mathrm{nm}$.

protocol	$\rho_{\mathrm{sp,db}}$ g^{-1}	$\rho^{V}_{\mathrm{sp,db}}$ cm^{-3}	$\rho^{\mathrm{part.}}_{\mathrm{sp,db}}$	$\rho^{A}_{\mathrm{sp,db}}$ nm^{-2}
RayND	$1.86(2)\times10^{19}$	$5.58(5)\times10^{19}$	3.62(4)	0.046
RayND SAUD	$1.77(2)\times10^{19}$	$5.32(5)\times10^{19}$	3.46(3)	0.044
acid-treat. RayND	$1.89(2)\times10^{19}$	$5.67(5)\times10^{19}$	3.68(3)	0.047
base-treat. RayND	$1.69(2)\times10^{19}$	$5.07(5)\times10^{19}$	3.29(3)	0.042
hydroxyl. RayND	$1.78(2)\times10^{19}$	$5.33(5)\times10^{19}$	3.46(3)	0.044
fluorinat. RayND	$1.51(3)\times10^{19}$	$4.52(9)\times10^{19}$	2.94(6)	0.037
oxidized RayND	$2.68(5)\times10^{19}$	$8.05(9)\times10^{19}$	5.23(9)	0.067
hydrazon. RayND	$1.62(2)\times10^{19}$	$4.86(6)\times10^{19}$	3.16(4)	0.040
de-hydrazon. RayND	$1.82(4)\times10^{19}$	$5.46(9)\times10^{19}$	3.55(8)	0.045
mND	$9.5(9)\times10^{17}$	$2.8(3)\times10^{18}$	96(9)	0.020
base-treat. mND	$8.0(4)\times10^{17}$	$2.4(1)\times10^{18}$	80(4)	0.016

comparing the $\rho_{\mathrm{sp,db}}$ values. In this study spin counting was achieved using a TEMPOL (4-Hydroxy-TEMPO) standard. It should be noted, however, that in Ref. [284] dangling bond surface area density $\rho^A_{\mathrm{sp,db}}$ is estimated by $1\,\mathrm{nm}^{-2}$ and $13\,\mathrm{nm}^{-2}$, respectively. The first value is obtained by applying the Fermi "golden rule" and certain assumptions like lorentzian lineshape and sudden jump model. The second value was determined by W band EPR spectroscopy using the area of the P1 signal as spin standard. However, since this reference does not specify how the P1 signal was recovered from the total EPR signal, it is difficult to explain the discrepancy with our values.

4.6.6 Details on ODMR measurements

In the following we provide further details about the ODMR measurements.
For these experiments we decided to use milled ND material (mND, see Chap. 4.6.2), which contains a higher content of NV centers, and which in preliminary investigations both, showed stable fluorescence signals and allowed the performance of pulse experiments in a reliable manner in contrast to RayND. In order be able to correlate the ODMR results with those obtained previously in the bulk EPR experiments, we also carried out an EPR study on this material beforehand. For sample preparation in the case of pristine mND, 1 mL of the as-received slurry was centrifuged, the supernatant removed and the sediment washed three times with 1 mL *iso*-propanol. After the last of these steps, 1 mL of the suspension, which nominally contained 1 mg mND, was transferred into an EPR tube and dried overnight in the oven at 150 °C. The base treatment of the mND material rendered the protocol described in Chap. 4.6.2**(0)&(2)**. To conduct EPR measurements, 1.5 mg of the dried base-treated mND was transferred into an EPR tube.
The results are presented in Fig. 68. As in the case of the RayND material, the area of the double-integrated signal is smaller for the base-treated sample than for the pristine mNDs. The deconvolution according to the two-spin model described in chapter 4.6.4 results in relative weights for the dangling bond signal of pristine and base-treated mND, respectively, that are comparable with each other ($w_{\mathrm{db,pristine}} = 81\,\%$ vs. $w_{\mathrm{db,base\text{-}tr.}} = 84\,\%$). Thus, the surface area of the double-integrated EPR signals corresponds directly to the dangling bond spin density $\rho_{\mathrm{sp.,db}}$. The computation yields for the pristine material $\rho_{\mathrm{sp.,db}} = 5.4(5) \times 10^{14}\,\mathrm{mg}^{-1}$ and for base-treated mND $\rho_{\mathrm{sp.,db}} = 4.6(2) \times 10^{14}\,\mathrm{mg}^{-1}$. So it can be stated that within 3σ error margins the surface spin density has decreased by 15(9) % because of base treatment, whereby the high uncertainty of the result is mainly due to the

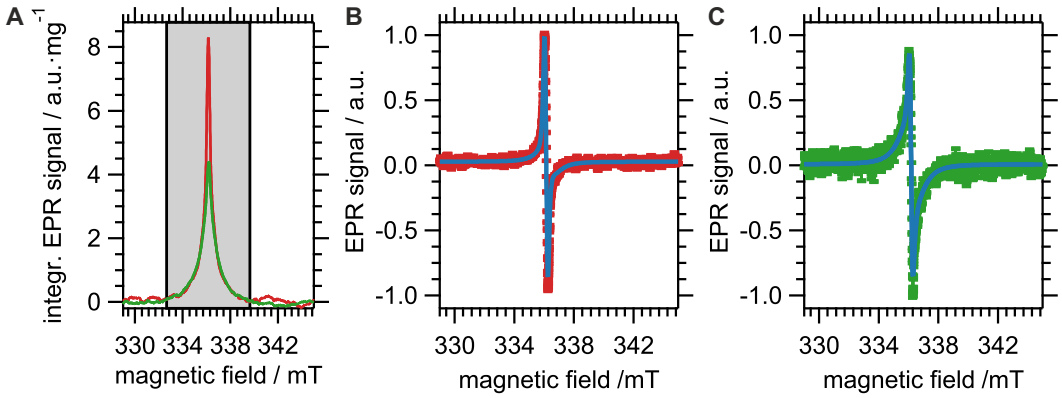

Figure 68: Bulk EPR investigation of milled ND (mND). **(A)** Double-integrated EPR signal of pristine (red) and base-treated (green) mND. The gray area indicates the magnetic field interval over which numerical integration was performed. **(B)** Deconvolution of the EPR signal (red) of pristine mND by means of the two-spin model (blue line) which reveals $g_{\mathrm{P1}} = 2.0028$, $lw_{\mathrm{lor,P1}} = 0.35\,\mathrm{mT}$, $H_{\mathrm{str.,P1}} = 0.20\,\mathrm{MHz}$, $w_{P1} = 1.0 \times 10^{-3}$; $g_{\mathrm{db}} = 2.0027$, $lw_{\mathrm{lor,db}} = 1.17\,\mathrm{mT}$, $H_{\mathrm{str.,db}} = 23\,\mathrm{MHz}$, $w_{\mathrm{db}} = 4.4 \times 10^{-3}$. **(C)** Deconvolution of the EPR signal (green) of base-treated mND by means of the two-spin model (blue line) which reveals $g_{\mathrm{P1}} = 2.0028$, $lw_{\mathrm{lor,P1}} = 0.23\,\mathrm{mT}$, $H_{\mathrm{str.,P1}} = 0.85\,\mathrm{MHz}$, $w_{P1} = 0.24$; $g_{\mathrm{db}} = 2.0028$, $lw_{\mathrm{lor,db}} = 1.03\,\mathrm{mT}$, $H_{\mathrm{str.,db}} = 0.01\,\mathrm{MHz}$, $w_{\mathrm{db}} = 4.8$.

weighing inaccuracy during sample preparation. The corresponding result for the RayND material is 9(1) %, which gives a good agreement regarding the effect of the base treatment on the averaged spin density of the two different ND materials. Furthermore, it can be seen that the absolute value of the spin density for mND is decreased by a factor of about 34(6) compared to the laser-ablated ND. Without treating this point in too much detail, a size-dependent effect can be used as a simple explanation for it has also been found in other reports.[269,271] If in the simplest case a linear dependence of the dangling bond spin density on the size is assumed, the values given in [271] for an increase in size by a factor of 8, which also applies to our investigation, result in a decrease for $\rho_{\mathrm{sp.,db}}$ by a factor of approximately 17.
ODMR experiments for both, pristine and base-treated mNDs, were conducted as follows. Fluorescence spots representing ND cluster were selected unbiased, i.e. without any preference with respect to their absolute photon count rate or signal-to-background ratio.
Subsequently, on selected ND clusters coincidence measurements, i.e. measuring the probability that two photons are emitted at the very same time, were undertaken by using Hanbury Brown and Twiss arrangement of two detectors with

photon counting rates $I_1(t)$ and $I_2(t)$ at time t, respectively, which can be transformed to a Second-order autocorrelation function

$$g^{(2)}_{\mathrm{corr}}(\Delta t_{01}) = \frac{\langle I_{1,\mathrm{corr}}(t_0)\rangle \langle I_{2,\mathrm{corr}}(t_1 - t_0)\rangle}{\langle I_{1,\mathrm{corr}}(t_0)\rangle \langle I_{2,\mathrm{corr}}(t_0)\rangle} = \frac{\langle I_{1,\mathrm{corr}}(t_0)\rangle \langle I_{2,\mathrm{corr}}(\Delta t_{01})\rangle}{\langle I_{1,\mathrm{corr}}(t_0)\rangle \langle I_{2,\mathrm{corr}}(t_0)\rangle}$$

by appropriate background correction (see Chap. 2.4.2),[149,151] where $\langle\cdot\rangle$ means time averaging. For a single photon emitter holds true $g^{(2)}_{\mathrm{corr}}(\Delta t_{01} \to 0) < 0.5$, which is because of its finite excited state lifetime, and for a small number n of emitters $g^{(2)}_{\mathrm{corr}}(\Delta t_{01} \to 0) = 1 - \frac{1}{n}$.[149] However, cf. Ref. [205] for recent results on the limitation of this procedure. An example data set together with its evaluation is given in Fig. 69**A**. Next, a cw-ODMR spectrum was recorded. In summary, the spectra are characterized by a broad linewidth ($10 - 30$ MHz) and often a fine structure can be observed. Nevertheless, no systematic patterns can be seen that would allow a distinction between pristine and base-treated mND with regard to specific spectroscopic parameters. Possible causes for the splitting of a particular

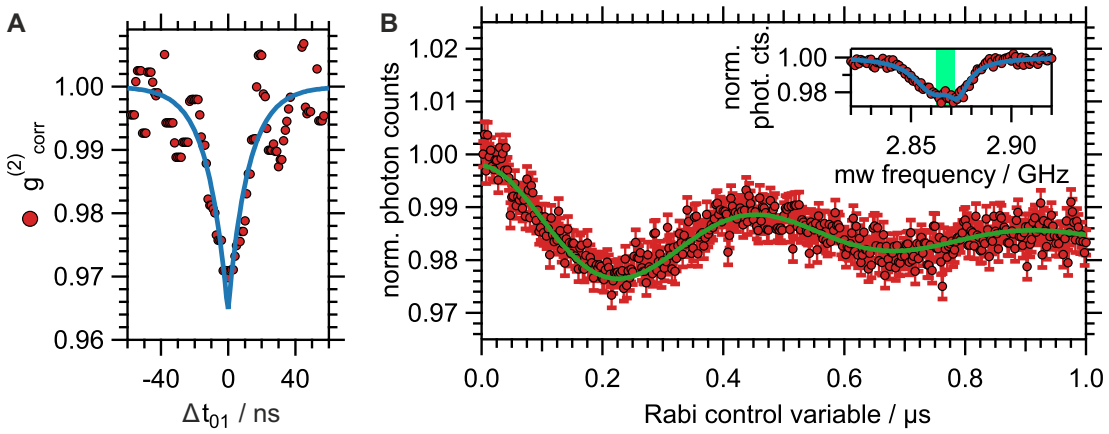

Figure 69: (A) Example second order autocorrelation function measurement on mND cluster. Data (red) were approximated by an exponential function depending on conditional delay time $\Delta_{01} = t_1 - t_0$. **(B)** Inset: Example cw-ODMR data (red) recorded on mND. The blue line is a two Lorentzian fit ($\nu_1 = 2.61(1)$ GHz, $lw_{1,\mathrm{lor}} = 12(3)$ MHz, $\nu_2 = 2.873(1)$ GHz, $lw_{2,\mathrm{lor}} = 13(2)$ MHz), the light green bar symbolizes the typical excitation bandwidth for relaxation time measurements. Data (red) in the main graph shows spin state oscillation under a Rabi control sequence for which the microwave pulse length (control variable) is incremented. The fit model (green) is a sinusoidal function with exponentially decaying envelope, where the Rabi frequency is given by $\Omega/2\pi = 2.191(2)$ MHz and the decay time by $T_{\mathrm{Rabi}} = 4.0(2) \times 10^2$ ns.

signal are hyperfine interaction with nearby nuclear species, especially ^{13}C, and surface-induced crystal strain, which may rank in the few-MHz regime.[299,300] The inset of Fig. 69**B** shows an example cw-ODMR spectrum.

The characteristic Rabi frequency Ω of the $|0\rangle \leftrightarrow |\pm 1\rangle$ spin state oscillation depends according to $\Omega = \gamma B_1$ (with gyromagnetic ratio γ) on the microwave amplitude B_1 which in turn is a function of the distance between ND cluster and microwave antenna. Since ND clusters were randomly distributed with respect to the latter, we next performed Rabi oscillation measurements by incrementing the duration of the microwave pulse after polarizing the NV^- center ensemble into the $m_s = 0$ spin sub-state (see Fig. 70**A**). Spin state readout was achieved by optical laser addressing with $\lambda = 520\,\text{nm}$ excitation wavelength and counting of red-shifted emission photons (see Chap. 2.4.1 for details).

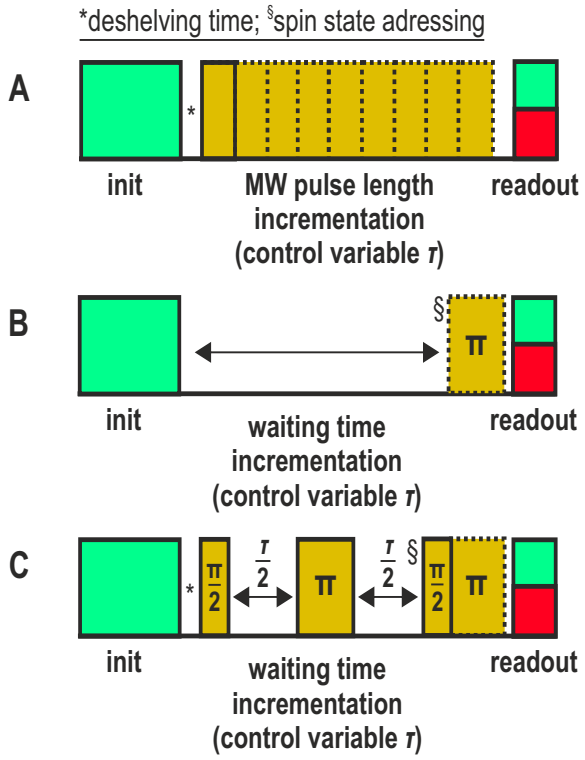

Figure 70: Pulse schemes used. **(A)** Rabi, **(B)** T_1, **(C)** Hahn echo measurement. See text for details.

Due to internal level transition dynamics, spin state information is encoded within the first $\approx 400\,\text{ns}$ of the responsive emission, while later photon counts in the range $2 - 3\,\mu\text{s}$ after starting the readout represent equilibrium which is used for normalization and initialization. The later is completed by a $1.5\,\mu\text{s}$ dark time in which population from the singlet shelving state decays to the $m_s = 0$ ground state.[20] Typical values of the Rabi frequency were in the range of $\Omega/2\pi = 1.5 - 2.5\,\text{MHz}$ which corresponds to a $\frac{\pi}{2}$ pulse length of 167 ns at the lower and 100 ns at the upper frequency limit, and gives rise to a microwave excitation bandwidth of $\approx 1\,\text{MHz}$. Determination of the longitudinal T_1 spin relaxation time was designed as differential measurement protocol, which includes spin state addressing by either applying no mw pulse (readout of $m_s = 0$ state population) or a π pulse (readout of $m_s = \pm 1$ state population) and subsequent differential normalization of both data sets (see

Fig. 70**B**).[205,301] After initialization, an incremented waiting time (control variable τ) allows for free evolution of the NV^- center spin Hamiltonian, whose diagonal elements in our case (zero magnetic field) are mainly governed by the zero field splitting parameter $D = 2.87\,\mathrm{GHz}$ and off-diagonal magnetic field contributions characterizing the spin bath which couple the spin states $|0\rangle$ and $|\pm1\rangle$.[40] The evolution of the population $\rho_0^-(0)$ and $\rho_{\pm1}^-(0)$ of the initial spin states $m_s = 0$ and $m_s = \pm1$ after polarization due to dipolar coupling is given by[205]

$$\rho_0^-(\tau) = \left(\frac{1}{3} + \frac{2}{3}\exp\left(-\frac{\tau}{T_{1,\mathrm{db}}}\right)\right)\rho^-(0) \tag{4.8}$$

and

$$\rho_{\pm1}^-(\tau) = \left(\frac{1}{3} - \frac{1}{3}\exp\left(-\frac{\tau}{T_{1,\mathrm{db}}}\right)\right)\rho^-(0) \tag{4.9}$$

where $\rho^-(0) = \rho_0^-(0) + \rho_{-1}^-(0) + \rho_{+1}^-(0)$ and $\frac{1}{T_{1,\mathrm{db}}} = \Gamma_{1,\mathrm{db}} \propto \omega_{db}$, with ω_{db} is the coupling strength between NV^- center and dangling bond spin-bath (Note that we assume ideal spin polarization, which, in general, is not the case under experimental conditions). However, when charge state transitions are present, i.e. $NV^- \leftrightarrow NV^0 + e^-$, $\rho^-(0)$ is no longer time-independent. Two scenarios have to be considered differently, which we illustrate only for $\rho_0^-(\tau)$ due to its spin state invariance.[205] Charge state recombination, $NV^0 + e^- \rightarrow NV^-$,

$$\rho_0^-(\tau) = \left(\frac{1}{3} - \frac{1}{3}\exp\left(-\frac{\tau}{T_{1,\mathrm{db}}}\right)\right)\rho^-(0) + \frac{1}{3}\left(\rho^-(\tau) - \rho^-(0)\right) \tag{4.10}$$

and ionization, $NV^- \rightarrow NV^0 + e^-$,

$$\rho_0^-(\tau) = \left(\frac{1}{3} - \frac{1}{3}\exp\left(-\frac{\tau}{T_{1,\mathrm{db}}}\right)\right)\rho^-(\tau) \tag{4.11}$$

when for both processes $\rho^-(\tau) = \rho_0^-(\tau) + \rho_{-1}^-(\tau) + \rho_{+1}^-(\tau)$.
Conducting the differential protocol, the total photon emission em_{ph} in a measurement, where the π pulse is absent, is given by the sum of the population-weighted photon emission of the particular states

$$em_{\mathrm{ph}}(\tau) = em_{\mathrm{ph},0}^-\rho_0^-(\tau) + em_{\mathrm{ph},+1}^-\rho_{+1}^-(\tau) + em_{\mathrm{ph},\text{-}1}^-\rho_{-1}^-(\tau) + em_{\mathrm{ph}}^0\rho^0(\tau) \tag{4.12}$$

accounting for NV^0 luminescence by $em_{\mathrm{ph}}^0\rho^0(\tau)$. After applying a π pulse resonant

with the $|0\rangle \leftrightarrow |+1\rangle$ transition, Eq. (4.12) reads

$$em_{\mathrm{ph},\pi}(\tau) = em^{-}_{\mathrm{ph},0}\rho^{-}_{+1}(\tau) + em^{-}_{\mathrm{ph},+1}\rho^{-}_{0}(\tau) + em^{-}_{\mathrm{ph},\text{-}1}\rho^{-}_{-1}(\tau) + em^{0}_{\mathrm{ph}}\rho^{0}(\tau). \tag{4.13}$$

Subtraction of both data sets leads to

$$em_{\mathrm{ph},\Delta}(\tau) = em_{\mathrm{ph}}(\tau) - em_{\mathrm{ph},\pi}(\tau) = \left(em^{-}_{\mathrm{ph},0} - em^{-}_{\mathrm{ph},+1}\right)\left(\rho^{-}_{0}(\tau) - \rho^{-}_{+1}(\tau)\right). \tag{4.14}$$

Casting Eq. (4.10) or Eq. (4.11) into (4.14), let us receive

$$em^{\mathrm{recomb.}}_{\mathrm{ph},\Delta}(\tau) = K\exp\left(-\frac{\tau}{T_{1,\mathrm{db}}}\right) \tag{4.15}$$

and

$$em^{\mathrm{ion.}}_{\mathrm{ph},\Delta}(\tau) = K\exp\left(-\frac{\tau}{T_{1,\mathrm{db}}}\right)\left(\frac{\rho^{-}(\tau)}{\rho^{-}(0)}\right) \tag{4.16}$$

whereas $K = \frac{em^{-}_{\mathrm{ph},0} - em^{-}_{\mathrm{ph},+1}}{\rho^{-}(0)}$. From Eq. (4.15) we can deduce that the differential measurement protocol mask $\mathrm{NV}^-/\,\mathrm{NV}^0$ recombination processes, therefore, revealing the pure T_1 spin relaxation time. Ionization processes, however, still contribute to the measurement outcome and may interfere with the T_1 value. Assuming for it a first-order kinetic with rate constant $\Gamma_{\mathrm{ion.}} = \frac{1}{T_{\mathrm{ion.}}}$ Eq. (4.16) transforms to

$$em^{\mathrm{ion.}}_{\mathrm{ph},\Delta}(\tau) \propto K\exp\left(-\frac{\tau}{T_{1,\mathrm{db}}}\right)\exp\left(-\frac{\tau}{T_{1,\mathrm{ion.}}}\right) \propto K\exp\left(-\frac{T_{1,\mathrm{db}} + T_{1,\mathrm{ion.}}}{T_{1,\mathrm{db}}T_{1,\mathrm{ion.}}}\tau\right) \tag{4.17}$$

with a new apparent decay time $T_{\mathrm{app.}} = \frac{T_{1,\mathrm{db}}T_{1,\mathrm{ion.}}}{T_{1,\mathrm{db}}+T_{1,\mathrm{ion.}}}$. Two notes on this: 1. Since Ref. [205] propose also a mitigation protocol to suppress charge state ionization, future T_1 measurements should include this pulse scheme extension. 2. Our functionalization protocols aimed to improve the sensing properties of ND hosted NV^- centers. Thus, if the average prolongation of the T_1 relaxation time due to base treatment is partly caused by the suppression of ionization processes, this still represents an improvement, which would call for further investigations.

In Fig.s 71 - 74 we present complete contrast data sets obtained in course of the experiments, while Fig.s 71, 72 represent the measurements on pristine and Fig. 73, 74 on base-treated mND. For both mND materials a raw data set of

both traces, i.e. without and with applying a π pulse (pristine mND: Fig. 72**D**, base-treated mND: Fig. 73**A**) is given.

The characteristic decay time constant which is obtained by the Hahn echo pulse sequence is the transversal T_2 relaxation time (Fig. 70**C**). We take this quantity as a figure of merit which indicates whether a NV^- center is an appropriate sensor since it comprises a first estimate of its sensitivity; only dipolar coupling frequencies in the range of $\frac{\omega_{\mathrm{coupl}}}{2\pi} \leq \frac{1}{T_2}$ are detectable by this sequence. However, dynamic decoupling approaches allow for prolongation of T_2 (see Chap. 1.4).[23]

We turn to the characteristics of our measurements. The final mw pulse is alternatively chosen as $\frac{\pi}{2}$ or $\frac{3}{2}\pi$ pulse for the very same reason discussed above - to mitigate spin-independent contributions by differential contrast. In Fig. 75**F** and 76**G** we present a data set which contains a corresponding measurement outcome for pristine and base-treated mND, respectively. The remaining data sets in Fig. 75 and Fig. 76 are already shown in the contrast representation. When examining the results, it is obvious that they do not show mono-exponential dependencies. However, this behavior is known from literature and explained as effects due to pulse errors and incomplete refocusing.[302] Therefore, to extract the T_2 relaxation time we adopted a two-exponential model discarding the contribution of the initial increasing in spin state contrast. The T_2 values correspondingly obtained are given with the presentation of the corresponding data sets.

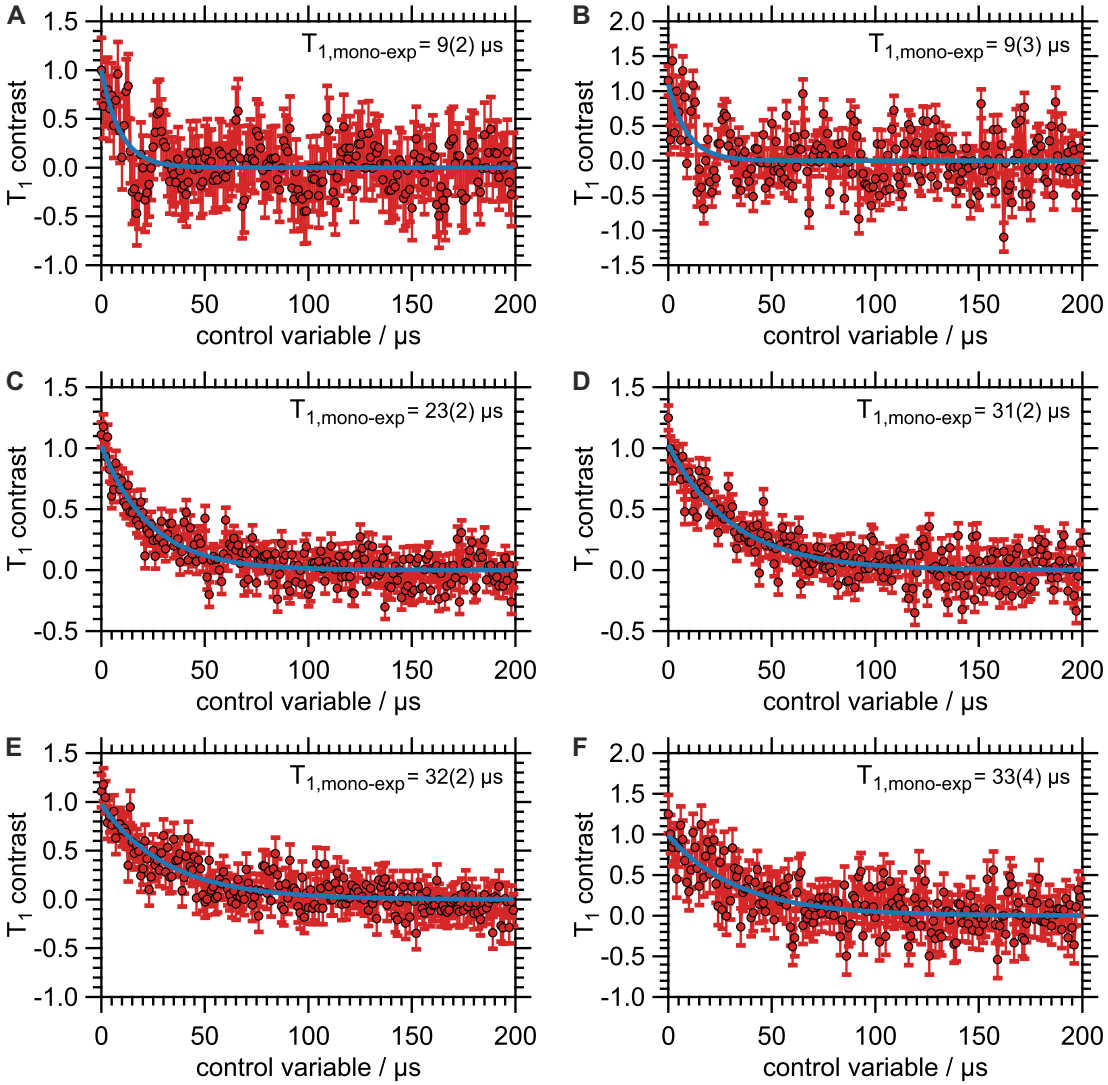

Figure 71: (A) - (F) Normalized data sets (red) of T_1 relaxation time measurements on pristine mND were obtained by subtraction of the $|0\rangle$ and $|\pm1\rangle$ projection measurement data (see example: Fig. 72**D**). Blue lines display mono-exponential decay functions. The corresponding decay time T_1 is noted for every data set.

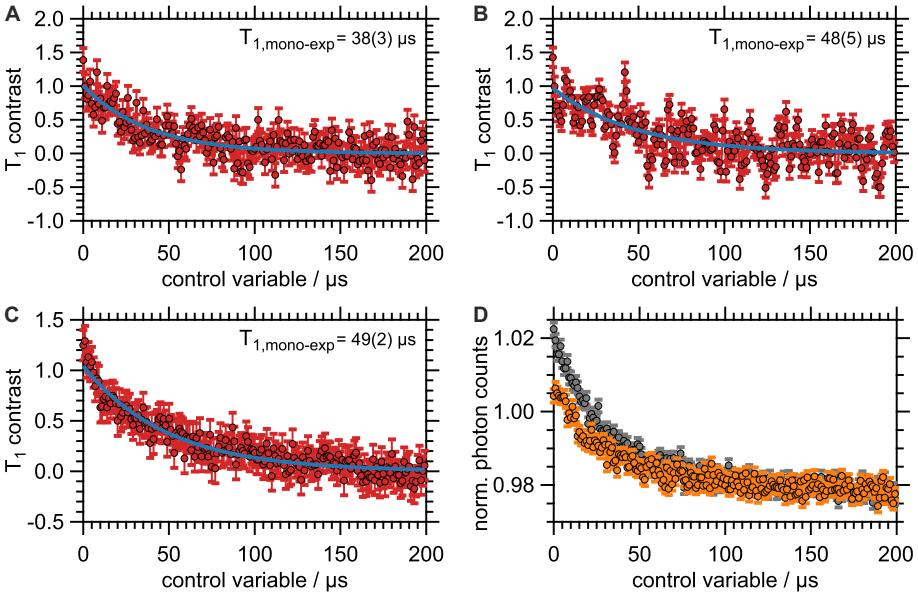

Figure 72: **(A)** - **(C)** Normalized data sets (red) of T_1 relaxation time measurements on pristine mND were obtained by subtraction of the $|0\rangle$ and $|\pm1\rangle$ projection measurement data; example: **(D)**. Blue lines display mono-exponential decay functions. The corresponding decay time T_1 is noted for every data set.

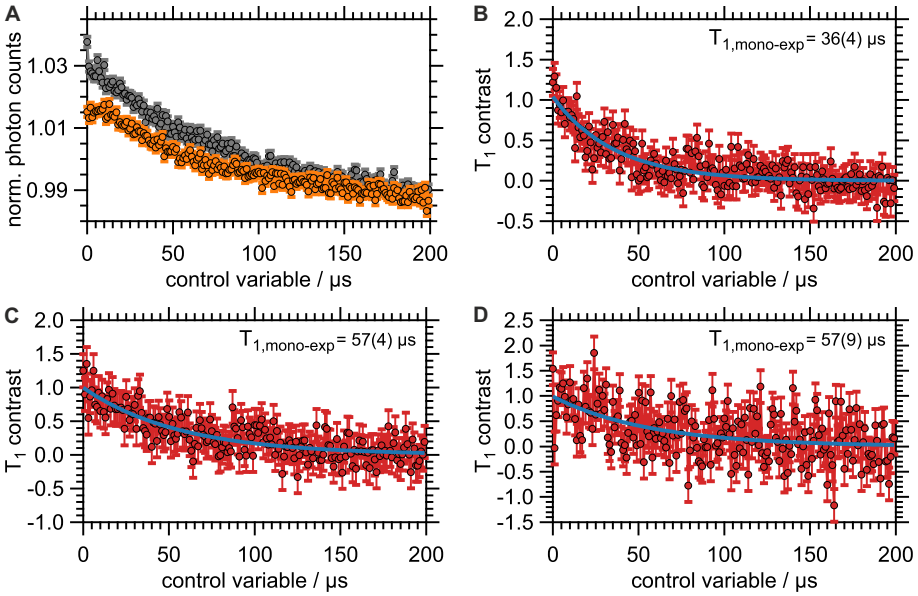

Figure 73: **(B)** - **(D)** Normalized data sets (red) of T_1 relaxation time measurements on base-treated mND were obtained by subtraction of the $|0\rangle$ and $|\pm1\rangle$ projection measurement data; example: **(A)**. Blue lines display mono-exponential decay functions. The corresponding decay time T_1 is noted for every data set.

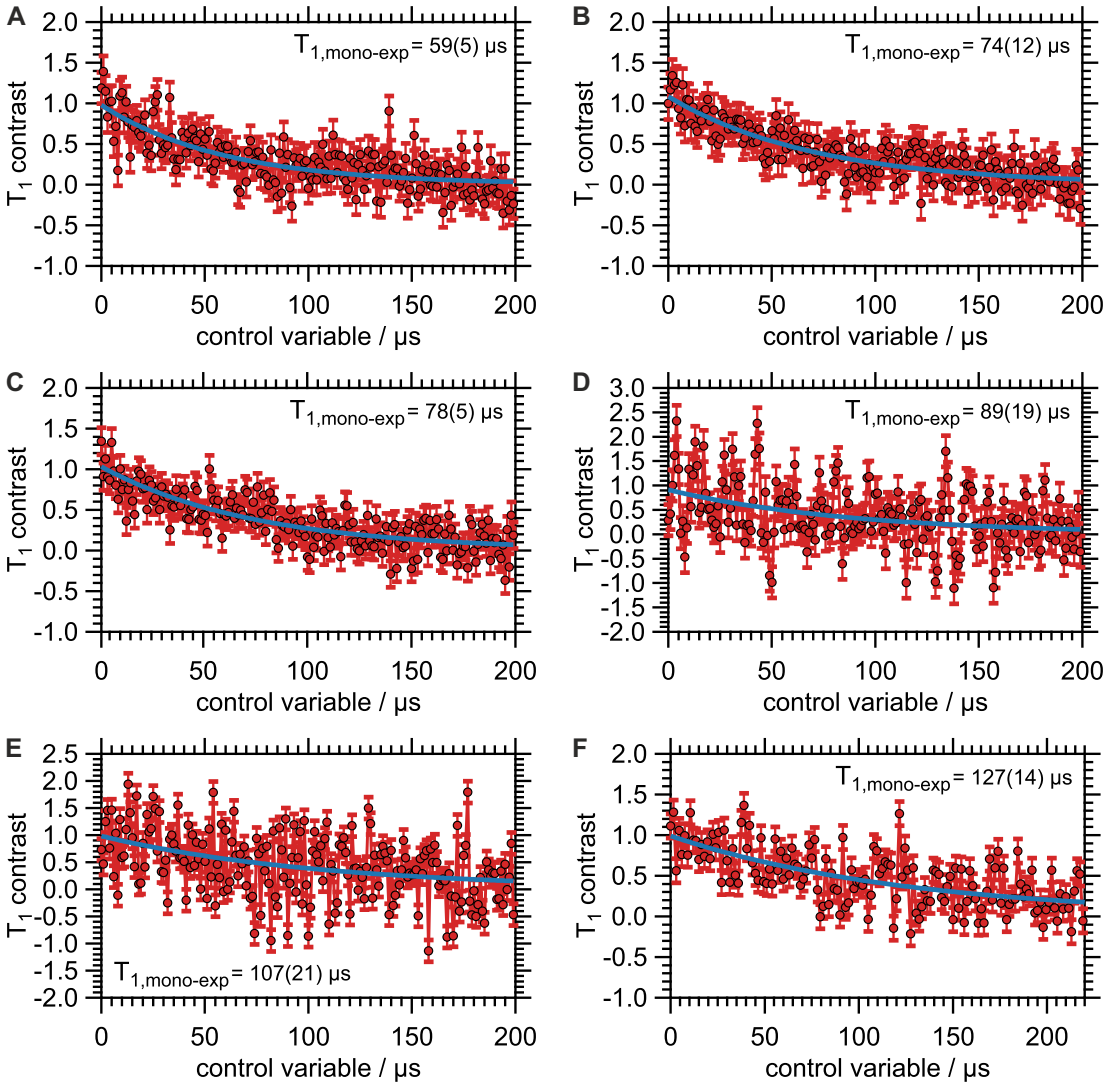

Figure 74: **(A)** - **(F)** Normalized data sets (red) of T_1 relaxation time measurements on base-treated mND were obtained by subtraction of the $|0\rangle$ and $|\pm 1\rangle$ projection measurement data (see example: Fig. 73**A**). Blue lines display mono-exponential decay functions. The corresponding decay time T_1 is noted for every data set.

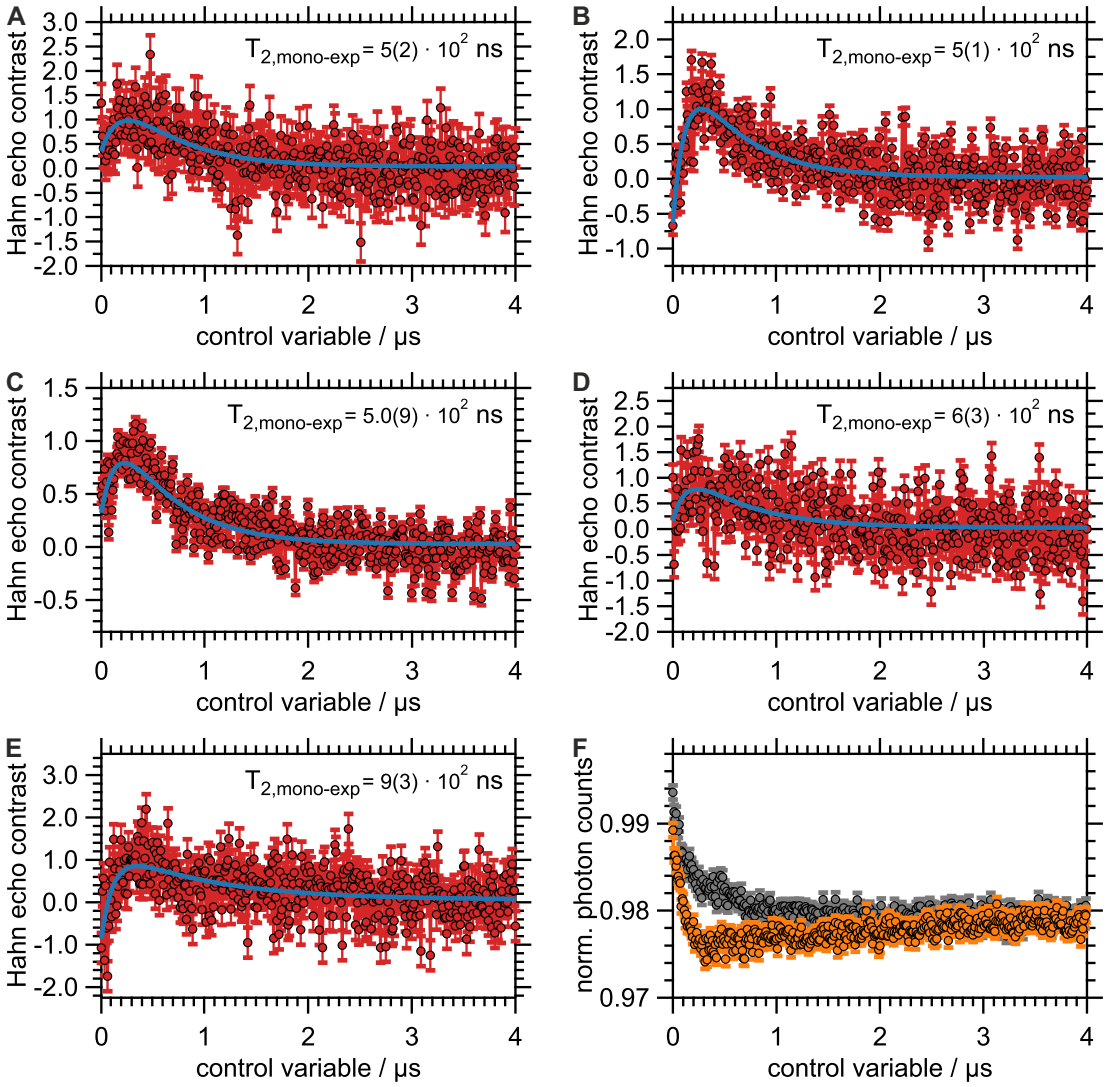

Figure 75: (A) - (E) Normalized data sets (red) of T_2 relaxation time Hahn echo measurements on pristine mND were obtained by subtraction of the $|0\rangle$ and $|\pm1\rangle$ projection measurement data; example: **(F)**. Blue lines display double-exponential decay functions, the reason for which is explained in the text. The corresponding mono-exponential decay time T_2 is noted for every data set.

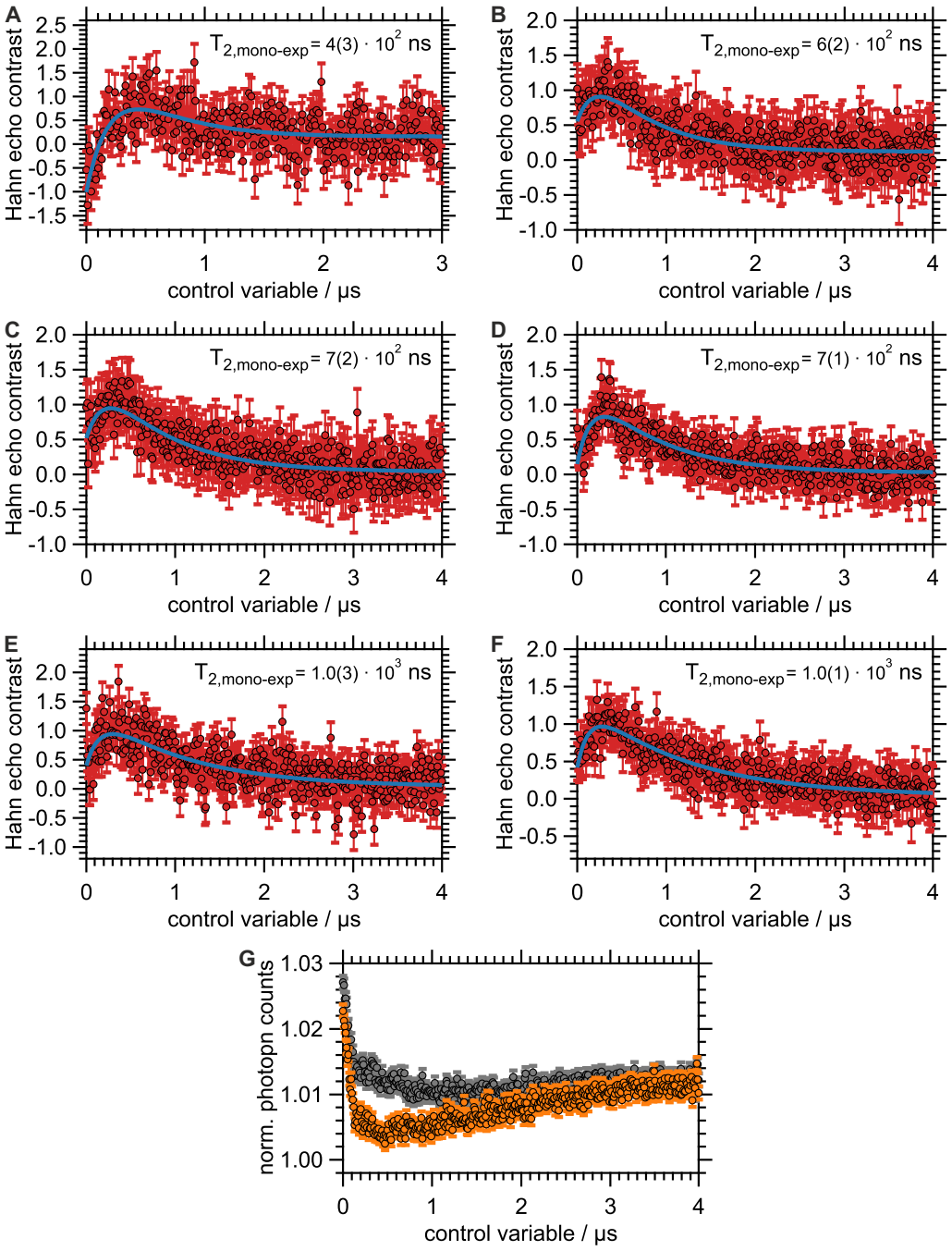

Figure 76: (A) - (E) Normalized data sets (red) of T_2 relaxation time Hahn echo measurements on base-treated mND were obtained by subtraction of the $|0\rangle$ and $|\pm1\rangle$ projection measurement data; example: **(G)**. Blue lines display double-exponential decay functions, the reason for which is explained in the text. The corresponding mono-exponential decay time T_2 is noted for every data set.

5 Detecting an electron transfer reaction in the single-molecule regime using a diamond based quantum sensor

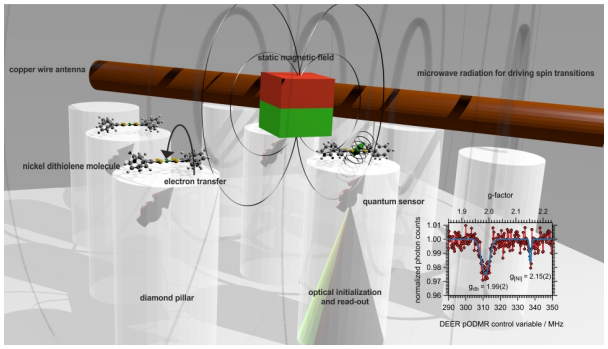

A magnetic field sensor possessing nanometer-resolution and single spin sensitivity, sheltered in a chemically resilient matrix to boot, seems to surpass a chemist's dreams. Yet, the negatively charged nitrogen-vacancy (NV^-) center, a diamond lattice defect, already meets the aforementioned requirements and, hence, augurs fruitful applications in a plenty of scientific issues, for instance in catalysis, surface, and life science research. Despite scant examples hereto, in which organic or biological species attached to the diamond surface have been investigated, NV center-assisted optically detected magnetic resonance measurements are still in their infancy and bides for the eligible recognition of the respective communities. Here, we address the electrochemical behavior of few neutral and EPR-silent transition metal complex molecules, namely nickel bis(diphenyldithiolene), onto an oxygen-terminated diamond surface. By employing a nearby located NV^- center quantum sensor we gain strong evidence of a reduction process occurring on the nickel complex which we ascribe to an electron transfer from the diamond substrate. The g-factor of the reduced nickel species significantly differs from values previously obtained in NV^- center-assisted electron paramagnetic resonance spectroscopy on either bulk-inherent paramagnetic centers or surfaced-attached biological and organic samples. Both, Hahn echo spin locking and double electron-electron resonance quantum sensing protocols, certify that our experiments probe the single-molecule regime where thermal polarization is overcome. Supported by quantum chemical calculations, thus, we are capable of garnering additional insights into the nature of the electron transfer reaction.The presented coherent control of the nickel complex's spin levels should allow a complete elucidation of its spin constituents and spin environment in future.

5.1 Introduction

With the emerging of methods such as scanning probe microscopy, high-resolution fluorescence microscopy, and surface- as well as tip-enhanced Raman spectroscopy impressive progress has been made in recent decades that now allows for observing processes on the scale of single molecules.[6,7,9,10,14–16] However, magnetic resonance methods could only recently accomplish measurements in this range with the development of the diamond-hosted NV^- center as a magnetic field sensor (see Chap. 0.2). The results achieved so far in the field of sensing electron spins, which are located outside the diamond matrix, have been achieved on bioorganic samples.[303,304] Here we try to investigate for the first time the electron spin of a transition metal complex, namely nickel bis(diphenyldithiolene) (see Fig. 77). Initially, our experiment was designed to first apply the neutral complex to the diamond surface in order to conduct preliminary investigations. Only the chemical reduction should lead to the spin-active $[Ni(S_2C_2Ph_2)_2]^-$ anion. Remarkably, the results of this chapter will, however, show that this step is unnecessary as the diamond surface may act as a reducing agent. We have chosen nickel bis(diphenyldithiolene) as the subject of our investigations because this transition metal complex has an easily accessible redox chemistry.[305] In current research, it is the focus of the research of artificial photosynthesis systems,[306] is used in optoelectronics,[307] and recently has been proposed as possible qubit.[308]

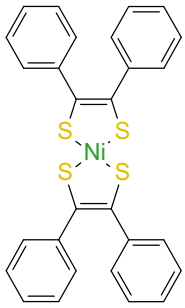

Figure 77: Ni bis(diphenyldithiolene)

The following part of this thesis is currently in preparation for publication in a peer-reviewed journal: R. Wieczorek, J. M. Kurzhals, W. Harneit, Detecting an electron transfer reaction in the single-molecule regime using a diamond based quantum sensor, in preparation.

5.2 Results

The sensing experiments which aimed to detect $Ni(S_2C_2Ph_2)_2$ deposited on the diamond surface were preceded by preliminary investigations regarding both, the nickel bis(diphenyldithiolene) precursor (see Chap. 5.2.1) and the NV^- center quantum sensor (see Chap. 5.2.4). Due to technical reasons a g-scale calibration of the MHz frequency band had to be carried out (see Chap. 5.2.3). A brief introduction to NV-DEER spectroscopy is presented in Chap. 5.2.2. The ODMR results indicating an electron transfer reaction are given in Chap. 5.2.5.

5.2.1 Pre-characterization of nickel bis(diphenyldithiolene) in bulk

Before we conducted NV^- center-assisted ODMR sensing experiments, which basically rendered a canonical before/after-type concept, we produced and characterized the nickel complex under investigation. The synthesis of nickel bis(diphenyl-

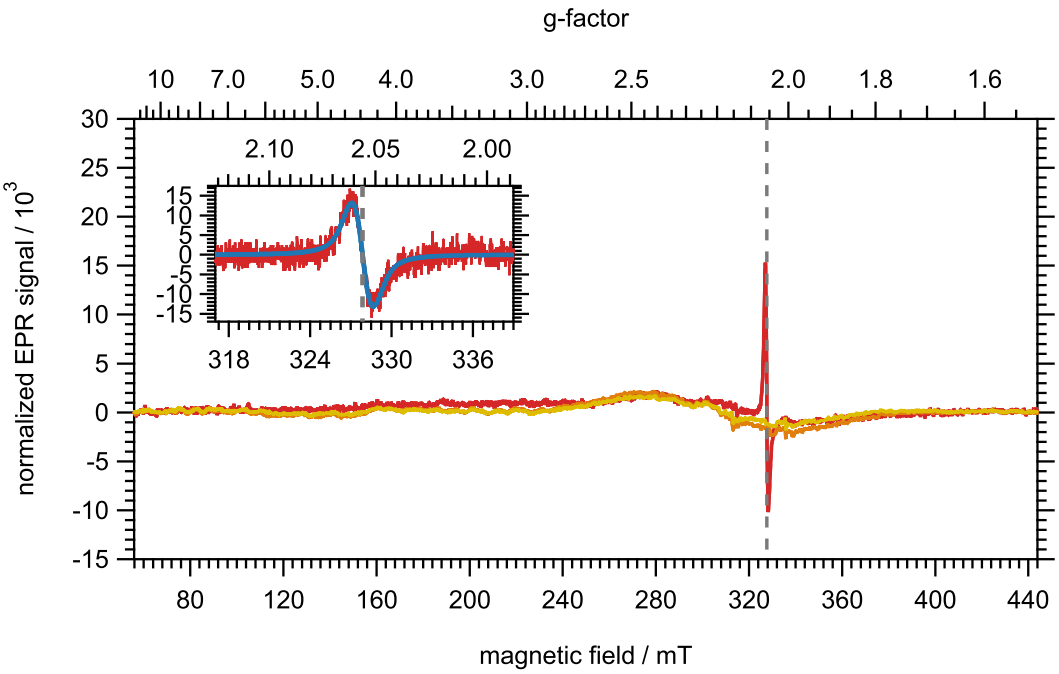

Figure 78: EPR spectra of $Ni(S_2C_2Ph_2)_2$ (orange), $[Ni(S_2C_2Ph_2)_2]^-$ (red), and $[Ni(S_2C_2Ph_2)_2]^{2-}$ (yellow). Background modulation is due to power-dependent cavity effects. Inset: (same units as main figure) High-resolved EPR spectrum of $[Ni(S_2C_2Ph_2)_2]^-$. The blue line indicates pseudo-Voigtian fit. In both data sets the gray line marks the inflection point of the pseudo-Voigtian model, where $g = 2.0561(8)$.

dithiolene) was conducted according to the classical literature protocol using NiS and diphenylacetylene (see Chap. 5.4.2)[309] without taking advantage of more sophisticated strategies, which may be given by the utilization of 1,3-dithiol-2-ones or alkylated phosphorus intermediates.[310,311] Besides its simplicity the chosen protocol convinces by its phosphorus-free approach. Since electron-electron dipolar coupling frequencies are expected to be around 1×10^2 kHz under our experimental conditions, with a static magnetic field of $\approx 10\,\mathrm{mT}$, the corresponding ^{31}P Lamor frequency ($\gamma_{^{31}\mathrm{P}} = 17.2\,\mathrm{MHzT}^{-1}$) would fall in the same range and could lead to spurious signals.
We confirmed the success of our reaction by IR spectroscopy, which reveals the characteristic vibration signals of the $[NiS_2C_2]$ core (see Chap. 5.4.3). Additionally, we investigated the reduction cascade $Ni(S_2C_2Ph_2)_2 \rightarrow [Ni(S_2C_2Ph_2)_2]^- \rightarrow$, $[Ni(S_2C_2Ph_2)_2]^{2-}$ by using *p*-phenylenediamin to perform one-electron reduction and $BH_3 \cdot THF$ to produce the di-anion either starting from the neutral complex or the mono-anion. The energy $E.$ of d orbitals of the nickel complex in a D_{4h} symmetric square planar crystal field is given by $E_{xz} = E_{yz} < E_{z^2} < E_{xy} < E_{x^2-y^2}$. We assume nickel to be in the oxidation state 2+ (d^6). Consequently, the xy orbital constitutes its LUMO. Thus, the aforementioned electron transfer reactions are supposed to cause a change in the spin quantum number S according to $S = 0$, $S = \frac{1}{2}$, and $S = 0$, respectively. EPR measurements could confirm this expectation, and we obtained for the mono-anion an isotropic *g*-factor of $g = 2.0561(8)$ which is in good accordance with the reported value (see Fig. 78 and Chap. 5.4.5).[312]

5.2.2 Basics of NV^- center double electron-electron resonance measurements

Before we present the spectroscopic results, we briefly introduce NV-DEER spectroscopy, which facilitates the detection of spins in the vicinity of the NV^- center via dipolar electron-electron interaction. The Hamiltonian of this system according to secular approximation is given by[31]

$$\hat{H} = 2\pi \cdot D\hat{S}^2_{z,\mathrm{NV}} + \gamma_\mathrm{e}^\mathrm{NV}\hat{S}_{z,\mathrm{NV}} + \gamma_\mathrm{e}^\mathrm{db}\hat{S}_{z,\mathrm{db}} + \gamma_\mathrm{e}^\mathrm{NV}\gamma_\mathrm{e}^\mathrm{db}\hat{S}_z\omega_\mathrm{ee}\hat{S}_{z,\mathrm{db}}, \tag{5.1}$$

with dipolar coupling constant ω_ee and index db refers to a coupled electron spin on the surface, which is denoted as dangling bond spin.[28] Since ω_ee (kHz range) is small against D, $\gamma_\mathrm{e}^\mathrm{NV}$, and $\gamma_\mathrm{e}^\mathrm{db}$, we can assume it as small disturbance. Then, we can

[28] In general, this spin is optical not addressable. Therefore, it is often referred to as dark spin.

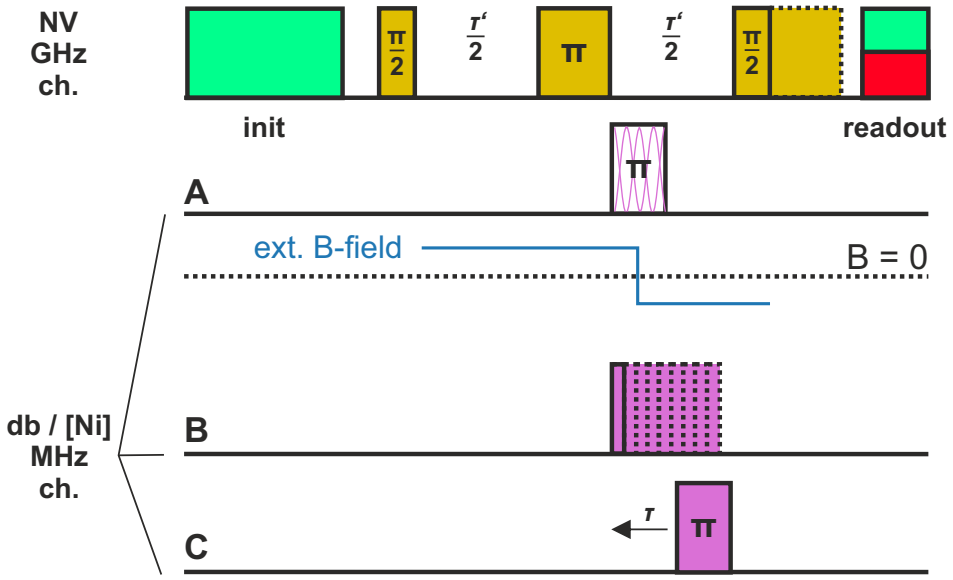

Figure 79: NV-DEER spectroscopy. On the NV^- center electron spin a Hahn echo filter sequence is applied. **(A)** The spectrum of the dangling bond can be measured by applying a pulsed ODMR measurement, i.e. the carrier frequency of the π pulse is swept (upper trace). If the π pulse is resonant with the db spin transition the external magnetic field exerted by the db spin alters; phase pickup is then given by Eq. (5.1) **(B)** Rabi measurement on the db spin by incrementing the mw pulse length. **(C)** Coupling strength measurement is accomplished by sweeping the position of the π pulse, see Eq. (5.3).

assume that the dangling bond spin excerts an effective magnetic field on the NV^- center spin which is given by $B_{\mathrm{db}} = 2B_{\mathrm{db},0}\hat{S}_{z,\mathrm{db}}$ and $B_{\mathrm{db},0} = -\frac{1}{2}\gamma_{\mathrm{e}}^{\mathrm{db}}\omega_{\mathrm{ee}}$. If $S = \frac{1}{2}$, B_{db} possesses two distinct values $\pm B_{\mathrm{db},0}$ which value depends on the distance between the NV^- center spin and the db spin and their mutual orientation. This is encoded in ω_{ee} (see Chap. 1.2).
If we recall the filter characteristics of the Hahn echo measurement from Chap. 1.4, which is given by

$$\varphi = \gamma_{\mathrm{e}}^{\mathrm{NV}}\left(\int_0^{\frac{\tau}{2}} B\left(t\right)\mathrm{d}t - \int_{\frac{\tau}{2}}^{\tau} B\left(t\right)\mathrm{d}t\right) \overset{B_{\mathrm{db}}}{\Rightarrow} \gamma_{\mathrm{e}}^{\mathrm{NV}}\left(\int_0^{\frac{\tau}{2}} B_{\mathrm{db}}\left(t\right)\mathrm{d}t - \int_{\frac{\tau}{2}}^{\tau} -B_{\mathrm{db}}\left(t\right)\mathrm{d}t\right) = 2\gamma_{\mathrm{e}}^{\mathrm{NV}}B_{\mathrm{db}}, \quad (5.2)$$

we may find that we can map the spectral information about the dark spin onto the phase pickup of the NV^- center, if we alter the B_{db} value deliberately in one filter window. Thereby, the db spin spectrum can be measured if a π pulse is applied, whose carrier frequency is swept (see Fig. 79**A**). The elucidation of spin state

transition oscillations is accessible via Rabi measurements (see Fig. 79**B**). These pulse schemes mimics the corresponding experiments described for the NV^- center in Chap. 2.2.3. Since both, the surface-related dangling bond and the electron spin of the nickel bis(diphenyldithiolene), have a spin quantum number of $S = \frac{1}{2}$, the transition frequencies range in the MHz-range. The third pulse scheme, presented in Fig. 79**C**, consists of sweeping the position of a resonant π pulse within the detection window. The measurement signal results in[313]

$$V(\tau) = V_0 \prod_{k \neq i} \left[1 - \lambda_k \left(1 - \cos\left(\omega_{ik}\tau\right)\right)\right] \tag{5.3}$$

with dangling bond flipping probability λ_k and $i = \mathrm{NV}$ and $k = \mathrm{db}$ and $\omega_{ik} = \omega_{\mathrm{ee}}$ for a particular NV^- center-db pair. However, this measurement output can only be observed if the coupling spins have no spin-bath properties, i.e. they interact more strongly with the NV^- sensor than with each other. The presence of a spin bath is proven by a mono-exponential decay of the measuring signal $V(t) = V_0 \exp(-\frac{\tau}{T_{bath}})$.[313]

5.2.3 *g*-scale calibration

Due to technical reasons we could not conduct measurements either in zero field or under the application of a slight static magnetic for the NV^- center quantum sensor utilized in the $Ni(S_2C_2Ph_2)_2$ experiments to obtain the exact magnetic field

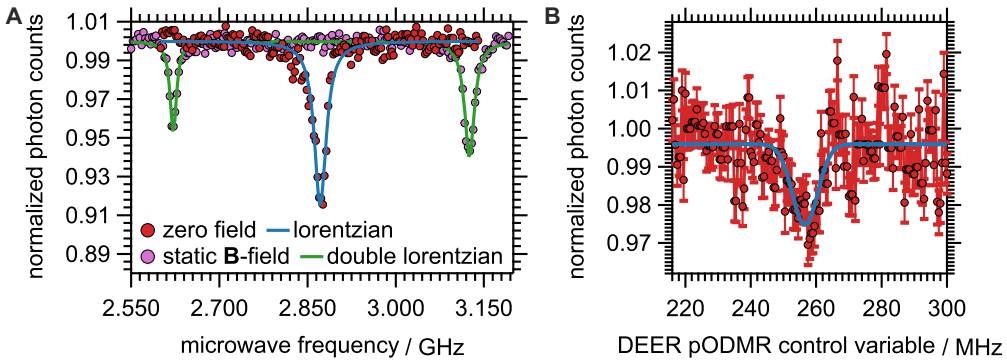

Figure 80: Measurement data required for *g*-scale calibration of the MHz frequency band. **(A)** cw-ODMR spectrum exhibiting in zero field $\nu_{\mathrm{zf}} = 2.8717(4)\,\mathrm{GHz}$ and in a slight magnetic field $\nu_{|-1\rangle} = 2.6217(3)\,\mathrm{GHz}$ and $\nu_{|+1\rangle} = 2.6217(3)\,\mathrm{GHz}$. **(B)** NV-DEER pulsed ODMR spectrum revealing $\nu_{\mathrm{db}} = 256.6(5)\,\mathrm{MHz}$.

projection onto the NV^- center symmetry axis. Therefore, we decided to accomplish a g-scale calibration of the MHz-frequency area in which we expected the $Ni(S_2C_2Ph_2)_2$ signal since data was available for a neighboring NV^- center. Note that this procedure is only justified if an isotropic g-factor can be assumed for the db spin. However, this is generally accepted in the literature (cf. Chap. 4).
We proceeded as follows. From the cw ODMR data in Figure 80**A** we took the frequency of ν_{zf}, $\nu_{|-1\rangle}$, and $\nu_{|+1\rangle}$. Using Eq. (2.9) and (2.10) we obtained $\Delta_{NVB} = 13.3(1)^\circ$ and $B_{0\|NV} = 9.23(5)\,mT$. From the corresponding NV-DEER spectrum of the dangling bond, which is depicted in Fig. 80**B**, its transition frequency ν_{db} was deduced. This results in a g-factor of the surface-related db spin of $g_{db,calib.} = 1.99(2)$, which constitutes the internal standard in the NV-DEER measurements presented in Chap. 5.2.5.

5.2.4 Pre-characterization of the NV^- center used as quantum sensor

The spectroscopic characterization of the NV^- center before deposition of the nickel bis(diphenyldithiolene) complex included the determination of the maximum Rabi period, the elucidation of the intrinsic nuclear spin environment by pulsed ODMR spectroscopy, Ramsey interferometry and Hahn echo measurement. The data have already been presented in Chapter 2.2.3. We therefore only recall the most important results here. The NV^- center quantum sensor is coupled to the NV^- center-intrinsic ^{15}N and a far-located ^{13}C nuclear spin. The T_2 decoherence time is given by $43.3(8)\,\mu s$ which corresponds to an approximate sensing radius of 13 nm. Since NV^- centers in our sample are located $5 - 10\,nm$ below the diamond surface, this value is estimated to be sufficient to measure electron spins deposited on the surface. Additionally, it provides a Hahn echo filter window of $\approx \frac{1}{22\,\mu s} = 46\,kHz$ for coupling strength measurements (see Eq. (5.3)). Additionally, we recorded a NV-DEER spectrum. the experimental finding is shown in Fig. 82**A**. The signal at $3.1(7) \times 10^2\,MHz$ is clearly visible. No further signals can be observed over the given frequency range.

5.2.5 ODMR results indicating an electron transfer reaction

To conduct ODMR-based quantum sensing experiments on $Ni(S_2C_2Ph_2)_2$ we drop-casted $10\,\mu L$ of a $30\,pM$ solution of this compound in toluene on the diamond membrane. This amount mathematically corresponds to roughly five moleculs per diamond pillar. (see Chap. 5.4.6). Two measurement schemes were applied: 1. Hahn echo frequency locking and 2. NV-DEER spectroscopy.

Hahn echo measurements were conducted according to the descriptions in Chap. 2.2.3. A corresponding example result is given in Chap. 5.4.7 together with the analysis. Here we concentrate on the FFT analysis, which is depicted in Fig. 81.

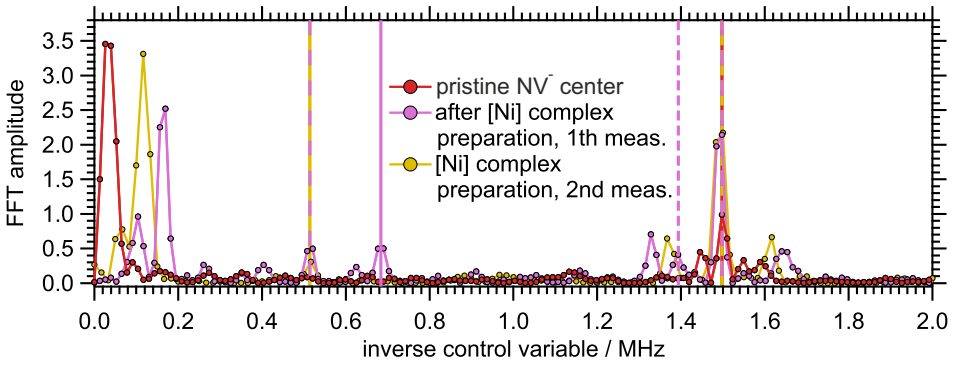

Figure 81: FFT analysis of Hahn echo measurements prior to $Ni(S_2C_2Ph_2)_2$ deposition (red) and after preparing $Ni(S_2C_2Ph_2)_2$ onto the diamond membrane, where two measurements of different τ-spacing are shown (yellow and magenta). Vertical lines indicate signals that came after the preparation of $Ni(S_2C_2Ph_2)_2$. Note that the signals symmetric around $\nu_{NV,ESEEM} = 1.50(2)$ MHz are sidebands caused by non-synchronous sampling of the signal.

All three data sets exhibit a FFT signal at $\nu_{NV,ESEEM} = 1.50(2)$ MHz, which we ascribe to ^{15}N-caused ESEEM.[133] Signals below 200 kHz we assign to uptake of nuclear Lamor precession frequencies, which under our experimental conditions fall in this range. These signals fully describe the FFT spectrum of the data set before the preparation of $Ni(S_2C_2Ph_2)_2$. Remarkably, new signals are added after the preparation of the nickel complex, namely at $\nu_1 = 0.52(2)$ MHz, $\nu_2 = 0.68(2)$ MHz, and $\nu_3 = 1.39(2)$ MHz. These signals can neither come from spin species within the diamond matrix nor from stable surface spins, because otherwise they would have had to be present before preparation. This means that they originate either from the nickel complex, which must then have been reduced because we have prepared the neutral compound, or from electron spins created due to the nickel complex preparation. Yet, both explanations presuppose a reduction process on the nickel complex.[29] The distances resulting from the frequency values

[29] Thermodynamically this process is allowed. The ionization potential of the diamond surface is 1.7 eV (see Chap. 2.3). From DFT calculations we obtained in accordance with the literature an activation energy for the reduction of nickel bis(diphenyldithiolene) of 2.55 eV.[307]

are given by 3.3(2) nm, 4.2(2) nm, and 4.6(2) nm. Accordingly, the NV^- center would be located very close to the diamond surface. Although the expectation of the distribution of the distance of the NV^- center to the surface at our sample is 10 nm, which results from the implantation energy used, simulations show that lower distances are possible. Furthermore, in literature stable NV^- centers are reported with a distance range of $3 - 4$ nm.[205] Another explanation is that we have recorded electron-electron dipolar coupling between nickel and surface electron spins. For these two coupling partners no distance restriction exists. In order be able to make a decision here, the distance of the NV^- center to the diamond surface can in future be determined using an independent method, such as proton NMR.[42]

Finally, it should be noted that ESEEM caused by dipolar coupling is rarely observed in pulsed EPR. This is for two reasons.[61] 1. Technical conditions make it difficult to completely excite the spectrum of dark spins, which in this context are called spectator spins. 2. The thermal polarization of dark spins generally is weak. The first limitation does not apply to our measurement method, since we excite on two well-separated frequency bands. With regard to the second limitation, we note that in the case of the statistical or strong coupling regime, the signal is no longer determined by the Boltzmann factor. The signal is proportional to $\sqrt{N}$ in the first case and to N in the second, when N is the number of coupled spins.[314] The statistical regime is reached when for the number of detected spins $N < \left(\frac{2kT}{\hbar\gamma_e B}\right)^2$ applies. Under our measurement conditions, this results in $N \approx 2 \times 10^9$ which condition we regard as fulfilled (cf. Chap. 4.6.5). Conversely, we see the fact that we have recorded additional signals in the Hahn echo that can plausible be attributed to electron-electron dipolar coupling interactions as a clear indication that we are detecting molecules below the ensemble level.

NV-DEER measurements Next, we performed NV-DEER spectroscopy at two slightly different B-field values. The outcome is presented in Fig. 82, whereby in Fig. 82**A** the NV-DEER spectrum of the diamond sample before the preparation of $Ni(S_2C_2Ph_2)_2$ is given for comparison. Both spectra show a broad signal that we identify with the db spin. According to our calibration it has the g-factor $g = g_{\mathrm{db,calib.}} = 1.99(2)$. However, a second signal can also be noticed. The respective g-factor obtained using the g-scale calibration results in $g_{[\mathrm{Ni}],1} = 2.15(2)$ and $g_{[\mathrm{Ni}],2} = 2.14(2)$, which we ascribe to the nickel complex due to the significant deviation to g_e. Note, however, that this value is greater than the isotropic g-factor we obtained for the nickel bis(diphenyldithiolene) anion and also exceeds any entry of

its g-matrix, which values are given as $g_x = 1.999$, $g_y = 2.041$, and $g_z = 2.122$ in the literature.[315] We therefore assume that an additional chemical change has taken place at the surface nickel complex, which we denote as [Ni] due to its unknown chemical composition in the following. To demonstrate coherent control over its spin states, we conducted NV-DEER Rabi experiments varying the B_1 amplitude. An example experimental result is presented in Fig. 83**B**. The FFT analysis of all three data sets is given in Fig. 83**C**. For technical reasons, we could not record a Rabi measurement at full AWG output amplitude, therefore such a measurement on the db spin is attached in Fig. 83**A** as reference point. The Rabi frequencies, as they can be taken from the FFT analysis in Figure 83**C**, depend linearly on the AWG output amplitude and thus on the B_1 amplitude. This relationship is expected according to $\Omega = \frac{g_e^{[Ni]} \mu_b B_1}{\hbar}$. A more detailed evaluation can be found in chapter 5.4.8. Thus, we could show that we can coherently control the spin transitions of the [Ni] species. This is necessary to enable further investigations, like the determination of the relaxation times of the [Ni] spin or, for example, the performance of triple electron-electron resonance experiments to measure the coupling between single [Ni] complexes.[304]

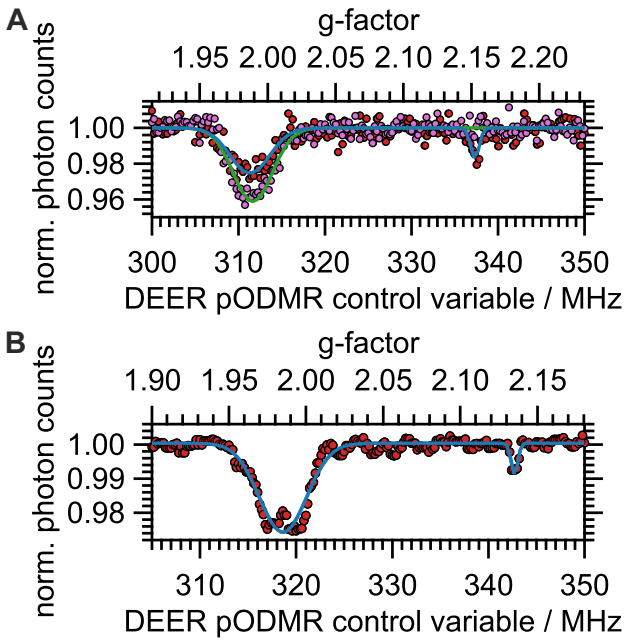

Figure 82: **(A)** NV-DEER spectra before (magenta) and after deposition (red) of $Ni(S_2C_2Ph_2)_2$. Blue (green) line shows Gaussian fits of the corresponding signals. **(B)** NV-DEER spectrum after deposition of $Ni(S_2C_2Ph_2)_2$. Blue line indicates Gaussian fits of the corresponding signals.

In order to verify the assumption made during the analysis of the Hahn echo measurements, that we detect the [Ni] complex molecules in the statistical or even strong coupling regime, we performed NV-DEER coupling strength measurements. We start with the investigation of the db signal. The measurement outcome is presented in Fig. 84. We followed a differential protocol, therefore 84**A** shows contrast

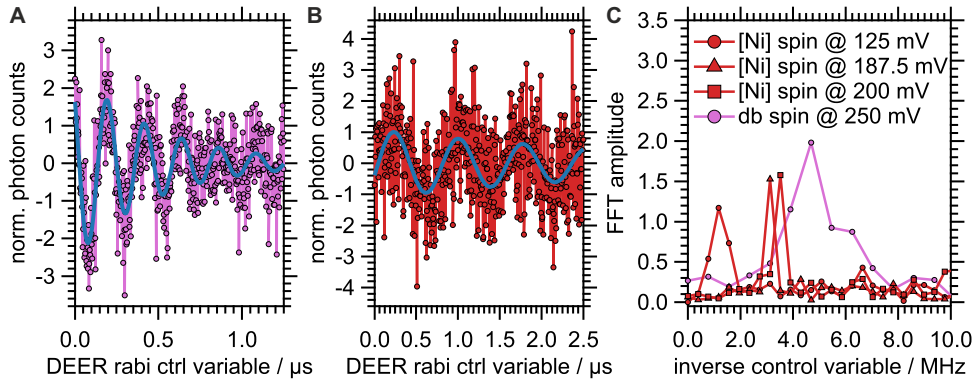

Figure 83: NV-DEER Rabi measurements on **(A)** db dark spin at 250 mV and **(B)** [Ni] spin at 125 mV AWG output amplitude. **(C)** FFT analysis of all conducted NV-DEER Rabi measurements.

data, which was obtained by subtraction of the corresponding $|-1\rangle$ and $|0\rangle$ projection measurements. The signal curve shows an exponential decrease whose time constant is given by 5.3(3) µs. If the surface dangling bonds have a short coherence time, then their signal would be transient and for increasing delay times no longer distinguishable from the background of the spin bath dynamics. Therefore, we analyzed a time domain that covers the first 3 µs of the measurement finding in more detail and subjected the data to an FFT analysis. However, no signal

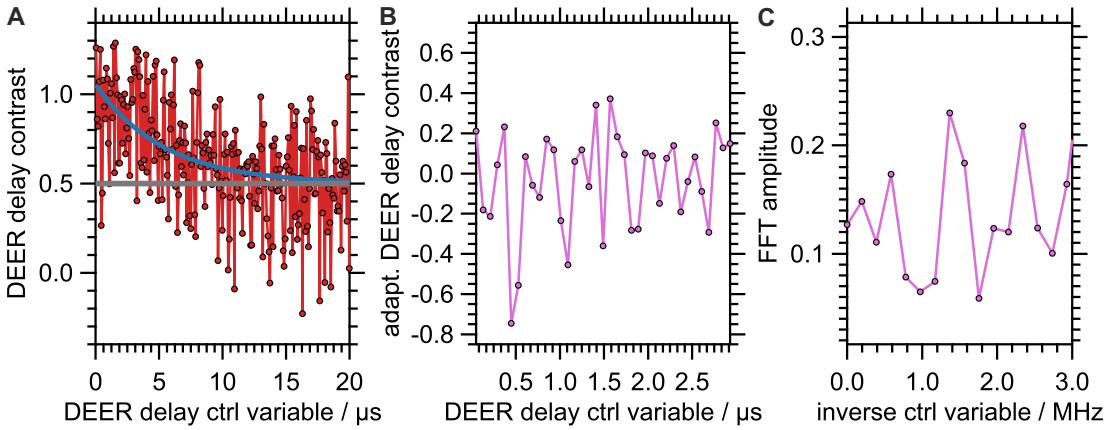

Figure 84: NV-DEER coupling strength (DEER delay) measurement on db spin. **(A)** Contrast data set (red) obtained by subtraction of the corresponding $|-1\rangle$ and $|0\rangle$ projection measurements. The blue line indicates a mono-exponential fit. **(B)** Differential trace of data and mono-exponential fit from **(A)**. Note that the time scale has been reduced. **(C)** FFT of the time trace in **(B)**.

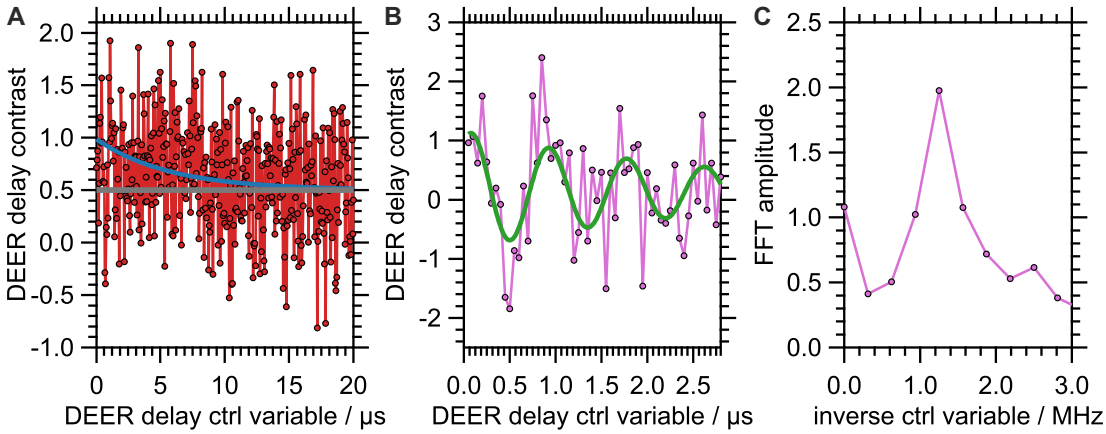

Figure 85: NV-DEER coupling strength (DEER delay) measurement on [Ni] spin. **(A)** Contrast data set (red) obtained by subtraction of the corresponding $|-1\rangle$ and $|0\rangle$ projection measurements. The blue line indicates a mono-exponential fit. **(B)** Differential trace of data and mono-exponential fit from **(A)** In contrast to Fig. 84, an oscillation can be observed. A sinusoidal fit reveals a frequency of $\nu = 1.38(4)$ MHz. Note that the time scale has been reduced in comparison to **(A)**. **(C)** FFT of the time trace in **(B)**. A clear signal can be seen, which is absent in the corresponding db measurement.

indicating an oscillation can be observed. This leads us to conclude that surface spins have spin-bath characteristics. Notice, however, that they presumably still fall into the statistical polarization regime.

We turn to coupling strength measurement on the [Ni] species. The measurement results can be found in the contrast evaluation in Fig. 85. For short π pulse delay times, an oscillation can be recognized on the background of an exponential decay, whose time constant results in 5.7(3) µs (see Fig. 85**A**). This becomes more obvious in Figure 85**B**, where only the first 3 µs are considered. The sinusoidal fit reveals an oscillation frequency of 1.38(4) MHz. The same result is derived from the FFT analysis. Thus, we have shown that the signal of the [Ni] complex is produced by coherent coupling to a few [Ni] complex molecules. An exact determination of the number is possible via a quantitative evaluation according to Eq. (5.3), but our data does not allow for this. Remarkably, we also found the frequency of 1.38(4) MHz in the FFT evaluation of the Hahn echo measurements. This means that both methods partially achieve similar results.

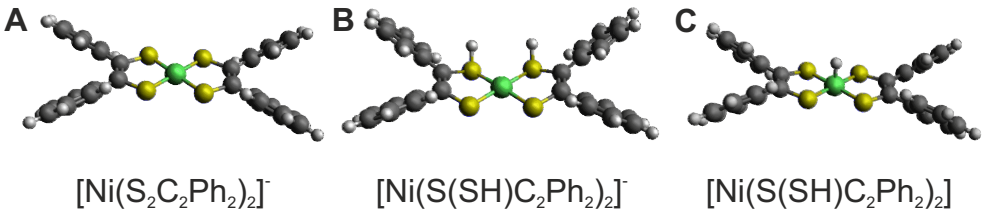

Figure 86: Calculated structures of three selected nickel complexes.

5.2.6 Discussion

In order to gain a better insight into the potential nature of the chemical reaction, we refer in more detail to the g-factor of the [Ni] species. Due to the low spectroscopic resolution of our cw-ODMR data, the g-factor values obtained from NV-DEER spectroscopy are only of minor statistical significance. For further discussion, we therefore calculate the mean value of both obtained values in order be able to make at least a small statistical statement. This evaluation leads to $g_{[\mathrm{Ni}]} = 2.143(17)$, where $\sigma_t = \pm 0.017$ is the one-sided 90% confidence interval according to the t-distribution. With this result, we conclude again that $[\mathrm{Ni}(\mathrm{S_2C_2Ph_2})_2]^-$ cannot be present on the diamond surface, since the g-factor at the lower limit of the selected confidence interval, $g = 2.126$, is still greater than the largest main axis value of $[\mathrm{Ni}(\mathrm{S_2C_2Ph_2})_2]^-$.

Table 14: Results of the DFT calculations. g_x, g_y, g_z are the entries of the g-matrix of the respective complex, in addition selected binding distances are indicated. exp. or lit. refers to experimental data or calculations in the literature.

complex	g_x	g_y	g_z	$d_{\text{Ni-S}}$ / Å	$d_{\text{C=C}}$ / Å
$[\mathrm{Ni}(\mathrm{S_2C_2Ph_2})_2]^-$	2.018	2.040	2.114	2.230	1.388
$[\mathrm{Ni}(\mathrm{S_2C_2Ph_2})_2]^-_{\text{exp.}}$ [315]	1.999	2.041	2.122		
$[\mathrm{Ni}(\mathrm{S(SH)C_2Ph_2})_2]^-$	2.079	2.081	2.129	2.367	1.389
$[\mathrm{Ni}(\mathrm{S(SH)C_2Ph_2})_2]^-_{\text{lit.}}$ [316]				2.369	1.359
$[\mathrm{Ni}(\mathrm{H})(\mathrm{S_2C_2Ph_2})_2]$	2.027	2.070	2.097	2.309	1.397

Since we saw a protonation of the complex as the simplest explanation for a chemical change, we carried out DFT[30] calculations on two complexes known from the

[30] All calculations were performed using ORCA, version 4.1.1.[317] We used the BP86 functional with an unrestricted self-consistent field. The resolution of identy approximation was applied. Valence double-zeta basis set was chosen accompanied with the Def2/J auxillary basis set.

literature.[316,318] To verify the reliability of our chosen DFT method, we performed a double comparison with known values. We compared the calculated anisotropic g-factors of the nickel bis(diphenyldithiolene) anion with experimental values. In addition, we validated the calculated binding distances of $[Ni(S(SH)C_2Ph_2)_2]^-$ with those computed in the literature (see Tab. 14). In both cases good agreement is achieved. The best agreement with the g-factor determined by us is with the double protonated complex $[Ni(S(SH)C_2Ph_2)_2]^-$, which was proposed as an intermediate in the catalysis of the reduction of protons to hydrogen.

5.3 Conclusion

In this chapter we were able to present the first detection of the electron spin of a transition metal complex on the diamond surface. Remarkably, this also involves the proof of an electron transfer from the diamond surface to the neutral precursor nickel bis(diphenyldithiolene). Thermodynamically this process is favorable. However, a closer look on the g-factor obtained exhibited that this process is accompanied by a chemical transformation of the complex. Using DFT calculations, we examined a possible protonation and found a good agreement for $[Ni(S(SH)C_2Ph_2)_2]^-$. The quantum sensing protocols used also showed that we probed the investigated complex in the single-molecule regime. The coherent control of the spin states of the nickel complex was demonstrated by NV-DEER Rabi measurements. The results obtained here give rise to further research. On the one hand, the system investigated here should be characterized in more detail, for example, with regard to its relaxation times and the spin environment. But also the extension to other transition metal complexes is conceivable. The role of the "non-innocent" character of the ligands should especially be taken into account. Furthermore, it should be investigated whether the method of quantum sensing is able to investigate dynamic processes of transition metal complexes, which would be a natural extension to the investigation of catalysis cycles. This is conceivable due to the possibility of using filter functions to record processes in the range of a few MHz. Reported turn over frequencies of nickel dithiolene analogues are in the range of $1000\,s^{-1}$, which is well accessible for measurement.[319] Conversely, transition metal complexes, whose redox-active properties can be adapted via appropriate ligand decoration, can be used to determine the electrochemical parameters of the diamond surface on the nanometer scale.

5.4 Supplementary

5.4.1 Spectroscopic methods

IR spectroscopy The infrared spectrum was recorded on a Bruker Vertex 70 spectrometer equipped with a diamond ATR unit. Internal CO_2 background correction was used. To enhance signal-to-noise ratio, the spectrum is a sum of eight measurement runs.
For analysis, the region of $\tilde{\nu} = 1800 - 2800\,\mathrm{cm}^{-1}$ was omitted due to incomplete background correction therein.

EPR spectroscopy EPR data was obtained using a Magnettech Miniscope MS 400 spectrometer.
g-factor calibration was realized by measuring the spectrum of a manganese(II) standard embedded in a zinc sulfide crystal for whose third hyperfine line is known $g_{\mathrm{std,\ 3.\ HF}} = 2.0267(2)$. When additionally recording the microwave frequency of the EPR signal both, for the standard ν_{std} and the sample ν_{pr}, computation of the apparent g-factor scale is accomplished through:

$$g_{\mathrm{pr}} = \nu_{\mathrm{pr}} \cdot g_{\mathrm{std,\ 3.\ HF}} / \nu_{\mathrm{std,\ 3.\ HF}}.$$

ODMR measurements were conducted at room temperature, ambient conditions, and in in a small magnetic field using **1.** a home-built confocal microscopy setup provided with **2.** a pulsed microwave generating and applying unit and **3.** a permanent magnet. For details see Chap. 2.4.1

5.4.2 Synthesis protocols and sample preparation

All chemicals were purchased from commercial suppliers and used without further purification steps.

5.4.3 Synthesis of nickel bis(diphenyldithiolene) (1)

Nickel bis(diphenyldithiolene) was prepared according to literature.[309] $NiCl_2 \cdot 6\,H_2O$ (1.000 g, 4.207 mmol) was dissolved in 50 mL of aqueous hydrochloric acid (pH $\approx$ 5). $(NH_4)_2S$ (2.147 g, 3.150 mmol) was added dropwise. The precipitate (NiS) was vacuumed, washed with 20 mL of 0.1 M sodium hydroxide, and dried at air. Yield: 0.2759 g, 3.040 mmol, 97%.
Diphenylacetylene (1.120 g, 6.284 mmol) was taken up in 50 ml of toluene and NiS

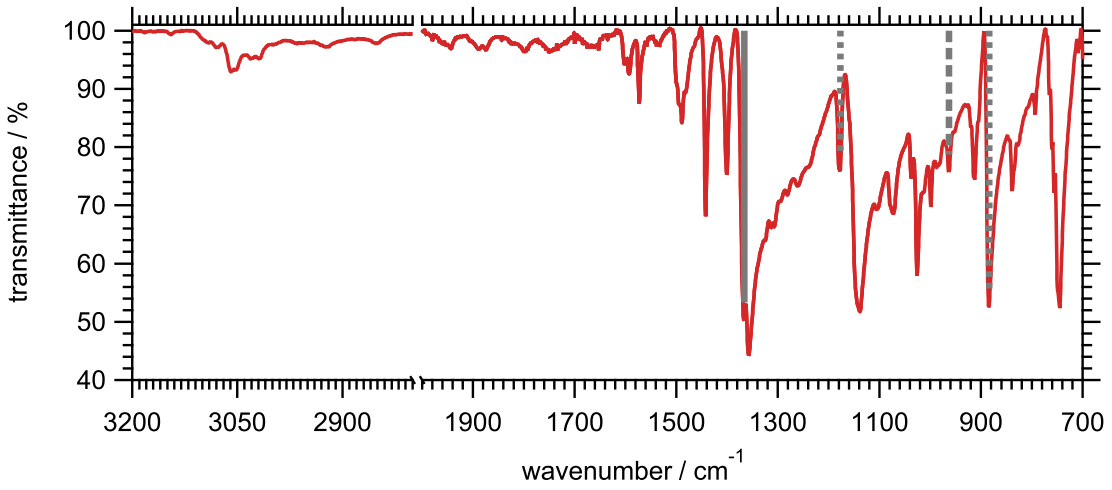

Figure 87: IR spectrum of $Ni(S_2C_2Ph_2)_2$. Distinctly structured grey bars represent values from literature indicating the $[NiS_2C_2]$ core with a maximum deviation of $|\tilde{\nu}_{lit.} - \tilde{\nu}_{exp.}| = 4\,cm^{-1}$.[320]

(0.2759 g, 3.040 mmol) was added. Then, the mixture was refluxed for 28 hours at 120 °C. The reaction suspension was filtered and washed with 30 ml toluene. The organic phase was concentrated under reduced pressure to give a volume of approximately 20 mL and crystallization was done over night in the refrigerator. Purification was accomplished by recrystallization from *n*-hexane and subsequent column chromatography on silica gel using toluene as solvent and eluent. Yield: 0.158 g, 0.0274 mmol, 9%.
ATR-FTIR (Figure 87):[320] $\tilde{\nu}\,(cm^{-1}) = 3060, 3052, 3032, 3019$ (w, Aryl-H); 1943, 1889, 1875, 1780, 1750, 1663 (w, aromatic combination bands and overtones); 1367 (s, C=C, lit. 1365); 1178 (m, C−Ph + C−S, lit. 1175); 964 (w, C−S + C−Ph, lit. 960); 884 (s, C−S, lit. 880); 745 (s, aromatic C−H out-of-plane bending corresponding to mono-substitution of benzene moiety).

5.4.4 One- and two-electron reduction of (1)

One-electron reduction to obtain $[(C_2H_5)_4N][Ni(S_2C_2Ph_2)_2]$ **(2)** was performed under slightly modified conditions of literature procedure.[312] **(1)** (0.150 g, 0.260 mmol) and *p*-phenylenediamine (0.105 g, 0.971 mmol) was dissolved in 2.000 mL of DMSO under a constant flow of argon. *Fait accompli* of the reaction was instantaneously indicated by a red-brownish color. Into this mixture a solution of tetraethylammonium bromide (0.100 g, 0.476 mmol) in 5.000 mL of ethanol was poured to stabilize the anionic nickel complex. Since solely the EPR signal was of interest (Fig. 78)

no quantification was done.
Overall two-electron reduction was conducted by starting either from **(1)** or **(2)**. According to Ref. [321] $BH_3 \cdot THF$ is a suitable reduction agent. A solution of **(1)** in toluene (50 µl, 2 µmol) and 50 µl of the raw product mixture of **(2)**, respectively, was transferred in an EPR tube and 50 µl of 1 M $BH_3 \cdot THF$ solution was added. In both cases an intense dark brown color developed immediately.

5.4.5 EPR measurements

The EPR spectrum of nickel bis(diphenyldithiolene) **(1)** was obtained from a 0.1 M solution in toluene. The product of the one- and two-electron reduction was investigated *in situ* by transferring 50 µl of the corresponding reaction mixture in an ESR tube.
Overview EPR spectra were recorded under the following conditions: mw power $P_{\mathrm{mw}} = 1\,\mathrm{mW}$, modulation amplitude $B_{\mathrm{mod}} = 0.3\,\mathrm{mT}$, resolution 0.1 mT/bin, sweep rate 1.3 mT/s (see Fig. 78).
The g-factor of $[Ni(S_2C_2Ph_2)_2]^-$ was determined from a high-resolution EPR spectrum obtained by the following parameters: $P_{\mathrm{mw}} = 0.1\,\mathrm{mW}$, $B_{\mathrm{mod}} = 0.2\,\mathrm{mT}$, resolution 0.0085 mT/bin, sweep rate 0.2 mT/s. sum over 99 spectra (Inset of Fig. 78). The inflection point of the data fitted pseudo-voigtian model yields: $g = 2.0561(8)$ (lit. $g = 2.0568(3)$).[312]

5.4.6 Diamond substrate and sample preparation

The diamond substrate (size $\approx 4\,\mathrm{mm}^2$, thickness $\approx 30\,\mu\mathrm{m}$) was provided by Dr. Rainer Stöhr (3rd Physics Institut, University of Stuttgart). The sample started as a commercially available (100)-oriented ultrapure electronic grade CVD diamond with natural ^{13}C abundance from Element Six. Firstly, the sample was overgrown with a nanometre-thin boron-doped diamond layer to suppress the formation of paramagnetic vacancy centers[322] and was then implanted with 10 keV ^{15}N ions of dose $7 \times 10^9\,\mathrm{cm}^{-2}$. An enhancement of the photon flux of a single NV center up to $\approx 2 \times 10^6\,\mathrm{s}^{-1}$ can be achieved by fabricating tapered waveguide structures onto the diamond substrate.[323] Therefore, our sample is fabricated with such pillar patterns possessing diameters of $450 - 500\,\mathrm{nm}$ at the apex.
In order to clean the diamond sample prior to experiments it was refluxed in a 1 : 1 : 1 (volume ratio) mixture of sulfuric acid (96%), nitric acid (64-66%), and perchloric acid (70%) for 6 hours. Subsequent washing procedure included neutralization in ultrapure water, cleaning in *iso*-propanol, and storing in ultrapure

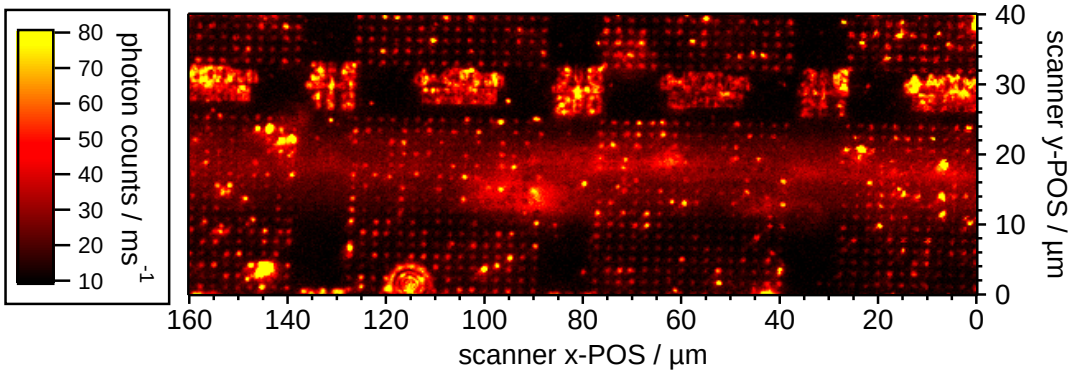

Figure 88: Example fluorescence mapping of the diamond membrane. The NV^- centers are arranged in quadratic fields, coarser structures are markers. The blurred line in the middle of the image represents the mw antenna.

water for 30 minutes under stirring. The sample was mounted on a home-built microwave feeding holder using NOA 86T and the copper wire was fixed on the pillar-decorated side.
After pre-characterization of the NV center quantum sensor $2 \cdot 5\,\mu l$ of a 30 pM solution of **(1)** in toluene was dropcasted on the diamond sample. This corresponds mathematically to ≈ 5 molecules per pillar ($3.14\,\mu m^2$) assuming homogeneous covering of only half the substrate. This is justified since adhesive fixation constrained us to this accessible area.

5.4.7 Data set of Hahn echo measurement after $Ni(S_2C_2Ph_2)_2$ preparation

The results of an example Hahn Echo measurement after deposition of $Ni(S_2C_2Ph_2)_2$ onto the diamond surface are presented in Fig. 89. The experiment was designed as differential protocol which includes the separate addressing of the time-dependent population of the $|0\rangle$ and $|-1\rangle$ state, respectively, by either applying a $\frac{\pi}{2}$ or $3\frac{\pi}{2}$ pulse as projection operation (see Fig. 89**A**). An explanation for this measurement method lies in the elimination of non-spin-dependent decay paths (cf. discussion in Chap. 4.6.6). Both traces show qualitatively comparable FFT analysis. Frequencies are given by $\nu_1 = 0.10(2)\,MHz$, $\nu_2 = 0.16(2)\,MHz$, $\nu_3 = 0.52(2)\,MHz$ and $\nu_4 = 1.50(2)\,MHz$. Note that the signals symmetrically located around $\nu_4 = 1.50(2)\,MHz$ at $\nu = 1.33(2)\,MHz$ and $\nu = 1.65(2)\,MHz$ are sidebands. They originate from non-synchronous sampling of the $\nu_4 = 1.50(2)\,MHz$

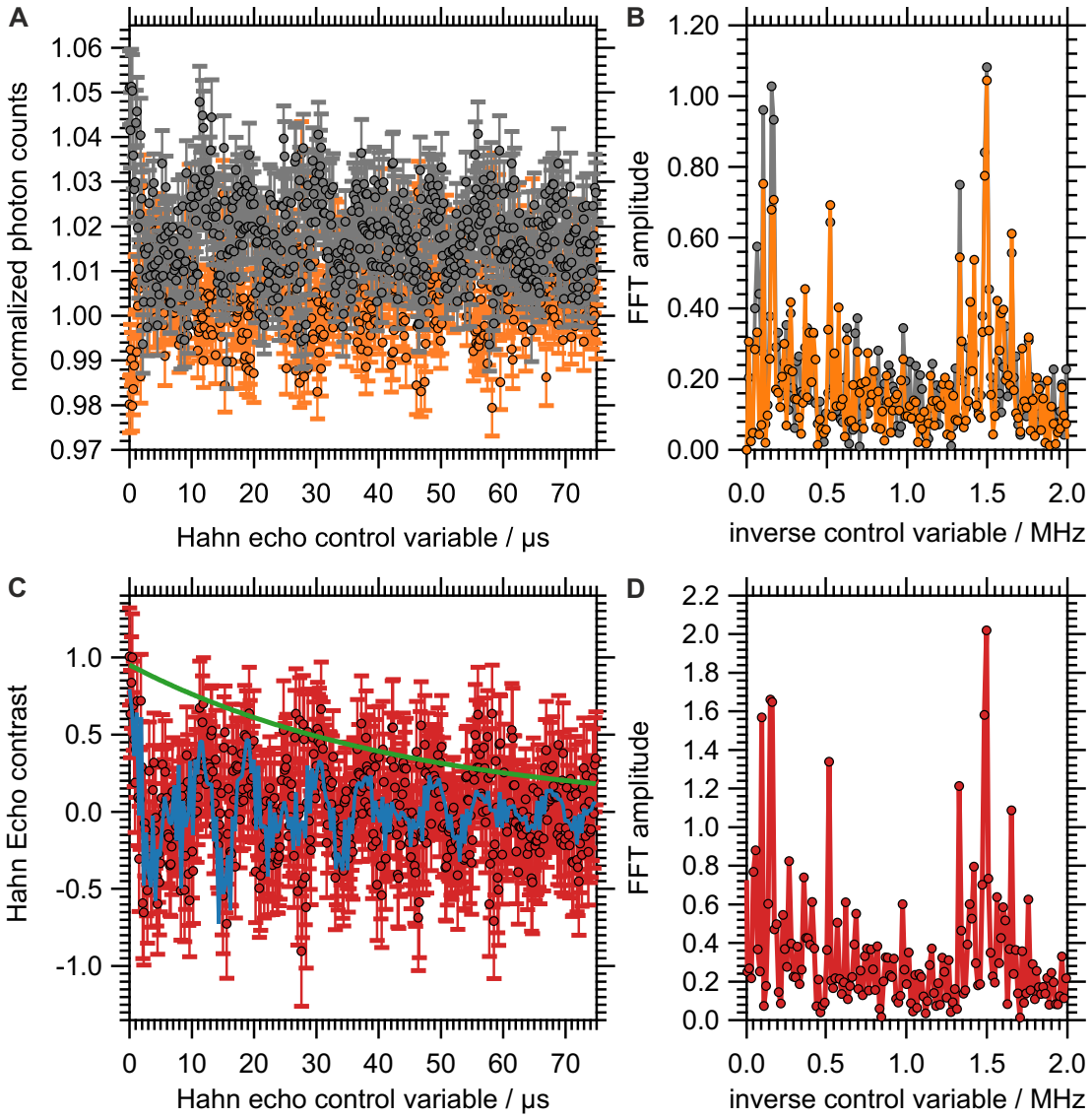

Figure 89: Hahn Echo measurement after $Ni(S_2C_2Ph_2)_2$ deposition onto the diamond membrane. **(A)** $|0\rangle$ (gray) and $|-1\rangle$ (orange) projection measurement. **(B)** Corresponding FFT analysis. **(C)** Contrast data set, obtained by subtraction of both time traces in **(A)**. The blue line is a four-tone sinusoidal with mono-exponential decay factor whose contribution is indicated by the green line. The T_2 decoherence time amounts to 38.2(3) µs **(D)** FFT analysis of **(C)**.

ESEEM frequency. The evaluational of the contrast data set is demonstrated in Fig. 89**C**. We applied a four-tone sinusoidal with mono-exponential decay factor to obtain the T_2 decoherence time.

5.4.8 Analysis of NV-DEER Rabi measurements

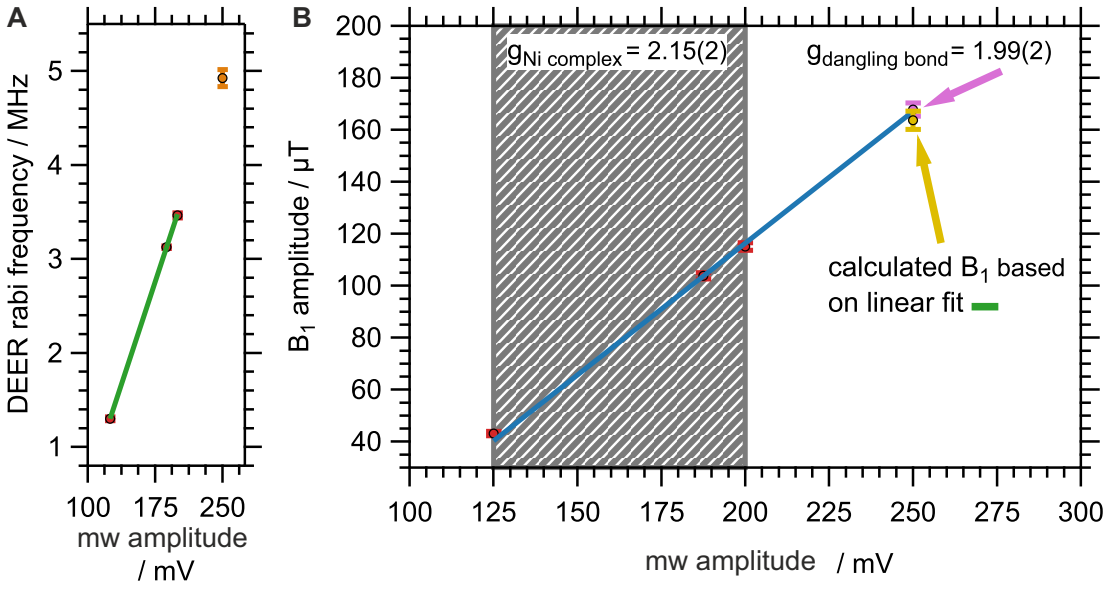

Figure 90: Analysis of NV-DEER Rabi measurements. **(A)** shows the linear dependence of the NV-DEER Rabi frequency of the [Ni] signal (green line) on the mw amplitude. The data point at 250 mV corresponds to the reference point of the db signal. **(B)** Dependence of the B_1 amplitude, evaluated according to $\Omega = \gamma_e^{[\mathrm{Ni}]} B_1$, on the mw amplitude as applied to the output of the AWG. Extrapolating this data to 250 mV allows comparison with the reference point calculated accordingly. Both values are in agreement within the error limits.

6 Conclusion and outlook

The concept of quantum sensing is a framework in which the utilization of quantum systems as sensors at the interplay of theory and application is studied. In this work we concentrated in particular on the last aspect. However, basic theoretical concepts of quantum sensing, which has been used in the experiments (see Chap. 1), were explained first. Two examples of quantum sensors were presented: the molecular group-V endohedral fullerene $^{14}N@C_{60}$ and the diamond-hosted negatively charged nitrogen-vacancy (NV^-) center (see Chap. 2).

For $^{14}N@C_{60}$ only few investigations have been reported, but its spin relaxation times, in principle, allow to use it as a quantum sensor. In particular, techniques have been presented recently which enable the readout of its spin information on the level of few to single molecules. Thereby, it has become apparent that the obtained spectra indicate further presumably charged fullerene species. Here we have carried out a closer investigation on the generation of C_{60} radical cations on zeolites loaded with redox-active metal ions (see Chap. 3). Our studies initially served to examine a literature-known protocol in more detail. We identified the thermal behavior of the zeolite matrix in the presence of Fe^{3+} and the material factors determining the linewidth of the C_{60} cation EPR signal. This allowed us to precisely determine the g-factors of C_{60}^+, C_{70}^+, and $C_{120}O_2^{2\bullet}$ using $N@C_{60}$ as the high-accuracy spin standard. By replacing the Fe^{3+} oxidizing agent with Ce^{4+}, in the form of $Ce(SO_4)_2$, we were able to significantly reduce the thermal demand of the oxidation reaction. Thus, it was possible to obtain the both spin species C_{60}^+ and $N@C_{60}$ simultaneously to a sufficient amount and we tried to measure bulk EPR dipolar coupling spectra on this system. The first results are ambiguous. However, more detailed investigations of the thermodynamics and kinetics of this system, the use of a higher $N@C_{60}$ filling factor, and measurements using pulsed EPR could provide clearer results. A more detailed understanding of bulk coupling spectra of C_{60} ions can help to interpret the results obtained in the more advanced few to single molecule readout techniques.

We first examined the NV^- center in its nanodiamond (ND) matrix (see Chap. 4). This is characterized by the fact that the surface of the ND exerts a strong influence on the T_1 and T_2 relaxation time of the NV^- center. We applied novel wet-chemical surface functionalization approaches, namely DAST-mediated fluorination and hydrazonation in course of a Bamford-Stevens-olefination. We also carried out the treatment with strong bases. These protocols were investigated by EPR spectroscopy for their ability to reduce the surface spin density. We were

able to determine that each of the above methods achieved this objective, with fluorination providing the best result. First explanatory approaches for the occurrence of surface spin density reduction were found. In addition, optically detected magnetic resonance (ODMR) investigations of the base treated ND were carried out. At the level of few ND these showed results that are in accordance with the ensemble data. We hypothesize that the results found here are relevant for ND research. Studies on the targeted wet-chemical functionalization of ND with the aim of reducing and demonstrating its surface radical density are not known to us. They represent an extension of the plasma processes otherwise used in general.

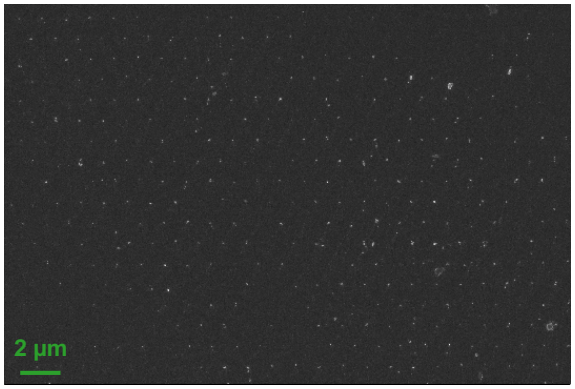

Figure 91: SEM image of stamped ND using mesoporous silica stamps.[324]

Furthermore, preliminary results on the structured deposition of ND on surfaces were found with cooperation partners. So far, this is technically demanding.[325,326] Our approach, is to use micro-structured, mesoporous silicate stamps wetted with ND-*i*-propanol ink. The deposition process consists of attaching the stamp to the surface, thereby, the ink evaporates and ND aggregates are formed in a pattern imposed by the stamp structure. An example result can be found in Fig. 91. However, the pattern shown could not be confirmed by confocal fluorescence microscopy. We suspect that the reason for this is that the ND material used contains only a very small amount of fluorescent NV^- centers, which means that only a random selection of deposited NDs is detected. The results from Chap. 4 may help to achieve an optimization by chemically improving the NDs to be stamped before the stamping process.

The use of the NV^- center as a quantum sensor for the detection of charged transition metal complexes is investigated in Chapter 5. Using Hahn echo measurements and NV-related double electron electron spectroscopy (NV-DEER) we observed an unexpected electron transfer between the diamond surface and nickel bis(diphenyldithiolene). The *g*-factor obtained for this complex also indicates that an additional proton transfer took place. We used simple DFT calculations to identify a possible product. The proof that only a few molecules were detected was

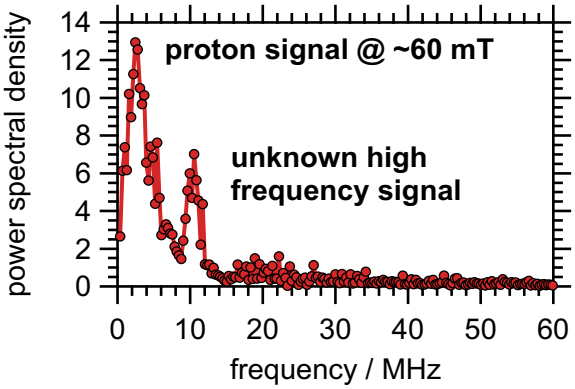

Figure 92: Spectral power density of Fe^{4+} sample.

also provided. We hypothesize that this first successful detection of the electron spin of few transition metal complex molecules can have a relevance in different research fields. The orientation on the surface can be precisely determined by a spectroscopically more accurate determination of the g-factor or the full g-matrix. Adsorption geometries are thus accessible. Possibly, cyclic processes such as catalytic processes associated with a change in the spin quantum number can be detected by frequency locking methods using various quantum sensor protocols.

Transition metal complexes on the diamond surface may lead to new and so far unexplored phenomena as shown by preliminary investigations carried out by us. Spectral decomposition techniques[327] that allow to study the spectral power density of the spin bath of a NV^- center have shown that after the deposition of a stable, due to high zero field splitting presumably spin-silent Fe^{4+}-TAML (tetraamide macrocyclic ligands) complexes, the spin bath is significantly altered (see Fig. 92).[328] While the proton signal is expected and unambiguously assigned, the occurrence of a signal at 10 MHz is remarkable. Whether it is a measurement artifact or detects dipolar coupling should be examined in further investigations.

The overall aim of this work was to examine the material properties of quantum sensors and to apply them to relevant questions.

Abbreviations

∇_x	$\left(\frac{\partial}{\partial x_1}, \frac{\partial}{\partial x_2}, \frac{\partial}{\partial x_3}\right)^{\mathrm{T}}$
lw	linewidth, defined as full width at half maximum
ATR-FTIR	attenuated total reflectance - Fourier-transform infrared spectroscopy
AWG	arbitrary waveform generator
CAN	ceric ammonium nitrate
CVD	chemical vapour deposition
cw	continuous wave
DAST	diethylaminosulfur trifluoride
DCM	dichlormethane
DI	deionized
EPR	electron paramagnetic resonance
FFT	Fast Fourier Transform
HOMO	highest occupied molecular orbital
HPHT	high pressure-high temperature
HPLC	high pressure liquid chromatography
HSAB	hard and soft (Lewis) acid and bases
IUPAC	International Union of Pure and Applied Chemistry
LUMO	lowest unoccupied molecular orbital
MeCN	acetonitrile
mw	microwave
ND	nanodiamond, interchangeably used with NDs: nanodiamonds
NMR	nuclear magnetic resonance
ODMR	optically detected magnetic resonance
r.t.	room temperature
SM	single molecule
THF	tetrahydrofuran
TLS	two-level system
TOF	turn over frequency
vdW	van der Waals

List of tables

List of figures

References

[1] K. R. Popper, *The Logic of scientific discovery*, Repr. 2008 (twice), Routledge, London, **2008** (cit. on p. 1).

[2] D. L. Massart, *Handbook of chemometrics and qualimetrics*, Elsevier, Amsterdam and New York, **2010** (cit. on p. 2).

[3] B. Dong, Y. Pei, F. Zhao, T. W. Goh, Z. Qi, C. Xiao, K. Chen, W. Huang, N. Fang, *Nat. Catal.* **2018**, *1*, 135–140 (cit. on pp. 3, 4).

[4] N. M. Andoy, X. Zhou, E. Choudhary, H. Shen, G. Liu, P. Chen, *J. Am. Chem. Soc.* **2013**, *135*, 1845–1852 (cit. on pp. 3, 4).

[5] T. Kumagai, F. Hanke, S. Gawinkowski, J. Sharp, K. Kotsis, J. Waluk, M. Persson, L. Grill, *Nat. Chem.* **2014**, *6*, 41–46 (cit. on p. 3).

[6] G. Binnig, H. Rohrer, C. Gerber, E. Weibel, *Appl. Phys. Lett.* **1982**, *40*, 178–180 (cit. on pp. 3, 142).

[7] Binnig, Quate, Gerber, *Phys. Rev. Lett.* **1986**, *56*, 930–933 (cit. on pp. 3, 142).

[8] C. E. Hall, *J. Biophys. Biochem. Cytol.* **1956**, *2*, 625–628 (cit. on p. 4).

[9] S. W. Hell, *Opt. Commun.* **1994**, *106*, 19–24 (cit. on pp. 4, 142).

[10] E. Betzig, *Opt. Lett.* **1995**, *20*, 237–239 (cit. on pp. 4, 142).

[11] E. Chung, D. Kim, Y. Cui, Y.-H. Kim, P. T. C. So, *Biophys. J.* **2007**, *93*, 1747–1757 (cit. on p. 4).

[12] S. T. Hess, T. P. K. Girirajan, M. D. Mason, *Biophys. J.* **2006**, *91*, 4258–4272 (cit. on p. 4).

[13] M. J. Rust, M. Bates, X. Zhuang, *Nat. Methods* **2006**, *3*, 793–795 (cit. on p. 4).

[14] Nie, Emory, *Science* **1997**, *275*, 1102–1106 (cit. on pp. 4, 142).

[15] K. Kneipp, Y. Wang, H. Kneipp, L. T. Perelman, I. Itzkan, R. R. Dasari, M. S. Feld, *Phys. Rev. Lett.* **1997**, *78*, 1667–1670 (cit. on pp. 4, 142).

[16] M. S. Anderson, *Appl. Phys. Lett.* **2000**, *76*, 3130–3132 (cit. on pp. 4, 142).

[17] A. Gruber, *Science* **1997**, *276*, 2012–2014 (cit. on p. 4).

[18] F. Jelezko, J. Wrachtrup, *phys. stat. sol. (a)* **2006**, *203*, 3207–3225 (cit. on p. 4).

[19] J. R. Maze, A. Gali, E. Togan, Y. Chu, A. Trifonov, E. Kaxiras, M. D. Lukin, *New J. Phys.* **2011**, *13*, 025025 (cit. on pp. 4, 34, 35).

[20] J. Wrachtrup, A. Finkler, *J. Magn. Reson.* **2016**, *269*, 225–236 (cit. on pp. 4, 6, 24, 132).

[21] D. Suter, F. Jelezko, *Prog. Nucl. Magn. Reson. Spectrosc.* **2017**, *98-99*, 50–62 (cit. on pp. 4, 6, 43).

[22] M. A. Nielsen, I. L. Chuang, *Quantum computation and quantum information*, 10th anniversary ed., Cambridge Univ. Press, Cambridge, **2010** (cit. on pp. 4, 5).

[23] C. L. Degen, F. Reinhard, P. Cappellaro, *Rev. Mod. Phys.* **2017**, *89*, 3141 (cit. on pp. 4–6, 19, 20, 24, 41, 79, 135).

[24] V. Giovannetti, S. Lloyd, L. Maccone, *Nat. Photonics* **2011**, *5*, 222–229 (cit. on pp. 4, 24).

[25] F. Troiani, A. Ghirri, M. Paris, C. Bonizzoni, M. Affronte, *J. Magn. Magn. Mat.* **2019**, *491*, 165534 (cit. on pp. 4, 24).

[26] J.-W. Zhou, P.-F. Wang, F.-Z. Shi, P. Huang, X. Kong, X.-K. Xu, Q. Zhang, Z.-X. Wang, X. Rong, J.-F. Du, *Front. Phys.* **2014**, *9*, 587–597 (cit. on p. 6).

[27] J. M. Taylor, P. Cappellaro, L. Childress, L. Jiang, D. Budker, P. R. Hemmer, A. Yacoby, R. Walsworth, M. D. Lukin, *Nature Phys* **2008**, *4*, 810–816 (cit. on p. 6).

[28] A. Laraoui, J. S. Hodges, C. A. Meriles, *Nano Lett.* **2012**, *12*, 3477–3482 (cit. on pp. 6, 126).

[29] H. S. Knowles, D. M. Kara, M. Atatüre, *Nat. Mater.* **2014**, *13*, 21–25 (cit. on p. 6).

[30] C. Abeywardana, V. Stepanov, F. H. Cho, S. Takahashi, *J. Appl. Phys.* **2016**, *120*, 123907 (cit. on p. 6).

[31] F. Shi, Q. Zhang, B. Naydenov, F. Jelezko, J. Du, F. Reinhard, J. Wrachtrup, *Phys. Rev. B* **2013**, *87* (cit. on pp. 6, 144).

[32] P. Huang, X. Kong, N. Zhao, F. Shi, P. Wang, X. Rong, R.-B. Liu, J. Du, *Rev. Mod. Phys.* **2011**, *2*, 1043 (cit. on p. 6).

[33] T. H. Taminiau, J. J. T. Wagenaar, T. van der Sar, F. Jelezko, V. V. Dobrovitski, R. Hanson, *Phys. Rev. Lett.* **2012**, *109*, 137602 (cit. on p. 6).

[34] S. Kolkowitz, Q. P. Unterreithmeier, S. D. Bennett, M. D. Lukin, *Phys. Rev. Lett.* **2012**, *109*, 137601 (cit. on p. 6).

[35] N. Zhao, J. Honert, B. Schmid, M. Klas, J. Isoya, M. Markham, D. Twitchen, F. Jelezko, R.-B. Liu, H. Fedder, J. Wrachtrup, *Nat. Nanotechnol.* **2012**, *7*, 657–662 (cit. on p. 6).

[36] J.-P. Tetienne, T. Hingant, L. Rondin, A. Cavaillès, L. Mayer, G. Dantelle, T. Gacoin, J. Wrachtrup, J.-F. Roch, V. Jacques, *Phys. Rev. B* **2013**, *87* (cit. on pp. 6, 80).

[37] S. Steinert, F. Ziem, L. T. Hall, A. Zappe, M. Schweikert, N. Götz, A. Aird, G. Balasubramanian, L. Hollenberg, J. Wrachtrup, *Nat. Commun.* **2013**, *4*, 1607 (cit. on p. 6).

[38] A. O. Sushkov, N. Chisholm, I. Lovchinsky, M. Kubo, P. K. Lo, S. D. Bennett, D. Hunger, A. Akimov, R. L. Walsworth, H. Park, M. D. Lukin, *Nano Lett.* **2014**, *14*, 6443–6448 (cit. on p. 6).

[39] S. Kaufmann, D. A. Simpson, L. T. Hall, V. Perunicic, P. Senn, S. Steinert, L. P. McGuinness, B. C. Johnson, T. Ohshima, F. Caruso, J. Wrachtrup, R. E. Scholten, P. Mulvaney, L. Hollenberg, *Proc. Natl. Acad. Sci. U.S.A.* **2013**, *110*, 10894–10898 (cit. on pp. 6, 80).

[40] T. Rendler, J. Neburkova, O. Zemek, J. Kotek, A. Zappe, Z. Chu, P. Cigler, J. Wrachtrup, *Nat. Commun.* **2017**, *8*, 14701 (cit. on pp. 6, 80, 133).

[41] H. J. Mamin, M. Kim, M. H. Sherwood, C. T. Rettner, K. Ohno, D. D. Awschalom, D. Rugar, *Science* **2013**, *339*, 557–560 (cit. on p. 6).

[42] T. Staudacher, F. Shi, S. Pezzagna, J. Meijer, J. Du, C. A. Meriles, F. Reinhard, J. Wrachtrup, *Science* **2013**, *339*, 561–563 (cit. on pp. 6, 149).

[43] J. M. Boss, K. Chang, J. Armijo, K. Cujia, T. Rosskopf, J. R. Maze, C. L. Degen, *Phys. Rev. Lett.* **2016**, *116*, 197601 (cit. on p. 6).

[44] J. M. Boss, K. S. Cujia, J. Zopes, C. L. Degen, *Science* **2017**, *356*, 837–840 (cit. on p. 6).

[45] D. R. Glenn, D. B. Bucher, J. Lee, M. D. Lukin, H. Park, R. L. Walsworth, *Nature* **2018**, *555*, 351–354 (cit. on p. 6).

[46] A. O. Sushkov, I. Lovchinsky, N. Chisholm, R. L. Walsworth, H. Park, M. D. Lukin, *Phys. Rev. Lett.* **2014**, *113* (cit. on p. 6).

[47] C. Müller, X. Kong, J.-M. Cai, K. Melentijević, A. Stacey, M. Markham, D. Twitchen, J. Isoya, S. Pezzagna, J. Meijer, J. F. Du, M. B. Plenio, B. Naydenov, L. P. McGuinness, F. Jelezko, *Nat. Commun.* **2014**, *5*, 4703 (cit. on p. 6).

[48] L. J. Rogers, K. D. Jahnke, M. H. Metsch, A. Sipahigil, J. M. Binder, T. Teraji, H. Sumiya, J. Isoya, M. D. Lukin, P. Hemmer, F. Jelezko, *Phys. Rev. Lett.* **2014**, *113*, 263602 (cit. on p. 6).

[49] A. Morello, J. J. Pla, F. A. Zwanenburg, K. W. Chan, K. Y. Tan, H. Huebl, M. Möttönen, C. D. Nugroho, C. Yang, J. A. van Donkelaar, A. D. C. Alves, D. N. Jamieson, C. C. Escott, L. C. L. Hollenberg, R. G. Clark, A. S. Dzurak, *Nature* **2010**, *467*, 687–691 (cit. on p. 7).

[50] N. Bar-Gill, L. M. Pham, A. Jarmola, D. Budker, R. L. Walsworth, *Nat. Commun.* **2013**, *4*, 1743 (cit. on p. 7).

[51] A. A. Popov, S. Yang, L. Dunsch, *Chem. Rev.* **2013**, *113*, 5989–6113 (cit. on pp. 7, 26).

[52] W. Harneit, *Phys. Rev. A* **2002**, *65*, 350 (cit. on pp. 7, 56).

[53] W. Harneit, C. Meyer, A. Weidinger, D. Suter, J. Twamley, *phys. stat. sol. (b)* **2002**, *233*, 453–461 (cit. on p. 7).

[54] A. Ardavan, M. Austwick, S. C. Benjamin, G. A. D. Briggs, T. J. S. Dennis, A. Ferguson, D. G. Hasko, M. Kanai, A. N. Khlobystov, B. W. Lovett, G. W. Morley, R. A. Oliver, D. G. Pettifor, K. Porfyrakis, J. H. Reina, J. H. Rice, J. D. Smith, R. A. Taylor, D. A. Williams, C. Adelmann, H. Mariette, R. J. Hamers, *Philos. Trans. A Math. Phys. Eng. Sci.* **2003**, *361*, 1473–1485 (cit. on p. 7).

[55] T. Wakahara, T. Kato, K. Miyazawa, W. Harneit, *Carbon* **2012**, *50*, 1709–1712 (cit. on pp. 7, 33).

[56] S. P. Cornes, S. Zhou, K. Porfyrakis, *Chem. Commun.* **2017**, *53*, 12742–12745 (cit. on pp. 7, 33).

[57] M. Eckardt, PhD thesis, Johannes Gutenberg-Universität Mainz, Mainz, **2016** (cit. on pp. 7, 30, 33, 56).

[58] W. Harneit in *Endohedral Fullerenes: Electron Transfer and Spin*, (Ed.: A. A. Popov), Nanostructure Science and Technology, Springer International Publishing, Cham, **2017**, pp. 297–324 (cit. on pp. 7, 33).

[59] D. Pinto, D. Paone, B. Kern, T. Dierker, R. Wieczorek, D. Dasari, W. Harneit, J. Wrachtrup, K. Kern, *in preparation* (cit. on pp. 7, 32, 33, 56).

[60] C. P. Slichter, *Principles of magnetic resonance*, 3., enl. and updated ed., corr. 3. printing, Springer, Berlin, **1996** (cit. on pp. 8, 9, 11).

[61] A. Schweiger, G. Jeschke, *Principles of pulse electron paramagnetic resonance*, Reprinted., Oxford Univ. Press, Oxford, **2005** (cit. on pp. 8, 9, 12, 13, 15, 16, 40, 149).

[62] N. M. Atherton, *Principles of electron spin resonance*, Horwood, New York, **1993** (cit. on pp. 12, 15, 17, 18).

[63] P. Gast, E. J. Groenen in *eMagRes*, *Vol. 34*, (Eds.: R. K. Harris, R. L. Wasylishen), John Wiley & Sons, Ltd, Chichester, UK, **2007**, pp. 1435–1444 (cit. on p. 14).

[64] A. Abragam, B. Bleaney, *Electron paramagnetic resonance of transition ions*, Reprinted., Clarendon Press, Oxford, **2013** (cit. on p. 16).

[65] A. Abragam, *The principles of nuclear magnetism*, Reprinted., Oxford Univ. Press, Oxford, **2007** (cit. on pp. 16, 17).

[66] J. A. Weil, J. R. Bolton, *Electron paramagnetic resonance: Elementary theory and practical applications*, 2nd ed., Wiley-Interscience, Hoboken, N.J, **2007** (cit. on pp. 16, 18, 125).

[67] A. Gali, M. Fyta, E. Kaxiras, *Appl. Magn. Reson.* **2008**, *77*, 94 (cit. on p. 16).

[68] F. Bloch, *Phys. Rev.* **1946**, *70*, 460–474 (cit. on p. 18).

[69] C. P. Poole, *Electron spin resonance: A comprehensive treatise on experimental techniques*, 2nd ed., John Wiley & Sons, Inc, New York, **1983** (cit. on pp. 18, 58, 104).

[70] P. Neumann, PhD Thesis, Universität Stuttgart, Stuttgart, **2012** (cit. on pp. 23, 38, 40, 43).

[71] H. W. Kroto, J. R. Heath, S. C. O'Brien, R. F. Curl, R. E. Smalley, *Nature* **1985**, *318*, 162–163 (cit. on p. 25).

[72] W. Krätschmer, L. D. Lamb, K. Fostiropoulos, D. R. Huffman, *Nature* **1990**, *347*, 354–358 (cit. on pp. 25, 28).

[73] H. W. Kroto, *Nature* **1987**, *329*, 529–531 (cit. on p. 25).

[74] T. G. Schmalz, W. A. Seitz, D. J. Klein, G. E. Hite, *Chem. Phys. Lett.* **1986**, *130*, 203–207 (cit. on p. 25).

[75] R. B. King, *Applications of graph theory and topology in inorganic cluster and coordination chemistry*, CRC Press, Boca Raton, **1993** (cit. on pp. 25, 26).

[76] Prinzbach, Weiler, Landenberger, Wahl, Worth, Scott, Gelmont, Olevano, B. v. Issendorff, *Nature* **2000**, *407*, 60–63 (cit. on p. 25).

[77] C. Piskoti, J. Yarger, A. Zettl, *Nature* **1998**, *393*, 771–774 (cit. on p. 25).

[78] S. I. Troyanov, S. Yang, C. Chen, E. Kemnitz, *Chem. Eur. J.* **2011**, *17*, 10662–10669 (cit. on p. 25).

[79] N. B. Tamm, L. N. Sidorov, E. Kemnitz, S. I. Troyanov, *Angew. Chem. Int. Ed. Engl.* **2009**, *48*, 9102–9104 (cit. on p. 25).

[80] A. Hirsch, *The Chemistry of the Fullerenes*, Wiley-VCH, Hoboken, **2008** (cit. on pp. 25, 26).

[81] W. H. Powell, F. Cozzi, G. P. Moss, C. Thilgen, R. J.-R. Hwu, A. Yerin, *Pure Appl. Chem.* **2002**, *74*, 629–695 (cit. on pp. 25, 26).

[82] J. Cioslowski, E. D. Fleischmann, *J. Chem. Phys.* **1991**, *94*, 3730–3734 (cit. on p. 26).

[83] W. E. Barth, R. G. Lawton, *J. Am. Chem. Soc.* **1966**, *88*, 380–381 (cit. on p. 26).

[84] J. M. Hawkins, A. Meyer, T. A. Lewis, S. Loren, F. J. Hollander, *Science* **1991**, *252*, 312–313 (cit. on p. 26).

[85] S. Liu, Y. J. Lu, M. M. Kappes, J. A. Ibers, *Science* **1991**, *254*, 408–410 (cit. on p. 26).

[86] K. Hedberg, L. Hedberg, D. S. Bethune, C. A. Brown, H. C. Dorn, R. D. Johnson, M. de Vries, *Science* **1991**, *254*, 410–412 (cit. on p. 26).

[87] G. B. Adams, M. O'Keeffe, R. S. Ruoff, *J. Phys. Chem.* **1994**, *98*, 9465–9469 (cit. on pp. 27, 29).

[88] N. O. McHedlov-Petrossyan, *Chem. Rev.* **2013**, *113*, 5149–5193 (cit. on pp. 27, 28).

[89] L.-S. Wang, J. Conceicao, C. Jin, R. E. Smalley, *Chem. Phys. Lett.* **1991**, *182*, 5–11 (cit. on p. 27).

[90] Y. Marcus, *J. Phys. Chem. B* **1997**, *101*, 8617–8623 (cit. on p. 27).

[91] G. E. Scuseria, *Chem. Phys. Lett.* **1991**, *180*, 451–456 (cit. on p. 27).

[92] A. L. Balch, V. J. Catalano, J. W. Lee, M. M. Olmstead, S. R. Parkin, *J. Am. Chem. Soc.* **1991**, *113*, 8953–8955 (cit. on p. 27).

[93] H. Ajie, M. M. Alvarez, S. J. Anz, R. D. Beck, F. Diederich, K. Fostiropoulos, D. R. Huffman, W. Kraetschmer, Y. Rubin, et al., *J. Phys. Chem.* **1990**, *94*, 8630–8633 (cit. on p. 27).

[94] R. D. Johnson, G. Meijer, J. R. Salem, D. S. Bethune, *J. Am. Chem. Soc.* **1991**, *113*, 3619–3621 (cit. on p. 27).

[95] N. Komatsu, T. Ohe, K. Matsushige, *Carbon* **2004**, *42*, 163–167 (cit. on p. 27).

[96] R. R. Zope, *J. Phys. Chem. B* **2007**, *40*, 3491–3496 (cit. on p. 27).

[97] C. A. Reed, R. D. Bolskar, *Chem. Rev.* **2000**, *100*, 1075–1120 (cit. on pp. 28, 55).

[98] Q. Xie, E. Perez-Cordero, L. Echegoyen, *J. Am. Chem. Soc.* **1992**, *114*, 3978–3980 (cit. on p. 28).

[99] M. J. Rosseinsky, *Chem. Mater.* **1998**, *10*, 2665–2685 (cit. on p. 28).

[100] C. B. Winkelmann, N. Roch, W. Wernsdorfer, V. Bouchiat, F. Balestro, *Nature Phys* **2009**, *5*, 876–879 (cit. on p. 28).

[101] G. Dennler, M. C. Scharber, C. J. Brabec, *Adv. Mater.* **2009**, *21*, 1323–1338 (cit. on p. 28).

[102] L. K. Shrestha, R. G. Shrestha, J. P. Hill, K. Ariga, *J. Oleo Sci.* **2013**, *62*, 541–553 (cit. on p. 28).

[103] H. Li, B. C.-K. Tee, J. J. Cha, Y. Cui, J. W. Chung, S. Y. Lee, Z. Bao, *J. Am. Chem. Soc.* **2012**, *134*, 2760–2765 (cit. on p. 28).

[104] S. Goodarzi, T. Da Ros, J. Conde, F. Sefat, M. Mozafari, *Mater. Today* **2017**, *20*, 460–480 (cit. on p. 28).

[105] R. E. Haufler, J. Conceicao, L. P. F. Chibante, Y. Chai, N. E. Byrne, S. Flanagan, M. M. Haley, S. C. O'Brien, C. Pan, et al., *J. Phys. Chem.* **1990**, *94*, 8634–8636 (cit. on p. 28).

[106] A. Anctil, C. W. Babbitt, R. P. Raffaelle, B. J. Landi, *Environ. Sci. Technol.* **2011**, *45*, 2353–2359 (cit. on pp. 28, 29).

[107] L. T. Scott, M. M. Boorum, B. J. McMahon, S. Hagen, J. Mack, J. Blank, H. Wegner, A. de Meijere, *Science* **2002**, *295*, 1500–1503 (cit. on p. 29).

[108] M. Mojica, J. A. Alonso, F. Méndez, *J. Phys. Org. Chem.* **2013**, *26*, 526–539 (cit. on p. 29).

[109] D. R. Lide, *CRC Handbook of chemistry and physics: A ready-reference book of chemical and physical data*, 90th ed., CRC Press, Boca Raton, FL, **2009** (cit. on pp. 29, 46, 64).

[110] M. A. Heald, R. Beringer, *Phys. Rev.* **1954**, *96*, 645–648 (cit. on p. 29).

[111] M. T. Almeida, Pawlik, Weidinger, Höhne, Alcala, Spaeth, *Phys. Rev. Lett.* **1996**, *77*, 1075–1078 (cit. on p. 29).

[112] C. Knapp, K.-P. Dinse, B. Pietzak, M. Waiblinger, A. Weidinger, *Chem. Phys. Lett.* **1997**, *272*, 433–437 (cit. on p. 29).

[113] H. Mauser, A. Hirsch, N. J. R. van Eikema Hommes, T. Clark, B. Pietzak, A. Weidinger, L. Dunsch, *Angew. Chem. Int. Ed. Engl.* **1997**, *36*, 2835–2838 (cit. on p. 29).

[114] L. Tsetseris, *J. Phys. Chem. C* **2011**, *115*, 3528–3533 (cit. on p. 29).

[115] P. Jakes, K.-P. Dinse, C. Meyer, W. Harneit, A. Weidinger, *Phys. Chem. Chem. Phys.* **2003**, *5*, 4080 (cit. on p. 30).

[116] M. Waiblinger, K. Lips, W. Harneit, A. Weidinger, E. Dietel, A. Hirsch, *Phys. Rev. B* **2001**, *64*, 1075 (cit. on p. 30).

[117] S. Tóth, D. Quintavalle, B. Náfrádi, L. Korecz, L. Forró, F. Simon, *J. Phys. Chem. B* **2008**, *77*, 11540117 (cit. on p. 30).

[118] M. Eckardt, R. Wieczorek, W. Harneit, *Carbon* **2015**, *95*, 601–607 (cit. on pp. 30, 32, 60).

[119] A. Weidinger, M. Waiblinger, B. Pietzak, T. Almeida Murphy, *Appl. Phys. A* **1998**, *66*, 287–292 (cit. on p. 30).

[120] W. A. Scrivens, P. V. Bedworth, J. M. Tour, *J. Am. Chem. Soc.* **1992**, *114*, 7917–7919 (cit. on p. 31).

[121] J. J. Wittmann, T. V. Can, M. Eckardt, W. Harneit, R. G. Griffin, B. Corzilius, *J. Magn. Reson.* **2018**, *290*, 12–17 (cit. on pp. 32, 60, 70).

[122] J. J. L. Morton, PhD thesis, University of Oxford, Oxford, **2005** (cit. on pp. 32, 33).

[123] A. Grupp, Pietzak B., Waiblinger M., Murphy T. A., Weidinger A., Roduner E. in Molecular Nanostructures, (Eds.: H. Kuzmany, J. Fink, M. Mehring, S. Roth), World Scientific, **1998**, p. 224 (cit. on p. 33).

[124] R. T. Harding, A. Folli, J. Zhou, G. A. D. Briggs, K. Porfyrakis, E. A. Laird, High pressure electron spin resonance of the endohedral fullerene 15NC60, **2017**, `http://arxiv.org/pdf/1712.05991v1` (cit. on p. 33).

[125] M. Waiblinger, Goedde B., Lips K., Harneit W., Jakes P., Weidinger A., Dinse K.-P. in AIP Conference Proceedings, AIP, **4-11 March 2000**, pp. 195–198 (cit. on p. 33).

[126] R. M. Brown, A. M. Tyryshkin, K. Porfyrakis, E. M. Gauger, B. W. Lovett, A. Ardavan, S. A. Lyon, G. A. D. Briggs, J. J. L. Morton, *Phys. Rev. Lett.* **2011**, *106*, 110504 (cit. on p. 33).

[127] A. Mateo-Alonso, D. Bonifazi, M. Prato in *Carbon Nanotechnology*, Elsevier, **2006**, pp. 155–189 (cit. on p. 34).

[128] Lenef, Rand, *Phys. Rev. B* **1996**, *53*, 13441–13455 (cit. on pp. 34, 35).

[129] M. W. Doherty, N. B. Manson, P. Delaney, F. Jelezko, J. Wrachtrup, L. C. Hollenberg, *Phys. Rep.* **2013**, *528*, 1–45 (cit. on pp. 34, 35, 37).

[130] L. M. Pham, N. Bar-Gill, D. Le Sage, C. Belthangady, A. Stacey, M. Markham, D. J. Twitchen, M. D. Lukin, R. L. Walsworth, *Phys. Rev. B* **2012**, *86* (cit. on p. 34).

[131] G. Balasubramanian, I. Y. Chan, R. Kolesov, M. Al-Hmoud, J. Tisler, C. Shin, C. Kim, A. Wojcik, P. R. Hemmer, A. Krueger, T. Hanke, A. Leitenstorfer, R. Bratschitsch, F. Jelezko, J. Wrachtrup, *Nature* **2008**, *455*, 648–651 (cit. on p. 39).

[132] A. Dréau, M. Lesik, L. Rondin, P. Spinicelli, O. Arcizet, J.-F. Roch, V. Jacques, *Phys. Rev. B* **2011**, *84* (cit. on p. 39).

[133] B. A. Myers, A. Das, M. C. Dartiailh, K. Ohno, D. D. Awschalom, A. C. Bleszynski Jayich, *Phys. Rev. Lett.* **2014**, *113*, 027602 (cit. on pp. 45, 148).

[134] S. N. Monteiro, A. L. D. Skury, M. G. de Azevedo, G. S. Bobrovnitchii, *J. Mater. Res. Technol.* **2013**, *2*, 68–74 (cit. on p. 46).

[135] R. S. Balmer, J. R. Brandon, S. L. Clewes, H. K. Dhillon, J. M. Dodson, I. Friel, P. N. Inglis, T. D. Madgwick, M. L. Markham, T. P. Mollart, N. Perkins, G. A. Scarsbrook, D. J. Twitchen, A. J. Whitehead, J. J. Wilman, S. M. Woollard, *J. Phys.: Condens. Matter* **2009**, *21*, 364221 (cit. on pp. 46, 47).

[136] B. Xu, Y. Tian, *J. Phys. Chem. C* **2015**, *119*, 5633–5638 (cit. on p. 46).

[137] G. Popovici, L. K. Bigelow, M. A. Prelas, *Handbook of Industrial Diamonds and Diamond Films*, Routledge, Boca Raton, **2018** (cit. on pp. 46–48).

[138] N. Yang, S. Yu, J. V. Macpherson, Y. Einaga, H. Zhao, G. Zhao, G. M. Swain, X. Jiang, *Chem. Soc. Rev.* **2019**, *48*, 157–204 (cit. on p. 47).

[139] S. Baluchová, A. Daňhel, H. Dejmková, V. Ostatná, M. Fojta, K. Schwarzová-Pecková, *Anal. Chim. Acta* **2019**, *1077*, 30–66 (cit. on p. 47).

[140] K. Muzyka, J. Sun, T. H. Fereja, Y. Lan, W. Zhang, G. Xu, *Anal. Methods* **2019**, *11*, 397–414 (cit. on p. 47).

[141] Y. Borzdov, Y. Pal'yanov, I. Kupriyanov, V. Gusev, A. Khokhryakov, A. Sokol, A. Efremov, *Diam. Rel. Mater.* **2002**, *11*, 1863–1870 (cit. on p. 47).

[142] R. Abbaschian, H. Zhu, C. Clarke, *Diam. Rel. Mater.* **2005**, *14*, 1916–1919 (cit. on p. 47).

[143] M. Schreck, J. Asmussen, S. Shikata, J.-C. Arnault, N. Fujimori, *MRS Bull.* **2014**, *39*, 504–510 (cit. on p. 47).

[144] N. Mizuochi, J. Isoya, J. Niitsuma, T. Sekiguchi, H. Watanabe, H. Kato, T. Makino, H. Okushi, S. Yamasaki, *J. Appl. Phys.* **2007**, *101*, 103501 (cit. on p. 47).

[145] K. Ohno, F. Joseph Heremans, L. C. Bassett, B. A. Myers, D. M. Toyli, A. C. Bleszynski Jayich, C. J. Palmstrøm, D. D. Awschalom, *Appl. Phys. Lett.* **2012**, *101*, 082413 (cit. on p. 47).

[146] A. K. Tiwari, J. P. Goss, P. R. Briddon, N. G. Wright, A. B. Horsfall, R. Jones, H. Pinto, M. J. Rayson, *Phys. Rev. B* **2011**, *84* (cit. on pp. 48, 96).

[147] M. Nimmrich, M. Kittelmann, P. Rahe, A. J. Mayne, G. Dujardin, A. von Schmidsfeld, M. Reichling, W. Harneit, A. Kühnle, *Phys. Rev. B* **2010**, *81* (cit. on p. 48).

[148] J. M. Binder, A. Stark, N. Tomek, J. Scheuer, F. Frank, K. D. Jahnke, C. Müller, S. Schmitt, M. H. Metsch, T. Unden, T. Gehring, A. Huck, U. L. Andersen, L. J. Rogers, F. Jelezko, **2017**, *6*, 85–90 (cit. on p. 50).

[149] M. Berthel, O. Mollet, G. Dantelle, T. Gacoin, S. Huant, A. Drezet, *Phys. Rev. B* **2015**, *91* (cit. on pp. 52, 54, 131).

[150] Kurtsiefer, Mayer, Zarda, Weinfurter, *Phys. Rev. Lett.* **2000**, *85*, 290–293 (cit. on p. 53).

[151] Y. Sonnefraud, A. Cuche, O. Faklaris, J.-P. Boudou, T. Sauvage, J.-F. Roch, F. Treussart, S. Huant, *Opt. Lett.* **2008**, *33*, 611 (cit. on pp. 53, 131).

[152] R. D. Bolskar, PhD, University of Southern California, Los Angeles, **1997** (cit. on pp. 55–57, 60).

[153] H. Ohkita, S. Ito, *Polymer* **2011**, *52*, 4397–4417 (cit. on p. 55).

[154] W. Harneit, C. Boehme, S. Schaefer, K. Huebener, K. Fostiropoulos, K. Lips, *Phys. Rev. Lett.* **2007**, *98*, 216601 (cit. on p. 56).

[155] S. G. Kukolich, D. R. Huffman, *Chem. Phys. Lett.* **1991**, *182*, 263–265 (cit. on p. 56).

[156] M. Baumgarten, L. Gherghel, *Appl. Magn. Reson.* **1996**, *11*, 171–182 (cit. on p. 56).

[157] F. I.-G. S. Cataldo, *Eur. Chem. Bull.* **2014**, 920–924 (cit. on p. 56).

[158] A. A. Slinkin, S. C. Emberson, E. G. Derouane, *Kinet. Catal.* **1994**, 102–105 (cit. on p. 56).

[159] S. Fukuzumi, T. Suenobu, T. Urano, K. Tanaka, *Chem. Lett.* **1997**, *26*, 875–876 (cit. on pp. 56–58, 73).

[160] C. C. Yang, K. C. Hwang, *J. Am. Chem. Soc.* **1996**, *118*, 4693–4698 (cit. on p. 56).

[161] L. Dunsch, F. Ziegs, C. Siedschlag, J. Mattay, *Chem. Eur. J.* **2000**, *6*, 3547–3550 (cit. on p. 56).

[162] G. G. Fedoruk, *Phys. Solid State* **2000**, *42*, 1182–1185 (cit. on pp. 59, 61).

[163] S. Stoll, A. Schweiger, *J. Magn. Reson.* **2006**, *178*, 42–55 (cit. on pp. 61, 70, 94, 125).

[164] Völkel, Pöppl, Simon, Hoentsch, Orlinskii, Klos, Gotschy, *Phys. Rev. B* **1995**, *52*, 10188–10193 (cit. on p. 63).

[165] Q. Xie, F. Arias, L. Echegoyen, *J. Am. Chem. Soc.* **1993**, *115*, 9818–9819 (cit. on p. 64).

[166] R. W. Schwartz, N. J. Hill, *J. Chem. Soc. Faraday Trans. 2* **1974**, *70*, 124 (cit. on p. 64).

[167] V. Sridharan, J. C. Menéndez, *Chem. Rev.* **2010**, *110*, 3805–3849 (cit. on p. 64).

[168] P. Sivaguru, A. Lalitha, *Chin. Chem. Lett.* **2014**, *25*, 321–323 (cit. on pp. 64, 71).

[169] P. Sivaguru, K. Bhuvaneswari, R. Ramkumar, A. Lalitha, *Tetrahedron Lett.* **2014**, *55*, 5683–5686 (cit. on p. 64).

[170] P. N. Keizer, J. R. Morton, K. F. Preston, *J. Chem. Soc. Chem. Commun.* **1992**, 1259 (cit. on p. 65).

[171] P. Neta, R. W. Fessenden, *J. Phys. Chem.* **1974**, *78*, 523–529 (cit. on p. 65).

[172] L. Hermosilla, J. M.G. d. La Vega, C. Sieiro, P. Calle, *J. Chem. Theory Comput.* **2011**, *7*, 169–179 (cit. on p. 65).

[173] J. Duran, H. Panepucci, H. A. Farach, C. P. Poole, *J. Magn. Reson.* **1982**, *46*, 374–384 (cit. on p. 66).

[174] E. P. Barrett, L. G. Joyner, P. P. Halenda, *J. Am. Chem. Soc.* **1951**, *73*, 373–380 (cit. on pp. 70, 74).

[175] J. Landers, G. Y. Gor, A. V. Neimark, *Colloids Surf. A* **2013**, *437*, 3–32 (cit. on pp. 70, 74).

[176] J. A. Kaduk, J. Faber, *The Rigaku Journal* **1995**, 14–34 (cit. on pp. 71, 72).

[177] R. K. Iler, *The chemistry of silica: Solubility, polymerization, colloid and surface properties, and biochemistry*, [Nachdr.], Wiley, New York, NY, **2004** (cit. on p. 71).

[178] V. van Speybroeck, K. Hemelsoet, L. Joos, M. Waroquier, R. G. Bell, C. R. A. Catlow, *Chem. Soc. Rev.* **2015**, *44*, 7044–7111 (cit. on p. 72).

[179] D. H. Olson, *Zeolites* **1995**, *15*, 439–443 (cit. on p. 72).

[180] S. Brunauer, P. H. Emmett, E. Teller, *J. Am. Chem. Soc.* **1938**, *60*, 309–319 (cit. on p. 73).

[181] M. Thommes, K. Kaneko, A. V. Neimark, J. P. Olivier, F. Rodriguez-Reinoso, J. Rouquerol, K. S. Sing, *Pure Appl. Chem.* **2015**, *87*, 1051–1069 (cit. on pp. 73, 74).

[182] S. L. Hailu, B. U. Nair, M. Redi-Abshiro, R. Aravindhan, I. Diaz, M. Tessema, *RSC Adv.* **2015**, *5*, 88636–88645 (cit. on p. 75).

[183] N. P. Evmiridis, *Inorg. Chem.* **1986**, *25*, 4362–4369 (cit. on p. 76).

[184] C. Finel, L. Kevan, *Faraday Trans.* **1993**, *89*, 2559 (cit. on p. 76).

[185] B. Wichterlová, *Zeolites* **1981**, *1*, 181–185 (cit. on p. 76).

[186] J.-C. Arnault, *Nanodiamonds: Advanced Material Analysis, Properties and Applications*, Elsevier Ltd, Amsterdam, Netherlands, **2017** (cit. on pp. 78, 80).

[187] *Nanodiamond*, (Ed.: O. A. Williams), Royal Society of Chemistry, Cambridge, **2014** (cit. on pp. 78, 94).

[188] K. Turcheniuk, V. N. Mochalin, *Nanotechnology* **2017**, *28*, 252001 (cit. on pp. 78, 95).

[189] D. Terada, T. Genjo, T. F. Segawa, R. Igarashi, M. Shirakawa, *Biochim. Biophys. Acta. Gen. Subj.* **2019**, 1–15 (cit. on p. 78).

[190] F.-J. Hsieh, Y.-W. Chen, Y.-K. Huang, H.-M. Lee, C.-H. Lin, H.-C. Chang, *Anal. Chem.* **2018**, *90*, 1566–1571 (cit. on p. 78).

[191] X.-Q. Zhang, M. Chen, R. Lam, X. Xu, E. Osawa, D. Ho, *ACS Nano* **2009**, *3*, 2609–2616 (cit. on p. 78).

[192] J. Wehling, R. Dringen, R. N. Zare, M. Maas, K. Rezwan, *ACS Nano* **2014**, *8*, 6475–6483 (cit. on p. 78).

[193] R. Schirhagl, K. Chang, M. Loretz, C. L. Degen, *Annu. Rev. Phys. Chem.* **2014**, *65*, 83–105 (cit. on p. 78).

[194] A. Nagl, S. R. Hemelaar, R. Schirhagl, *Anal. Bioanal. Chem.* **2015**, *407*, 7521–7536 (cit. on p. 78).

[195] M. H. Alkahtani, F. Alghannam, L. Jiang, A. Almethen, A. A. Rampersaud, R. Brick, C. L. Gomes, M. O. Scully, P. R. Hemmer, *Nanophotonics* **2018**, *7*, 1423–1453 (cit. on p. 78).

[196] L. P. McGuinness, Y. Yan, A. Stacey, D. A. Simpson, L. T. Hall, D. Maclaurin, S. Prawer, P. Mulvaney, J. Wrachtrup, F. Caruso, R. E. Scholten, L. C. L. Hollenberg, *Nat. Nanotechnol.* **2011**, *6*, 358–363 (cit. on p. 78).

[197] S. Huo, S. Jin, X. Ma, X. Xue, K. Yang, A. Kumar, P. C. Wang, J. Zhang, Z. Hu, X.-J. Liang, *ACS Nano* **2014**, *8*, 5852–5862 (cit. on p. 79).

[198] R. Martín, M. Alvaro, J. R. Herance, H. García, *ACS Nano* **2010**, *4*, 65–74 (cit. on p. 79).

[199] T. Gaebel, M. Domhan, I. Popa, C. Wittmann, P. Neumann, F. Jelezko, J. R. Rabeau, N. Stavrias, A. D. Greentree, S. Prawer, J. Meijer, J. Twamley, P. R. Hemmer, J. Wrachtrup, *Nature Phys* **2006**, *2*, 408–413 (cit. on p. 79).

[200] N. Aslam, G. Waldherr, P. Neumann, F. Jelezko, J. Wrachtrup, *New J. Phys.* **2013**, *15*, 013064 (cit. on p. 79).

[201] Y. Doi, T. Fukui, H. Kato, T. Makino, S. Yamasaki, T. Tashima, H. Morishita, S. Miwa, F. Jelezko, Y. Suzuki, N. Mizuochi, *Phys. Rev. B* **2016**, *93* (cit. on p. 79).

[202] M. V. Hauf, B. Grotz, B. Naydenov, M. Dankerl, S. Pezzagna, J. Meijer, F. Jelezko, J. Wrachtrup, M. Stutzmann, F. Reinhard, J. A. Garrido, *Phys. Rev. B* **2011**, *83* (cit. on p. 79).

[203] A. N. Newell, D. A. Dowdell, D. H. Santamore, *J. Appl. Phys.* **2016**, *120*, 185104 (cit. on p. 79).

[204] S. Dhomkar, H. Jayakumar, P. R. Zangara, C. A. Meriles, *Nano Lett.* **2018**, *18*, 4046–4052 (cit. on p. 79).

[205] D. Bluvstein, Z. Zhang, A. C. B. Jayich, *Phys. Rev. Lett.* **2019**, *122*, 076101 (cit. on pp. 79, 131, 133, 134, 149).

[206] A. Krueger, D. Lang, *Adv. Funct. Mater.* **2012**, *22*, 890–906 (cit. on pp. 79, 80, 95, 116).

[207] O. A. Shenderova, G. E. McGuire, *Biointerphases* **2015**, *10*, 030802 (cit. on p. 79).

[208] J. Neburkova, J. Vavra, P. Cigler, *Curr. Opin. Solid St. M.* **2017**, *21*, 43–53 (cit. on p. 79).

[209] W. S. Yeap, S. Chen, K. P. Loh, *Langmuir* **2009**, *25*, 185–191 (cit. on p. 79).

[210] S. Osswald, G. Yushin, V. Mochalin, S. O. Kucheyev, Y. Gogotsi, *J. Am. Chem. Soc.* **2006**, *128*, 11635–11642 (cit. on p. 79).

[211] O. Shenderova, A. Koscheev, N. Zaripov, I. Petrov, Y. Skryabin, P. Detkov, S. Turner, G. van Tendeloo, *J. Phys. Chem. C* **2011**, *115*, 9827–9837 (cit. on p. 79).

[212] V. N. Mochalin, O. Shenderova, D. Ho, Y. Gogotsi, *Nat. Nanotechnol.* **2011**, *7*, 11–23 (cit. on p. 79).

[213] T. Meinhardt, D. Lang, H. Dill, A. Krueger, *Adv. Funct. Mater.* **2011**, *21*, 494–500 (cit. on p. 80).

[214] X. Zhang, C. Fu, L. Feng, Y. Ji, L. Tao, Q. Huang, S. Li, Y. Wei, *Polymer* **2012**, *53*, 3178–3184 (cit. on p. 80).

[215] M. S. Chan, L. S. Liu, H. M. Leung, P. K. Lo, *ACS Appl. Mater. Interfaces* **2017**, *9*, 11780–11789 (cit. on p. 80).

[216] H. M. Leung, M. S. Chan, L. S. Liu, S. W. Wong, T. W. Lo, C.-H. Lau, C. Tin, P. K. Lo, *ACS Sustainable Chem. Eng.* **2018**, *6*, 9671–9681 (cit. on p. 80).

[217] J. Giammarco, V. N. Mochalin, J. Haeckel, Y. Gogotsi, *J. Colloid. Interface Sci.* **2016**, *468*, 253–261 (cit. on p. 80).

[218] M. Kaviani, P. Deák, B. Aradi, T. Frauenheim, J.-P. Chou, A. Gali, *Nano Lett.* **2014**, *14*, 4772–4777 (cit. on pp. 80, 96).

[219] K. Ohashi, T. Rosskopf, H. Watanabe, M. Loretz, Y. Tao, R. Hauert, S. Tomizawa, T. Ishikawa, J. Ishi-Hayase, S. Shikata, C. L. Degen, K. M. Itoh, *Nano Lett.* **2013**, *13*, 4733–4738 (cit. on p. 80).

[220] A. Stacey, K. M. O'Donnell, J.-P. Chou, A. Schenk, A. Tadich, N. Dontschuk, J. Cervenka, C. Pakes, A. Gali, A. Hoffman, S. Prawer, *Adv. Mater. Interfaces* **2015**, *2*, 1500079 (cit. on pp. 80, 97).

[221] J.-P. Chou, A. Retzker, A. Gali, *Nano Lett.* **2017**, *17*, 2294–2298 (cit. on pp. 80, 97).

[222] A. Stacey, N. Dontschuk, J.-P. Chou, D. A. Broadway, A. K. Schenk, M. J. Sear, J.-P. Tetienne, A. Hoffman, S. Prawer, C. I. Pakes, A. Tadich, N. P. de Leon, A. Gali, L. C. L. Hollenberg, *Adv. Mater. Interfaces* **2019**, *6*, 1801449 (cit. on pp. 80, 96, 97, 99).

[223] P. Han, D. Antonov, J. Wrachtrup, G. Bester, *Phys. Rev. B* **2017**, *95*, 733 (cit. on p. 80).

[224] M. Hesse, H. Meier, B. Zeeh, *Spectroscopic methods in organic chemistry: 100 tables*, 2. ed., Thieme, Stuttgart, **2008** (cit. on pp. 82, 85, 115).

[225] O. Shenderova, A. M. Panich, S. Moseenkov, S. C. Hens, V. Kuznetsov, H.-M. Vieth, *J. Phys. Chem. C* **2011**, *115*, 19005–19011 (cit. on pp. 82, 84, 85, 109).

[226] V. Y. Dolmatov, I. I. Kulakova, V. Myllymäki, A. Vehanen, A. N. Panova, A. A. Voznyakovskii, *J. Superhard Mater.* **2014**, *36*, 344–357 (cit. on pp. 82, 104, 107, 109–111, 113, 115).

[227] T. Petit, L. Puskar, T. Dolenko, S. Choudhury, E. Ritter, S. Burikov, K. Laptinskiy, Q. Brzustowski, U. Schade, H. Yuzawa, M. Nagasaka, N. Kosugi, M. Kurzyp, A. Venerosy, H. Girard, J.-C. Arnault, E. Osawa, N. Nunn, O. Shenderova, E. F. Aziz, *J. Phys. Chem. C* **2017**, *121*, 5185–5194 (cit. on p. 82).

[228] I. I. Kulakova, *Phys. Solid State* **2004**, *46*, 636–643 (cit. on p. 82).

[229] J.-S. Tu, E. Perevedentseva, P.-H. Chung, C.-L. Cheng, *J. Chem. Phys.* **2006**, *125*, 174713 (cit. on p. 82).

[230] T. Jiang, K. Xu, *Carbon* **1995**, *33*, 1663–1671 (cit. on p. 82).

[231] P. John, N. Polwart, C. E. Troupe, J. I. B. Wilson, *J. Am. Chem. Soc.* **2003**, *125*, 6600–6601 (cit. on p. 82).

[232] L. N. Markovskij, V. E. Pashinnik, A. V. Kirsanov, *Synthesis* **1973**, *1973*, 787–789 (cit. on p. 83).

[233] W. J. Middleton, *J. Org. Chem.* **1975**, *40*, 574–578 (cit. on pp. 83, 84).

[234] M. Hudlický in *Organic Reactions*, *Vol. 1964*, John Wiley & Sons, Inc, Hoboken, NJ, USA, **2004**, pp. 513–637 (cit. on pp. 83, 84).

[235] C. F. Lane, *Chem. Rev.* **1976**, *76*, 773–799 (cit. on pp. 84–86).

[236] A. Krüger, Y. Liang, G. Jarre, J. Stegk, **2006**, *16*, 2322–2328 (cit. on pp. 84, 85, 108).

[237] K. Ray, T. Petrenko, K. Wieghardt, F. Neese, *Dalton Trans.* **2007**, 1552–1566 (cit. on pp. 85, 87).

[238] H. Schwertfeger, C. Würtele, H. Hausmann, J. E. P. Dahl, R. M. K. Carlson, A. A. Fokin, P. R. Schreiner, *Adv. Synth. Catal.* **2009**, *351*, 1041–1054 (cit. on pp. 85–87, 110).

[239] Y. Liu, Z. Gu, J. L. Margrave, V. N. Khabashesku, *Chem. Mater.* **2004**, *16*, 3924–3930 (cit. on pp. 85, 87, 110).

[240] H. C. Brown, P. Heim, N. M. Yoon, *J. Am. Chem. Soc.* **1970**, *92*, 1637–1646 (cit. on p. 85).

[241] A. S. Kende, Fludzinski P., *Org. Synth.* **1986**, *64*, 104 (cit. on p. 85).

[242] H. C. Brown, B. C. S. Rao, *J. Am. Chem. Soc.* **1956**, *78*, 5694–5695 (cit. on p. 85).

[243] D. J. Pasto, C. C. Cumbo, J. Hickman, *J. Am. Chem. Soc.* **1966**, *88*, 2201–2207 (cit. on p. 86).

[244] J. Havlik, H. Raabova, M. Gulka, V. Petrakova, M. Krecmarova, V. Masek, P. Lousa, J. Stursa, H.-G. Boyen, M. Nesladek, P. Cigler, *Adv. Funct. Mater.* **2016**, *26*, 4134–4142 (cit. on p. 87).

[245] A. M. Panich, H.-M. Vieth, A. I. Shames, N. Froumin, E. Ôsawa, A. Yao, *J. Phys. Chem. C* **2010**, *114*, 774–782 (cit. on pp. 87, 93, 97).

[246] E. M. Zagrebina, A. V. Generalov, A. Y. Klyushin, K. A. Simonov, N. A. Vinogradov, M. Dubois, L. Frezet, N. Mårtensson, A. B. Preobrajenski, A. S. Vinogradov, *J. Phys. Chem. C* **2015**, *119*, 835–844 (cit. on p. 87).

[247] T. Mallouk, N. Bartlett, *J. Chem. Soc. Chem. Commun.* **1983**, 103 (cit. on p. 87).

[248] I. Palchan, M. Crespin, H. Estrade-Szwarckopf, B. Rousseau, *Chem. Phys. Lett.* **1989**, *157*, 321–327 (cit. on p. 87).

[249] R. Hagiwara, M. Lerner, N. Bartlett, *J. Chem. Soc. Chem. Commun.* **1989**, 573 (cit. on p. 87).

[250] T. Nakajima, M. Molinier, M. Motoyama, *Carbon* **1991**, *29*, 429–437 (cit. on p. 87).

[251] C. Osterkamp, J. Lang, J. Scharpf, C. Müller, L. P. McGuinness, T. Diemant, R. J. Behm, B. Naydenov, F. Jelezko, *Appl. Phys. Lett.* **2015**, *106*, 113109 (cit. on p. 87).

[252] A. Freedman, C. D. Stinespring, *Chem. Phys. Lett.* **1990**, *57*, 1194–1196 (cit. on p. 87).

[253] K. J. Rietwyk, M. Wanke, H. M. Vulling, M. T. Edmonds, P. L. Sharp, Y. Smets, Q.-H. Wu, A. Tadich, S. Rubanov, P. J. Moriarty, L. Ley, C. I. Pakes, *Phys. Rev. B* **2011**, *84* (cit. on p. 87).

[254] K. J. Rietwyk, S. L. Wong, L. Cao, K. M. O'Donnell, L. Ley, A. T. S. Wee, C. I. Pakes, *Appl. Phys. Lett.* **2013**, *102*, 091604 (cit. on p. 87).

[255] C. Osterkamp, J. Scharpf, S. Pezzagna, J. Meijer, T. Diemant, R. Jürgen Behm, B. Naydenov, F. Jelezko, *Appl. Phys. Lett.* **2013**, *103*, 193118 (cit. on p. 87).

[256] V. N. Mitkin, *J. Struct. Chem.* **2003**, *44*, 82–115 (cit. on p. 88).

[257] C. Cavallari, M. Brunelli, S. Radescu, M. Dubois, N. Batisse, G. Vaughan, H. E. Fischer, V. Pischedda, *Carbon* **2019**, *147*, 1–8 (cit. on p. 88).

[258] W. R. Bamford, T. S. Stevens, *J. Chem. Soc.* **1952**, 4735 (cit. on p. 88).

[259] R. H. Shapiro in *Organic Reactions*, *Vol. 63*, John Wiley & Sons, Inc, Hoboken, NJ, USA, **2004**, pp. 405–507 (cit. on pp. 88, 96).

[260] L. Kürti, B. Czakó, *Strategic applications of named reactions in organic synthesis: Background and detailed mechanisms ; 250 named reactions*, [Nachdr.], Elsevier Acad. Press, Amsterdam, **2009** (cit. on pp. 89, 99).

[261] Ripalda, Diaz, Roman, Galan, Montero, Goldoni, Baraldi, Lizzit, Comelli, Paolucci, *Phys. Rev. Lett.* **2000**, *85*, 2132–2135 (cit. on p. 91).

[262] J. T. Titantah, D. Lamoen, *Diam. Rel. Mater.* **2007**, *16*, 581–588 (cit. on p. 91).

[263] M. Chandran, M. Shasha, S. Michaelson, A. Hoffman, *Appl. Phys. Lett.* **2015**, *107*, 111602 (cit. on p. 91).

[264] G. Tuci, L. Luconi, A. Rossin, E. Berretti, H. Ba, M. Innocenti, D. Yakhvarov, S. Caporali, C. Pham-Huu, G. Giambastiani, *ACS Appl. Mater. Interfaces* **2016**, *8*, 30099–30106 (cit. on p. 91).

[265] Y. S. Zou, Q. M. Wang, H. Du, G. H. Song, J. Q. Xiao, J. Gong, C. Sun, L. S. Wen, *Appl. Surf. Sci.* **2005**, *241*, 295–302 (cit. on p. 91).

[266] N. D. Samsonenko, G. V. Zhmykhov, V. S. Zon, V. K. Aksenov, *J. Struct. Chem.* **1980**, *20*, 951–953 (cit. on pp. 93, 126).

[267] A. I. Shames, A. M. Panich, W. Kempiński, A. E. Alexenskii, M. V. Baidakova, A. T. Dideikin, V. Osipov, V. I. Siklitski, E. Osawa, M. Ozawa, A. Y. Vul', *J. Phys. Chem. Solids* **2002**, *63*, 1993–2001 (cit. on pp. 93, 128).

[268] A. V. Fionov, A. Lund, W. M. Chen, N. N. Rozhkova, I. A. Buyanova, G. I. Emel'yanova, L. E. Gorlenko, E. V. Golubina, E. S. Lokteva, E. Osawa, V. V. Lunin, *Chem. Phys. Lett.* **2010**, *493*, 319–322 (cit. on pp. 93, 126).

[269] A. I. Shames, V. Y. Osipov, J. P. Boudou, A. M. Panich, H. J. von Bardeleben, F. Treussart, A. Y. Vul', *J. Phys. D: Appl. Phys.* **2015**, *48*, 155302 (cit. on pp. 93, 130).

[270] A. M. Panich, *Crit. Rev. Solid State* **2012**, *37*, 276–303 (cit. on p. 93).

[271] A. M. Panich, N. A. Sergeev, A. I. Shames, V. Y. Osipov, J.-P. Boudou, S. D. Goren, *J. Phys.: Condens. Matter* **2015**, *27*, 072203 (cit. on pp. 93, 130).

[272] A. M. Panich, A. I. Shames, *J. Phys. Chem. C* **2015**, *119*, 21286–21287 (cit. on p. 93).

[273] K. Turcheniuk, C. Trecazzi, C. Deeleepojananan, V. N. Mochalin, *ACS Appl. Mater. Interfaces* **2016**, *8*, 25461–25468 (cit. on pp. 95, 116).

[274] A. Krüger, F. Kataoka, M. Ozawa, T. Fujino, Y. Suzuki, A. E. Aleksenskii, A. Y. Vul', E. Osawa, *Carbon* **2005**, *43*, 1722–1730 (cit. on p. 95).

[275] F. A. Carey, R. J. Sundberg, *Structure and mechanisms*, 5. ed., corr. 2. printing, Springer, New York, NY, **2008** (cit. on p. 95).

[276] R. W. Baldock, P. Hudson, A. R. Katritzky, F. Soti, *J. Chem. Soc. Perkin Trans. 1* **1974**, 1422 (cit. on p. 96).

[277] T. W. Shanley, A. A. Martin, I. Aharonovich, M. Toth, *Appl. Phys. Lett.* **2014**, *105*, 063103 (cit. on p. 96).

[278] A. Albrecht, G. Koplovitz, A. Retzker, F. Jelezko, S. Yochelis, D. Porath, Y. Nevo, O. Shoseyov, Y. Paltiel, M. B Plenio, *New J. Phys.* **2014**, *16*, 093002 (cit. on pp. 97, 101).

[279] S. Stankovich, D. A. Dikin, R. D. Piner, K. A. Kohlhaas, A. Kleinhammes, Y. Jia, Y. Wu, S. T. Nguyen, R. S. Ruoff, *Carbon* **2007**, *45*, 1558–1565 (cit. on p. 97).

[280] S. Ayral-Kaloustian, W. C. Agosta, *J. Am. Chem. Soc.* **1980**, *102*, 314–323 (cit. on p. 98).

[281] K. N. Houk, J. Sims, R. E. Duke, R. W. Strozier, J. K. George, *J. Am. Chem. Soc.* **1973**, *95*, 7287–7301 (cit. on pp. 98, 99).

[282] J. P. Guthrie, *Can. J. Chem.* **1979**, *57*, 1177–1185 (cit. on p. 99).

[283] X.-Y. Zhang, S. Yang, Y. Wei, M. Shi, *Org. Biomol. Chem.* **2018**, *16*, 6399–6404 (cit. on p. 99).

[284] J. Tisler, G. Balasubramanian, B. Naydenov, R. Kolesov, B. Grotz, R. Reuter, J.-P. Boudou, P. A. Curmi, M. Sennour, A. Thorel, M. Börsch, K. Aulenbacher, R. Erdmann, P. R. Hemmer, F. Jelezko, J. Wrachtrup, *ACS Nano* **2009**, *3*, 1959–1965 (cit. on pp. 101, 129).

[285] M. A. Ray, T. Tyler, B. Hook, A. Martin, G. Cunningham, O. Shenderova, J. L. Davidson, M. Howell, W. P. Kang, G. McGuire, *Diam. Rel. Mater.* **2007**, *16*, 2087–2089 (cit. on p. 110).

[286] Spectral Database for Organic Compounds (SDBS): IR spectrum; SDBS No.: 3435; RN 1576-35-8, `https://sdbs.db.aist.go.jp/sdbs/` (cit. on pp. 113, 114).

[287] S. Lopes, I. Reva, R. Fausto, *Vib. Spectrosc.* **2015**, *81*, 68–82 (cit. on pp. 113, 114).

[288] W. L. Jolly, *Modern inorganic chemistry*, McGraw-Hill, New York, **1984** (cit. on p. 115).

[289] G.-W. Yang, J.-B. Wang, Q.-X. Liu, *J. Appl. Phys.* **1998**, *10*, 7923–7927 (cit. on p. 116).

[290] S. Pearce, S. J. Henley, F. Claeyssens, P. W. May, K. R. Hallam, J. A. Smith, K. N. Rosser, *Diam. Rel. Mater.* **2004**, *13*, 661–665 (cit. on p. 116).

[291] D. Amans, A.-C. Chenus, G. Ledoux, C. Dujardin, C. Reynaud, O. Sublemontier, K. Masenelli-Varlot, O. Guillois, *Diam. Rel. Mater.* **2009**, *18*, 177–180 (cit. on p. 116).

[292] H. Akaike in *Selected Papers of Hirotugu Akaike*, (Eds.: E. Parzen, K. Tanabe, G. Kitagawa), Springer Series in Statistics, Springer New York, New York, NY, **1998**, pp. 199–213 (cit. on p. 118).

[293] K. P. Burnham, D. R. Anderson, *Model selection and multimodel inference: A practical information-theoretic approach*, 2. ed., [4. printing], Springer, New York, NY, **2010** (cit. on p. 118).

[294] S. Cui, E. L. Hu, *Appl. Phys. Lett.* **2013**, *103*, 051603 (cit. on p. 119).

[295] *Handbook of x-ray spectrometry*, 2. ed., rev. and expanded., (Eds.: R. E. van Grieken, A. A. Markowicz), Marcel Dekker, New York, NY, **2002** (cit. on p. 125).

[296] E. Desimoni, G. I. Casella, T. Cataldi, C. Malitesta, *J. Electron. Spetrosc.* **1989**, *49*, 247–261 (cit. on p. 125).

[297] W. Hagen, D. Hearshen, R. Sands, W. Dunham, *J. Magn. Reson.* **1985**, *61*, 220–232 (cit. on p. 126).

[298] Aqualino, Brill, Bryce, Gerstman, *Phys. Rev. A* **1991**, *44*, 5257–5271 (cit. on p. 126).

[299] B. Smeltzer, L. Childress, A. Gali, *New J. Phys.* **2011**, *13*, 025021 (cit. on p. 132).

[300] F. Shi, X. Rong, N. Xu, Y. Wang, J. Wu, B. Chong, X. Peng, J. Kniepert, R.-S. Schoenfeld, W. Harneit, M. Feng, J. Du, *Phys. Rev. Lett.* **2010**, *105*, 040504 (cit. on p. 132).

[301] B. A. Myers, A. Ariyaratne, A. C. B. Jayich, *Phys. Rev. Lett.* **2017**, *118*, 197201 (cit. on p. 133).

[302] L. P. McGuinness, L. T. Hall, A. Stacey, D. A. Simpson, C. D. Hill, J. H. Cole, K. Ganesan, B. C. Gibson, S. Prawer, P. Mulvaney, F. Jelezko, J. Wrachtrup, R. E. Scholten, L. C. L. Hollenberg, *New J. Phys.* **2013**, *15*, 073042 (cit. on p. 135).

[303] F. Shi, Q. Zhang, P. Wang, H. Sun, J. Wang, X. Rong, M. Chen, C. Ju, F. Reinhard, H. Chen, J. Wrachtrup, J. Wang, J. Du, *Science* **2015**, *347*, 1135–1138 (cit. on p. 142).

[304] L. Schlipf, T. Oeckinghaus, K. Xu, D. B. R. Dasari, A. Zappe, F. F. de Oliveira, B. Kern, M. Azarkh, M. Drescher, M. Ternes, K. Kern, J. Wrachtrup, A. Finkler, **2017**, *3*, e1701116 (cit. on pp. 142, 150).

[305] *Dithiolene Chemistry*, (Ed.: E. I. Stiefel), John Wiley & Sons, Inc, Hoboken, NJ, USA, **2003** (cit. on p. 142).

[306] A. Das, Z. Han, W. W. Brennessel, P. L. Holland, R. Eisenberg, *ACS Catal.* **2015**, *5*, 1397–1406 (cit. on p. 142).

[307] L. Sun, S. Shu, Y. Zhou, S. Hou, Y. Liu, Z. Ke, *Materials* **2018**, *11* (cit. on pp. 142, 148).

[308] J. McGuire, H. N. Miras, J. P. Donahue, E. Richards, S. Sproules, *Chem. Eur. J.* **2018**, *24*, 17598–17605 (cit. on p. 142).

[309] G. N. Schrauzer, V. Mayweg, *J. Am. Chem. Soc.* **1962**, *84*, 3221 (cit. on pp. 144, 155).

[310] K. Arumugam, J. E. Bollinger, M. Fink, J. P. Donahue, *Inorg. Chem.* **2007**, *46*, 3283–3288 (cit. on p. 144).

[311] G. C. Papavassiliou, G. C. Anyfantis, G. A. Mousdis, *Crystals* **2012**, *2*, 762–811 (cit. on p. 144).

[312] A. Davison, N. Edelstein, R. H. Holm, A. H. Maki, *Inorg. Chem.* **1963**, *2*, 1227–1232 (cit. on pp. 144, 156, 157).

[313] B. Grotz, J. Beck, P. Neumann, B. Naydenov, R. Reuter, F. Reinhard, F. Jelezko, J. Wrachtrup, D. Schweinfurth, B. Sarkar, P. Hemmer, *New J. Phys.* **2011**, *13*, 055004 (cit. on p. 146).

[314] C. L. Degen, M. Poggio, H. J. Mamin, D. Rugar, *Phys. Rev. Lett.* **2007**, *99*, 250601 (cit. on p. 149).

[315] K. Udpa, S. Sarkar, *Polyhedron* **1987**, *6*, 627–631 (cit. on pp. 150, 153).

[316] A. Zarkadoulas, M. J. Field, C. Papatriantafyllopoulou, J. Fize, V. Artero, C. A. Mitsopoulou, *Inorg. Chem.* **2016**, *55*, 432–444 (cit. on pp. 153, 154).

[317] F. Neese, *Wiley Interdiscip. Rev.: Comput Mol Sci* **2012**, *2*, 73–78 (cit. on p. 153).

[318] I. Siewert, *Chem. Eur. J.* **2015**, *21*, 15078–15091 (cit. on p. 154).

[319] A. Zarkadoulas, E. Koutsouri, C. A. Mitsopoulou, *Coord. Chem. Rev.* **2012**, *256*, 2424–2434 (cit. on p. 154).

[320] C. W. Schlaepfer, K. Nakamoto, *Inorg. Chem.* **1975**, *14*, 1338–1344 (cit. on p. 156).

[321] K. Wang in *Dithiolene Chemistry*, (Ed.: E. I. Stiefel), Progress in Inorganic Chemistry, John Wiley & Sons, Inc, Hoboken, NJ, USA, **2003**, pp. 267–314 (cit. on p. 157).

[322] F. Fávaro de Oliveira, D. Antonov, Y. Wang, P. Neumann, S. A. Momenzadeh, T. Häußermann, A. Pasquarelli, A. Denisenko, J. Wrachtrup, *Rev. Mod. Phys.* **2017**, *8*, 15409 (cit. on p. 157).

[323] S. A. Momenzadeh, R. J. Stöhr, F. F. de Oliveira, A. Brunner, A. Denisenko, S. Yang, F. Reinhard, J. Wrachtrup, *Nano Lett.* **2015**, *15*, 165–169 (cit. on p. 157).

[324] M. Schmidt, PhD thesis, University Osnabrueck, Osnabrueck, **2019** (cit. on p. 162).

[325] M. Kianinia, O. Shimoni, A. Bendavid, A. W. Schell, S. J. Randolph, M. Toth, I. Aharonovich, C. J. Lobo, *Nanoscale* **2016**, *8*, 18032–18037 (cit. on p. 162).

[326] A. H. Heffernan, A. D. Greentree, B. C. Gibson, *Sci. Rep.* **2017**, *7*, 9252 (cit. on p. 162).

[327] N. Bar-Gill, L. M. Pham, C. Belthangady, D. Le Sage, P. Cappellaro, J. R. Maze, M. D. Lukin, A. Yacoby, R. Walsworth, *Rev. Mod. Phys.* **2012**, *3*, 858 (cit. on p. 163).

[328] S. Tomyn, S. I. Shylin, D. Bykov, V. Ksenofontov, E. Gumienna-Kontecka, V. Bon, I. O. Fritsky, *Rev. Mod. Phys.* **2017**, *8*, 14099 (cit. on p. 163).